MAGMATIC PROCESSES ASSOCIATED WITH THE DEVELOPMENT OF LARGE SILICIC CALDERAS

Ben Kennedy

Department of Earth & Planetary Sciences
McGill University, Montréal, Canada

December 2005

A thesis submitted to McGill University in partial fulfillment of the requirements of the degree of Doctor of Philosophy

Your file Votre référence
ISBN: 978-0-494-25185-0
Our file Notre référence
ISBN: 978-0-494-25185-0

ABSTRACT

Large caldera-forming eruptions are among the greatest hazards faced by mankind. Eruptive sequences from caldera-forming eruptions at Ossipee ring complex, New Hampshire, and Lake City caldera, Colorado, reveal that magmas underwent crystal fractionation to produce a zoned silicic magma chamber in each case before caldera formation. At Ossipee, magmatic inclusions with resorbed phenocrysts and positive Eu anomalies demonstrate that magma replenishment caused chamber rejuvenation and the initiation of caldera collapse. At Lake City, two ignimbrite units associated with episodes of caldera collapse have mafic-rich bases; this indicates that these collapse events were initiated by mafic magma replenishment. A numerical model is developed that describes how magma chamber rejuvenation causes a reduction in crystal content, a decrease in gas pressure, and hence caldera collapse. During caldera formation at Ossipee and Lake City, magmas from progressively deeper levels in the chambers were erupted and intruded to shallower levels. Periods of reverse compositional zonation and lateral compositional variation at the top of ignimbrite units and in post-collapse intrusions indicate that a period of accelerated magma interaction occurred in the chambers towards the end of subsidence. Scaled analogue experiments of caldera collapse into density-stratified magma chambers reveal a similar period of reverse zonation and dynamic fluid interaction as the subsiding block approaches the chamber base. Additionally, the experiments indicate that piecemeal or asymmetric collapse cause vortices to develop in the chamber which efficiently disrupt stratification. After caldera collapse at Ossipee and Lake City, replenishing magma caused mixed residual magma to intrude along caldera

faults to shallow levels and drive resurgence. The work illustrates how particular magmatic processes influence caldera collapse, and in turn, how caldera collapse affects particular magmatic processes.

RÉSUMÉ

Les grandes éruptions volcaniques associées à la formation de caldeiras comptent parmi les plus grands risques naturels auxquels l'humanité est exposée. Des séquences d'éruptions ayant formé des caldeiras au complexe annulaire d'Ossipee, New Hampshire et à la caldeira de Lake City, Colorado, révèlent que ces magmas ont d'abord évolué par cristallisation fractionnée pour produire une chambre magmatique silicique zonée avant formation de la caldeira. A Ossipee, des inclusions magmatiques contenant des phénocristaux résorbés et affichant une anomalie en Eu positive démontrent qu'une réalimentation de magma dans la chambre alors essentiellement cristallisée a causé la réjuvénation de la chambre puis initié l'effondrement de la caldeira. A Lake City, deux unités de l'ignimbrite associées à différents épisodes d'effondrement de la caldeira ont des bases plus mafiques; ceci indique que ces épisodes d'effondrement ont été initiés par une recharge par des magmas mafiques. Est proposé un modèle numérique décrivant comment la réjuvénation d'une chambre magmatique diminue le contenu en cristaux et la pression des gaz, entraînant finalement l'effondrement d'une caldeira,. Pendant la formation de la caldeira à Ossipee et Lake City, des magmas venant progressivement de niveaux de plus en plus profonds de la chambre ont été émis à la surface puis plus tard ont formé des intrusions près de la surface. Certains niveaux du toit des différentes unités

de l'ignimbrite et des intrusions post-effondrement sont inversement et latéralement zonés en composition, indiquant une période d'interaction magmatique exacerbée ayant eu lieu dans les chambres vers la fin de la subsidence. Des expériences analogiques dimensionnées d'effondrements de caldeira dans des chambres magmatiques stratifiées en densité révèlent un phénomène similaire de zonation et d'interactions de fluides dynamiques lorsque le bloc en subsidence approche la base de la chambre. De plus, ces expériences indiquent que des effondrements de type asymétrique et « piecemeal » sont capables de créer des vortex dans la chambre, perturbant efficacement la stratification. Après l'effondrement de la caldeira à Ossipee et Lake City, le nouveau magma rechargeant la chambre a forcé le magma résiduel homogénéisé à migrer le long des failles de la caldeira jusqu'à des niveaux superficiels et à initier de la résurgence. Ce travail illustre comment certains processus magmatiques influencent l'effondrement des caldeiras, et en retour, comment l'effondrement des caldeiras influence ces processus magmatiques.

ACKNOWLEDGEMENTS

First and foremost I thank John Stix for providing constant assistance with all aspects of this thesis. He has been a mentor and friend without whom my thesis was in danger of remaining a garbled mess of volcanological ideas. I also thank Nelson Eby who kindly provided unpublished data and discussion for Chapter 1. Robert Martin helped greatly with editing and discussion in Chapter 1, Peter Lipman furnished useful advice for Chapter 2, and Professor Andrew Hynes and Dr. Steve Blake provided helpful discussions for Chapter 3.

I am indebted to the McGill group of "Volcano dorks", Yan (La Banane) Lavallée, Mathieu Richer, Crystal Mann, Marc-Antoine (Marc 7) Longpré, Ricky Breger, (Bahama) John Hansen, John (De-Luxe) Davidson, Tyler (T-Phase) Barton, Geneviève (Geeves) Robert and Guillame (Geoid) Girard who all assisted with field work or in other aspects involved in the preparation of this thesis. Alain Garand, Nick Kaoukis and Sheldon Modeland provided support, beer and relaxation in the various bars of St. Laurent (mostly Biftek and Vol de Nuit).

The Kimball family showed great kindness and offered accommodation, pies and other goodies during several field excursions to the Ossipee Mountains. Jeff Coombs of the Ossipee Mountain Land Company, and Tom Curren of the Lakes Region Conservation Trust graciously provided access to land at Ossipee. Andi Kron and Charlie Thorne kindly provided accommodation during fieldwork at Lake City.

I would also like to thank various members of the Earth & Planetary Sciences staff. Anne Kosowski, Carol Matthews, and other EPS secretaries patiently provided

constant help with my financial catastrophes and without their help I probably would have been thrown out of McGill long ago. George Panagiotidis basically assisted with experimental design and thin section preparation. Shi Lang, Tariq Ahmedali, and Glenna Keating helped with the analyses at McGill.

Financial support was provided by funds from the Department of Earth and Planetary Sciences, McGill University (Lynch and McGregor scholarships), and from GEOTOP, Université du Québec à Montréal, and by a research grant to J.Stix from the Natural Sciences and Engineering Research Council of Canada. I also acknowledge support from NSF Grant EAR-0125631.

Lastly, I would like to thank my beautiful girlfriend Signe Wiingaard and my loving family for keeping me inspired.

TABLE OF CONTENTS

CONTRIBUTIONS OF AUTHORS

John Stix is a co-author in all my papers assisting in the development of ideas and editing. Ken Hon is second author of Chapter 2 and third author of Chapter 4, providing unlimited access to his Ph.D. dataset from Lake City. He also provided me with constant email assistance on both field and geochemical issues. Richard Breger is third author in Chapter 3 helping with experimental design, construction and procedure. He also assisted with editing and formatting this thesis.

GENERAL INTRODUCTION

INTRODUCTION

The chemical and textural diversity of intrusive and volcanic rocks at large silicic calderas are the result of 10^4-10^6 years of magmatic evolution (Wolff et al., 1990; Petford et al., 2000; Jellinek and DePaolo, 2003) overprinted by 10^1-10^2 hours of dynamic magma movement during caldera subsidence and eruption (Wolfe and Hoblitt, 1996; Wilson and Hildreth, 1997). Many authors use chemical characteristics of volcanic and intrusive rocks from caldera systems to understand magmatic processes (e.g. Hildreth, 1979); however, very little is known about how caldera collapse affects these magmas. This thesis aims to better understand the magmatic processes that occur before, during, and after caldera collapse. These processes include crystal fractionation, magma chamber replenishment and rejuvenation, magma mingling and mixing, assimilation, vesiculation, eruption, and resurgence. The processes have fundamental importance central to volcanology, igneous petrology, and the evolution of the upper crust. I hypothesize that these processes affect caldera formation, and in turn, caldera formation affects these processes.

Before a caldera forms, magma must accumulate at shallow levels in the crust. The morphology and internal structure of magma at shallow levels in the crust is poorly constrained. Field studies of batholiths frequently show complex internal relationships and evidence of episodic emplacement, re-intrusion, mingling, and stoping (e.g. Zak and Paterson, 2005). The study of volcanic deposits erupted during caldera collapse also provides data concerning the nature of these large magmatic systems (e.g., Hildreth, 1979). Volcanic rocks are relevant to study, as an exposure of a few tens of meters of

stratigraphic height can represent magma of several hundred meters of vertical extent in a magma chamber (e.g. Hildreth, 1979). Large volume eruptions from calderas are commonly highly evolved and may show various types of zonation. Zonation may be chemical in terms of major elements (e.g. Hildreth, 1979), trace elements (e.g., Bachman and Bergantz, 2004), volatiles (e.g. Anderson et al., 1989), isotopes (e.g. Bindeman and Valley, 2003), and crystal content (Bacon and Druitt, 1988). Chemical zonation is also inherently linked to gradients in the physical properties of the magma (Wolff et al., 1990). A chemically zoned magma chamber also will be zoned in terms of magmatic temperature, viscosity and density. The development of zonation in shallow magma chambers is controlled by (1) crystal fractionation, (2) magma replenishment, (3) magma mixing and mingling, and (4) assimilation of country rock (Spera and Bohrson, 2004).

MAGMATIC PROCESSES

PRIOR TO CALDERA COLLAPSE

During magma ascent to shallow levels in the crust, the chemical and textural characteristics of magma evolve. The mechanism that dominates shallow magmatic evolution is crystal fractionation (e.g. Anderson et al., 2000). The bulk chemistry of the magma changes if the melt and the crystals are separated by fractional crystallization. Mixing or mingling may modify magma as a chamber is replenished (Sparks and Marshall, 1986). At sufficiently high temperatures, magma also can melt surrounding rocks and assimilate this material into the magma, thus changing the bulk composition of the magma (Dungan and Davidson, 2004).

Researchers have proposed many different mechanisms for fractional crystallization: (1) crystal settling (Bowen, 1928), (2) sidewall crystallization and convection (e.g., Parsons and Brown, 1988), (3) compaction and expulsion (Philpotts et al., 1998), and (4) gas driven filter pressing (Sisson and Bacon, 1999). While these different mechanisms are feasible under magmatic conditions, particular magmatic conditions may favor one mechanism over another.

Crystal settling is the mechanism first envisaged to explain crystal fractionation (Bowen, 1928). The first minerals to crystallize are frequently denser than the melt and will sink. These crystals stop sinking when they reach the base of the magma chamber. Accumulations of crystals at the base of the chamber form a crystal cumulate. This mechanism can produce a chemically and texturally stratified magma chamber (e.g., Druitt and Bacon, 1989). Crystal settling times are long for small crystals in magma with a high viscosity, e.g., crystals of orthoclase 1 mm in diameter, in a rhyolitic melt with 1 wt. % water and viscosity of 10^6 Pa s, take 10^4 years to settle 1 km. Alternatively, the crystals may be less dense than the melt and rise or float (Morse, 1993). This process is likely in mafic magmas but less relevant to the silicic magmas discussed here.

All magmas in reservoirs of appreciable size (> 1 km in thickness) have Rayleigh numbers sufficiently high to convect. Under these conditions, convection rates exceed crystal-settling rates, indicating that many crystals remain suspended for extended periods of time (Sparks et al, 1984). At the same time, many authors have shown that crystal settling is a viable mechanism to explain horizontal magmatic layering in magma chambers (e.g., Anderson et al., 2000).

Crystal fractionation can occur by other means in a convecting magma chamber. A magma chamber will cool from the margins towards the center, precipitating crystals in advancing crystallization fronts (Marsh, 2000). These fronts can capture crystals from the liquid part of the magma chamber as it convects. The captured crystals become part of the crystallization front as the melt convects back into the main body of magma. In contrast to crystal settling, the melt moves away from the crystals. In this manner, a magma chamber will develop concentric chemical or textural stratification rather than horizontal stratification (Marsh, 1988).

Convection becomes increasingly complex when compositional, viscosity, and dissolved volatile gradients are present in the chamber (Sparks et al., 1984; Koyaguchi et al., 1990; Bagdassarov and Fradkov, 1993). A strong compositional gradient accompanied by a thermal gradient may allow double diffusive convection to control magma dynamics by generating a rhyolitic cap of melt, which is too buoyant to convect with the rest of the chamber (McBirney, 1980; Sparks et al., 1984). Such a chamber will crystallize eventually to produce a horizontally stratified chamber. Hence, convection can produce both horizontal and concentric stratification.

Studies of basaltic lava flows have shown that crystal fractionation processes occur in the absence of convection by compaction and collapse of crystallization fronts (Philpotts et al., 1998). Crystals in a crystallization front can become interconnected, forming a network with yield strength (Philpotts et al., 1998). This network also contains trapped melt of evolved composition. As crystallization continues, the network of interconnected crystals becomes increasingly thick and unstable. The stress exerted by the mass of the crystal network eventually exceeds the yield strength of the network; the

network then collapses, expelling melt from the network. Similar to other fractionation processes, this mechanism separates more silicic melt from mafic crystals. As this mechanism relies on gravity, it produces horizontal stratification.

Crystal fractionation also occurs by gas-driven filter pressing, expelling melt from crystallization fronts (Sisson and Bacon, 1999). If the crystallizing magma becomes saturated in gas, bubbles may be trapped in the network of the crystallization front. As these bubbles respond to increasing pressure in the magma chamber, melt is expelled from the crystallization fronts and crystal fractionation occurs. This mechanism is relevant to gas-saturated magmas that become overpressured during crystallization. A recent study by Bachman and Bergantz (2004) suggests that filter pressing can be aided by gas sparging from deeper magmas during magma chamber rejuvenation.

Magma replenishment can affect the chemistry and textures of magma. The replenishing magma may mix with resident magma to produce hybrid magma with intermediate chemical and textural characteristics. Hybrid magmas form if (1) the viscosity and temperature contrasts between the two interacting magmas are small (Sparks and Marshall, 1986), (2) the Reynolds number for the system is high (Bergantz, 2000), and (3) the mixing time is sufficiently long. If the temperature contrast is too large and the proportion of hot to cool magma too small, the hotter magma will chill and crystallize, creating a viscosity contrast and inhibiting mixing. High Reynolds numbers produce turbulent conditions by allowing instabilities to develop between two magmas, thus increasing the contact area between the magmas. If viscosity contrasts are too high or Reynolds numbers and mixing times insufficient, magmas may mingle but never mix to produce intermediate compositions. During mingling, magmas may become banded

(Sumner and Wolf, 2003), contain enclaves of the other magma (Vernon, 1990), or exhibit highly irregular contacts (Wiebe et al., 2004), but the original magma compositions remain chemically distinguishable.

Replenishment also can affect the resident magma indirectly by heat exchange between the magmas (Bachman and Bergantz, 2003; Spera and Bohrson, 2004). A change in magma temperature will affect viscosity, density, pressure, and hence many magmatic processes. A reduction in viscosity can increase the Stokes settling velocity, the Reynolds number for turbulence, and the Rayleigh number for convection. Additionally, an increase in temperature may cause melting, reduce crystallinity, and affect the liquid composition of the melt. This melting also may affect the chamber pressure.

The composition of the magma can be further modified by the assimilation of country rock. As magma rises through the crust, country rock in contact with the rising magma may begin to melt. Silicic minerals are the first to melt (Bowen, 1928), producing an evolved melt that may be assimilated into the rising magma. The chemical composition and isotopic ratios of the magma change according to the volume and chemical signature of the assimilated country rocks (Dungan and Davidson, 2004). The ingestion of large volumes of cold country rock may cool the magma, increasing crystallization rates and affecting other magmatic processes.

These processes generally occur on timescales of 10^2 -10^5 years. During eruption and caldera collapse, however, magmatic processes are accelerated due to the short duration of the subsidence event.

DURING AND AFTER CALDERA COLLAPSE

Volumetric eruption rates of historic plinian eruptions are on the order of 10^5 m^3 s^{-1} (Koyaguchi and Ohno, 2001). However, ring fracture eruptions are poorly constrained, with eruption rates potentially as high as 10^7 m^3 s^{-1} (Folch et al., 2001). These elevated rates correspond to high magma velocities at greater depths in the magma chamber. Magma movement in the chamber during eruption has been modeled and discussed by several authors (e.g., Spera, 1984). These studies have suggested that rapid magma withdrawal will increase the likelihood of magma mixing and mingling between stratified magmatic layers (Blake and Ivey, 1986a; Koyaguchi, 1985), promote magma replenishment (Kennedy and Stix, 2003), cause the disruption of crystallization fronts (Fulignati et al. 2004), and affect crystal fractionation mechanisms (Chapter 1, this thesis). A recent study illustrates the importance of decompression-driven crystallization using melt enclave data from Mt. St. Helens, demonstrating that significant crystallization can occur on eruptive timescales (Blundy and Cashman, 2005). This study shows the importance of syn-eruptive processes on crystal fractionation mechanisms. However, the effect of caldera collapse on magmatic processes, rather than simple withdrawal of magma, is rarely discussed or modeled.

Several studies have discussed the origin of textures in pumices from caldera-forming eruptions; in some cases these textures have been attributed directly to caldera collapse. For example, Fulignati et al. (2004) suggested that crystallization fronts may become disrupted during caldera collapse, thus accounting for crystallinity variation in the erupted ignimbrites. Several authors suggest that mingling textures in pumices may be caused by magma interactions during eruption and collapse rather than before collapse

on longer timescales, e.g. Amealco caldera, Mexico (Aguirre-Diaz, 2001). In addition, ignimbrites with mixed bulk compositions can be explained by post-fragmentation mechanical mixing following the simultaneous withdrawal of different layers from a stratified magma chamber (Spera et al., 1986; Sumner and Wolf, 2003).

Mingling and mixing processes during eruption have been modeled using numerical and analogue models of magma withdrawal or conduit flow (Blake and Ivey, 1986a; Blake and Ivey, 1986b; Spera, 1984; Spera et al., 1986; Trial et al., 1992). The numerical models can predict the evolution of eruption isochrons and stream functions within the chamber as magma is withdrawn. The variables investigated include eruption rate, magma viscosity, density, size and shape of the chamber and vent, and stationary versus subsiding chamber roofs (Spera, 1984; Spera et al., 1986; Trail et al., 1992). Recently, numerical models of caldera collapse using finite element modeling have shown that magma flow within the magma chamber can produce vortices in the predicted streamlines beneath the ring fault (Folch et al., 2001). The vortices illustrated in these models indicate the importance of the geometry of the chamber and the subsiding block. Yet, these numerical models never have been experimentally validated, and different collapse and chamber geometries have not been investigated.

After caldera collapse, magmatic processes will continue in the chamber. This period of magmatic activity is termed resurgence (Smith and Bailey, 1968). The processes active before collapse can continue to cause magmatic evolution and interaction. However, certain fundamental changes to the magmatic system have been produced by collapse and eruption. Lithostatic pressure may be reduced and magma rise encouraged (Kennedy and Stix, 2003). In addition, the structural continuity of the rocks

surrounding the magma chamber will be reduced which promotes magma rise above the main magma chamber (Kennedy and Stix, 2003).

THESIS ORGANIZATION

This thesis is divided into a general introduction and four chapters. All four chapters are manuscripts to be submitted to relevant journals. The principal conclusions, contributions to knowledge, and topics for future work are presented after Chapter 4. The objectives of the four manuscripts are outlined below.

OBJECTIVES

Before discussing the specific objectives of each chapter, I pose some fundamental questions that this thesis will address:

(1) How do replenishment and rejuvenation of large silicic magma chambers produce conditions suitable for caldera collapse?

(2) Why do these magma chambers erupt, and how is caldera collapse initiated?

(3) How does magma behave in a magma chamber during caldera formation?

(4) How do post-collapse magmas relate to magmas erupted earlier during caldera formation?

The different chapters of this thesis have specific objectives, each of which contributes towards a better understanding of the magmatic processes associated with the formation of large silicic calderas. The field studies in the first two chapters discuss magmatic processes recorded in intrusions and ignimbrites before, during, and after caldera collapse. The analogue experiments in Chapter 3 provide an experimental

validation for magmatic interactions that occur during collapse and eruption. Chapter 4 synthesizes the results of the first three chapters, allowing me to develop a novel numerical model that explains the initiation of caldera collapse by magma chamber rejuvenation.

Chapter 1 examines and interprets magmatic processes active during the development of Ossipee ring complex. The first objective of this study was to determine whether the rhyolite at Ossipee was pyroclastic or intrusive in origin, as both interpretations had been suggested in the literature (Kingsley, 1931; Carr, 1980). This objective addressed the process of magma fragmentation and establishes that Ossipee ring complex does represent a caldera, rather than an entirely subsurface subsidence structure. The second objective was to understand the magmatic processes that link the crystal-rich quartz syenite in the ring dyke with the rhyolite erupted in the caldera depression. The third objective was to determine the origin of magmatic enclaves in the quartz syenite and the rhyolite. This, in turn, led to the fourth objective, which was to establish the role of mafic magma in magma chamber rejuvenation, caldera formation and resurgence.

Chapter 2 examines and interprets the magmatic processes active during the development of Lake City caldera. The first objective was to chemically distinguish the different magma batches that erupted during the formation of the caldera. The second objective was to establish the magmatic processes responsible for these magma batches. The third objective was to constrain the temporal evolution of magmatic and eruptive activity during caldera formation, using the zonation and distribution of magmatic enclaves in the ignimbrites and intrusions. The fourth objective was to ascertain the

manner by which caldera collapse affected the style of renewed magmatism and resurgence after collapse.

Chapter 3 uses analogue experiments to illustrate the disruption of magmatic stratification during caldera collapse. The first objective of these experiments was to design a model of caldera collapse governed by fluid dynamics similar to a natural system. The second objective was to investigate the role of subsidence rate upon the timing and style of magma interaction. The third objective was to investigate how various collapse styles affect the timing and nature of magma interaction. The fourth objective was to illustrate the applicability of the experiments to natural systems.

Chapter 4 integrates the results of Chapters 1 to 3 into a general discussion of magma chamber processes associated with caldera collapse. The first objective was to develop a numerical model of magma chamber rejuvenation leading to caldera formation, using supporting evidence from Ossipee ring complex. The second objective was to use results from my experiments and field areas to illustrate the behavior of magma during caldera collapse. The third objective was to illustrate how caldera collapse affects the styles of resurgence seen at both field areas.

REFERENCES

Aguirre-Diaz, G.J., 2001, Recurrent magma mingling in successive ignimbrites from Amealco Caldera, central Mexico: Bulletin of Volcanology, v. 63, p. 238-251.

Anderson, A.T., Newman, S., Williams, S.N., Druitt, T.H., Skirius, C., and Stolper, E., 1989, H_2O, CO_2, Cl, and gas in Plinian and ash-flow Bishop rhyolite: Geology, v. 17, p. 221-225.

Anderson, A.T., Davis, A.M., and Lu, F.Q., 2000, Evolution of Bishop Tuff rhyolitic magma based on melt and magnetite inclusions and zoned phenocrysts: Journal of Petrology, v. 41, p. 449-473.

Bachman, O., and Bergantz, G.W., 2003, Rejuvenation of the Fish Canyon magma body: A window into the evolution of large-volume silicic magma systems: Geology, v. 31, p. 789-792.

Bachman, O., and Bergantz, G.W., 2004, On the origin of crystal-poor rhyolites: extracted from batholithic crystal mushes: Journal of Petrology, v. 45, p. 1565-1582.

Bacon, C.R., and Druitt, T.H., 1988, Compositional evolution of the zoned calcalkaline magma chamber of Mount Mazama, Crater Lake, Oregon: Contributions to Mineralogy and Petrology, v. 98, p. 224-256.

Bagdassarov, N.S., and Fradkov, A.S., 1993, Evolution of double diffusion convection in a felsic magma chamber: Journal of Volcanology and Geothermal Research, v. 54, p. 291-308.

Bergantz, G.W., 2000, Extracting rate information from magmatic data sets; a general template for working with the differing structure and granularity of compositional and kinematic information: Abstracts with Programs - Geological Society of America, v. 32,

p. 171.

Bindeman, I.N., and Valley, J.W., 2003, Rapid generation of both high- and low-delta (super 18) O, large-volume silicic magmas at the Timber Mountain/Oasis Valley caldera complex, Nevada: Geological Society of America Bulletin, v. 115, p. 581-595.

Blake, S., and Ivey G.N., 1986a, Magma mixing and the dynamics of withdrawal from stratified reservoirs: Journal of Volcanology and Geothermal Research, v. 27, p. 153-178.

Blake S., and Ivey, G.N., 1986b, Density and viscosity gradients in zoned magma chambers, and their influences on withdrawal dynamics: Journal of Volcanology and Geothermal Research, v. 30, p. 201-230.

Blundy, J., and Cashman, K., 2005, Rapid decompression-driven crystallization recorded by melt inclusions from Mount St. Helens Volcano: Geology, v. 33, p. 793-796.

Bowen, N.L., 1928, The Evolution of the Igneous Rocks: Dover Publications, Inc., 1956 reprint, 334p.

Carr, R.S., 1980, Geology and Petrology of the Ossipee ring-complex, Carroll County, New Hampshire, Masters thesis, Dartmouth College, 174 p.

Druitt, T.H., and Bacon, C.R., 1989, Petrology of the zoned calcalkaline magma chamber of Mount Mazama, Crater Lake, Oregon: Contributions to Mineralogy and Petrology, v. 101, p. 245-259.

Dungan, M.A., and Davidson, J., 2004, Partial assimilative recycling of the mafic plutonic roots of arc volcanoes; an example from the Chilean Andes: Geology, v. 32, p. 773-776.

Folch, A., Codina, R., and Marti, J., 2001, Numerical modeling of magma withdrawal during explosive caldera-forming eruptions: Journal of Geophysical Research, v. 106, p. 16,163-16,175.

Fulignati, P., Marianelli, P., Santacroce, R., and Sbrana, A, 2004, Probing the Vesuvius magma chamber-host rock interface through xenoliths: Geological Magazine, v. 141, p. 417-428.

Hildreth, E.W., 1979, The Bishop Tuff: Evidence for the origin of compositional zonation in silicic magma chambers: In Chapin, C.E., and Elston, W.E. (eds.), Ash-Flow Tuffs: Geological Society of America Special Paper 180, p. 43-72.

Hon, K.A., 1987, Geologic and petrologic evolution of the Lake City Caldera, San Juan Mountains, Colorado. Ph.D. Thesis, University of Colorado, Boulder, Colorado, 244 p.

Jellinek, A.M., and DePaolo, D.J., 2003, A model for the origin of large silicic magma chambers; precursors of caldera-forming eruptions: Bulletin of Volcanology, v. 65, p. 363-381.

Kennedy, B., and Stix, J., 2003, Stages in the temporal evolution of calderas: Geoscience Canada, v. 30, p. 129-140.

Kingsley, L., 1931, Cauldron subsidence of the Ossipee Mountains: American Journal of Science, v. 22, p. 139-168.

Koyaguchi, T., 1985, Magma mixing in a conduit, Journal of Volcanology and Geothermal Research, v. 25, p. 365-369.

Koyaguchi, T., Hallworth, M.A., Huppert, H.E., and Sparks, R.S.J., 1990, Sedimentation of particles from a convecting fluid: Nature, v. 343, p. 447-450.

Koyaguchi, T., and Ohno, M., 2001, Reconstruction of eruption column dynamics on the basis of grain size of tephra fall deposits; 2, Application to the Pinatubo 1991 eruption: Journal of Geophysical Research, v. 106, p. 6513-6533.

Lipman, P.W., 1976, Caldera-collapse breccias in the western San Juan Mountains, Colorado: Geological Society of America Bulletin, v. 87, p. 1397–1410.

Marsh, B.D, 1988, Crystal capture, sorting and retention in convecting magma: Geological Society of America Bulletin, v. 100, p. 1720-1737.

Marsh, B.D., 2000, Magma Chambers: In Sigurdsson, H., Houghton, B., McNutt, S., Rymer, H., and Stix, J. (eds.), Encyclopedia of Volcanoes: Academic Press, San Diego, USA, p. 191-206.

McBirney, A.R., 1980, Mixing and unmixing of magmas: Journal of Volcanology and Geothermal Research, v. 7, p. 357-371.

Morse, S.A., 1993, Behavior of a perched crystal layer in a magma ocean: Journal of Geophysical Research, v. 98, p. 5347□5353.

Parsons, I., and Brown, W.L., 1988, Sidewall crystallization in the Klokken Intrusion; zoned ternary feldspars and coexisting minerals: Contributions to Mineralogy and Petrology, v. 98, p. 431-443.

Petford, N., Cruden, A.R., McCaffrey, K.J.W., and Vigneresse, J.L., 2000, Granite magma formation, transport and emplacement in the Earth's crust: Nature, v. 408, p. 669-673.

Philpotts, A.R., Shi, J., and Brustman, C., 1998, Role of plagioclase crystal chains in the differentiation of partly crystallized basaltic magma: Nature, v. 395, p. 343-346.

Sisson, T.W., and Bacon, C.R., 1999, Gas driven filter pressing in magmas: Geology, v 27, p. 613-616.

Smith, R.L., and Bailey, R.A., 1968, Resurgent cauldrons: Memoir - Geological Society of America, p. 613-662.

Sparks, R.J., Huppert, H.E., and Turner, J.S., 1984, The Fluid dynamics of evolving magma chambers: Philosophical Transactions of the Royal Society of London, v. A310, p. 511-534.

Sparks, R.J., and Marshall, L.A., 1986, Thermal and mechanical constraints on mixing between mafic and silicic magmas: Journal of Volcanology and Geothermal Research, v. 29, p. 99-124.

Spera, F.J., 1984, Some numerical experiments on the withdrawal of magma from crustal reservoirs: Journal of Geophysical Research, v. 89, p. 8222-8236.

Spera, F.J., Yuen, D.A., Greer, J.C., and Sewell, G., 1986, Dynamics of magma withdrawal from stratified magma chambers: Geology, v. 14, p. 723-726.

Spera, F.J., and Bohrson, W.A., 2004, Open-system magma chamber evolution; an energy-constrained geochemical model incorporating the effects of concurrent eruption, recharge, variable assimilation and fractional crystallization (EC-E'RAchi FC): Journal of Petrology, v. 45, p. 2459-2480.

Sumner, J.M., and Wolff, J., 2003, Petrogenesis of mixed-magma, high-grade, peralkaline ignimbrite "TL" (Gran Canaria); diverse styles of mixing in a replenished, zoned magma chamber: Journal of Volcanology and Geothermal Research, v. 126, p. 109-126.

Trial, A.F., Spera, F.J., Greer, J., and Yuen, D.A., 1992, Simulations of magma withdrawal from compositionally zoned bodies: Journal of Geophysical Research, v. 97, p. 6713-6733.

Vernon, R.H., 1990, Crystallization and hybridism in microgranitoid enclave magmas; microstructural evidence: Journal of Geophysical Research, v. 95, p. 17,849-17,859.

Wiebe, R.A., Manon, M.R., Hawkins, D.P., and McDonough W.F., 2004, Late stage mafic injection and rejuvenation of the Vinalhaven granite, Coastal Maine: Journal of Peterology, v. 45, p. 2133-2153.

Wilson, C.J.N., and Hildreth, W.H., 1997, The Bishop Tuff; new insights from eruptive stratigraphy: Journal of Geology, v. 105, p. 407-439.

Wolfe E.W., and Hoblitt, R.P., 1996, Overview of the eruptions: In Newhall, C.G., and Punongbayan, R.S. (eds.), Fire and Mud, Eruptions and Lahars of Mount Pinatubo, Philippines: Philippine Institute of Volcanology and Seismology and the University of Washington Press, p. 3-20.

Wolff, J.A., Woerner, G., and Blake, S., 1990, Gradients in physical parameters in zoned felsic magma bodies; implications for evolution and eruptive withdrawal: Journal of Volcanology and Geothermal Research, v. 43, p. 37-55.

Zak, J., and Paterson, S.R., 2005, Characteristics of internal contacts in the Tuolumne Batholith, central Sierra Nevada, California (USA); implications for episodic emplacement and physical processes in a continental arc magma chamber: Geological Society of America Bulletin, v. 117, p. 1242-1255.

CHAPTER 1

Magmatic processes associated with caldera collapse at Ossipee ring dyke, New Hampshire

Ben Kennedy and John Stix

ABSTRACT

A ring dyke is an annular intrusion of solidified magma, 2 to 50 km in diameter, which forms as a magma chamber roof collapses. We texturally and geochemically investigate a section through the Ossipee ring dyke in New Hampshire, which provides a remarkably comprehensive record of magmatic and volcanic events during caldera formation. The majority of the ring dyke consists of quartz syenite with syenite, rhyolite, and basalt also present as small mingled dykes, xenoliths or magmatic enclaves. The quartz syenite is crystal rich and contains enclaves of fine-grained syenite. These enclaves are more primitive, exhibit a positive Eu anomaly, and are depleted in crystals relative to the host. The composition of anorthoclase feldspar crystals in the enclaves is similar to the bulk-rock composition of the enclaves. These anorthoclase phenocrysts have unusually high CaO contents, indicating magmatic temperatures up to 1050 °C. Rhyolite in the ring dyke is texturally and geochemically equivalent to large volumes of ignimbrite which crop out inside the caldera. Basalt in the ring dyke occurs as both xenoliths from earlier volcanoes and as basaltic dykes which mixed and mingled with rhyolitic dykes during eruption.

Our analysis of the ring dyke at Ossipee suggests the following events. (1) A magma chamber fractionated to form a large volume of rhyolitic magma overlying crystal-rich quartz syenite and cumulate syenite. (2) Basalt partially melted the anorthoclase cumulate that comprised the base of the chamber to form a layer of hot mobile syenitic liquid (the enclaves now in the ring dyke). (3) The intrusion of the basalt triggered massive eruptions of rhyolitic ignimbrite which ponded inside the caldera as the

roof of the magma chamber collapsed. (4) Caldera collapse stirred various layers in the magma chamber and mingled and mixed rhyolitic, quartz syenitic, and syenitic magma. (5) Quartz syenite, rhyolite and small volumes of basalt magma intruded simultaneously into the ring dyke, causing the basalt and rhyolite to mingle explosively.

We show that convection, crystal settling, and the filtration of melt away from crystallization fronts contributed to forming a zoned magma chamber before caldera collapse. Basalt replenished and rejuvenated the magma chamber at Ossipee, driving eruption, and facilitating dyke intrusion. We suggest that the development of vortices around the base of subsiding blocks during caldera collapse explains the mixing and mingling textures seen at Ossipee. The magma within the Ossipee ring dyke represents residual magma from a period of dynamic chamber processes, which were accelerated and accentuated by caldera collapse.

INTRODUCTION

Ring complexes provide a rare exposure of shallow magmatic plumbing beneath a caldera; both volcanic and intrusive rocks are frequently exposed (Marshall and Sparks, 1984; Johnson et al., 2002; Troll et al., 2004). A section of the ring dyke at Ossipee ring complex (New Hampshire, USA) contains a remarkably comprehensive record of the volcanic and magmatic rock types and textures found throughout the complex. This unique exposure illustrates the dynamic volcanic and magmatic history of a caldera collapse event. The rocks from the Ossipee ring dyke show evidence for crystal fractionation, magma replenishment, remelting, rejuvenation, magma mixing and

mingling, degassing and fragmentation. The study of these rocks demonstrates how these magmatic processes influence the style and timing of caldera collapse. In turn, the collapse of the caldera causes profound changes in the magmatic system. This synergy and feedback between magma chamber and caldera processes is the main focus of this study.

In this paper, we concentrate on an area of the ring dyke spectacularly exposed in a river section. We present detailed field relationships, as well as chemical and textural data outlining the different magma types, enclaves and crystals. We hypothesize that (1) the rhyolite, quartz syenite, and syenite represent different parts of a zoned magma chamber prior to collapse, (2) basaltic magma replenished the magma chamber and melted the syenitic cumulate base of the chamber, initiating events leading to caldera collapse, (3) mixing and mingling of the different magmas occurred during the collapse event, and (4) the rhyolite represents ignimbrite ponded inside a subsiding caldera.

BACKGROUND GEOLOGY

The Ossipee ring complex is located in New Hampshire between the towns of Sandwich and Ossipee, 10 km south of the White Mountain Batholith. This complex is among the youngest of the alkaline, anorogenic, White Mountain magma series (200 to 110 Ma) (Fig. 1a) and is dated at 121 ±2 Ma (Foland and Faul, 1977). The anorogenic character of Ossipee ring complex is illustrated by largely bimodal magmatism. The regional tectonics at the time of emplacement was largely extensional and related to the opening of the Atlantic ocean. The ring complex represents a caldera eroded to a level of about 3 km (Kingsley, 1931). The Ossipee complex is the best-preserved caldera

FIGURE 1. (a) Location map of Ossipee ring complex, redrawn from Creasy and Eby (1993). (b) Geological map of Ossipee ring complex, modified from Carr (1980). (c) Detailed geology of the Cold Brook section, also showing the location of figure 2a.

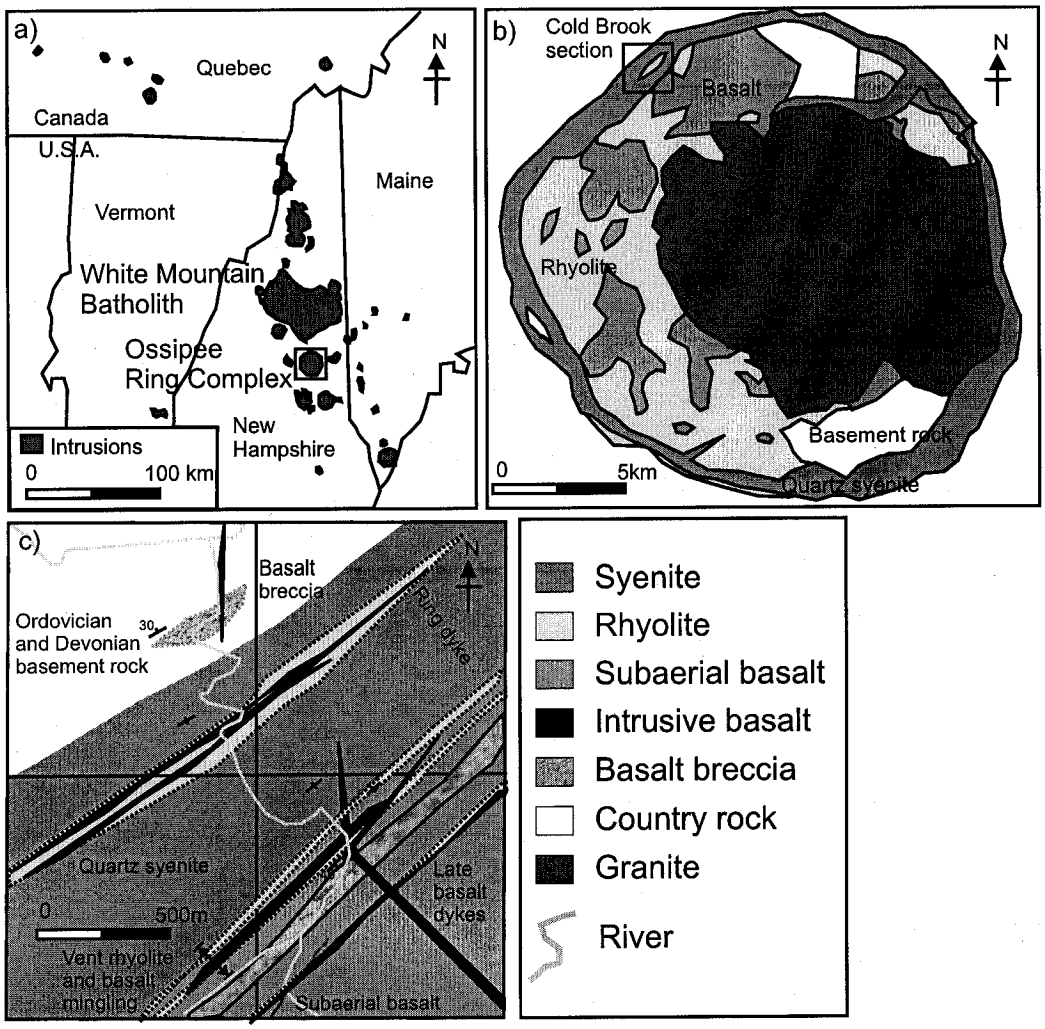
a)
Quebec
Canada
U.S.A.
Vermont
Maine
White Mountain
Batholith
Ossipee
Ring Complex
New
Hampshire
Intrusions
0
100 km
N
b)
Cold Brook
section
Basalt
Rhyolite
Basement rock
Quartz syenite
0
5km
N
c)
Basalt
breccia
Ring dyke
Ordovician
and Devonian
basement rock
30
Quartz syenite
0
500m
Late
basalt
dykes
Vent rhyolite
and basalt
mingling
Subaerial basalt
N
Syenite
Rhyolite
Subaerial basalt
Intrusive basalt
Basalt breccia
Country rock
Granite
River

structure in the White Mountain Magma Series, and is one of the best examples of a ring complex in the world. The complex contains a complete ring dyke, and the rocks are generally well-preserved with no metamorphic overprint. The subsidence at Ossipee juxtaposes volcanic rocks erupted during caldera collapse against a ring dyke filled with magmas that never erupted (Fig.1b). In spite of these exceptional geological relationships, very little work has been done on the complex (Kingsley, 1931; Billings, 1943; Chapman, 1972; Carr, 1980).

The ring complex intruded into Devonian country rock mostly composed of schist, diorite and pegmatite. The complex consists of rhyolite and basalt encircled by a quartz syenite ring dyke and subsequently intruded by granitic magma. The rhyolite and basalt within the caldera originally were interpreted as interbedded volcanic deposits that were erupted explosively and ponded within a caldera subsiding along ring faults now represented by the ring dyke (Kingsley, 1931). Carr (1980) later challenged this interpretation and reinterpreted the rhyolite as a shallow intrusion. In terms of the volcanic history of the complex, these two interpretations are very different. The shallow intrusion suggested by Carr (1980) implies that the ring complex is not a true caldera but instead a series of magma chambers formed by stoping. In this paper, we analyze the textures and compositions of the rhyolite and the other ring dyke magmas to test the hypothesis that the rhyolite is pyroclastic and that the complex does indeed represent a caldera.

The ring dyke represents an annular subsidence fault intruded by quartz syenitic and other magmas (Billings, 1943). The ring dyke is fundamentally important to the complex, as it sheds light on eruptive and magmatic processes. The ring dyke contains

mingled alkaline magmas derived from various structural levels of the underlying reservoir and so preserves information on the development and disruption of magmatic stratification within a magma reservoir. Also, the ring dyke contains evidence of complex mixing and mingling between basaltic and rhyolitic magmas (Carr, 1980), as well as evidence for the fragmentation of magma (Kingsley, 1931). The ring dyke also encircles a central granite intrusion which was intruded later and is geochemically distinct (Carr, 1980). For these reasons, it is not examined in detail in this paper.

METHODS

This study is based on detailed field mapping conducted during the summers of 2001 and 2003, supplemented by textural and geochemical analysis. We mapped textural and petrological changes throughout the ring complex. We identified key localities and mapped these in detail. In this report, we present a map of a river-polished section through the most texturally diverse area of the ring dyke (Fig. 1c). In addition, we made in situ textural analyses by taking photos of 10 cm^2 river-polished slabs. The photos were traced to distinguish individual crystals. Two-dimensional crystal size distributions were generated using the image analysis program Image J (Higgins, 1996). Since crystals have highly irregular shapes, conversions into three-dimensional crystal-size distributions could not be made.

We also sampled the ring complex systematically and collected over 300 hand samples. From these samples, over 60 thin sections were made and examined. In addition to providing textural information, these thin sections helped us select samples for

geochemical analysis. We chose our samples for geochemical analysis by carefully considering the geochemical results of Kingsley (1931), Carr (1980), and Eby and Kennedy (2004). We focused on rocks containing textural evidence for magma mingling. Many samples contained substantial numbers of enclaves, necessitating careful preparation of the samples. Some enclaves were isolated for analysis, whereas others were removed from samples before analysis to obtain pure compositions. Geochemical analyses were done by X-ray fluorescence (XRF). Prepared samples were crushed and ground into powder, made into fused beads, and analyzed for whole-rock major-element and trace-element concentrations by XRF techniques. We also analysed selected rocks for rare earth elements (REE) by Inductively Coupled Plasma Mass Spectrometry (ICP-MS). The REE data were normalized to chondrites using the values of Taylor and McLennan (1985). The XRF and REE results are listed in Table 1.

We examined thin sections to choose fresh feldspar grains suitable for compositional analysis, from a range of rock types and enclaves. We again focused on crystals that appeared to have undergone transfer between magma types. We measured feldspar compositions with the electron microprobe (JEOL JXA-8900L) using wavelength dispersive analysis. The oxide weight percentage data were converted to cation weight percentages and plotted in a Na-K-Ca triangular diagram. The feldspar data are listed in Appendix I.

TABLE 1. Whole rock major, trace and rare earth elements analysis using XRF and ICP-MS. Trace elements marked with an * and major elements were analysed using XRF by McGill Geochemical Laboratories, Montréal. Trace elements and all rare earth elements were analysed using ICP-MS, and sample OSP14* using XRF, by Activation Laboratories, Ancaster.

Sample		OSP-7 granitic country rock	OSP-310 granitic ring dyke	OSP-2005-05 pyro-clastic rhyolite	OSP-106B pyro-clastic rhyolite	OSP-19B porphrytic rhyolite	OSP-05 granitic ring dyke	OSP-97B granitic ring dyke
SiO_2	wt. %	72.40	74.19	72.52	73.50	73.60	74.24	73.85
TiO_2	wt. %	0.22	0.22	0.27	0.25	0.38	0.24	0.25
Al_2O_3	wt. %	14.78	12.83	12.66	12.71	12.13	12.30	12.64
Fe_2O_3	wt. %	1.56	2.56	3.17	3.06	3.61	3.19	2.90
MnO	wt. %	0.05	0.08	0.10	0.09	0.04	0.11	0.09
MgO	wt. %	0.35	0.14	0.18	0.14	0.41	0.12	0.14
CaO	wt. %	0.53	0.26	1.26	0.41	0.98	0.31	0.37
Na_2O	wt. %	3.54	4.23	4.05	4.20	4.61	4.35	4.26
K_2O	wt. %	5.56	5.00	5.02	5.12	3.61	4.72	5.10
P_2O_5	wt. %	0.16	0.05	0.04	0.04	0.05	0.03	0.05
LOI	wt. %	0.88	0.47	0.95	0.45	0.68	0.20	0.44
Total	wt. %	100.03	100.03	100.22	99.98	100.09	99.81	100.09
V	ppm	12.00	2.00	5.00	6.00	22.00	3.00	4.00
Cr_2O_3	ppm	51.00	48.00	31.00	38.00	62.00	43.00	39.00
Ni	ppm	10.00	7.00	9.00	5.00	7.00	6.00	5.00
Zn	ppm				280	< 30	120	100
Ga	ppm				30	26	26	31
Ge	ppm				1.7	1.5	1.5	1.8
Rb	ppm				187	93	120	221
Rb*	ppm	322.2	219.7		185.9	92.6	154.9	179.3
Sr	ppm				13	91	73	16
Sr*	ppm	98.4	19.7		16.6	96.3	12.9	13.0
Y	ppm				57.5	65	46.1	65.4
Y*	ppm	14.4	65.1		57.5	65.7	59.7	49.8
Zr	ppm				591	494	623	498
Zr*	ppm	144.9	441.9		573.2	469.0	494.8	571.3
Nb	ppm				77.9	84.1	59.9	81.5
Nb*	ppm	11.4	90.7		82.5	95.7	94.6	91.5
Mo	ppm				4	< 2	2	3
Ag	ppm				0.6	< 0.5	0.7	0.7
In	ppm				0.2	0.1	< 0.1	< 0.1
Sn	ppm				4	4	3	4
Sb	ppm				< 0.2	< 0.2	< 0.2	< 0.2
Cs	ppm				2.4	0.9	8.4	3.3
Ba	ppm				83	220	810	113
BaO	ppm	425.00	115.00	52.00	72.00	250.00	45.00	84.00
Hf	ppm				14.1	13.2	13.1	13.1
Ta	ppm				5.03	5.73	4.01	5.71
W	ppm				1.1	0.6	1.2	1.2
Tl	ppm				1.11	0.76	0.71	1.22
Pb	ppm				28	< 5	24	55
Pb*	ppm	50.0	34.4		28.8	6.6	18.9	12.6
Bi	ppm				1.5	0.1	0.1	5.4
Th	ppm				22	24.3	15.5	26.1
U	ppm				5.22	5.08	3.66	6.4

Sample		OSP-7 granitic	OSP-310 granitic	OSP-2005-05 pyro-	OSP-106B pyro-	OSP-19B porphrytic	OSP-05 granitic	OSP-97B granitic

		country rock	ring dyke	clastic rhyolite	clastic rhyolite	rhyolite	ring dyke	ring dyke
La	ppm				115	108	93	113
Ce	ppm				232	210	185	216
Pr	ppm				26.4	24.6	21.5	25.8
Nd	ppm				95.5	90.1	82.1	94.6
Sm	ppm				17.1	17.5	14.5	17.9
Eu	ppm				0.838	0.562	3.44	0.82
Gd	ppm				14.7	15.9	12.2	16
Tb	ppm				2.18	2.45	1.78	2.46
Dy	ppm				11.3	12.5	9.25	12.8
Ho	ppm				2.1	2.34	1.71	2.4
Er	ppm				5.87	6.67	4.78	6.79
Tm	ppm				0.823	0.985	0.685	0.995
Yb	ppm				5.06	5.89	4.05	5.91
Lu	ppm				0.707	0.803	0.583	0.804

Sample		OSP-13 quartz syenite	OSP-14 quartz syenite	OSP-14* quartz syenite	OSP-30 quartz syenite	OSP-38 quartz syenite	OSP-14 syenite inclusion (type 1)	OSP-14 * syenite inclusion (type 1)
SiO_2	wt. %	67.66	68.85	68.87	67.83	69.81	60.55	60.61
TiO_2	wt. %	0.47	0.47	0.46	0.49	0.46	0.89	0.89
Al_2O_3	wt. %	14.68	14.17	14.21	14.37	13.97	17.64	17.85
Fe_2O_3	wt. %	3.68	3.81	3.77	3.79	3.74	5.37	5.43
MnO	wt. %	0.13	0.16	0.15	0.16	0.15	0.20	0.20
MgO	wt. %	0.39	0.41	0.40	0.48	0.42	0.70	0.74
CaO	wt. %	1.48	1.34	1.31	1.42	1.14	2.08	2.03
Na_2O	wt. %	3.57	4.11	3.96	4.50	4.34	3.93	3.76
K_2O	wt. %	6.47	5.68	5.55	5.37	5.37	7.45	7.27
P_2O_5	wt. %	0.19	0.18	0.16	0.19	0.17	0.45	0.44
LOI	wt. %	1.04	0.59	0.59	1.05	0.20	0.69	0.85
Total	wt. %	99.76	99.76	99.43	99.65	99.77	99.95	100.07
V	ppm	14.00	9.00		7.00	7.00	25.00	
Cr_2O_3	ppm	35.00	39.00	< 0.01	32.00	36.00	32.00	< 0.01
Ni	ppm	5.00	2.00		3.00	4.00	1.00	
Zn	ppm	80	80	210				
Ga	ppm	27	27	29				
Ge	ppm	1.4	1.6	1.5				
Rb	ppm	140	118	158				
Rb*	ppm	141.7	120.5		122.0	134.9	158	161.9
Sr	ppm	102	83	180				
Sr*	ppm	100.7	82.2		74.0	50.4	180	186.8
Y	ppm	46.4	48.7	27.6				
Y*	ppm	43.7	45.4		44.0	41.3	27.6	26.8
Zr	ppm	620	685	695				
Zr*	ppm	615.1	623.0		621.2	613.2	695	708.7
Nb	ppm	60.1	63.3	30.3				
Nb*	ppm	38.8	42.4		39.9	62.3		<d/l
Mo	ppm	< 2	< 2	< 2				
Ag	ppm	0.5	0.7	0.5				
In	ppm	0.1	0.1	< 0.1				
Sn	ppm	2	2	< 1				
Sb	ppm	< 0.2	< 0.2	< 0.2				
Cs	ppm	1.5	2.9	5.9				
Ba	ppm	940	771	1980				
BaO	ppm	1086.00	876.00		918.00	617.00	2400.00	
Hf	ppm	12.7	14.4	12				
Ta	ppm	3.8	4.09	1.89				
W	ppm	1.4	1.5	1.1				
Tl	ppm	0.96	0.61	1.09				
Pb	ppm	11	23	19				
Pb*	ppm	10.6	27.1		20.6	21.9		16.0
Bi	ppm	0.2	0.2	0.2				
Th	ppm	14.9	16.8	4.66				
U	ppm	3.33	3.72	1.33				

Sample		OSP-13 quartz	OSP-14 quartz	OSP-14* quartz	OSP-30 quartz	OSP-38 quartz	OSP-14 syenite	OSP-14 * syenite

		syenite	syenite	syenite	syenite	syenite	inclusion (type 1)	inclusion (type 1)
La	ppm	90.1	103	58.2				
Ce	ppm	179	204	116				
Pr	ppm	20.8	23.5	14				
Nd	ppm	79.5	88.6	57.6				
Sm	ppm	13.9	15.3	9.68				
Eu	ppm	3.3	3.22	6.98				
Gd	ppm	11.9	13.1	8.38				
Tb	ppm	1.79	1.88	1.14				
Dy	ppm	9.02	9.7	5.6				
Ho	ppm	1.69	1.82	1.05				
Er	ppm	4.76	5.03	2.82				
Tm	ppm	0.679	0.725	0.392				
Yb	ppm	4.25	4.34	2.44				
Lu	ppm	0.592	0.619	0.345				

Sample		OSP-03-11 syenite inclusion (type 2)	OSP-108C porphrytic basalt	OSP-145 porphrytic basalt	OSP-149 basalt	OSP-303 basalt	Detection limits
							(ppm)
SiO_2	wt. %	63.24	52.26	49.72	49.56	51.67	60.00
TiO_2	wt. %	0.64	2.35	2.29	3.13	2.90	35.00
Al_2O_3	wt. %	17.32	19.03	17.90	17.12	16.36	120.00
Fe_2O_3	wt. %	4.28	10.13	9.94	11.85	11.36	30.00
MnO	wt. %	0.20	0.20	0.24	0.18	0.26	30.00
MgO	wt. %	0.60	3.05	4.63	3.56	3.76	95.00
CaO	wt. %	1.78	8.00	10.51	9.05	8.18	15.00
Na_2O	wt. %	5.18	2.71	2.60	3.45	3.01	75.00
K_2O	wt. %	6.30	2.11	1.66	1.58	2.20	25.00
P_2O_5	wt. %	0.26	0.37	0.31	0.52	0.41	35.00
LOI	wt. %	0.31	0.23	0.57	0.50	0.41	100.00
Total	wt. %	100.11	100.45	100.37	100.50	100.53	
V	ppm	4.00	244.00	287.00	283.00	303.00	10.00
Cr_2O_3	ppm	46.00	6.00	80.00	8.00	26.00	15.00
Ni	ppm	11.00	-6.00	-2.00	-8.00	-8.00	3.00
Zn	ppm	100					30
Ga	ppm	24					1
Ge	ppm	1.3					0.5
Rb	ppm	82					1
Rb*	ppm	82	49.4	61.5	45.3	160.4	
Sr	ppm	70					2
Sr*	ppm	70	480.9	444.8	503.9	399.6	
Y	ppm	29					0.5
Y*	ppm	29	33.4	31.9	33.4	34.4	
Zr	ppm	995					1
Zr*	ppm	995	278.0	221.4	273.1	263.6	5
Nb	ppm	32.9					0.2
Nb*	ppm		26.5	25.0	27.6	28.7	
Mo	ppm	< 2					2
Ag	ppm	0.8					0.5
In	ppm	< 0.1					0.1
Sn	ppm	< 1					1
Sb	ppm	< 0.2					0.2
Cs	ppm	3.9					0.1
Ba	ppm	883					3
BaO	ppm	1016.00	417.00	402.00	483.00	315.00	17.00
Hf	ppm	16.2					0.1
Ta	ppm	1.92					0.01
W	ppm	0.6					0.5
Tl	ppm	0.49					0.05
Pb	ppm	15					5
Pb*	ppm		16.4	27.3	41.1	2.9	
Bi	ppm	< 0.1					0.1
Th	ppm	4.9					0.05
U	ppm	1.45					0.01

Sample		OSP-03-11 syenite	OSP-108C porphrytic	OSP-145 porphrytic	OSP-149 basalt	OSP-303 basalt	Detection limits

		inclusion (type 2)	basalt	basalt	(ppm)
La	ppm	60.6			0.05
Ce	ppm	117			0.05
Pr	ppm	14.4			0.01
Nd	ppm	58			0.05
Sm	ppm	9.78			0.01
Eu	ppm	5.65			0.005
Gd	ppm	8.25			0.01
Tb	ppm	1.16			0.01
Dy	ppm	5.7			0.01
Ho	ppm	1.07			0.01
Er	ppm	2.93			0.01
Tm	ppm	0.402			0.005
Yb	ppm	2.58			0.01
Lu	ppm	0.377			0.002

RESULTS

GEOLOGICAL RELATIONSHIPS

Kingsley (1931), Smith et al. (1939), Quinn, (1941, 1953), Wilson (1969), and Carr (1980) have identified the main features and relationships displayed by the complex (Fig. 1b). Our mapping at Ossipee concentrated upon detailed examination of the best-exposed areas rather than remapping the entire complex. However, we propose minor modifications to the map of Carr (1980). The ring dyke is probably complete, as originally mapped by Kingsley (1931), since patchy exposures can be found in the southwestern corner of the map, as mapped by Carr (1980). In this area, the ring dyke is complex and appears to thin and bifurcate. In addition, the composition of the ring dyke is generally granitic rather than quartz syenitic, resulting from multiple intrusions. We also mapped thin dykes of porphyritic rhyolite that crosscut the rhyolite and basalt within the caldera. In addition, the distribution of basalt within the rhyolite is far more intricate than indicated on the map of Carr (1980). The basalt is generally not massive but rather brecciated with irregular boundaries gradually disaggregating into the rhyolite.

A complete ring dyke gives the impression that Ossipee is a simple piston-like structure. However, closer examination reveals a strong degree of asymmetry in the complex for the following reasons. (1) In the eastern half of the caldera, Ordovician and Devonian basement is exposed, whereas in the west thick sequences of rhyolite and basalt exist (Kingsley, 1931) (Fig. 1b). (2) In the eastern half of the complex, faults juxtapose rocks from different stratigraphic levels (Fig. 1b). (3) Apophoses of the ring dyke intrude the caldera in the northeast and southwest as originally mapped by Kingsley (1931) (Fig.

1b). These observations indicate that the caldera floor was broken into a series of blocks before the ring dyke intruded, and differential subsidence occurred on these blocks.

Figure 1c illustrates the complexities of the ring dyke, as well as exposures of intracaldera and extracaldera volcanic rocks at Cold Brook. This area is located in the northwestern part of the complex and provides almost continuous exposure from outside the caldera, through the ring dyke, and into volcanic rocks inside the caldera (Fig. 1b). Although rare at Ossipee, volcanic rocks are found outside the ring dyke at this locality. A small exposure of basaltic breccia with fragmental rhyolite clasts overlies Ordovician schist and Devonian granite, dipping away from the complex centre at 15 to 45°. Late basaltic dykes crosscut these rocks. The ring dyke at Cold Brook consists of vertically dipping quartz syenite rich in dark grey enclaves. The margin of the ring dyke grades into fragmental rhyolite, exhibiting fluidal mingling and the transfer of crystals between the two magmas. Mixed basaltic and rhyolitic breccias also are exposed within the rhyolite. Another 300 m thick zone of syenite forms the rest of the ring dyke. The inner margin of the quartz syenite grades into fragmental rhyolite, mingled basalt and basaltic andesite dykes (Figs. 2a to d). This zone consists of multiple dykes, with crystals and magma found in various stages of fragmentation, mingling, crystal exchange, and hybridization (Figs. 2a to d). The dips of these interbedded fragmental basalt and rhyolite rocks vary from near-vertical adjacent to the ring dyke to 45° to the southeast toward the centre of the complex (Fig. 1c). Further towards the caldera centre, fragmental rhyolite, basaltic mesobreccias containing blocks of country rock, and basaltic lava flows are exposed. In summary, the margins of the ring dyke at this locality show various magmas interacting in different ways, with evidence of pyroclastic eruptions.

FIGURE 2. (a) View looking northwest down Cold Brook, illustrating the proximity and diversity of textures in this section of the ring dyke. (b) An area of mixed and mingled quartz syenite and fragmental rhyolite also containing syenite enclaves. (c) Porphyritic rhyolite mixing and fragmenting with basalt to produce a basaltic andesite hybrid containing 2 cm epidotized phenocrysts. (d) Fragmental rhyolite mingling with basalt to produce intricate banding.

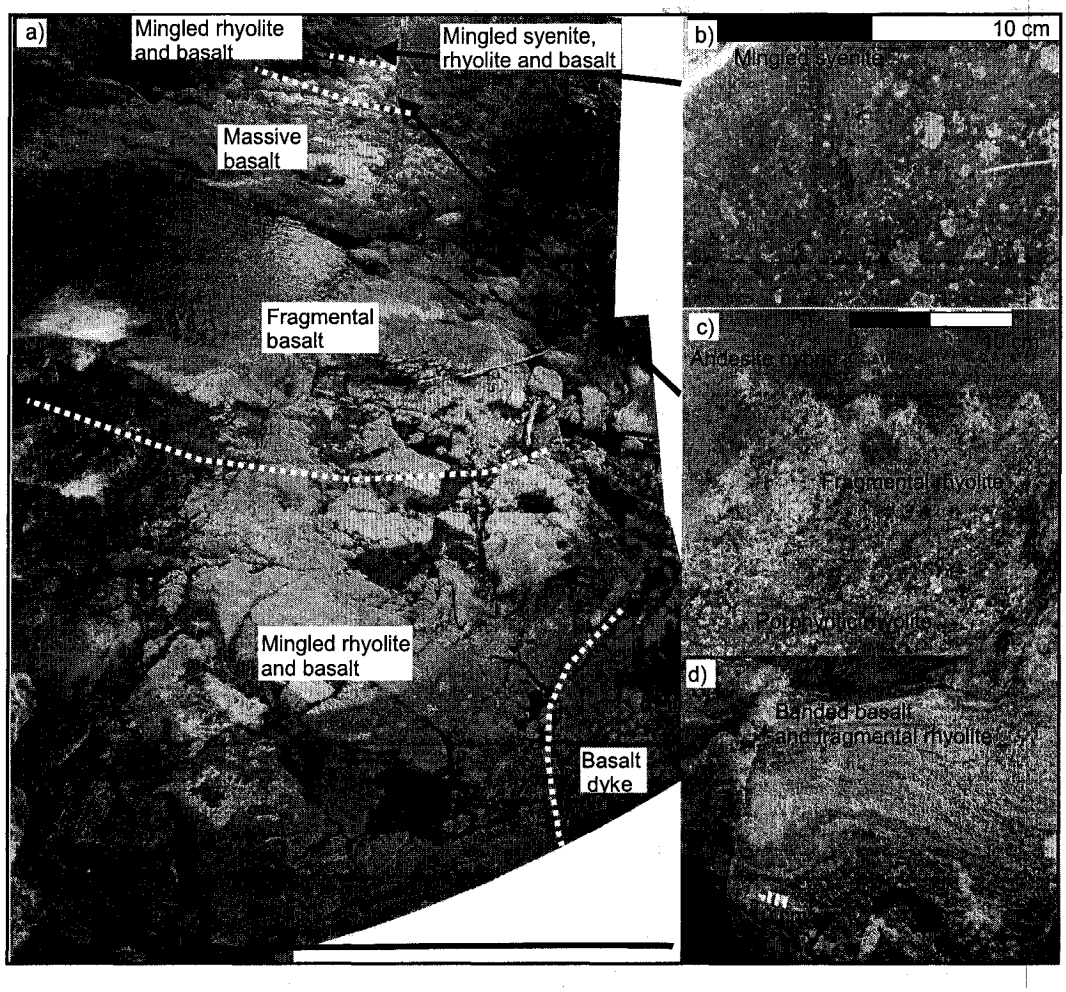
a)
Mingled rhyolite and basalt
Mingled syenite, rhyolite and basalt
Massive basalt
Fragmental basalt
Mingled rhyolite and basalt
Basalt dyke
b)
10 cm
Mingled syenite
c)
Andesite
Fragmental rhyolite
Porphyritic rhyolite
d)
Banded basalt and fragmental rhyolite

PETROLOGICAL DESCRIPTIONS OF ROCK TYPES

In this section, we present petrological descriptions of the common rock types found within the complex. The observations are a synthesis of field and thin-section descriptions as well as textural analysis.

The rhyolite in the ring dyke and in other areas of the complex has a fine-grained recrystallized grey matrix, with a spherulitic texture seen in some samples. The majority of the rhyolite contains angular fragments and shards of pink K-feldspar and quartz 1 to 5 mm long and in proportions of 15 to 20 % and 5 to 10 %, respectively (Fig. 3a); rare grey fragments of alkaline feldspar also can be seen in thin section. Fragments of quartz also contain embayments on unfractured crystal surfaces. Commonly the rhyolite contains angular basaltic lithic fragments, which in some cases occur as layers (Fig. 3b). Fiamme and eutaxitic textures can be seen in the ring dyke at Cold Brook and in many outcrops across the complex (Fig. 3a). The pyroclastic textures are best seen adjacent to blocks of basaltic breccia or where the rhyolite contains dark fluidal enclaves. Some relict pumice fragments contain larger, less fragmented crystals. In Cold Brook and other areas of the complex, basalt and fragmental rhyolite have mingled on metre and millimetre scales, producing banded and brecciated zones. At the margins of dykes, magma interaction between basalt and rhyolite has produced basaltic andesite hybrids. In Cold Brook, the fragmental rhyolite also exhibits gradational contacts with the quartz syenite.

A coarsely porphyritic variety of rhyolite is found as small dykes and enclaves within the fragmental rhyolite and syenite in some areas of the complex (Fig. 3c). The groundmass is dark grey and recrystallized, and may in some cases contain a spherulitic texture (Carr, 1980). This variety of rhyolite contains pink K-feldspar and quartz 5 to 20

FIGURE 3. (a) Rhyolite containing fragments of orthoclase crystals; a fiamme structure is also shown that we interpret as a relict fragment of pumice. (b) Fragmental rhyolite containing angular clasts of basalt. Some basalt clasts show in-situ fracturing and contain veins of fragmental rhyolite. (c) Porphyritic rhyolite with xenocrystic anorthoclase, and a small enclave of syenite containing a large crystal clump of anorthoclase. (d) Quartz syenite containing a diffuse relict syenite enclave. (e) A discrete enclave showing evidence for crystal transfer into and out of the enclave. Xenocrystic orthoclase and a rimmed xenocryst of quartz are also seen in the enclave. (f) Syenite with type 1 and type 2 enclaves. Type 2 enclaves contain small crystals of anorthoclase and occasional plagioclase. (g) Massive basalt with plagioclase phenocrysts; some of these are glomerocrysts. (h) A hybrid basaltic andesite with large laths of plagioclase replaced by epidote. (i) Basaltic breccia containing sub rounded clasts and fluidal basaltic shapes indicating a pepperitic origin.

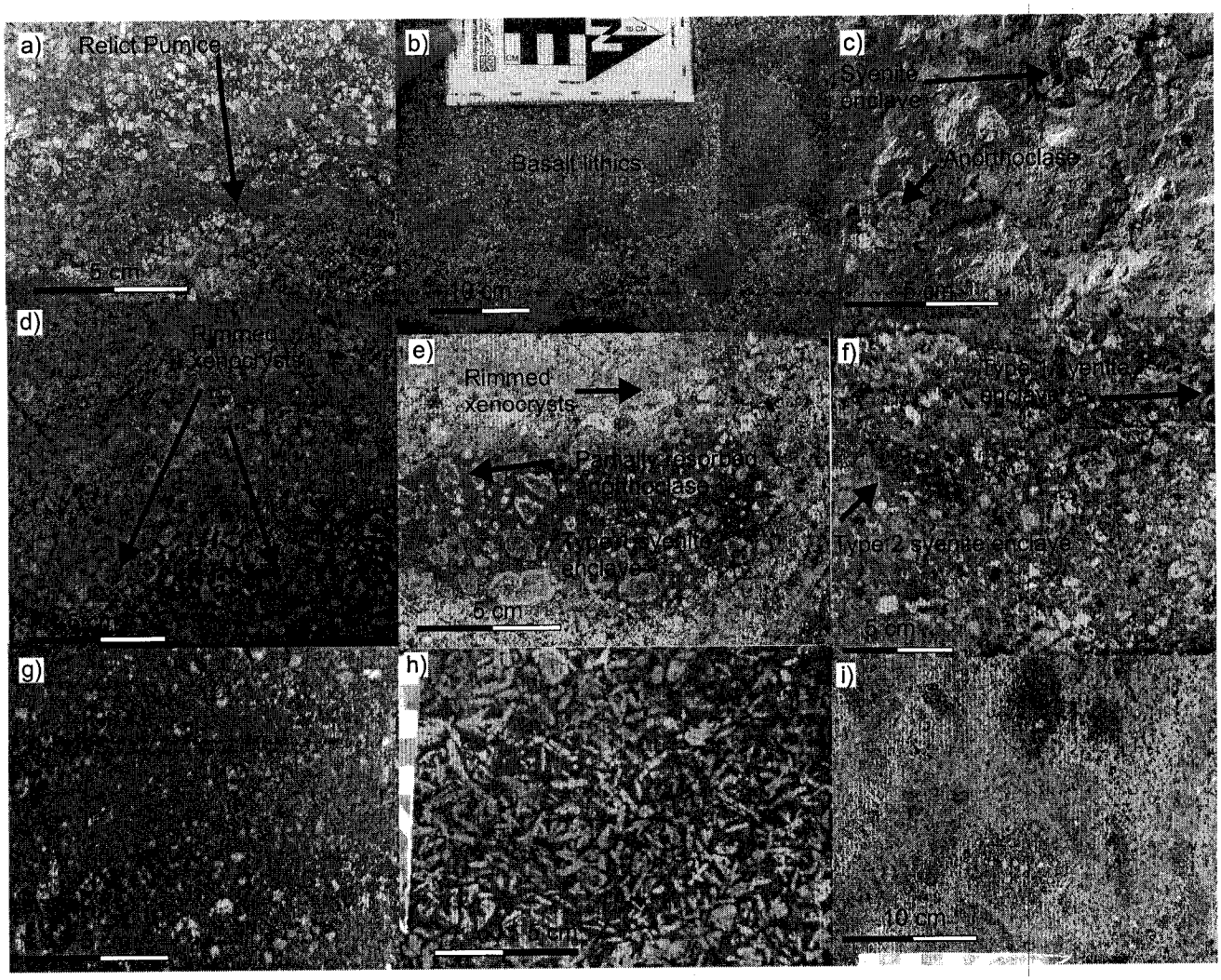
a)
Relict Pumice
5 cm
b)
Basalt lithics
10 cm
c)
Syenite enclave
Apatite
5 cm
d)
Rimmed Xenocrysts
e)
Rimmed Xenocrysts
Partially resorbed apatite
Type 1 syenite enclave
5 cm
f)
Type 1 syenite enclave
Type 2 syenite enclave
5 cm
g)
h)
15 cm
i)
10 cm

mm long and in proportions of 22 to 27 % and 5 to 12 %, respectively. The pink K-feldspar occur as individual crystals and in irregular clumps with ragged cores and distinct rims. The K-feldspar crystals are perthitic with sodic and potassic unmixing occurring on various scales. Quartz occurs as single crystals, frequently with a beta-quartz bipyramidal form. These quartz phenocrysts are also commonly embayed. Rare xenocrystic grey alkali feldspar crystals are also present in some localities (Fig. 3c). These feldspars appear to be derived from dark enclaves in this rhyolite that contain similar grey alkali feldspar crystals (Fig. 3c).

The quartz syenite ring dyke is richer in dark grey enclaves than the rhyolites. The composition of the ring dyke varies from granitic to quartz syenite, but it is invariably texturally distinguishable from the rhyolite discussed above. The rock of the ring dyke has a fine-grained groundmass with a salt and pepper texture in hand sample (Fig. 3d to f). In thin section, the groundmass shows an interconnected lattice of sub-mm sized K-feldspar crystals. In between these crystals is an intergrowth of quartz and orthoclase showing a granophyric texture. Due to the presence of these sub-millimetric sized crystals, the crystallinity of the quartz syenite is greater than 50 %. The rock is coarsely porphyritic containing 1 to 20 mm sized phenocrysts of K-feldspar, quartz, and grey alkali feldspar in proportions of 15 to 35 %, 3 to 5 % and, 5 to 18 %, respectively. Similar to the porphyritic rhyolite, the K-feldspar phenocrysts occur as individual crystals and clumps with irregular shapes, rims and altered zones (Fig. 3d). The cores of the crystals are spongy, frequently filled with recrystallized groundmass, and have multiple rims. Most crystals are perthitic, although the scale of unmixing depends on the zone within the crystal; commonly, only small areas in the cores are free from observable unmixing in

thin section. Pink K-feldspar is rimmed occasionally by grey alkali feldspar. The grey alkali feldspar crystals are similar in texture to the K-feldspar, although generally more ragged. These crystals have particularly spongy cores and are often glomeroporphrytic and rimmed by pink K-feldspar. Quartz crystals commonly show bipyramidal beta-quartz and are frequently embayed and rimmed by fine-grained opaque mafic minerals.

The abundant dark, relatively crystal poor enclaves in the ring dyke can be classified into three types. Type 1 enclaves are the most common, generally roughly spheroidal, 1 to 20 cm long, and contain large grey alkali feldspar crystals (Figs. 3e to f). These crystals have well developed rims but are extremely spongy, and their abundance in the enclaves varies from 0 to 35 %. In some cases, they contain an interconnected network of devitrified glass within the crystal. Type 1 enclaves have a diffuse margin and can contain xenocrystic pink K-feldspar crystals. Crystals of pink K-feldspar and grey alkali feldspar frequently occur at the boundaries between the enclaves and the host syenite. Quartz phenocrysts are very rare in enclaves, appearing to be xenocrystic and often rimed by K-feldspar. Type 1 enclaves occur in various states of disaggregation in the quartz syenite (Fig. 3d). Type 2 enclaves are 5 to 20 cm long, elongate with well-defined margins, generally crystal poor and contain plagioclase or anorthoclase crystals 1 to 3 mm in length. Type 3 enclaves are similar to the porphyritic variety of rhyolite, generally roughly spheroidal, 5 to 20 cm long and rich in pink K-feldspar and quartz with no grey alkali feldspar.

The mafic rocks in the ring complex show a variety of textures. In Cold Brook, dykes of basalt containing plagioclase phenocrysts 1 to 3 mm in length crop out alongside basaltic andesite with flow-aligned plagioclase laths up to 2 cm in length (Fig. 3g). These

plagioclase laths have been replaced by epidote (Fig. 3h). A coarsely porphyritic variety of basaltic andesite is also common in other areas of the complex; this variety contains glomeroporhyritic plagioclase crystals 10 mm in length. The groundmass of the basalt and basaltic andesite commonly contains flow-aligned plagioclase microlites. Hybrid mafic rocks exposed in Cold Brook frequently contain partially resorbed, skeletal and even sheared phenocrysts. Enclaves of rhyolite are frequently present in basalts close to rhyolite outcrops. Basaltic breccias are also common in Cold Brook and in the rest of the complex (Fig. 3i). These breccias are both monolithic and polylithic, depending on location; some also contain fluidal basalt or basaltic andesite clasts. Juvenile basaltic fragments contain a fine-grained recrystallized groundmass, indicating that these fragments may have once been glassy. Other breccias contain quartz grains in the matrix and have abundant clasts of dioritic country rock and rhyolite.

CRYSTAL-SIZE DISTRIBUTION

In this section, we use plots of overall phenocryst percentage and crystal size distributions to demonstrate the visible textural and compositional variability in select samples from Ossipee (Fig. 4a, b). The phenocryst percentage plot shows that the rhyolites have lower phenocryst percentages than the quartz syenites (Fig. 4a). The rhyolites also contain higher percentages of quartz and no visible grey alkali feldspar crystals. The phenocryst percentage of the syenite varies considerably, with syenites 2 and 3 having the highest phenocryst percentage and the lowest percentage of grey alkaline feldspar crystals. The type 1 enclave contains the most grey alkali feldspar, no quartz and a relatively small percentage of K-feldspar, yet with a relatively high overall

FIGURE 4. (a) The visible phenocryst content for quartz, anorthoclase and orthoclase in hand samples for nine rock types from Ossipee. (b) The crystal-size distribution for feldspar crystals (orthoclase and anorthoclase) for these nine rocks.

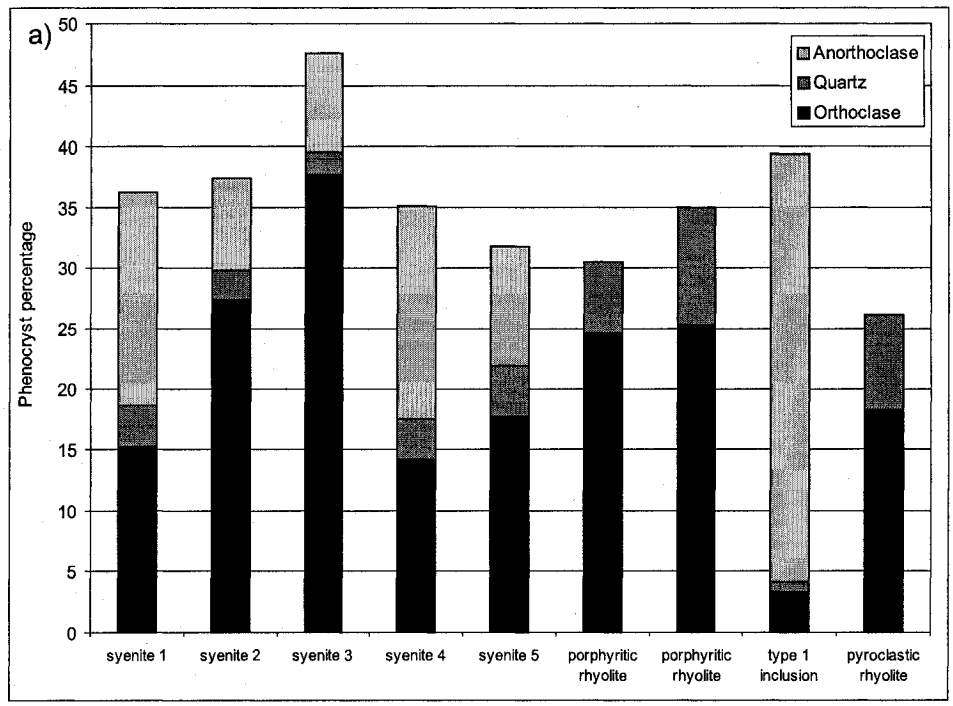
a)
Anorthoclase
Quartz
Orthoclase
Phenocryst percentage
0
5
10
15
20
25
30
35
40
45
50
syenite 1
syenite 2
syenite 3
syenite 4
syenite 5
porphyritic rhyolite
porphyritic rhyolite
type 1 inclusion
pyroclastic rhyolite

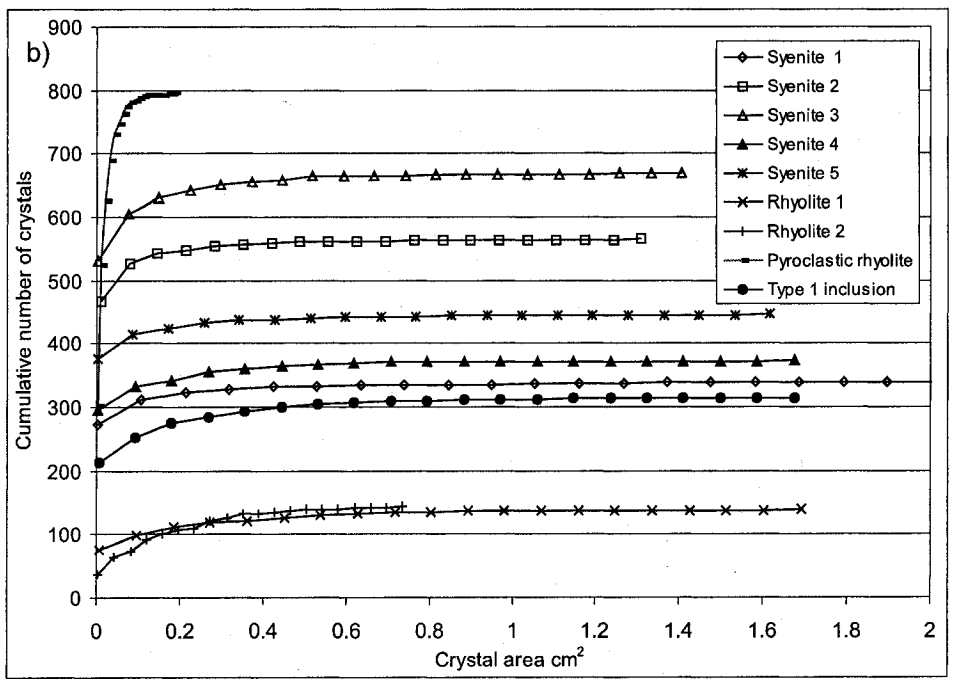
b)
Syenite 1
Syenite 2
Syenite 3
Syenite 4
Syenite 5
Rhyolite 1
Rhyolite 2
Pyroclastic rhyolite
Type 1 inclusion
Cumulative number of crystals
0
100
200
300
400
500
600
700
800
900
0
0.2
0.4
0.6
0.8
1
1.2
1.4
1.6
1.8
2
Crystal area cm2

phenocryst percentage. Crystal-size distribution plots of the alkali feldspars show that the fragmental rhyolite has a different distribution compared to the porphyritic rhyolite, the quartz syenite, or the type 1 enclave (Fig. 4b). The fragmental rhyolite contains large numbers of small crystals and few large crystals. The porphyritic rhyolite has fewer small crystals than the quartz syenite but similar distributions at large crystal sizes (Fig. 4b).

The crystal-size distributions of the feldspars in quartz syenite and type 1 enclaves are interesting. We plotted the pink and grey alkali feldspars together, and the distributions for the syenites are generally similar. However, differences do exist; for example, syenite 1 and 4 have fewer small feldspar crystals yet a higher percentage of large grey alkali feldspar crystals than the other syenites (Figs. 4a and b). Also, there are fewer but larger alkali feldspar phenocrysts in the enclaves compared to the quartz syenite samples. These crystal size distributions indicate a link between the presence of anorthoclase crystals and the lack of small crystal sizes.

GEOCHEMISTRY

Our major-element data for whole-rock and matrix compositions are plotted with the data of Carr (1980) and Eby (unpublished data). Figure 5a shows that TiO_2 decreases as SiO_2 increases. The plot shows two different slopes for the mafic rocks and the silicic rocks. The enclaves have less SiO_2 and more TiO_2 than the quartz syenites, which in turn have less SiO_2 and more TiO_2 than the rhyolites. In the mafic rocks and the enclaves, TiO_2 is lower in the groundmass than in the whole rock. Figure 5b shows that CaO decreases as SiO_2 increases in a similar manner to TiO_2. In addition, CaO shows an enrichment in the groundmass of the quartz syenite and one of the syenite enclaves. Both

FIGURE 5. XRF whole-rock analysis for Ossipee rocks, analyses made by (Carr 1981) and Eby (unpublished data), are also plotted for comparison. (a) TiO_2 plotted against SiO_2. (b) CaO plotted against SiO_2. (c) Na_2O plotted against SiO_2. (d) K_2O plotted against SiO_2. (e) Zr plotted against SiO_2. (f) Zr/Y plotted against Y. (g) Sr plotted against SiO_2. (h) Sr/Y plotted against Y. All major elements are normalized to anhydrous compositions.

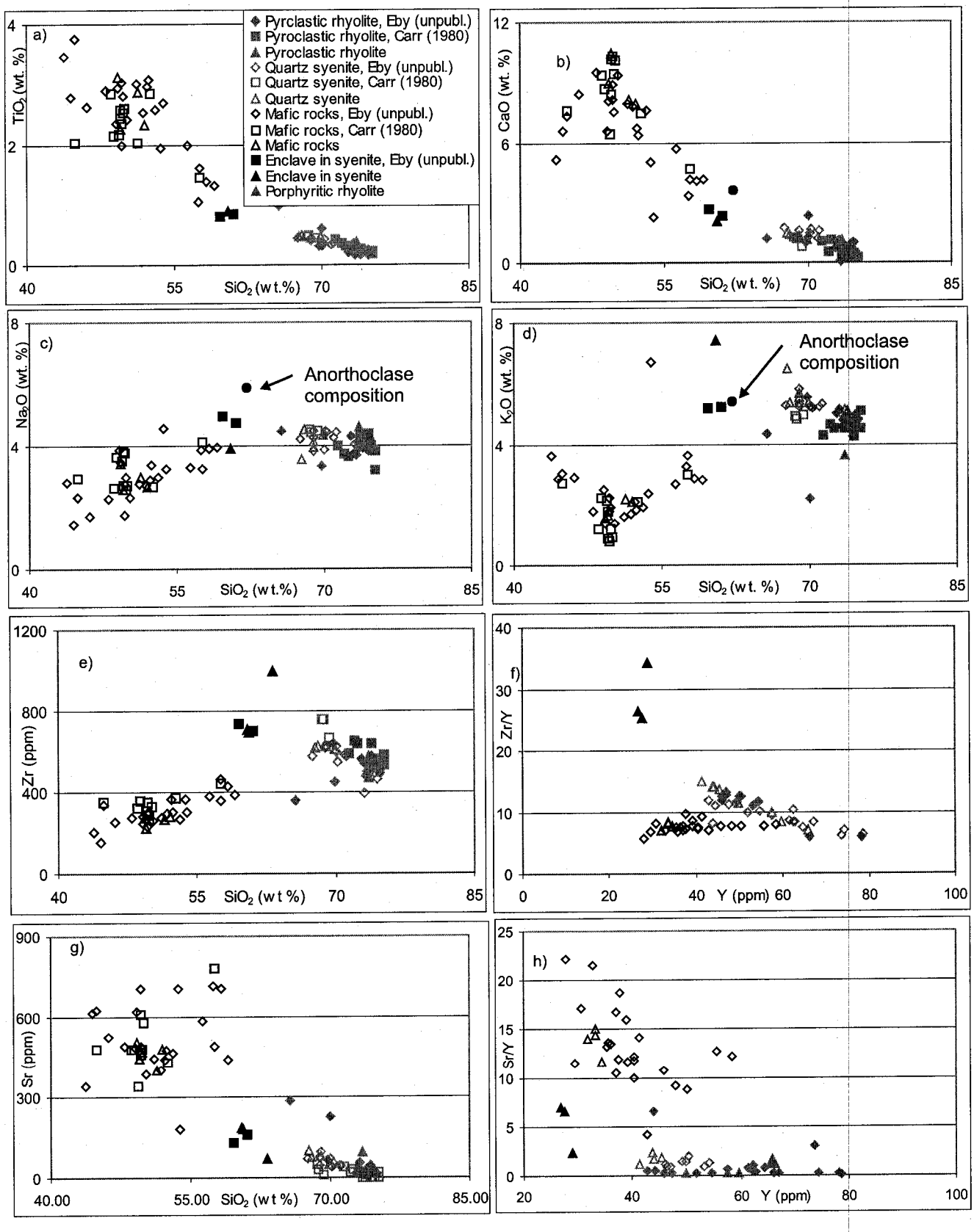
a)
TiO2 (wt. %)
SiO2 (wt.%)
Pyrclastic rhyolite, Eby (unpubl.)
Pyroclastic rhyolite, Carr (1980)
Pyroclastic rhyolite
Quartz syenite, Eby (unpubl.)
Quartz syenite, Carr (1980)
Quartz syenite
Mafic rocks, Eby (unpubl.)
Mafic rocks, Carr (1980)
Mafic rocks
Enclave in syenite, Eby (unpubl.)
Enclave in syenite
Porphyritic rhyolite
b)
CaO (wt. %)
SiO2 (wt. %)
c)
Na2O (wt. %)
Anorthoclase composition
d)
K2O (wt. %)
Anorthoclase composition
e)
Zr (ppm)
f)
Zr/Y
Y (ppm)
g)
Sr (ppm)
h)
Sr/Y
Y (ppm)

TiO_2 and CaO are compatible elements in these systems and are removed from the melt during crystallization of mafic minerals and plagioclase. Hence, crystallization and crystal fractionation cause Ca and Ti to become depleted in the silicic rocks and hence show a negative correlation with SiO_2.

Figure 5c and 5d show Na_2O, and K_2O plotted against SiO_2. The mafic rocks generally show increases in potassium as SiO_2 increases, whereas the silicic rocks show a small but noticeable decrease in alkali elements as SiO_2 increases. The increase in K and Na in the mafic rocks can be explained by K and Na incompatiblity during the crystallization of calcic plagioclase and mafic minerals phases which accumulated in the mafic magma. However, both Na and K are incorporated in the alkali feldspars that crystallized and fractionated in the silicic magmas. Therefore, the crystallization of alkali feldspar alone will deplete the melt in Na and K and could explain the decrease in total alkalis as SiO_2 increases in the felsic rocks. Alternatively, silica may have been enriched relative to alkali content due to the loss of alkali elements during devitrification in the formally glassy rhyolites (Yurtman and Rowbotham, 1999). A fluctuating ratio of K/Na indicates that there has been some secondary alkali exchange during hydration; this may explain some scatter in Figures 5c and d but will not significantly affect the total alkalis (Table 1).

Trace-element ratios help to distinguish magmatic evolution trends. Figure 5e shows Zr plotted against SiO_2; two distinct trends exist for the mafic rocks and the felsic rocks. Zr increases with SiO_2 in the mafic rocks and decreases with SiO_2 in the felsic rocks. Zirconium can behave as a compatible or incompatible element depending on whether zircon is crystallizing.

Figure 5f shows Zr/Y plotted against Y. Yttrium is a highly incompatible element; the mafic rocks show a constant Zr/Y ratio, whereas the silicic rocks show a strong decrease in Zr/Y as Y increases. In the mafic rocks, the constant Zr/Y ratio implies similar levels of incompatibility of Y and Zr as these elements were enriched in the melt phase in similar proportions as the magma evolved. In the felsic rocks, however, Zr behaves as a compatible element. Zr is depleted in the rhyolites, somewhat enriched in the quartz syenites, and strongly enriched in the syenite enclaves. This behaviour of Zr implies that zircon was crystallizing and fractionating in the silicic rocks but not in the mafic rocks (Watson, 1979). The high Zr/Y in the syenite enclaves implies that the zircon crystals that were fractionating from the rhyolite were accumulating in the magma represented by the syenite enclaves. The low and constant Zr/Y ratios of the mafic rocks imply no accumulation of zircon, and magmatic evolution distinct from the felsic magmas.

Figure 5g shows Sr plotted against SiO_2; Sr decreases as SiO_2 increases. Sr behaves as a compatible element partitioning into feldspars (Leeman and Phelps, 1981). The strong decrease in Sr with magma evolution implies that the chemical signature of Ossipee rocks is strongly influenced by feldspar fractionation. Figure 5h shows Sr/Y; again the felsic rocks form a trend separate from the mafic rocks. The mafic rocks have high Sr/Y, which decreases as Y increases; feldspar fractionation is consistent with this trend and would enrich Y in the melt phase and Sr in the plagioclase. In the felsic rocks the enclaves have higher Sr/Y values and generally lower Y values than do the syenites or the rhyolites; crystal fractionation also could explain this trend. However, the different

FIGURE 6. REE normalized to chondritic composition (Taylor and McLennon, 1985) for whole-rock compositions of felsic samples; mean values from Eby (unpublished data) are plotted for comparison.

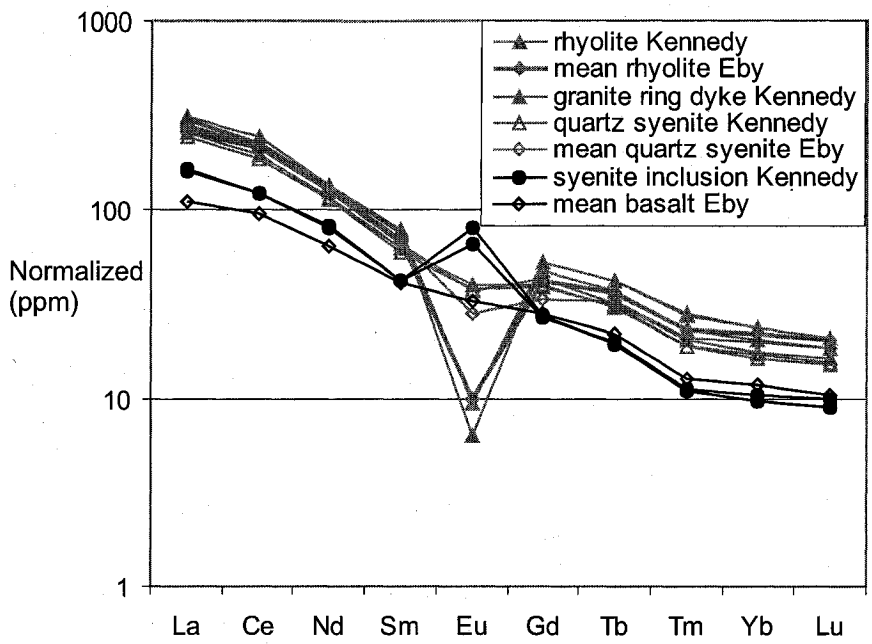
1000
100
10
1
Normalized (ppm)
La
Ce
Nd
Sm
Eu
Gd
Tb
Tm
Yb
Lu
rhyolite Kennedy
mean rhyolite Eby
granite ring dyke Kennedy
quartz syenite Kennedy
mean quartz syenite Eby
syenite inclusion Kennedy
mean basalt Eby

Sr/Y trends for the mafic and silicic rocks imply that the magmas evolved separately, consistent with the Zr/Y data.

Chondrite-normalised REE data for the rhyolites, quartz syenites, and syenitic enclaves are plotted on Figure 6, with additional data from Eby (unpublished data). Rhyolites have the highest REE concentrations, with the exception of Eu which is strongly depleted. The quartz syenites have lower REE concentrations relative to the rhyolites except for Eu which is only moderately depleted. The syenitic enclaves have lower concentrations in all REE relative to the other silicic rocks, except for Eu which shows a positive Eu anomaly and the highest Eu concentrations of all rocks studied. The REE trends for the felsic rocks are parallel to each other but steeper than for the basalts. The different REE slopes between the mafic and felsic rocks also imply that these two groups of rocks evolved separately.

As REE are generally incompatible, they become enriched in the melt during crystallization. Fractional crystallization of a syenitic magma would produce a rhyolite melt enriched in all REE except Eu, which behaves as a compatible element and is concentrated in feldspar crystals. Crystal fractionation removes feldspar from the melt, leaving the melt depleted in Eu. This mechanism can explain the Eu depletion in the rhyolites and quartz syenites. The Eu enrichment in the syenitic enclaves indicates feldspars accumulated in this magma during crystal fractionation.

The compositions of the unaltered feldspars in the Ossipee rocks provide a geothermometer (Fig. 7). Experiments have shown that certain ternary alkali feldspar compositions correspond to magmatic temperatures at particular pressures (Nekvasil, 1988). The majority of the pink K-feldspars in the rhyolite and syenite plot as orthoclase

FIGURE 7. Feldspar compositions from Ossipee rocks (Appendix I) plotted on a K, Na, Ca diagram, temperature fields are plotted for 1 Kb from Nekvasil (1988).

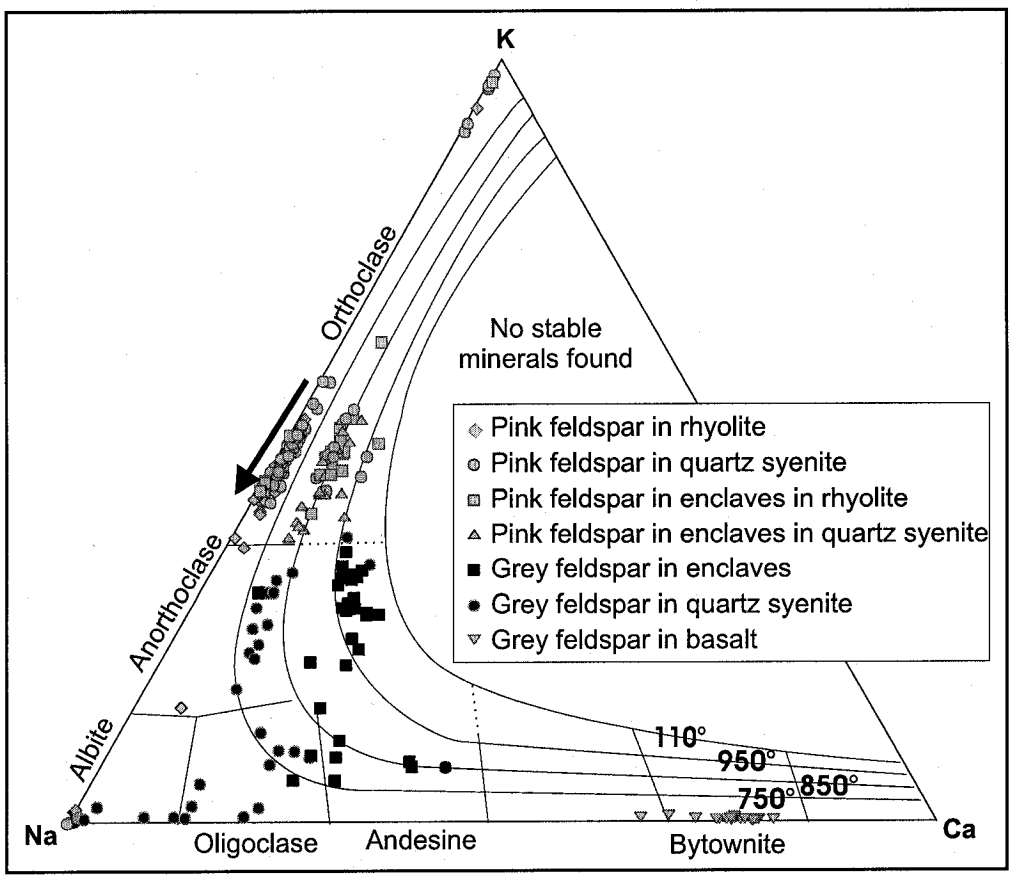
K
Orthoclase
Anorthoclase
Albite
Na
Ca
Oligoclase
Andesine
Bytownite
No stable
minerals found
Pink feldspar in rhyolite
Pink feldspar in quartz syenite
Pink feldspar in enclaves in rhyolite
Pink feldspar in enclaves in quartz syenite
Grey feldspar in enclaves
Grey feldspar in quartz syenite
Grey feldspar in basalt
110°
950°
750°
850°

in the normal temperature field for rhyolitic rocks (~750°C). Iron-titanium oxide equilibrium temperatures are ~700°C for the quartz syenite (Eby and Kennedy, 2004), consistent with the feldspar compositions. Some feldspars plot as nearly pure sodic or potassic end members; these are portions of crystals that have undergone coarse subsolidus unmixing probably involving interaction with a hydrothermal fluid (Parsons and Brown, 1984); these compositions are not considered further. It is likely that all alkali feldspar in this suite have undergone some subsolidus unmixing; however, the scale of this unmixing is less than the microprobe beam size and therefore should not affect the results. Pink K-feldspars in the syenite are more potassic (mean 8.48 wt. %) than pink K-feldspars in the rhyolite (mean 7.16 wt. %). The pink feldspars in syenitic enclaves found in both the rhyolite and quartz syenite have anomalously high calcic compositions (1.46 wt %) stable at around 850°C. Some zones of these feldspars indicate temperatures of up to 1050°C.

Grey alkali feldspars generally plot as anorthoclase and are frequently more sodic and calcic than the pink feldspars. The anorthoclase feldspars in the quartz syenite have Ca (mean 1.61 wt %) and Na (6.25 wt. %) indicating crystallization temperatures up to 850°C (Fig. 7). These feldspars show large variations in Na and Ca contents. The grey feldspars in the syenitic enclaves in the rhyolite and quartz syenite have the highest Ca (mean 3.62 wt. %) indicating temperatures up to 1050°C (Fig. 7). Some grey feldspars in enclaves from quartz syenite plot as plagioclase and are either andesine or oligoclase. The grey plagioclase feldspars found in the basalts plot as a distinct group of more calcic plagioclase.

Orthoclase and anorthoclase are found together in the quartz syenite and in the enclaves, yet these alkali feldspars are part of solid solution and could not have crystallized under the same magmatic composition, temperature, and pressure. The pressure and composition will vary slightly in this magmatic situation, but the most likely cause of variation is due to temperature (Fig. 7). In all likelihood, anorthoclase is xenocrystic in the quartz syenite and orthoclase is xenocrystic in the syenite enclaves; this is consistent with the textural data.

In summary, (1) the major and trace element compositions of felsic and mafic rocks can be explained by crystal fractionation or mixing processes in two separate chambers, (2) the trace element data support separate evolution of the mafic and felsic rocks by crystal fractionation, (3) the REE data further support fractional crystallization in the silicic rocks and reveal that the syenitic enclaves are at least in part cumulates, (4) the feldspar compositions show evidence of variable thermal and chemical magmatic conditions and crystal exchange in the felsic magmas. How these results relate to the caldera environment at Ossipee is discussed below.

DISCUSSION

The various types of data we have collected allow us to place constraints on the origin and evolution of the Ossipee ring complex. Carr (1980) discussed the deep origins of the Ossipee magmas and recognised a chemical signature due largely to crystal fractionation. We extend this interpretation, consider the shallow level evolution of these magmas, and discuss potential magma chamber arrangements. We discuss four

important questions: (1) the origin of the rhyolitic textures; (2) the relationship of the rhyolite to the quartz syenite in the ring dyke; (3) the origin of the magmatic enclaves; and (4) the role of basalt in the magmatic system. We discuss each of these issues in turn.

ORIGIN OF THE RHYOLITIC TEXTURES

Kingsley (1931) interpreted the rhyolite as mostly extrusive ignimbrite, whereas Carr (1980) interpreted the rhyolite as mostly intrusive. These fundamentally different conclusions have important implications for the formation of the complex. The textures and geochemistry of the rocks imply a similar magmatic history for the porphyritic rhyolite and the fragmental rhyolite. The phenocryst percentages, whole-rock and matrix compositions, and feldspar compositions of the fragmental and porphyritic rhyolite are similar. In many localities, field observations indicate that the porphyritic rhyolite is in the process of becoming fragmental rhyolite (Fig. 8a). For example, orthoclase and quartz in the rhyolite show in situ jigsaw-style fracturing. In other cases, enclaves or pumices in the fragmental rhyolite contain whole orthoclase or quartz crystals while the groundmass/matrix consists of crystal fragments. The crystal size distribution of the fragmental rhyolite is consistent with the fragmentation of large crystals to produce larger numbers of small crystals (Fig. 4b). Crystal fragments of quartz commonly show rounded or embayed edges indicating an original crystal morphology similar to the porphyritic rhyolite before fragmentation. The embayments in the quartz grains could be caused by the presence of gas bubbles in contact with quartz grains, enhancing diffusion gradients during growth or dissolution where bubbles touch the quartz (Donaldson and Henderson, 1988). The highly embayed quartz is suggestive of a vesicular magma susceptible to

FIGURE 8. (a) An outcrop of pyroclastic rhyolite where large crystals of orthoclase are fragmenting to form small angular phenocrysts. (b) Basaltic breccias disaggregating into pyroclastic rhyolite.

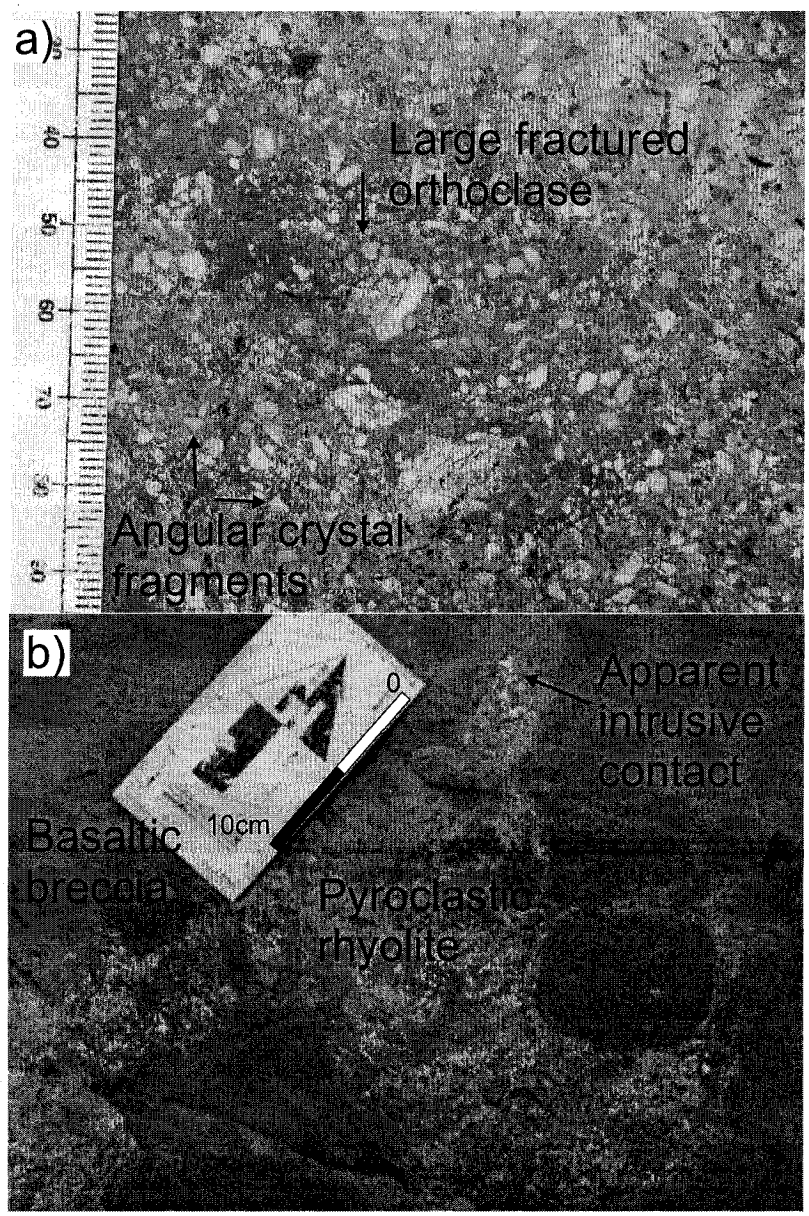
a)
Large fractured orthoclase
Angular crystal fragments
b)
0
10cm
Apparent intrusive contact
Basaltic breccia
Pyroclastic rhyolite

fragmentation (Spieler et al., 2004). Contrary to the interpretations of Carr (1980) and Lyons et al. (1997), we are confident that this fragmental rhyolite represents a highly welded and possibly rheomorphic ignimbritic equivalent of the porphyritic rhyolite, as originally mapped and interpreted by Kingsley in 1931. The apparently intrusive contacts of rhyolite into basalt discussed by Carr (1980), including rhyolite veining in basalt, are re-interpreted by us as the margins of fractured landslide megablocks of basaltic breccia which fell into the caldera as it subsided. During landsliding and deposition of the megablocks in ignimbrite, the hot plastic fragmental rhyolite was injected into these fractured megablocks, producing intrusive textures (Fig. 8b). Similar textures and structures were observed by Lipman (1976) for the San Juan calderas in Colorado. At outcrops where the fragmental rhyolite is in contact with the brecciated basalt, the enhanced cooling of the rhyolite against the cold basalt blocks allowed eutaxitic textures to be preserved. Thus the textures we observe are those of pyroclastic rhyolite which is capable of being remobilized and injected into fractures of megablocks.

Dykes of porphyritic rhyolite crosscut fragmental rhyolite and basaltic breccias. In most localities, the margins of these dykes are extremely irregular, indicating that the fragmental rhyolite was still hot and plastic. This observation demonstrates that these two types of rhyolite were essentially contemporaneous. The majority of the rhyolite was probably volatile-rich and erupted explosively, fragmenting the melt and crystals during eruption. However, pockets of unfragmented rhyolitic magma remained in the chamber and conduits, and these pockets were degassed and intruded soon afterward as porphyritic rhyolite dykes, possibly erupting as lava domes at the surface. By re-interpreting the

majority of the rhyolite as ignimbrite, we reinstate the Ossipee ring complex as a true caldera.

RELATIONSHIP BETWEEN RHYOLITE AND QUARTZ SYENITE

Many chemical similarities exist between the rhyolite and the quartz syenite, some of which were pointed out by Carr (1980). However, we propose that the rhyolitic and quartz syenitic magmas evolved together in a shallow magma chamber separately from the mafic rocks.

Within the ring dyke, crystal transfer occurs at gradational contacts between rhyolite and quartz syenite; the rhyolite and the quartz syenite were thus in a liquid state at the same time. In addition, the porphyritic rhyolite and the quartz syenite are also texturally similar in appearance (Figs. 2c, 3a). However, the quartz syenite is generally more phenocryst-rich than the porphyritic rhyolite due to a greater abundance of small phenocrysts (Fig. 5b), implying an extended period of crystallization for the quartz syenite. The crystal size distributions of both the quartz syenite and the porphyritic rhyolite indicate that Oswald ripening and crystal clumping are likely mechanisms to explain the large crystal sizes (Higgins, 1999). Dark alkali-rich enclaves and xenocrystic anorthoclase also are found in both magmas, although they are more common in the quartz syenite.

Compositionally, the rhyolite and quartz syenite magmas overlap. In fact, many outcrops that are mapped as quartz syenite are compositionally rhyolitic, because the quartz syenite and rhyolite can appear texturally identical. Despite the similarities, the quartz syenite is generally richer in mafic components (i.e., Ca, Mg) and contains less

SiO_2; the syenite also contains more alkali elements (Figs. 5a, b). Appropriate phase diagrams of the quartz-albite-orthoclase-anorthite system indicate that quartz is the last phase to crystallize; as a result the melt phase is enriched progressively in SiO_2 to produce a rhyolitic melt (James and Hamilton, 1969). The trace-element data show that the quartz syenites are enriched in Zr and Sr and depleted in Y relative to the rhyolites. The enrichment in Zr and Sr of the quartz syenite is consistent with less feldspar and zircon removal relative to rhyolites.

The orthoclase in the rhyolite is considerably more sodic than the feldspars in the quartz syenite (Fig. 7). The shift toward more sodic compositions is consistent with the temperature drop associated with crystallization and differentiation of the melt under constant H_2O pressure (Ginibre et al., 2004). The higher potassium in the syenite orthoclase also explains the increased potassium in the whole rock analysis of the quartz syenite relative to the rhyolite (Fig. 5c). In addition, the orthoclase in the rhyolites is slightly more evolved than in the syenites (Appendix I). For example, orthoclase found in the rhyolite has slightly lower amounts of iron and calcium relative to orthoclase in the quartz syenite, and trace elements such as Ba show enrichment in the orthoclase in the quartz syenite relative to the rhyolite. As Ba is compatible in orthoclase, the Ba trends are consistent with differentiation and crystallization of quartz syenite to produce rhyolite. The small compositional and textural differences are systematic, gradual, and consistent with fractional crystallization.

The REE plots for the rhyolite and quartz syenite are similar. Both exhibit steep parallel trends with the rhyolites exhibiting higher REE concentrations, except for Eu. The rhyolite shows a large negative Eu anomaly, whereas the quartz syenite shows a

smaller negative Eu anomaly (Fig. 6). The large negative Eu anomaly of the rhyolite is similar to that observed in anorogenic high-silica rhyolites erupted from large silicic magmatic systems such as Yellowstone, Valles and Long Valley calderas (Hildreth et al., 1979; Stix et al., 1988; Christiansen, 2001). Eu is compatible in feldspar and becomes depleted in the melt as feldspar crystallises; a negative Eu anomaly is produced if the feldspar is then removed from the liquid. The quartz syenites have a smaller Eu anomaly, indicating less feldspar removal.

The textural and geochemical trends that exist between the quartz syenite and the rhyolite imply that they are comagmatic and were derived from a single batch of magma in a large shallow chamber, rather than evolving separately and subsequently mixing together. Crystal fractionation could produce a stratified magma chamber with a large volume of mostly rhyolitic liquid, overlying progressively more crystal-rich quartz syenite below. The configuration of this stratification is poorly constrained. Two possible end-member configurations are possible: a vertically stratified or concentrically stratified chamber (Hildreth, 1981; Marsh, 2000). The probable configuration of the chamber is likely more complex, but the data presented above indicate that a crystal-poor, highly evolved rhyolitic magma was erupted, while a slightly more primitive crystal-rich mush remained in the chamber after caldera collapse.

ORIGIN OF MAGMATIC ENCLAVES

The grey enclaves abundant in the quartz syenite and rarer in the rhyolite invariably have a fluidal shape, show evidence of crystal exchange, and in some localities are seen disaggregating completely into their host. For these reasons, we agree with Carr

(1980) that they are magmatic in origin. The type 1 fine-grained enclaves contain ragged crystals and clumps of anorthoclase and occasionally xenocrystic orthoclase or rimmed quartz from the quartz syenite (Fig. 5a).

Textural and geochemical evidence indicate that some crystals are xenocrystic in the quartz syenite and in the enclaves. The anorthoclase crystals within the enclaves appear texturally similar to the frequently rimmed anorthoclase found in the quartz syenite. The anorthoclase crystals have irregular shapes and a spongy texture, with evidence of resorption. Some anorthoclase crystals appear to be rimmed clumps of crystals and in many cases fine grained enclave groundmass is trapped within the rims. Both anorthoclase and orthoclase are frequently found astride the interface between an enclave and the quartz syenite host. Most importantly, orthoclase and anorthoclase cannot crystallize under the same compositional, pressure, and temperature conditions which indicates that crystal transfer is necessary for these two alkali feldspars to coexist in a magma. Therefore, the orthoclase feldspars in the enclaves and the anorthoclase feldspars in the quartz syenite must be xenocrystic.

The feldspar data show a range of feldspar compositions between the anorthoclase in the enclaves and the orthoclase in the quartz syenite host (Fig. 7). This range implies that these crystals experienced a variety of different magmatic conditions. The xenocrystic pink orthoclase in the enclaves has magmatic temperatures which fall between those of the enclaves and those of the quartz syenite (750 to 950°C). This implies that these xenocrystic orthoclase crystals grew in a syenitic magma of hotter temperature. The crystal-size distribution of the alkali feldspar in the enclaves show less

and on average larger feldspar phenocysts than the quartz syenite (Fig. 5b). Melting due to the elevated temperature could have caused this absence of smaller crystals.

The enclaves have textural and compositional affinities with the rhyolite and quartz syenite. However, they contain dominantly anorthoclase crystals and no quartz phenocrysts. The major-element geochemistry shows that the enclaves plot as an intermediate magma between the felsic rocks and the mafic rocks (Fig. 5a to d). This indicates that the enclaves thus could either be a less evolved early cumulate from the rhyolite and quartz syenite, or a mix between the mafic rocks and the quartz syenite. However, the alkali and the trace element plots show that the enclaves are rich in alkalis and have Zr/Y or Sr/Y ratios and Y values that are not consistent with magma mixing (Figs. 5e to h). In addition, the parallel REE trends and Eu anomalies of the enclave quartz syenites and rhyolites show a pattern consistent with fractional crystallization (Fig. 6). The syenitic enclaves have a positive Eu anomaly, which indicates feldspar accumulation. We interpret the anorthoclase crystals and clumps in the enclaves as remnant cumulate crystals, which have been partially melted, resorbed and regrown. Thus, the enclaves represent a crystal mush from the base of the magma chamber. Paradoxically, the cumulate enclaves are comparatively poor in crystals.

The anorthoclase compositions indicate temperatures up to 1050°C (Nekvasil, 1988), which are unusually high for alkali silicic magmas. Fe/Ti oxide equilibrium temperatures are calculated to be around 700°C for the quartz syenite (Eby and Kennedy, 2004). A temperature of 1050°C is sufficiently hot to dissolve small alkali feldspars and cause the ragged textures in the larger anorthoclase crystals. The average composition of anorthoclase crystals in the enclaves is similar to the whole rock composition of the

enclaves (Fig. 5c, d; Table 1). These data support our interpretation that the enclaves are a cumulate, largely composed of anorthoclase. The high temperatures indicated by the feldspar compositions also explain the unusual anorthoclase textures and lack of smaller phenocrysts. The enclaves therefore represent a partially remelted anorthoclase cumulate.

Some enclaves are seen disaggregating and dissolving into the quartz syenite (Fig. 3d), a process that both introduces anorthoclase crystals into the quartz syenite and increases the alkali content of the syenite. This process is also reflected in the crystal size distributions. The two syenite samples with the most anorthoclase also have the fewest small alkali feldspar crystals. We interpret the presence of anorthoclase-rich quartz syenite as where the hot magmatic liquid from the enclave mixed with magmatic liquid of the quartz syenite groundmass, raised the local magmatic temperature, and dissolved small orthoclases. The temperatures of the xenocrystic anorthoclase in the quartz syenite indicate that the quartz syenite interacted with enclaves of various temperatures. In turn, xenocrysts of orthoclase and quartz were mixed into the enclaves from intermediate temperature magmas.

Hot basaltic magma was erupted during the intrusion of the ring dyke and so was available to provide the high temperatures necessary to melt a crystallized syenite cumulate to produce the dark enclaves. Eby and Kennedy (2004) have shown that some crystals of hornblende in the quartz syenite plot with hornblende from the basalts, which they interpret as evidence of crystal transfer between quartz syenitic and basaltic melts. Additionally, some type 2 enclaves contain andesine (Fig. 7). These andesine crystals may be derived from the basaltic magma by minor transfer of crystals from a basaltic

magma into the melted syenite cumulate. In general, however, interaction with basaltic magma was limited by viscosity contrasts (Sparks and Marshall, 1986).

The type 2 enclaves are generally more elongate, smaller in area, and contain fewer large anorthoclase crystals. This is not consistent with the model of Blake and Fink (1990), which predicts larger enclaves to be more elongate than smaller enclaves under the same cooling and shearing conditions. This discrepancy cannot be explained by chemistry because the slightly higher SiO_2 content of the type 2 enclaves (Table 1) implies a lower freezing temperature and hence a less ductile response to shear. We suggest the type 2 enclaves froze during a period of high shear, but the type 1 enclaves remained plastic and relaxed during a period of low shear into a more spherical form due to surface tension. However, enclave shape can be explained in a number of different ways (Paterson et al., 2004).

In summary, the enclaves represent a superheated remelted syenitic cumulate, which exchanged orthoclase and anorthoclase crystals with quartz syenite magma of varying temperatures. The variable disintegration of these enclaves into the quartz syenite is the major cause of textural and chemical diversity of quartz syenite in the ring dyke. A large-scale, high-shear mixing event followed by a period of low shear appears necessary in order to explain the different enclave morphologies and to distribute enclaves throughout the crystal-rich quartz syenite.

INTERPRETATION

ROLE OF MAFIC MAGMAS

The early and late basalts and basaltic andesites of Ossipee show broadly similar chemical signatures (Carr, 1980; Eby, unpublished data), but little compositional or textural overlap with the quartz syenite or the rhyolite (Figs. 3 to 6). The majority of the basalt and basaltic andesite was erupted before the caldera formed and, consisted of a variety of lavas, ash, dykes and sills (Carr, 1980).

When examined closely, the bulk of the mafic rocks not associated with the ring dyke are actually megablocks resting in a matrix of landslide breccia and ignimbrite. Therefore, the majority of these rocks erupted in earlier eruptive events are remnants of volcanoes that existed at Ossipee prior to the formation of the caldera. As the caldera developed, the mafic edifices became unstable and foundered into the caldera as landslides concurrent with ignimbrite eruptions.

We have observed several localities at Ossipee where mafic magma is comagmatic with rhyolite. In Cold Brook and other areas of the ring dyke, magma mingling and mixing occurs between basalt and rhyolite (Fig. 2). Thus, basaltic magma was present during the caldera-forming event. The magma interactions in Cold Brook are associated with explosive brecciation and very intricate laminations, in contrast to the diffuse spheroidal enclaves seen in the quartz syenite. Some dyke margins are hybrid basaltic andesite with evidence of magma interaction, indicating that small amounts of basaltic andesite were produced during mixing of basalt and felsic magmas. Mixing and mingling between the basalt and rhyolite is restricted to the margins of dykes where the

magmas are in direct contact, in contrast to the well-distributed enclaves in the quartz syenite. This observation indicates that the basalt-rhyolite interaction in Cold Brook is probably conduit-related rather than the result of chamber-scale convection.

The similarity of the REE and isotopic ratios between mafic and silicic rocks at Ossipee indicate they are derived from a similar mantle source (Carr, 1980; Eby, unpublished data). However, different slopes in major-element trends are observed for the alkali silicic rocks and the mafic rocks (Fig. 5), and the trace element ratios are also distinct (Fig. 6). These compositional differences between the mafic and silicic rocks indicate that the mafic rocks evolved separately despite a common mantle source.

Prior to caldera collapse, basaltic magma melted the syenitic cumulate base of the felsic chamber. The heat from this basalt also may have caused some remelting in the quartz syenite, which originally had a higher phenocryst content and fewer corroded phenocrysts (Wiebe et al., 2004). This influx of basalt at the base of the chamber could have formed the trigger necessary to initiate the caldera-forming eruption (e.g., Sparks et al., 1977). In addition, basalt could have aided the propagation of felsic dykes with high viscosities (Takeuchi, 2005). During collapse, basalt then interacted with the rhyolite in the ring dyke. Alkali-rich basaltic dykes with sharp margins also crosscut the volcanic rocks (Carr, 1980; Eby, unpublished data); these may be related to the basalt that melted the base of the silicic chamber. The primary role of mafic magma at Ossipee was to rejuvenate the magmatic system. This process is seen in many other magmatic systems (e.g., Bachman and Bergantz, 2003).

FIGURE 9. A cartoon of the major magmatic processes and the arrangement of stratification in the magma chamber. (a) Before collapse. (b) Early during collapse. (c) During intrusion of the syenite. (d) After erosion.

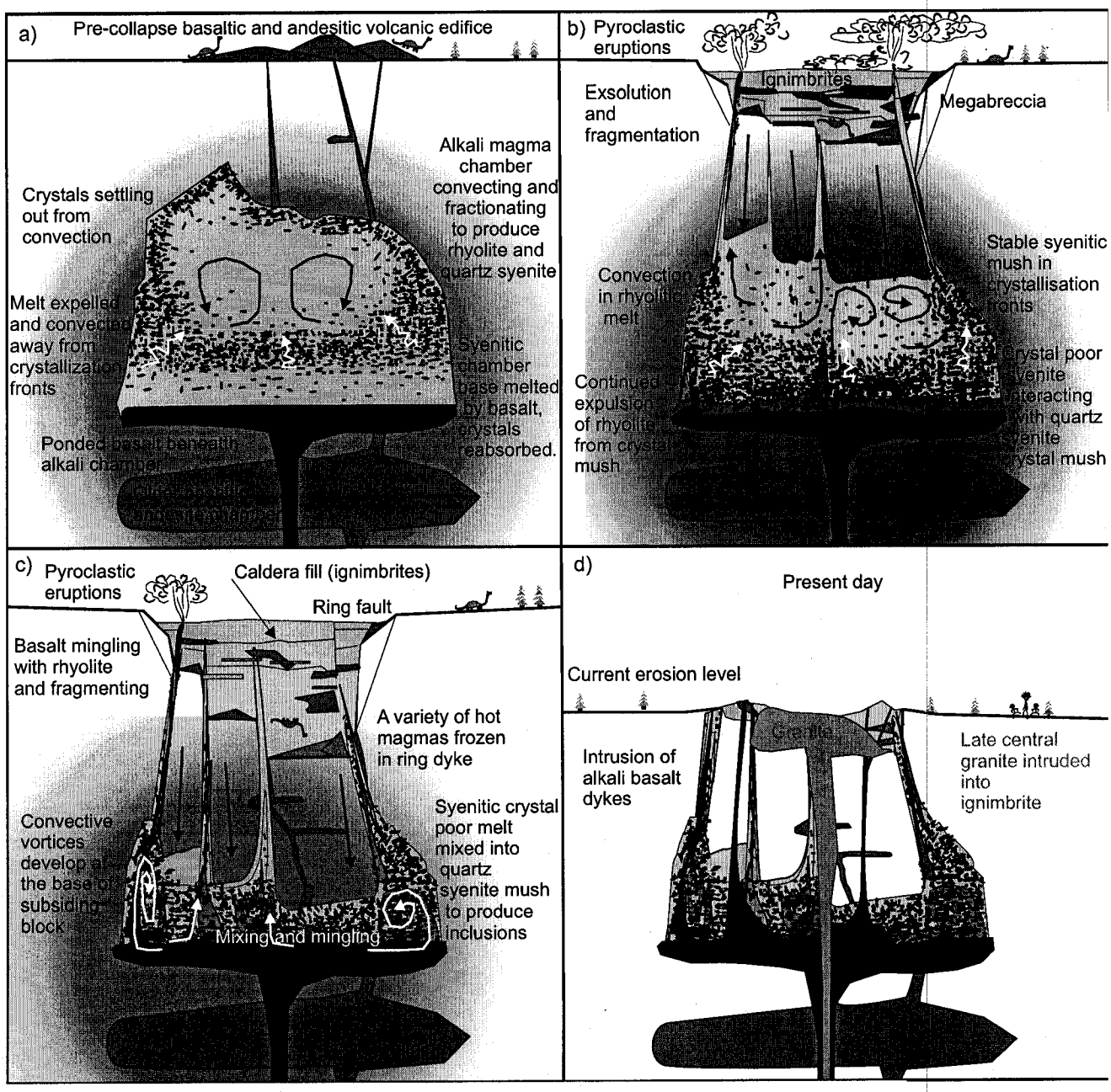
a)
Pre-collapse basaltic and andesitic volcanic edifice
Crystals settling out from convection
Alkali magma chamber convecting and fractionating to produce rhyolite and quartz syenite
Melt expelled and convected away from crystallization fronts
Syenitic chamber base melted by basalt, crystals reabsorbed.
Ponded basalt beneath alkali chamber
b) Pyroclastic eruptions
Ignimbrites
Exsolution and fragmentation
Megabreccia
Stable syenitic mush in crystallisation fronts
Convection in rhyolitic melt
Crystal poor syenite interacting with quartz syenite crystal mush
Continued expulsion of rhyolite from crystal mush
c)
Pyroclastic eruptions
Caldera fill (ignimbrites)
Ring fault
Basalt mingling with rhyolite and fragmenting
A variety of hot magmas frozen in ring dyke
Convective vortices develop at the base of subsiding block
Syenitic crystal poor melt mixed into quartz syenite mush to produce inclusions
Mixing and mingling
d)
Present day
Current erosion level
Granite
Intrusion of alkali basalt dykes
Late central granite intruded into ignimbrite

MAGMA PROCESSES ASSOCIATED WITH OSSIPEE RING COMPLEX

Magma dynamics before caldera formation

Caldera formation provides a unique environment where a wide variety of magmas can interact in different ways. There are an impressive variety of magma types within the ring dyke at Cold Brook. These magmas affect one another by mingling and mixing or simply heating and remelting crystals. The textural and chemical intricacies observed in the ring dyke are the result of processes that occurred within the magma chamber and conduits before and during caldera formation.

Mostly liquid rhyolite was separated from a quartz syenite mush before caldera collapse to allow rhyolite to be erupted first, followed by the intrusion of the quartz syenite into the ring dyke. The textural and compositional similarities between the quartz syenite of the ring dyke and the rhyolite ignimbrite imply that compositional stratification was gradational and developed in a single magma chamber. We envisage this configuration of the chamber as concentric crystallization fronts, modified by some form of gravity-controlled crystal accumulation toward the base (Fig. 9a). It is difficult to constrain the full extent of the processes involved in crystal fractionation. However, the quartz syenite contains abundant enclaves that are largely absent in the rhyolite, indicating that the quartz syenite was derived from deeper levels of the chamber above the remelted syenite. The adjacent positions of the two syenitic magmas near the base of the chamber allowed extensive interaction to occur. To achieve a vertically zoned chamber as described, some form of gravity-driven crystal accumulation must have occurred at the base of the chamber.

Crystal settling had to occur over distances of 0 to 3 km, which is the amount of subsidence estimated by Kingsley (1931) and Carr (1980). We estimate the duration of crystal settling using values appropriate for Ossipee. According to Stokes's law, a grain of orthoclase 5 mm in diameter of 2500 kg/m^3 density sinks in a crystal-free melt with a water content of 4 wt.%, density of 2300 kg/m^3, and viscosity of 10^5 Pa s (Hess and Dingwell, 1996), at 2.72 x 10^{-8} m/s. If the melt through which the crystal is settling contains 30% crystals, settling rates are reduced by ~30% (Bachman and Bergantz, 2004). Even considering hindered settling, crystal settling times are still only about 10^2 years to settle 1 km. Stokes's law is most sensitive to changes in crystal diameter and viscosity; if we consider small 1 mm diameter crystals of orthoclase in a viscous rhyolitic melt with only 1 wt. % water, 30% crystals, and viscosity of 10^6 Pa s, the settling time for 1 km settling increased to 10^4 years.

Crystal-settling calculations such as these make many assumptions, such as crystal shape, and a static magma chamber. In large rhyolitic magmatic systems >500 m thick with sufficient temperature gradients (>10°C from the base to the top of a magma chamber) and viscosities <10^7 Pa s, Rayleigh numbers are >10^6, indicating vigorous convection. Depending on the convective velocity, the size of convection cells, and the crystal settling rate, a crystal can either be retained in a convecting flow or can be deposited and captured by growing fronts of crystallization on the sidewalls, floor, or roof (Marsh, 1988). If the rate of convection is significantly faster than the Stokes's settling velocity, crystals may remain in suspension. Simple thermal convection rates calculated using equation 5 in Sparks et al. (1984) indicate that convection rates will

exceed settling rates under magmatic conditions applicable to Ossipee (temperature contrast >10°C, crystals with a diameter of < 2 cm, and a viscosity >10^3 Pa s).

We estimate the conditions for convection in the chamber using the following parameters: a viscosity of about 10^5 Pa s (rhyolite with 4 wt.% H_2O, Hess and Dingwell, 1996), a temperature contrast of 100°C (from feldspar geothermometry, Fig. 7), crystals of 1 cm diameter (Fig. 3c), a 1000 m thick chamber thickness (ignimbrite thickness and hence minimum subsidence and chamber thickness estimate, Kingsley, 1931). These values give a maximum thermal convective velocity two orders of magnitude greater than the crystal settling rate. However, convection cells with a large horizontal component will promote crystal settling, as the Stokes's settling velocities can dominate during horizontal flow (Marsh 1988). Also, the convective velocity may be significantly lower close to the margin of the convective cell (Sparks et al., 1984).

Concurrent with the development of convection systems and crystal settling from the convective body, crystallization fronts grow on the roof, floor, and walls of the chamber. A crystallization front has a high proportion of crystals and hence sufficiently high viscosity and yield strength to prevent convection. Mechanisms have been envisaged for the filtration of the melt phase through static crystal mush in the crystallization front. (1) The body of magma can convect evolved melt away from all crystallization fronts, causing convective fractionation (Sparks et al., 1984). (2) Gas-driven filter pressing forces melt out of the crystallization front as gas exsolves (Sisson and Bacon, 1999). (3) Crystals in the crystallization front also can compact, which will expel melt (Philpotts, 1998; Bachman and Bergantz, 2004). The melt from which the mush crystallized could then re-enter the convecting body, modifying the bulk chemistry of the convecting melt

phase. Melt migration is a mechanism shown to explain compositional diversity in granitic plutons (Srogi and Lutz, 1996). All three mechanisms of melt migration appear to be compatible within the magmatic constraints of the Ossipee magma chamber. For example, using magmatic conditions relevant to Ossipee and equation (5) from Sisson and Bacon (1999), a 5 % increase in porosity in a day can produce 2 MPa overpressure in a crystallization front (a partially crystalline magma with a bulk viscosity 10^9 Pa s). Crystal fractionation probably occurs both as melt migration away from the static mushy zones of crystallization fronts and as the settling of large crystals from the main convecting body. The relative importance of the different processes of fractionation will depend on how these processes affect one another, as well as on small changes in viscosity, chamber size, temperature and compositional gradients, and yield strength, which may vary during the magmatic evolution of the chamber.

The hot mobile syenitic magma suggests the presence of basaltic magma in the system prior to collapse as discussed above. The volume and temperature of the basalt were sufficient to melt the base of the syenitic crystal mush to produce a layer of superheated syenitic melt now found as enclaves in the quartz syenite ring dyke. The base of the cumulate syenite melt was superheated and mobile and overlain by cumulate syenitic magma with a yield strength that acted as a boundary preventing significant interaction with the rest of the chamber. Some of the quartz syenite also may have been partly remelted by heat transfer from the basalt. Corroded and reacted phenocryst textures in the quartz syenite are consistent with this possibility, and similar textures are described in the remelted Vinalhaven porphyry in Maine (Wiebe et al., 2004). Limited interaction of the superheated syenitic melt with the rest of the chamber may have occurred before

eruption, as sparse anorthoclase xenocrysts and syenite enclaves are found in the rhyolitic ignimbrite. However, these ignimbrite enclaves are rare and contrast strongly with the abundant distribution of enclaves and xenocrysts in the quartz syenite.

In summary, convection and crystal fractionation occurred in the Ossipee magma chamber before eruption. The magma chamber probably consisted of a thick upper layer of rhyolitic magma, a middle layer of quartz syenite crystal mush, and a lower syenite cumulate. Basalt then intruded the base of the magma chamber and began melting the syenite cumulate and possibly partially melting the quartz syenite (Fig. 9a). In this manner, the phenocryst content of the quartz syenite mush was reduced, and a layer of mobile superheated syenitic melt produced. During this rejuvenation, sufficient changes in chamber pressure occurred to initiate an eruption.

Magma dynamics during caldera collapse

In this section, we illustrate how magmatic processes affect textural and chemical characteristics of magma during an eruption. A striking feature of the magma interaction at Ossipee is the abundant and thorough distribution of enclaves and xenocrysts within the quartz syenite ring dyke, in contrast with their relative scarcity in the rhyolite. This difference implies that the superheated syenite did not mix and mingle throughout the entire chamber, yet managed to interact efficiently with a restricted volume of relatively crystal-rich quartz syenite (Fig. 9b). This behaviour could be explained by several situations. (1) A chamber-scale mixing event that occurred only after the majority of the rhyolitic magma had erupted. (2) Chamber-scale mixing was restricted to a basal layer of the chamber. At Ossipee, however, there is no evidence for two separate eruptions or

sharp changes in magma composition that would allow this type of restricted mixing. (3) We envisage that as the caldera subsided, dynamic collapse-driven mixing occurred at the base of the magma chamber (Marshall and Sparks, 1984), driven by vortices developing around the base of the subsiding block (Folch et al., 2001).

We propose that magma mixing and mingling in a magma chamber that is undergoing collapse will be enhanced relative to an eruption without collapse. First, during an eruption involving caldera collapse, a ring dyke acts as the conduit, increasing the potential area for conduit-flow mixing. This type of mixing may have caused the local mixing and mingling observed at dyke boundaries between basalt and rhyolite in the ring dyke at Ossipee. Second, as the caldera subsides, pressure fluctuations will occur at the base of the subsiding block or blocks. During piston style subsidence in a magma chamber of uniform viscosity ($<10^4$ Pa s), flow vortices develop at the base of the ring dyke that can drive mixing and mingling (Folch et al., 2001).

At Ossipee and many other calderas, the situation is more complex than the situation modelled by Folch et al. (2001), since (1) the caldera did not subside as a coherent block and (2) it contained layers of magma with contrasting viscosities (Fig. 9a) (Chapman, 1976). If multiple blocks subside at different rates, they create vortices in different areas of the chamber (Chapter 3, this thesis), and enhance mixing in the magma remaining in the chamber (Fig. 9c). Folch et al. (2001) concluded that vortices are only likely to develop where viscosities are lower than 10^4 Pa s. The viscosity of the quartz syenite with 35% crystals may be closer to 10^5 Pa s (Lejeune and Richet, 1995; Hess and Dingwell, 1996), but the superheated syenitic magma at the base of the chamber locally reduced crystal contents and viscosities, promoting the development of vortices. In

addition, multiple collapse blocks and irregular chamber geometry could allow vortices to develop at higher viscosities (Chapter 3, this thesis). The development of flow vortices also may disrupt the yield strength of a crystal mush at the base of the chamber, to allow intrusion of superheated syenitic magma and basaltic magma through the crystal mush into the quartz syenite. Collapse-driven mixing is inherent to caldera collapse events, particularly in a case such as Ossipee, where there are multiple subsiding blocks. Collapse-driven mixing may be dominant during subsidence at many calderas. For example, a similar style of mixing is seen at Lake City caldera, Colorado (Hon, 1987; Chapter 2, this thesis) that is consistent with this type of collapse-driven mixing.

EMPLACEMENT OF THE RING DYKE

The collapse of the caldera caused the disruption of stratified magmatic layers. During this disruption, relatively crystal-rich, quartz-bearing syenitic magma mixed with a superheated crystal-poor melt (Fig. 9c). Unreasonable overpressures are required to propagate a viscous rhyolitic dyke, however, a lower viscosity dyke requires much less overpressure (Rubin, 1995, Takeuchi and Nakamura, 2001; Takeuchi, 2004). The high temperatures indicated by feldspar compositions in the quartz-bearing syenitic magma reduced viscosity and aided intrusion. During caldera collapse, lithostatic equilibrium becomes significantly disrupted (Kennedy and Stix, 2003). This disequilibrium may cause the quartz syenite magma to rise, thereby intruding overlying rocks and magma. Reduced viscosity and lithostatic imbalance provide an ideal environment for ring dyke intrusion.

In the Cold Brook section, basaltic magma also intruded the ring dyke driving explosive eruptions as it interacted with rhyolite in the ring dyke. This activity continued as alkali basaltic dykes crosscut the complex after collapse (Fig. 9c) (Eby, unpublished data). New structural pathways and lithostatic changes following caldera collapse also may have promoted the rise of basaltic magma into the shallow Ossipee magmatic system. Lastly, a shallow laccolith of granitic magma also intruded the complex after collapse, and its rise also may have been influenced by the drop in lithostatic pressure following collapse. The fluids associated with the rise of the granitic magma may have been responsible for hydrothermal reactions modifying the mineralogy of the rhyolite, quartz syenite, and basalt. Therefore, at Ossipee, caldera collapse may have driven magma mixing phenomena within the chamber, facilitated ring dyke emplacement and induced magma chamber replenishment.

CONCLUSIONS

The ring dyke section at Cold Brook exposes rock from throughout the caldera-forming event at the Ossipee ring complex. The textures and mineral chemistry of the rocks observed at Cold Brook reveal volcanic and shallow magmatic processes prior to and during caldera formation. This study has allowed us to add considerable detail to the formation of the Ossipee Complex.

Our main conclusions are as follows. (1) The textural and chemical gradients between the rhyolite and quartz syenite indicate that they were produced by crystal fractionation, and the physical properties of the rhyolitic magma indicate that chamber convection, crystal settling, and fractionation from crystallization fronts were likely

processes. (2) The magmatic enclaves in the quartz syenite represent superheated syenitic melt produced by melting of an anorthoclase cumulate. The heat for this melting was probably provided by basalt, which ponded beneath the chamber. (3) Rhyolitic magma erupted explosively from the top of the magma chamber, fragmenting and ponding in a subsiding caldera to form ignimbrite sheets associated with landslide megabreccias. (4) During caldera collapse, the basal superheated syenitic melt layer was mixed into the quartz syenite magma by vortices produced by multiple subsiding blocks. This mixing caused extensive dispersal of enclaves and xenocrysts throughout the quartz syenite. (5) Basaltic magma was drawn up into the ring dyke at late stages, locally mixing at dyke margins with explosively erupting rhyolite.

The rocks at the Ossipee ring complex record evidence for crystal fractionation, replenishment, rejuvenation and mixing. These processes appear to be ubiquitous for many large felsic magma chambers (Troll et al., 2004; Bachman and Bergantz, 2003). The mapping and analysis we have done at Ossipee help us understand how these processes fit into the caldera collapse cycle of Smith and Bailey (1968). The magma within a ring dyke is residual from a period of dynamic chamber processes, accelerated by caldera collapse. This magma would normally remain in the chamber; however, a well-chosen section of a ring dyke can be used to reconstruct the volcanic and magmatic history of a complex such as Ossipee. Our work illustrates the complicated interplay between petrological magmatic processes and physical processes associated with the development of a caldera.

ACKNOWLEDGEMENTS

We thank Yan Lavallée, Marc-Antoine Longpré and the Kimball family for assistance in the field. Financial support was provided to B.K. by funds from the Department of Earth and Planetary Sciences, McGill University, and from GEOTOP, Université du Québec à Montréal, and by a research grant to J.S from the Natural Sciences and Engineering Research Council of Canada. We also acknowledge support from NSF Grant EAR-0125631.

REFERENCES

Bachman, O., and Bergantz, G.W., 2003, Rejuvenation of the Fish Canyon magma body: A window into the evolution of large-volume silicic magma systems: Geology, v. 31, p. 789-792.

Bachman, O., and Bergantz, G.W., 2004, On the origin of crystal-poor rhyolites: extracted from batholithic crystal mushes: Journal of Petrology, v. 45, p. 1565-1582.

Billings, M.P., 1943, Ring-dykes and their origin: Transactions of the New York Academy of Sciences, v. 5, p. 131-144.

Blake, S., and Fink, J.H., 1987, The dynamics of magma withdrawal from a density stratified dyke: Earth and Planetary Science Letters, v. 85, p. 516-524.

Branney, M.J., 1991, Eruption and depositional facies of the Whorneyside Tuff: an exceptionally large magnitude phreatoplinian eruption: Geological Society of America Bulletin, v. 202, p. 886-897.

Carr, R.S., 1980, Geology and Petrology of the Ossipee ring-complex, Carroll County, New Hampshire, Masters thesis, Dartmouth College, 174p.

Chapman, C.A., 1976, Structural evolution of the White Mountain Magma Series: Geological Society of America Memoir, v. 146, p. 281-300.

Christiansen, R.L., 2001, The Quaternary and Pliocene Yellowstone Plateau Volcanic Field of Wyoming, Idaho, and Montana: US Geological Survey Professional Paper 729-G, 145p.

Creasy, J.W. and Eby, G.N., 1993, Ring dikes and plutons: A deeper view of calderas as illustrated by the White Mountain igneous province, New Hampshire: In Cheney, J. T. and Hepburn, J. C. (eds.) Field Trip Guidebook for the Northeastern United States: 1993 Boston GSA, Vol. 1. Contribution No. 67, Department of Geology and Geography, University of Massachusetts, Amherst, MA, p. N1-N25.

Donaldson, C.H., and Henderson, C.M.B., 1988, A new interpretation of round embayments in quartz crystals: Mineralogical Magazine, v. 52, p. 27-33.

Eby, G.N., and Kennedy, B., 2004, The Ossipee ring complex, New Hampshire: In Hanson, L. (ed.) Guidebook to Field Trips from Boston, MA to Saco Bay, ME. New England Intercollegiate Geological Conference, Salem, MA, p. 61-72.

Folch, A., Marti, J., and Codina, R., 2001, Numerical modelling of magma withdrawal during caldera-forming eruptions: Journal of Geophysical Research, v. 106, p. 16,163-16,175.

Foland, K. A., and Faul, H., 1977, Ages of the White Mountain intrusives, New Hampshire, Vermont, and Maine, USA: American Journal of Science, v. 277, p. 888-904.

Ginibre, C., Worner, G., and Kronz, A., 2004, Structure and dynamics of the Laacher See magma chamber (Eifel, Germany) from major and trace element zoning in Sanidine: a cathodoluminesence and electron microprobe study: Journal of Petrology, v. 45, p. 2197-2223.

Hawkins, D., and Wiebe, R.A., 2004, Discrete stopping events in granite plutons: A signature of eruptions from silicic magma chambers: Geology, v. 32; p. 1021–1024.

Hess, K.U., and Dingwell, D.B., 1996, Viscosities of hydrous leucogranitic melts: A non-Arrhenian model: American Mineralogist, v. 81, p. 1297-1300.

Higgins, M.D., 1996, Magma dynamics beneath Kameni volcano, Greece, as revealed by crystal size and shape measurements: Journal of Volcanology and Geothermal Research v. 70, p. 37-48.

Higgins, M.D., 1999. Origin of megacrysts in granitoids by textural coarsening: A crystal size distribution (CSD) study of microcline in the cathedral peak granodiorite, Sierra Nevada, California: Fernandez C., and Castro, A. (eds), Understanding Granites: Integrating Modern and Classical Techniques: Special Publication 158, Geological Society of London, p. 207-219.

Hildreth, E.W., 1979, The Bishop Tuff: Evidence for the origin of compositional zonation in silicic magma chambers: In Chapin, C.E., and Elston, W.E. (eds.), Ash-Flow Tuffs: Geological Society of America Special Paper 180, p. 43-72.

Hildreth, E.W., 1981, Gradients in silicic magma chambers: Implications for lithospheric magmatism: Journal of Geophysical Research, v. 86, p. 10,153-10,192.

Hon, K.A., 1987, Geologic and petrologic evolution of the Lake City Caldera, San Juan Mountains, Colorado. Ph.D. Thesis, University of Colorado, Boulder, Colorado, 244p.

James R.S., and Hamilton, D.L., 1969, Phase relations in the system $NaAlSiO_3$-$KalsiO_3O_8$-$CaAl_2Si_2O_8$-SiO_2 at 1 kilobar water vapour pressure: Contributions to Mineralogy and Petrology, v. 21, p. 111-141.

Johnson, S.E., Schmidt, K.L., and Tait, M.C., 2002, Ring complexes in the Penninsular Ranges Batholith, Mexico and the USA: magma plumbing systems in the middle and upper crust: Lithos, v. 61, p. 187-208.

Kennedy, B., and Stix, J., 2003, Stages in the temporal evolution of calderas: Geoscience Canada, v. 30, p. 129-140.

Kingsley, L., 1931, Cauldron subsidence of the Ossipee Mountains: American Journal of Science, v. 22, p. 139-168.

Lejeune, A.-M., and Richet, P., 1995, Rheology of crystal-bearing silicate melts: An experimental study at high viscosities: Journal of Geophysical Research, v. 100, p. 4215-4229.

Lipman, P.W., 1976, Caldera-collapse breccias in the western San Juan Mountains, Colorado: Geological Society of America Bulletin, v. 87, p. 1397–1410.

Lyons, J.B., Bothner, W.A., Moench, R.H. and Thompson, J.B. Jr., 1997, Bedrock geologic map of New Hampshire: U. S. Geological Survey, U. S. Department of the Interior, 2 sheets.

Marsh, B.D, 1988, Crystal capture, sorting and retention in convecting magma: Geological Society of America Bulletin, v. 100, p. 1720-1737.

Marsh, B.D., 2000, Magma Chambers: In Sigurdsson, H., Houghton, B., McNutt, S., Rymer, H., and Stix, J. (eds.), Encyclopedia of Volcanoes: Academic Press, San Diego, USA, p. 191-206.

Marshall, L.A., and Sparks, R.J., 1984, Origin of some mixed magma and net-veined ring intrusions: Journal of the Geological Society of London, v. 141, p. 171-182.

Nekvasil, H., 1988, Calculation of equilibrium crystallization paths of compositionally simple hydrous felsic melts: American Mineralogist, v 73, p. 956-965.

Nekvasil, H., 1990, Reaction relations in the granite system: Implications for trachytic and syenitic magmas: American Mineralogist, v. 75, p. 560-571.

Paterson, S.R., Pignotta, G.S., and Vernon, R.H., 2004, The significance of microgranitoid enclave shapes and orientations: Journal of Structural Geology, v. 26, p. 1465–1481.

Philpotts, A.R., Shi, J., and Brustman, C., 1998, Role of plagioclase crystal chains in the differentiation of partly crystallized basaltic magma: Nature, v. 395, p. 343-346.

Quinn, A., 1941, The geology of Winnipesaukee Quadrangle New Hampshire: New Hampshire Planning and Development Commission, 21p.

Quinn, A., 1953, The geology of the Wolfeboro Quadrangle New Hampshire: New Hampshire Planning and Development Commission, 21p.

Rubin, A.M., 1995, Getting granite dikes out of the source region: Journal of Geophysical Research, v. 100, p. 5911-5929.

Sisson, T.W., and Bacon, C.R., 1999, Gas driven filter pressing in magmas: Geology, v 27, p. 613-616.

Smith, A.P., Kingsley, L., and Quinn, A., 1939, The geology of Mt. Chocorua Quadrangle New Hampshire: New Hampshire Planning and Development Commission, 24p.

Sparks, R.J., Sigurdsson, H., and Wilson, L., 1977, Magma mixing: a mechanism for triggering acid explosive eruptions: Nature, v. 267, p. 315-318.

Sparks, R.J., Huppert, H.E., and Turner, J.S., 1984, The Fluid dynamics of evolving magma chambers: Philosophical Transactions of the Royal Society of London, v. A310, p. 511-534.

Sparks, R.J., and Marshall, L.A., 1986, Thermal and mechanical constraints on mixing between mafic and silicic magmas: Journal of Volcanology and Geothermal Research, v. 29, p. 99-124.

Spieler, O., Kennedy, B., Kueppers, B., Dingwell, D.B., Scheu, B., and Taddeucci J., 2004, The fragmentation threshold of pyroclastic rocks: Earth and Planetary Science Letters, v. 226, p. 139-148.

Srogi, L. and Lutz, T.M., 1996, The role of residual melt migration in producing compositional diversity in a suite of granitic rocks: Earth and Planetary Science Letters, v. 144, p. 563-576.

Stix, J., Goff, F., Gorton M., Heiken G., and Garcia, S., 1988, Restoration of compositional zonation in the Bandelier silicic magma chamber between two caldera-forming eruptions; geochemistry and origin of the Cerro Toledo Rhyolite, Jemez Mountains, New Mexico: Journal of Geophysical Research, v. 93, p. 6129-6147.

Takeuchi, S., and Nakamura, M., 2001, Role of precursory less-viscous mixed magma in the eruption of phenocryst-rich magma; evidence from the Hokkaido-Komagatake 1929 eruption: Bulletin of Volcanology, v. 63, p. 365-376.

Takeuchi, S., 2004, Precursory dike propagation control of viscous magma eruptions: Geology, v. 32, p. 1001-1003.

Taylor, S.R., and McLennan, S.M., 1985, The Continental Crust: its Composition and Evolution. Blackwell Scientific Publications (Oxford), 312p.

Troll, V.R., Donaldson, C.H., and Emeleus, C.H., 2004, Pre-eruptive magma mixing in ash-flow deposits of the Tertiary Rum Igneous Centre, Scotland: Contributions to Mineralogy and Petrology, v. 147, p. 722–739.

Watson, E.B., 1979, Zircon saturation in felsic liquids; experimental results and applications to trace element geochemistry: Contributions to Mineralogy and Petrology, v. 70, p. 407-419.

Wiebe, R.A., Manon, M.R., Hawkins, D.P., and McDonough W.F., 2004, Late stage mafic injection and rejuvenation of the Vinalhaven granite, Coastal Maine: Journal of Peterology, v. 45, p. 2133-2153.

Wilson, J.R., 1969, The geology of the Ossipee Lake Quadrangle New Hampshire: New Hampshire Department of Resources and Economic Development Bulletin, v. 3, 111p.

Yurtman, S., and Rowbotham, S., 1999, A scanning electron microscope study of post-depositional changes in the northeast Nigde ignimbrites, South Central Anatolia, Turkey: Mineralogical Magazine, v.63, p. 131-141.

APPENDIX I

TABLE A-I. Feldspar compositions analysed by McGill Microprobe Laboratory, Montréal. Uncertainties are less than 1% and measurement conditions are presented after the table.

Sample	Colour	Rock type	Dist from rim for zoned crystals (μm)	SiO_2 (wt. %)	TiO_2 (wt. %)	Al_2O_3 (wt. %)	FeO (wt. %)	MgO (wt. %)	CaO (wt. %)	Na_2O (wt. %)	K_2O (wt. %)	BaO (wt. %)	SrO (wt. %)	Total (wt. %)
osp0311	pink	quartz syenite		67.02	0.00	18.59	0.19	0.01	0.38	5.70	8.72	0.00	0.00	100.61
osp0311	pink	quartz syenite		66.97	0.00	18.65	0.17	0.00	0.38	5.94	8.12	0.00	0.00	100.23
osp0311	pink	quartz syenite		67.12	0.02	18.29	0.20	0.01	0.25	5.45	9.02	0.02	0.00	100.38
osp0311	pink	quartz syenite		67.22	0.03	18.36	0.22	0.01	0.27	5.42	9.04	0.00	0.00	100.57
osp0311	pink	quartz syenite		66.62	0.00	18.50	0.18	0.00	0.30	5.06	9.69	0.00	0.03	100.39
osp0311	pink	quartz syenite		66.27	0.00	18.50	0.18	0.00	0.27	4.64	10.17	0.01	0.00	100.03
osp0311	pink	quartz syenite		66.71	0.04	18.52	0.18	0.00	0.20	5.57	8.97	0.00	0.00	100.20
osp0311	pink	quartz syenite		66.56	0.02	18.55	0.18	0.01	0.22	5.69	8.81	0.00	0.00	100.03
osp0311	pink	quartz syenite		66.93	0.04	18.52	0.20	0.00	0.22	5.78	8.63	0.02	0.00	100.33
osp0311	pink	quartz syenite		66.84	0.00	18.46	0.21	0.01	0.22	5.69	8.85	0.00	0.00	100.28
osp0311	pink	quartz syenite		67.02	0.03	18.52	0.23	0.00	0.25	5.53	8.76	0.09	0.01	100.45
osp0311	pink	quartz syenite		67.18	0.00	18.57	0.22	0.01	0.27	5.48	8.83	0.00	0.00	100.55
osp14b	pink	quartz syenite	300	67.05	0.02	18.34	0.22	0.00	0.30	5.50	8.75	0.01	0.01	100.21
osp14b	pink	quartz syenite	rim	66.26	0.00	18.13	0.20	0.00	0.13	3.76		0.04	0.00	100.16
osp14b	pink	quartz syenite	0	67.03	0.01	18.36	0.26	0.00	0.15	6.04	8.12	0.00	0.00	99.97
osp14b	pink	quartz syenite	300	67.36	0.00	18.31	0.20	0.00	0.16	6.13	8.08	0.03	0.00	100.28
osp14b	pink	quartz syenite	600	67.28	0.05	18.38	0.16	0.00	0.17	6.16	8.09	0.03	0.00	100.32
osp14b	pink	quartz syenite	900	67.51	0.00	18.51	0.23	0.00	0.14	6.10	8.25	0.00	0.00	100.74
osp14b	pink	quartz syenite	1200	67.38	0.04	18.34	0.22	0.00	0.20	5.79	8.55	0.00	0.01	100.52
osp14b	pink	quartz syenite	rim	67.12	0.00	18.22	0.19	0.01	0.26	5.72	8.61	0.00	0.00	100.13
osp14b	pink	quartz syenite	250	66.44	0.00	18.25	0.19	0.00	0.08	4.72		0.01	0.00	99.86
osp14b	pink	quartz syenite	200	66.79	0.00	18.54	0.16	0.01	0.10	6.18	7.98	0.00	0.01	99.77
osp14b	pink	quartz syenite	400	67.11	0.01	18.53	0.17	0.00	0.09	6.08	8.30	0.03	0.00	100.32
osp14b	pink	quartz syenite	550	67.20	0.03	18.47	0.17	0.00	0.15	5.59	8.79	0.05	0.00	100.46
osp14b	pink	quartz syenite	rim	67.29	0.00	18.51	0.20	0.00	0.22	5.59	8.69	0.00	0.01	100.51
osp15a	pink	quartz syenite		66.99	0.00	18.37	0.18	0.00	0.17	5.58	9.00	0.00	0.03	100.31
osp15a	pink	quartz syenite		66.85	0.00	18.39	0.16	0.00	0.23	5.48	9.11	0.00	0.00	100.22
osp15a	pink	quartz syenite		67.00	0.00	18.22	0.19	0.01	0.19	5.52	8.93	0.00	0.03	100.09
osp15a	pink	quartz syenite		66.98	0.03	18.44	0.19	0.00	0.20	5.41	8.97	0.00	0.02	100.24
osp15a	pink	quartz syenite		66.35	0.02	18.14	0.12	0.00	0.13	4.95	9.55	0.01	0.00	99.26
osp15a	pink	quartz syenite		66.81	0.00	18.42	0.18	0.00	0.22	5.32	9.10	0.00	0.00	100.04
osp15a	pink	quartz syenite		66.59	0.01	18.35	0.14	0.00	0.29	5.37	9.20	0.00	0.00	99.95

Sample	Colour	Rock type	Dist from rim for zoned crystals (μm)	SiO_2 (wt. %)	TiO_2 (wt. %)	Al_2O_3 (wt. %)	FeO (wt. %)	MgO (wt. %)	CaO (wt. %)	Na_2O (wt. %)	K_2O (wt. %)	BaO (wt. %)	SrO (wt. %)	Total (wt. %)
osp15a	pink	quartz syenite		66.87	0.03	18.38	0.17	0.00	0.17	5.34	9.16	0.00	0.00	100.12
osp15a	pink	quartz syenite		65.69	0.01	17.93	0.23	0.01	0.02	1.77		0.06	0.00	100.30
osp15a	pink	quartz syenite		67.07	0.01	18.43	0.21	0.00	0.08	5.71	8.81	0.00	0.00	100.31
osp15a	pink	quartz syenite		67.31	0.00	18.36	0.23	0.00	0.13	5.64	8.88	0.00	0.00	100.56
osp15a	pink	quartz syenite		67.22	0.00	18.20	0.19	0.00	0.15	5.35	9.25	0.00	0.00	100.35
osp15a	pink	quartz syenite	50	67.05	0.00	18.30	0.17	0.01	0.27	5.96	8.04	0.02	0.00	99.82
osp15a	pink	quartz syenite	50	67.11	0.01	18.44	0.17	0.00	0.24	6.01	8.16	0.04	0.00	100.20
osp15a	pink	quartz syenite		67.26	0.01	18.54	0.19	0.01	0.18	6.25	8.01	0.02	0.00	100.47
osp15a	pink	quartz syenite		67.16	0.00	18.53	0.17	0.00	0.20	6.14	7.85	0.00	0.00	100.06
osp15a	pink	quartz syenite		67.01	0.00	18.44	0.18	0.00	0.25	6.16	8.09	0.00	0.01	100.13
osp15a	pink	quartz syenite		67.08	0.00	18.50	0.16	0.00	0.25	6.21	7.90	0.00	0.00	100.11
osp14a	pink	quartz syenite		66.71	0.00	18.57	0.15	0.01	0.48	6.05	7.80	0.01	0.00	99.77
osp14a	pink	quartz syenite		67.06	0.00	18.19	0.25	0.00	0.25	5.79	8.32	0.00	0.00	99.85
osp14a	pink	quartz syenite		67.12	0.00	18.28	0.18	0.00	0.28	5.87	8.15	0.00	0.02	99.89
osp14a	pink	quartz syenite		66.96	0.00	18.47	0.23	0.00	0.30	5.93	8.12	0.00	0.03	100.03
osp14a	pink	quartz syenite		67.29	0.00	18.25	0.17	0.01	0.28	5.88	8.26	0.02	0.00	100.14
osp14a	pink	quartz syenite		66.85	0.02	18.78	0.17	0.00	0.47	6.44	7.54	0.01	0.00	100.27
osp14a	pink	quartz syenite		66.77	0.00	18.45	0.26	0.00	0.18	5.95	8.36	0.03	0.02	100.02
osp14a	pink	quartz syenite		67.30	0.00	18.53	0.23	0.01	0.19	5.98	8.43	0.02	0.00	100.68
osp14a	pink	quartz syenite		67.15	0.00	18.66	0.19	0.00	0.24	6.03	8.08	0.00	0.01	100.35
osp14a	pink	quartz syenite		66.95	0.00	18.35	0.18	0.00	0.25	5.60	8.67	0.00	0.01	100.01
osp11	pink	quartz syenite	190	66.76	0.00	18.25	0.33	0.00	0.07	6.20	8.25	0.03	0.00	99.89
osp11	pink	quartz syenite	385	66.75	0.00	18.38	0.27	0.00	0.12	5.92	8.52	0.00	0.02	99.99
osp11	pink	quartz syenite	80	66.32	0.00	18.58	0.17	0.00	0.19	5.71	8.72	0.04	0.04	99.76
osp11	pink	quartz syenite	250	66.52	0.01	18.49	0.14	0.00	0.25	5.84	8.65	0.00	0.00	99.90
osp11	pink	quartz syenite	600	66.20	0.00	18.54	0.20	0.00	0.31	6.25	7.94	0.00	0.00	99.44
osp11	pink	quartz syenite	600	66.73	0.00	18.56	0.14	0.00	0.27	6.12	8.20	0.00	0.00	100.03
osp11	pink	quartz syenite	180	66.41	0.01	18.36	0.33	0.00	0.18	5.65	8.85	0.00	0.00	99.79
osp11	pink	quartz syenite	500	66.08	0.00	18.12	0.43	0.00	0.18	5.58	9.03	0.00	0.00	99.40
osp11	pink	quartz syenite	0	66.62	0.02	18.44	0.19	0.00	0.22	6.01	8.22	0.00	0.00	99.72
osp11	pink	quartz syenite	570	66.19	0.02	18.61	0.19	0.00	0.24	6.10	8.26	0.00	0.00	99.61
osp0402	pink	rhyolite		66.57	0.02	18.56	0.18	0.00	0.13	5.29	9.42	0.02	0.00	100.17

Sample	Colour	Rock type	Dist from rim for zoned crystals (μm)	SiO_2 (wt. %)	TiO_2 (wt. %)	Al_2O_3 (wt. %)	FeO (wt. %)	MgO (wt. %)	CaO (wt. %)	Na_2O (wt. %)	K_2O (wt. %)	BaO (wt. %)	SrO (wt. %)	Total (wt. %)
osp0402	pink	rhyolite		66.63	0.01	18.60	0.17	0.00	0.22	6.32	7.73	0.03	0.01	99.72
osp0402	pink	rhyolite		66.90	0.00	19.00	0.15	0.00	0.44	7.09	6.46	0.00	0.00	100.03
osp0402	pink	rhyolite		66.28	0.00	18.59	0.16	0.00	0.15	5.81	8.58	0.00	0.04	99.61
osp0402	pink	rhyolite		66.56	0.03	18.36	0.28	0.00	0.18	6.10	8.24	0.01	0.03	99.79
osp0402	pink	rhyolite		65.71	0.03	18.36	0.30	0.00	0.26	6.24	8.04	0.00	0.01	98.96
osp0402	pink	rhyolite		66.40	0.03	18.39	0.29	0.00	0.12	6.06	8.32	0.03	0.00	99.63
osp0402	pink	rhyolite		65.56	0.00	18.31	0.23	0.00	0.41	6.29	7.84	0.00	0.00	98.64
osp0402	pink	rhyolite		66.93	0.01	18.45	0.31	0.01	0.03	6.38	7.96	0.00	0.00	100.08
osp0402	pink	rhyolite		66.53	0.01	18.43	0.31	0.01	0.03	6.43	7.83	0.01	0.00	99.59
osp0402	pink	rhyolite		66.64	0.00	18.35	0.31	0.00	0.04	6.17	8.26	0.00	0.00	99.77
osp0402	pink	rhyolite		66.91	0.01	18.35	0.33	0.00	0.02	6.37	7.96	0.00	0.00	99.94
osp90d	pink	rhyolite	400	68.08	0.01	19.14	0.18	0.00	0.03	11.39	0.33	0.00	0.00	99.15
osp90d	pink	rhyolite	400	66.21	0.03	18.48	0.19	0.00	0.07	6.10	8.39	0.02	0.00	99.50
osp90d	pink	rhyolite	1000	66.13	0.02	18.48	0.19	0.00	0.08	6.00	8.72	0.00	0.04	99.67
osp90d	pink	rhyolite	125	66.41	0.03	18.57	0.17	0.00	1.21	9.48	2.83	0.02	0.00	98.71
osp90d	pink	rhyolite	0	68.11	0.00	18.99	0.19	0.00	0.03	11.35	0.38	0.04	0.04	99.13
osp90d	pink	rhyolite	400	66.26	0.00	18.36	0.26	0.02	0.06	6.14	8.28	0.00	0.00	99.36
osp90d	pink	rhyolite	450	66.38	0.03	18.37	0.21	0.00	0.05	6.02	8.31	0.01	0.00	99.36
osp90d	pink	rhyolite	550	64.23	0.00	18.02	0.22	0.00	0.02	0.64		0.00	0.00	99.56
osp90d	pink	rhyolite		66.40	0.00	18.46	0.17	0.00	0.01	6.57	7.54	0.00	0.00	99.16
osp90d	pink	rhyolite		66.36	0.01	18.53	0.16	0.00	0.26	6.60	7.61	0.00	0.00	99.54
osp90d	pink	rhyolite	600	66.32	0.01	18.52	0.17	0.00	0.06	6.59	7.85	0.00	0.03	99.54
osp90d	pink	rhyolite	300	66.81	0.01	18.58	0.19	0.00	0.09	7.15	6.71	0.00	0.00	99.54
osp90d	pink	rhyolite	650	66.10	0.02	18.57	0.18	0.00	0.09	6.21	8.28	0.02	0.03	99.51
osp0402	pink	rhyolite		65.86	0.00	18.73	0.17	0.00	0.25	5.84	8.20	0.02	0.00	99.06
osp0402	pink	rhyolite		67.26	0.00	18.80	0.18	0.01	0.31	6.46	7.56	0.03	0.00	100.62
osp0402	pink	rhyolite		66.67	0.00	18.76	0.19	0.00	0.32	6.63	7.33	0.00	0.00	99.91
osp0402	pink	rhyolite		66.27	0.02	18.60	0.18	0.02	0.36	6.59	7.19	0.00	0.00	99.21
osp19b	pink	rhyolite		68.62	0.02	19.37	0.02	0.00	0.08	11.46	0.07	0.03	0.03	99.69
osp19b	pink	rhyolite		67.90	0.00	19.35	0.12	0.00	0.07	11.41	0.07	0.00	0.01	98.94
osp19b	pink	rhyolite		68.23	0.02	19.11	0.04	0.01	0.10	11.37	0.06	0.00	0.01	98.93
osp19b	pink	rhyolite		64.53	0.00	18.30	0.02	0.00	0.00	0.28	17.35	0.02	0.02	100.52

Sample	Colour	Rock type	Dist from rim for zoned crystals (μm)	SiO_2 (wt. %)	TiO_2 (wt. %)	Al_2O_3 (wt. %)	FeO (wt. %)	MgO (wt. %)	CaO (wt. %)	Na_2O (wt. %)	K_2O (wt. %)	BaO (wt. %)	SrO (wt. %)	Total (wt. %)
osp19b	pink	rhyolite		64.11	0.00	18.12	0.00	0.01	0.04	0.35	17.14	0.04	0.00	99.80
osp19b	pink	rhyolite		65.06	0.00	18.16	0.07	0.00	0.00	0.31	17.33	0.17	0.02	101.12
osp19b	pink	rhyolite		68.40	0.02	19.57	0.17	0.00	0.19	11.50	0.09	0.04	0.01	99.99
osp19b	pink	rhyolite		68.25	0.01	19.57	0.04	0.00	0.05	11.72	0.05	0.06	0.00	99.73
osp19b	pink	rhyolite		63.81	0.00	18.19	0.09	0.00	0.00	0.16	17.37	0.17	0.00	99.79
osp19b	pink	rhyolite		64.65	0.00	18.23	0.00	0.00	0.00	0.33	17.29	0.07	0.00	100.57
osp76a	grey	quartz syenite	300	62.00	0.15	23.08	0.25	0.01	4.87	7.74	1.53	0.67	0.07	100.36
osp76a	grey	quartz syenite	600	65.47	0.05	20.10	0.15	0.00	1.68	7.10	5.39	0.20	0.05	100.20
osp76a	grey	quartz syenite	900	63.17	0.09	22.55	0.18	0.01	4.12	9.04	0.18	0.11	0.03	99.47
osp76a	grey	quartz syenite	1200	64.17	0.12	21.04	0.19	0.00	2.19	8.05	3.06	1.18	0.00	100.00
osp76a	grey	quartz syenite	1500	64.20	0.14	20.91	0.20	0.00	2.04	7.17	4.51	1.39	0.01	100.57
osp76a	grey	quartz syenite	1800	63.20	0.09	22.67	0.27	0.00	4.39	8.81	0.40	0.17	0.03	100.04
osp76a	grey	quartz syenite	300	65.34	0.08	20.24	0.18	0.01	1.78	7.50	4.52	0.40	0.07	100.10
osp76a	grey	quartz syenite	600	65.37	0.07	20.35	0.20	0.00	2.06	7.79	3.98	0.09	0.00	99.90
osp76a	grey	quartz syenite	900	65.48	0.06	20.18	0.19	0.01	1.80	7.10	5.44	0.15	0.04	100.46
osp76a	grey	quartz syenite	1200	66.32	0.00	20.78	0.02	0.00	1.81	10.45	0.19	0.00	0.04	99.61
osp76a	grey	quartz syenite		64.62	0.11	21.51	0.21	0.00	2.78	9.67	0.43	0.21	0.02	99.56
osp76a	grey	quartz syenite		64.62	0.15	21.34	0.20	0.00	2.58	9.13	0.92	0.51	0.01	99.46
osp76a	grey	quartz syenite		64.48	0.02	22.26	0.05	0.01	2.73	9.75	0.15	0.05	0.01	99.50
osp76a	grey	quartz syenite		64.04	0.16	20.72	0.16	0.00	2.15	7.61	4.16	1.12	0.01	100.11
osp76a	grey	quartz syenite		65.22	0.08	20.09	0.19	0.00	1.61	7.36	5.02	0.51	0.06	100.14
osp76a	grey	quartz syenite		64.63	0.11	20.77	0.21	0.00	2.27	7.85	3.88	0.46	0.07	100.25
osp76a	grey	quartz syenite		65.46	0.10	21.28	0.16	0.00	2.49	9.94	0.19	0.21	0.00	99.82
osp76a	grey	quartz syenite		62.17	0.14	22.63	0.21	0.01	4.44	7.85	1.65	0.68	0.02	99.81
osp76a	grey	quartz syenite		64.02	0.14	20.49	0.20	0.00	1.64	6.67	5.46	1.94	0.01	100.57
osp76a	grey	quartz syenite		66.59	0.03	18.58	0.16	0.01	0.19	5.52	9.09	0.26	0.00	100.41
osp76a	grey	quartz syenite		64.14	0.14	20.43	0.23	0.01	1.91	6.44	5.69	1.28	0.00	100.27
osp15a	grey	quartz syenite		63.03	0.10	22.35	0.26	0.00	4.08	8.43	1.39	0.49	0.02	100.15
osp15a	grey	quartz syenite		62.96	0.11	20.68	0.09	0.00	2.19	4.81	7.78	1.64	0.02	100.28
osp15a	grey	quartz syenite		64.19	0.07	19.96	1.96	0.23	0.50	10.00	0.39	0.05	0.02	97.34
osp15a	grey	quartz syenite		67.92	0.01	19.22	0.43	0.01	0.22	11.20	0.19	0.04	0.00	99.23
osp14a	grey	quartz syenite		65.49	0.01	19.47	0.16	0.00	1.20	5.29	8.65	0.02	0.00	100.29

Sample	Colour	Rock type	Dist from rim for zoned crystals (μm)	SiO_2 (wt. %)	TiO_2 (wt. %)	Al_2O_3 (wt. %)	FeO (wt. %)	MgO (wt. %)	CaO (wt. %)	Na_2O (wt. %)	K_2O (wt. %)	BaO (wt. %)	SrO (wt. %)	Total (wt. %)
osp14a	grey	quartz syenite		64.88	0.03	19.43	0.17	0.00	1.21	4.62	9.74	0.08	0.01	100.17
osp14a	grey	quartz syenite		65.17	0.09	19.43	0.16	0.00	1.23	5.09	8.73	0.01	0.01	99.91
osp14a	grey	quartz syenite		65.33	0.04	19.72	0.19	0.00	1.35	5.27	8.64	0.06	0.00	100.60
osp14a	grey	quartz syenite		65.08	0.00	21.52	0.09	0.01	2.77	9.91	0.16	0.05	0.04	99.62
osp14a	grey	quartz syenite		64.66	0.00	18.04	0.02	0.00	0.03	1.00	16.20	0.24	0.00	100.19
osp14a	grey	quartz syenite		65.01	0.00	18.21	0.01	0.00	0.00	0.89	16.43	0.13	0.01	100.68
osp14a	grey	quartz syenite		68.46	0.00	19.52	0.04	0.00	0.39	11.17	0.14	0.00	0.00	99.71
osp14a	grey	quartz syenite		64.93	0.08	19.63	0.16	0.01	1.13	4.75	9.43	0.15	0.00	100.27
osp14b	grey	quartz syenite	0	64.83	0.08	19.74	0.21	0.00	1.42	5.28	8.37	0.16	0.07	100.15
osp14b	grey	quartz syenite	300	64.61	0.03	20.01	0.16	0.00	1.68	5.62	7.85	0.17	0.01	100.14
osp14b	grey	quartz syenite	600	65.20	0.09	19.58	0.19	0.00	1.22	5.59	8.04	0.28	0.00	100.19
osp14b	grey	quartz syenite	900	64.64	0.08	19.92	0.21	0.00	1.52	5.05	8.76	0.13	0.03	100.34
osp14b	grey	quartz syenite	rim	64.77	0.09	20.17	0.23	0.00	1.65	6.29	6.71	0.45	0.00	100.34
osp15a	grey	quartz syenite		63.51	0.12	20.27	0.17	0.02	2.02	5.29	7.55	0.51	0.05	99.51
osp15a	grey	quartz syenite		63.90	0.07	19.95	0.22	0.00	1.53	4.91	8.91	0.60	0.01	100.09
osp15a	grey	quartz syenite		63.97	0.06	20.62	0.19	0.01	2.43	5.51	7.11	0.04	0.05	99.98
osp15a	grey	quartz syenite		65.05	0.04	19.53	0.16	0.01	1.22	4.91	9.13	0.04	0.00	100.09
osp15a	grey	quartz syenite	500	64.81	0.05	19.87	0.17	0.01	1.51	4.52	9.30	0.16	0.02	100.43
osp15a	grey	quartz syenite	500	65.19	0.08	19.51	0.26	0.02	1.05	4.83	9.39	0.29	0.04	100.65
osp15a	grey	quartz syenite		65.66	0.03	19.63	0.18	0.02	1.37	6.28	7.13	0.14	0.00	100.43
osp15a	grey	quartz syenite		65.68	0.06	19.88	0.21	0.00	1.49	7.37	5.44	0.13	0.00	100.26
osp14a	grey	quartz syenite		65.49	0.01	19.47	0.16	0.00	1.20	5.29	8.65	0.02	0.00	100.29
osp14a	grey	quartz syenite		64.88	0.03	19.43	0.17	0.00	1.21	4.62	9.74	0.08	0.01	100.17
osp14a	grey	quartz syenite		65.17	0.09	19.43	0.16	0.00	1.23	5.09	8.73	0.01	0.01	99.91
osp0311	grey	quartz syenite	500	65.07	0.05	19.94	0.14	0.01	1.50	5.59	7.54	0.29	0.00	100.13
osp0311	grey	quartz syenite	500	65.15	0.08	19.74	0.16	0.01	1.40	5.15	8.66	0.24	0.02	100.59
osp0311	grey	quartz syenite	700	65.25	0.02	19.56	0.12	0.01	1.16	5.43	8.51	0.12	0.06	100.24
osp0311	grey	quartz syenite	700	65.05	0.06	19.83	0.17	0.00	1.41	5.48	8.09	0.19	0.04	100.32
osp0311	grey	quartz syenite	500	64.88	0.08	19.87	0.17	0.00	1.56	5.68	7.68	0.18	0.00	100.09
osp0311	grey	quartz syenite	0	64.87	0.04	20.01	0.19	0.00	1.65	5.57	7.61	0.02	0.05	99.99
osp0311	grey	quartz syenite	300	65.17	0.07	20.15	0.21	0.01	1.64	6.17	6.84	0.30	0.01	100.55
osp0311	grey	quartz syenite	500	64.93	0.09	20.01	0.21	0.00	1.47	5.60	7.65	0.38	0.01	100.35

Sample	Colour	Rock type	Dist from rim for zoned crystals (μm)	SiO_2 (wt. %)	TiO_2 (wt. %)	Al_2O_3 (wt. %)	FeO (wt. %)	MgO (wt. %)	CaO (wt. %)	Na_2O (wt. %)	K_2O (wt. %)	BaO (wt. %)	SrO (wt. %)	Total (wt. %)
osp0311	grey	quartz syenite	700	65.10	0.07	19.87	0.23	0.01	1.41	6.43	6.66	0.35	0.03	100.14
osp0311	grey	quartz syenite	500	65.16	0.05	19.82	0.19	0.00	1.26	5.95	7.33	0.31	0.00	100.06
osp0311	grey	quartz syenite	0	65.00	0.07	19.77	0.16	0.00	1.36	5.13	8.76	0.15	0.00	100.40
osp0311	grey	quartz syenite	600	65.30	0.08	19.96	0.16	0.00	1.49	6.23	6.97	0.25	0.01	100.45
osp0402	pink	enclave in rhyolite	300	64.68	0.04	19.69	0.17	0.02	1.29	5.03	8.98	0.00	0.00	99.91
osp0402	pink	enclave in rhyolite	500	64.42	0.07	19.94	0.16	0.00	1.51	4.99	8.51	0.32	0.00	99.90
osp0402	pink	enclave in rhyolite	500	64.51	0.04	20.08	0.20	0.00	1.75	5.20	8.25	0.01	0.00	100.05
osp0402	pink	enclave in rhyolite	600	64.91	0.07	19.81	0.21	0.01	1.53	5.02	8.67	0.07	0.06	100.36
osp0402	pink	enclave in rhyolite	400	64.13	0.15	19.54	0.18	0.00	2.31	4.62	9.05	0.30	0.00	100.28
osp0402	pink	enclave in rhyolite	400	64.40	0.09	20.32	0.18	0.01	1.59	5.91	7.18	0.37	0.00	100.05
osp0402	pink	enclave in rhyolite	600	64.17	0.04	19.74	0.19	0.00	1.33	5.03	8.70	0.33	0.05	99.57
osp0402	pink	enclave in rhyolite	700	64.89	0.05	19.69	0.18	0.00	1.23	5.17	8.63	0.15	0.03	100.02
osp0402	pink	enclave in rhyolite		64.70	0.02	19.64	0.16	0.00	1.32	5.02	9.01	0.07	0.00	99.93
osp0402	pink	enclave in rhyolite		65.12	0.10	19.56	0.15	0.00	1.12	4.95	9.32	0.03	0.01	100.36
osp0402	pink	enclave in rhyolite		64.87	0.05	19.84	0.17	0.00	1.27	5.47	8.06	0.03	0.03	99.77
osp0402	pink	enclave in rhyolite		64.74	0.06	19.60	0.16	0.00	1.17	5.25	8.43	0.02	0.00	99.43
osp0401	pink	enclave in rhyolite		66.60	0.00	18.46	0.24	0.01	0.03	5.67	9.12	0.00	0.01	100.13
osp0401	pink	enclave in rhyolite		66.82	0.00	18.57	0.19	0.00	0.06	6.28	8.01	0.02	0.06	100.02
osp0401	pink	enclave in rhyolite		66.91	0.00	18.43	0.24	0.00	0.07	6.44	7.80	0.02	0.03	99.95
osp0401	pink	enclave in rhyolite		66.58	0.00	18.59	0.19	0.02	0.08	6.25	7.89	0.01	0.00	99.61
osp0401	pink	enclave in rhyolite		67.33	0.00	18.63	0.20	0.01	0.06	6.42	7.77	0.01	0.00	100.43
osp0401	pink	enclave in rhyolite		61.91	0.01	19.00	0.09	0.01	0.02	0.24	16.81	0.07	0.00	98.17
osp15a	grey	enclave in qtz syenite	450	62.45	0.09	21.84	0.24	0.01	3.68	5.49	5.98	0.41	0.02	100.20
osp15a	grey	enclave in qtz syenite	700	63.05	0.08	21.05	0.20	0.01	2.83	5.67	6.71	0.48	0.08	100.14
osp15a	grey	enclave in qtz syenite	500	63.24	0.06	20.54	0.39	0.05	2.14	4.73	8.49	0.66	0.01	100.31
osp15a	grey	enclave in qtz syenite	400	57.74	0.11	25.69	0.26	0.04	8.19	6.00	1.29	0.12	0.07	99.50
osp15a	grey	enclave in qtz syenite		62.86	0.09	22.57	0.28	0.00	4.10	8.18	1.72	0.42	0.00	100.22
osp15a	grey	enclave in qtz syenite		63.67	0.09	21.93	0.25	0.01	3.38	8.18	2.10	0.59	0.03	100.22
osp11	grey	enclave in qtz syenite		61.70	0.08	23.12	0.31	0.00	4.84	8.17	0.99	0.50	0.03	99.73
osp11	grey	enclave in qtz syenite		61.43	0.06	23.13	0.31	0.01	4.90	7.75	1.55	0.58	0.04	99.76
osp11	grey	enclave in qtz syenite		61.54	0.11	22.54	0.26	0.01	4.22	6.23	4.17	0.91	0.08	100.07
osp11	grey	enclave in qtz syenite		60.32	0.09	23.79	0.39	0.05	5.74	7.52	0.97	0.51	0.02	99.41

Sample	Colour	Rock type	Dist from rim for zoned crystals (μm)	SiO_2 (wt. %)	TiO_2 (wt. %)	Al_2O_3 (wt. %)	FeO (wt. %)	MgO (wt. %)	CaO (wt. %)	Na_2O (wt. %)	K_2O (wt. %)	BaO (wt. %)	SrO (wt. %)	Total (wt. %)
osp0311	grey	enclave in qtz syenite	700	61.39	0.11	23.52	0.22	0.01	5.41	7.28	1.92	0.13	0.00	100.00
osp0311	grey	enclave in qtz syenite	1000	60.82	0.07	23.23	0.23	0.01	5.46	7.34	1.48	0.08	0.04	98.76
osp0311	grey	enclave in qtz syenite	700	58.65	0.06	24.92	0.29	0.02	7.31	6.36	1.26	0.20	0.02	99.08
osp0311	grey	enclave in qtz syenite	500	58.02	0.07	25.24	0.25	0.02	7.23	6.37	1.38	0.21	0.01	98.79
osp90d	grey	enclave in qtz syenite	400	62.88	0.08	21.29	0.19	0.02	3.01	5.88	5.96	0.14	0.01	99.45
osp90d	grey	enclave in qtz syenite	700	62.69	0.11	21.59	0.22	0.00	3.24	6.05	5.71	0.50	0.06	100.17
osp90d	grey	enclave in qtz syenite	700	63.93	0.11	19.68	0.19	0.01	1.30	4.65	9.43	0.42	0.00	99.72
osp90d	grey	enclave in qtz syenite	300	61.60	0.11	22.58	0.24	0.01	4.24	5.87	4.84	0.60	0.00	100.10
osp90d	grey	enclave in qtz syenite	100	61.61	0.14	22.13	0.24	0.02	3.93	6.00	4.96	0.68	0.06	99.76
osp90d	grey	enclave in qtz syenite	700	61.72	0.10	21.69	0.24	0.00	3.66	6.00	5.02	0.63	0.02	99.08
osp90d	grey	enclave in qtz syenite	300	61.76	0.06	21.63	0.25	0.00	3.34	5.79	5.72	0.72	0.06	99.34
osp90d	grey	enclave in qtz syenite	300	62.58	0.10	21.44	0.26	0.00	2.95	5.70	6.26	0.68	0.00	99.97
osp90d	grey	enclave in qtz syenite	600	62.41	0.05	22.10	0.30	0.02	3.67	7.12	3.78	0.70	0.05	100.19

Measurement Conditions for microprobe

WDS elements

Element	X-ray	Crystal	CH	Acc.v	Peak Pos. (Angstrom)	BG_L	BG_U (mm)
1 Na	Ka	TAP	(1)	15.0	129.466	11.91010	5.000	6.000
2 Mg	Ka	TAP	(2)	15.0	107.471	9.89000	5.000	4.000
3 K	Ka	PETJ	(3)	15.0	120.005	3.74140	5.000	6.000
4 Sr	La	PETJ	(4)	15.0	219.936	6.86280	2.200	3.000
5 Fe	Ka	LIFH	(5)	15.0	134.814	1.93604	5.000	5.000
6 Si	Ka	TAP	(1)	15.0	77.363	7.12542	7.000	7.000
7 Al	Ka	TAP	(2)	15.0	90.551	8.33934	5.000	5.000
8 Ca	Ka	PETJ	(3)	15.0	107.755	3.35839	5.000	4.000
9 Ba	La	LIFH	(5)	15.0	193.073	2.77595	2.400	3.000

Element	Peak	Back	Pksk	Gain	High.V	Base.L	Window.W	Mode
1 Na	20.0	10.0 (sec)	1	8	1702	0.2	9.3 (V)	Dif
2 Mg	20.0	10.0 (sec)	1	16	1702	0.2	- (V)	Int
3 K	20.0	10.0 (sec)	1	16	1684	0.2	- (V)	Int
4 Sr	30.0	15.0 (sec)	0	16	1676	0.2	- (V)	Int
5 Fe	20.0	10.0 (sec)	1	16	1698	0.2	- (V)	Int
6 Si	20.0	10.0 (sec)	1	8	1702	0.2	- (V)	Int
7 Al	20.0	10.0 (sec)	1	16	1702	0.2	- (V)	Int
8 Ca	20.0	10.0 (sec)	1	16	1684	0.2	3.0 (V)	Dif
9 Ba	20.0	10.0 (sec)	1	16	1698	0.2	- (V)	Int

Measurement Order of WDS

Order	Channel 1	2	3	4	5
1	Na	Mg	K	Sr	Fe
2	Si	Al	Ca	-	Ba

Calc. Elements : O (Anion)

Element	Standard name	Wt.(%)	ZAF Fac.	Z	A	F
1 Na2O	albite	11.4300	5.4858	10.7252	0.5094	1.0041
2 MgO	Diopside	17.9400	4.7341	7.8691	0.5985	1.0051
3 K2O	Orthoclase	16.9100	1.0758	1.2033	0.8940	1.0001
4 SrO	Sr-Feld	3.6300	2.8860	4.0306	0.7157	1.0004
5 FeO	Fe2O3m	89.9830	0.2140	0.2170	0.9864	1.0000
6 SiO2	Orthoclase	65.0300	3.2797	4.4186	0.7415	1.0011
7 Al2O3	Orthoclase	16.9800	4.3209	5.8692	0.7244	1.0163
8 CaO	Diopside	25.1800	0.8662	0.9351	0.9261	1.0002
9 BaO	Ba-Orth	4.0860	0.4646	0.4970	0.9348	1.0000

Standard Intensity of WDS

Element	Curr.(A)	Net(cps)	Bg-(cps)	Bg+(cps)	S.D.(%)	Date
1 Na	2.004E-08	1151.2	10.6	8.2	1.41	Feb 5 09:44 2004
2 Mg	2.001E-08	2600.3	14.2	10.9	0.66	Feb 5 09:31 2004
3 K	1.996E-08	1967.9	11.7	9.4	0.88	Feb 5 09:50 2004
4 Sr	2.009E-08	65.1	4.5	3.3	4.14	Feb 5 09:21 2004
5 Fe	2.008E-08	9852.6	53.6	51.1	0.34	Feb 5 09:12 2004
6 Si	1.996E-08	13057.3	51.2	46.7	0.34	Feb 5 09:50 2004
7 Al	1.996E-08	3448.7	28.1	18.4	0.81	Feb 5 09:50 2004
8 Ca	2.001E-08	2842.7	17.7	15.0	0.63	Feb 5 09:31 2004
9 Ba	2.007E-08	115.9	9.9	9.2	3.37	Feb 5 09:26 2004

UNK No. : 1

CHAPTER 2

Magma chamber replenishment and magma interactions during the formation of Lake City caldera, Colorado, USA.

Ben Kennedy, Ken Hon and John Stix

ABSTRACT

Lake City caldera is the youngest caldera in the San Juan Volcanic Field, Colorado. The 23 Ma caldera exhibits an exceptionally complete exposure of volcanic and intrusive rocks from different structural levels. The rocks show a large amount of chemical diversity attesting to a complex magmatic system beneath the caldera. We use field and geochemical data from zoned ignimbrites and intrusions to constrain the configuration of magma chambers and magma interactions during the formation of Lake City caldera. Two geochemically distinct magma batches erupted during caldera formation: high silica rhyolites, trachytes, and mafic trachytes (Batch A), and, dacites and andesites (Batch B). The ignimbrites of the Lower, Middle and Upper Sunshine Peak Tuff represent the majority of the erupted Batch A magma, showing a temporal progression in bulk composition from high silica rhyolite, through rhyolite, to trachyte. Major element, REE, and isotopic data are consistent with the sequential eruption from a zoned magma chamber formed by fractional crystallization. However, some aspects of the zonation are inconsistent with this interpretation. Compositional jumps and periods of reverse zonation suggest that replenishment, and accelerated periods of magma movement occurred in the magma chamber during caldera formation. After collapse, dacite lavas of Batch B erupted, concurrent with uplift from the shallow intrusion of residual Batch A and Batch B magma. Our results indicate that magma chamber replenishment and magma interaction play an integral role in caldera development. There is thus a complex interplay between chamber processes providing conditions suitable for caldera formation, and in turn, caldera formation affecting chamber processes.

INTRODUCTION

Lake City caldera formed at 22.93 ± 0.02 Ma (Bove et al., 2001) and is the youngest of the 15 Tertiary calderas of the San Juan Volcanic Field in Colorado (Steven and Lipman, 1976; Lipman et al., 1997) (Fig. 1a). Pyroclastic and intrusive rocks are well exposed at Lake City caldera, revealing the evolution of a large magmatic system. Extreme relief, differential subsidence and uplift expose over two kilometers of intracaldera stratigraphy and several resurgent magmatic intrusions (Fig 1b) (Hon, 1987; Hon and Lipman, 1989). This superb exposure reveals that several different magma types interacted, intruded, and erupted during the formation of the caldera. Both the ignimbrite and the subsequent intrusions at Lake City show chemical zonation from the beginning to the end of eruption (Hon, 1987; Hon and Lipman, 1989).

During the formation of calderas, chemically zoned ignimbrites commonly are erupted, and these eruptions have been used to infer the nature of large magmatic systems (e.g., Hildreth, 1981; Bacon, 1983; Eichelberger et al., 2000). Chemically zoned ignimbrites may show gradational changes from one magma type to another (Hildreth, 1979; 1981) or abrupt changes with compositional gaps (Bacon, 1983; Eichelberger et al., 2000). In situ fractional crystallization processes can produce gradual chemical zonation in a single large magma chamber (Hildreth, 1981). Fractional crystallization coupled with double diffusive convection can explain gaps in compositional zonation in some circumstances (Sparks et al., 1984). An alternative approach is to consider the chemical changes that occur during caldera forming eruptions as the result of separate magma batches. Distinct magma batches could exist independently in separate chambers, or

FIGURE 1. (a) The location of Lake City caldera within the San Juan Volcanic field, and the association with the Eureka Graben and Uncompaghre caldera. (b) Map of the major rock types at Lake City caldera redrawn from Hon (1987); scaled cross-sections drawn from the map of Hon (1987).

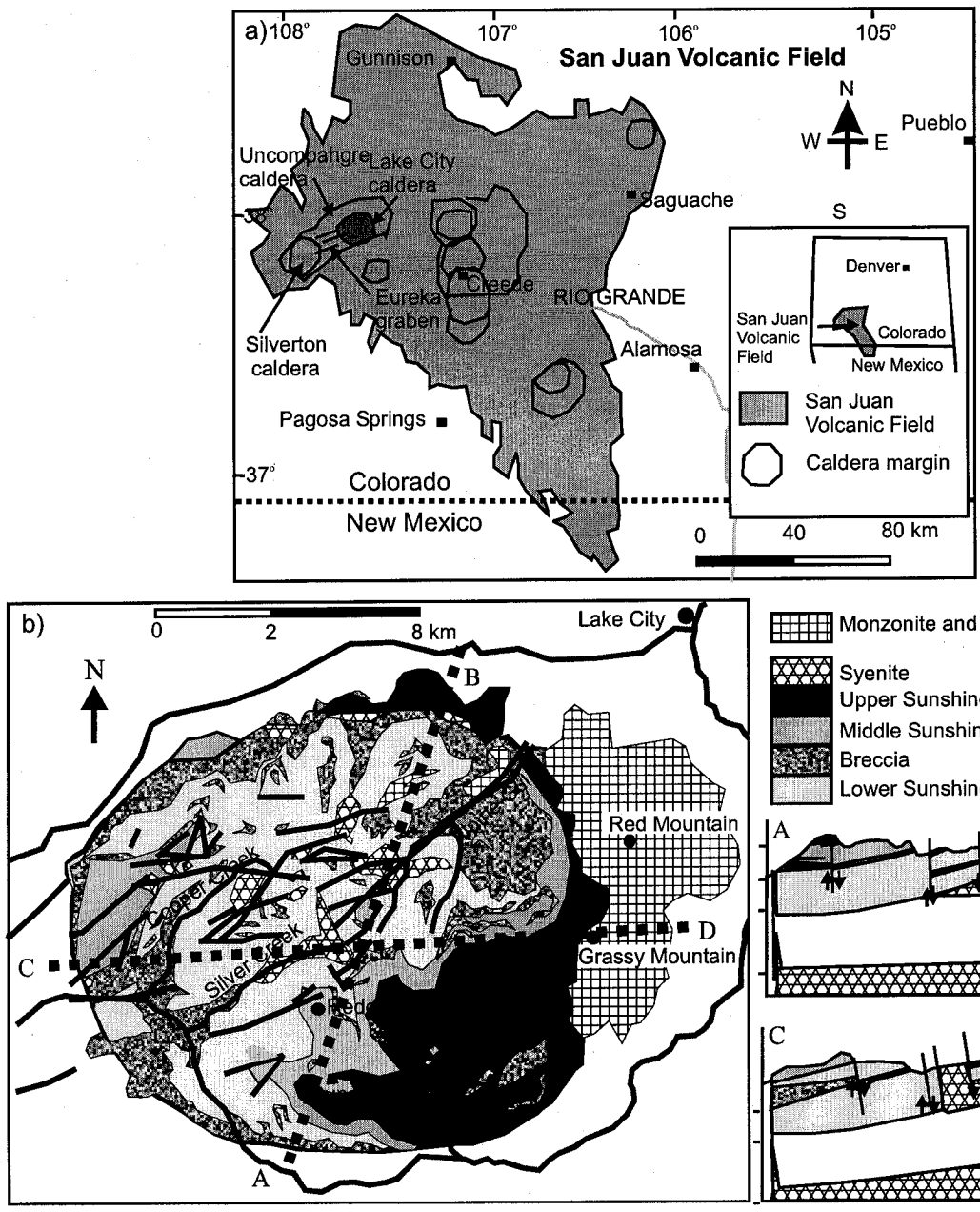
a)
108°
107°
106°
105°
San Juan Volcanic Field
Gunnison
N
W
E
Pueblo
Uncompahgre caldera
Lake City caldera
Saguache
S
Creede
RIO GRANDE
Eureka graben
Silverton caldera
Alamosa
Denver
San Juan Volcanic Field
Colorado
New Mexico
Pagosa Springs
37°
Colorado
New Mexico
San Juan Volcanic Field
Caldera margin
0
40
80 km
b)
0
2
8 km
Lake City
N
B
Red Mountain
Cooper Creek
Silver Creek
C
D
Grassy Mountain
A
Monzonite and dacite
Syenite
Upper Sunshine Peak Tuff
Middle Sunshine Peak Tuff
Breccia
Lower Sunshine Peak Tuff
A
B
C
D
3800m

could co-exist in a single chemically zoned chamber formed from repeated replenishments (Eichelberger et al., 2000). However, the compositional zonation of the ignimbrite does not necessarily reflect the original zonation of magma in the chamber. The zonation of the ignimbrite also can be affected by magma interaction during flow in the chamber and conduit, and during ignimbrite transport and emplacement (e.g., Spera, 1984).

Magma mixing or mingling can occur within the chamber itself prior to eruption, disrupting magmatic zonation. During magma chamber replenishment (Campbell and Turner, 1989; Nakamura, 1995; Bergantz, 1999), or caldera collapse (Folch et al., 2000), vortices may develop in magma chambers. These vortices will drive magma mingling, mixing will occur if the timescale, relative proportions, and temperature and viscosity contrasts are suitable (Bateman, 1995). Magma chamber mixing and mingling may destroy chemical and thermal zonation in the magma chamber.

During eruption, discrete magma batches stacked in a magma chamber can erupt simultaneously to produce ignimbrites with gradationally zoned bulk compositions (e.g., Trial et al., 1992). Two magmas can erupt simultaneously as discrete magmas, then fragment and mix mechanically during eruption and flow of the ignimbrite. The controls on this type of magma interaction have been investigated both experimentally and numerically (Blake and Ivey, 1986a; Blake and Ivey, 1986b; Spera et al., 1986; Trail et al., 1992). The product is a zoned mixed ignimbrite with a bulk composition that grades between the two end member magmas, which are represented by unmingled pumices in the ignimbrite.

The range of magma types and the well-documented zoned ignimbrites and intrusions of Lake City (Hon, 1987) make this caldera an ideal candidate to study the interaction of magmas during chamber and eruptive processes. Our principal goals were to distinguish and understand crystal fractionation, chamber mixing, and eruptive mixing processes, as well as to constrain the configuration of the magmatic plumbing system beneath the caldera.

LAKE CITY CALDERA

The magmatic system of Lake City caldera shows a greater range of magma types than earlier San Juan magmatic systems and is thought to be associated with the onset of regional extensional tectonism (Lipman et al., 1978). The intracaldera ignimbrite is zoned from high silica rhyolite to trachyte and subdivided into three units: the Lower, Middle, and Upper Sunshine Peak Tuffs. These units are separated by large wedges of megabreccia (Fig. 1b) (Hon, 1987; Hon and Lipman, 1989). Also within the caldera are a series of resurgent intrusions, rhyolite dykes, and syenitic and monzonitic stocks that crosscut the ignimbrites and breccias (Hon, 1987; Hon and Lipman, 1989). In addition, dacitic lava flows and dykes crosscut and cover the ignimbrite sheets. The system evolved from high silica rhyolite to trachyte during collapse to a combination of syenites, monzonites, and dacites during resurgence. This combination of magma types is rare amongst the San Juan calderas and is evidence of a complex magmatic system (Hon, 1987). Lake city erupts the largest range of SiO_2 of all calderas within the San Juan volcanic field. The eruption that formed Lake City caldera is also interesting because several magma types were erupted simultaneously.

The structure of Lake City caldera is well exposed. Subsidence and resurgence structures provide additional insight into the volcanic evolution of the caldera complex (Fig. 1b). The caldera is an elongate structure (10 to 12 km in diameter) parallel with regional faults related to the Eureka graben west of the caldera (Figs. 1a, b) (Lipman et al., 1978). Subsidence structures are well constrained in the caldera, and ring faults, topographic scallops and megabreccias can be correlated (Lipman, 1976) and used to temporally constrain collapse episodes (Hon, 1987). In the caldera center, a resurgent dome was formed by intrusion of syenite at the base of the ignimbrite. In the eastern part of the caldera, uplift due to the intrusion of monzonite at the base of the ignimbrite caused ring fault reactivation. Paleomagnetic data and $^{40}Ar/^{39}Ar$ dating show that the entire caldera sequence, from the earliest Sunshine Peak Tuff to the post-collapse dacite intrusions, erupted within 80,000-330,000 years (Bove et al., 2001). Lake City is thus a remarkably well-constrained magmatic system.

Many volcanic and intrusive rocks of Lake City contain different types of magmatic enclaves (Hon, 1987). These enclaves reveal that high silica rhyolites, trachytes, mafic trachytes, and andesites were interacting dynamically during caldera collapse and resurgence. In this paper, we relate the magmatic interaction to the framework of caldera formation and resurgence, as outlined by Lipman (1976), Hon (1987), and Hon and Lipman (1989). We illustrate how the configuration of magma chambers, collapse, eruption, replenishment, and resurgence are responsible for the distribution of magmatic enclaves in the Lake City rocks.

METHODS

This study incorporates detailed field mapping and geochemical data presented in Hon (1987) with additional mapping, sampling, and geochemical analyses conducted in the summers of 2002 and 2004. We mapped textural and petrological changes within the pyroclastic sequence and the intrusive rocks. We sampled the caldera rocks systematically, and collected and described over 300 hand samples. From these samples, over 60 petrographic thin sections were made and examined; these thin sections and samples are complementary to the samples (500+ hand samples, 100+ thin sections) of Hon (1987). In addition to providing textural information, these thin sections helped us select samples for geochemical analysis. We focused on rocks with low degrees of alteration which contained textural evidence for magma interaction. Many samples contained substantial numbers of enclaves, necessitating careful sample preparation. Some enclaves were isolated for analysis, whilst others were removed from samples before analysis. Prepared samples were crushed and ground into powder and analyzed for whole rock major and trace element compositions by X-Ray Fluorescence (XRF) techniques.

The rare earth elements (REE) were analyzed for selected samples using Inductively Coupled Plasma Mass Spectrometry (ICP-MS). These results are in good agreement with the REE data analyzed by Hon (1987) using Instrumental Neutron Activation Analysis (INAA).

We used thin sections to select fresh feldspars suitable for chemical analysis from a range of rock types and enclaves. We again focused on crystals that appeared to have

undergone transfer between different magma types. We measured feldspar compositions by electron microprobe (JEOL JXA-8900L) using wavelength dispersive analysis. We also present isotopic data from Hon (1987), which was measured using mass spectrometer techniques described in Hon (1987). Our results from the various geochemical techniques are presented below with the results of Hon (1987).

RESULTS

MAJOR AND TRACE ELEMENTS

Major and trace element graphs show the variety of different magma types erupted during the formation of Lake City caldera (Fig. 2). Results from this study are plotted together with data from Hon (1987). Plots of SiO_2 vs TiO_2, TiO_2 vs FeO, SiO_2 vs Zr, TiO_2 vs Zr, Y vs SiO_2, and TiO_2 vs Y illustrate the different volcanic and intrusive units and their magmatic enclaves (Fig. 2). The geochemical data can be divided into four magma groups (Fig. 2). Group 1 are samples from the Lower Sunshine Peak Tuff, and includes four silicic pumices from the Middle Sunshine Peak Tuff, one sample from the Upper Sunshine Peak Tuff, and two high silica rhyolite ring dyke intrusions. Group 2 are samples from the Middle Sunshine Peak Tuff and includes two bulk samples from the Upper Sunshine Peak Tuff and five samples from small rhyolitic intrusions. Group 3 are pumice and bulk samples from the Upper Sunshine Peak Tuff, including one pumice and one bulk sample from the Middle Sunshine Peak Tuff, and all the resurgent syenite intrusions. Group 4 are samples from the post-collapse dacites and includes one Middle

FIGURE 2. Results from XRF and ICP-MS analyses from this study, results from Hon (1987) were also plotted. (a) TiO_2 plotted against SiO_2. (b) TiO_2 plotted against FeO. (c) Zr plotted against SiO_2. (d) TiO_2 plotted against Zr. (e) Y plotted against SiO_2. (f) TiO_2 plotted against Y.

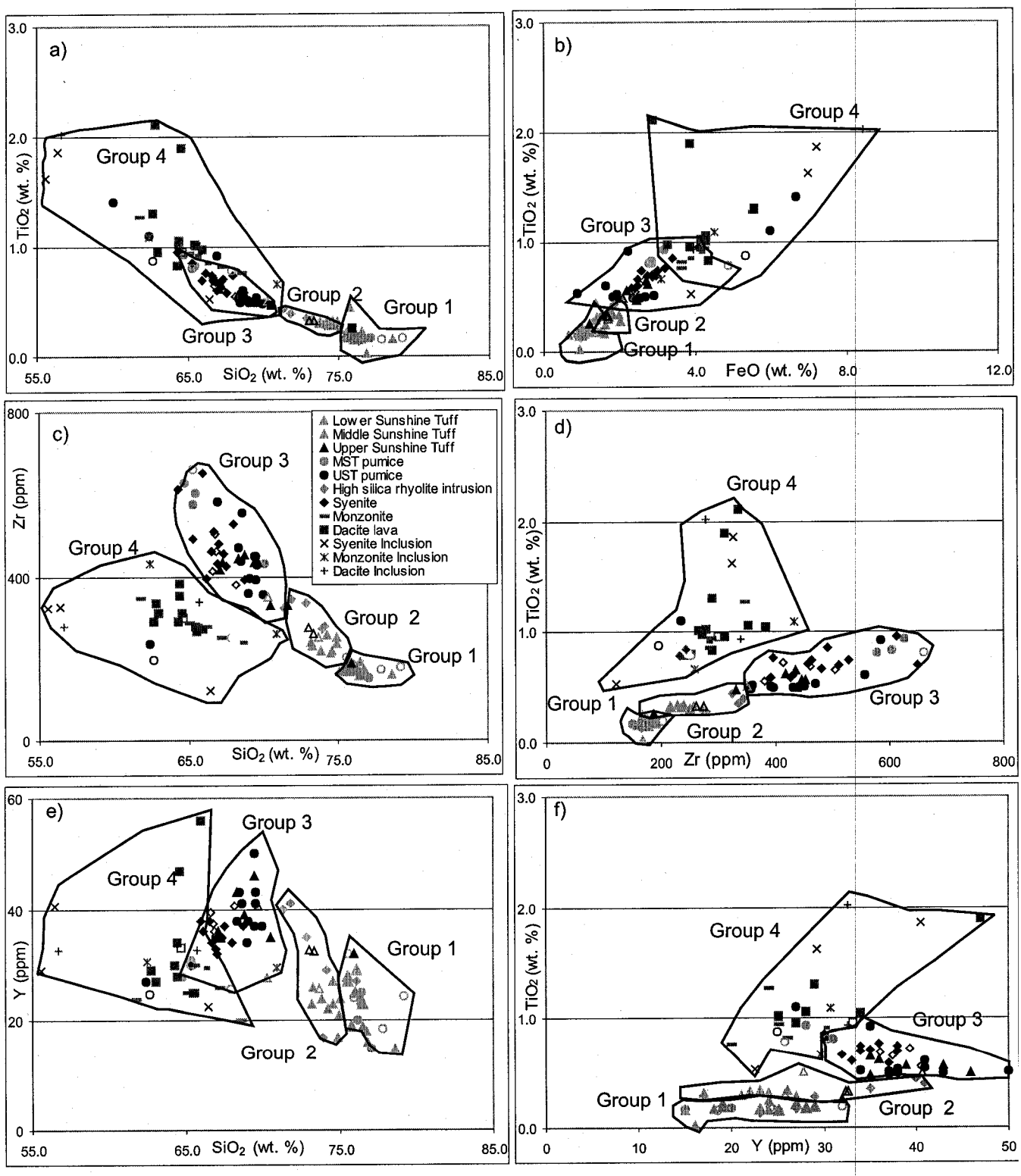
a)
Group 4
Group 2
Group 1
Group 3
TiO2 (wt. %)
SiO2 (wt. %)
3.0
2.0
1.0
0.0
55.0
65.0
75.0
85.0
b)
Group 4
Group 3
Group 2
Group 1
TiO2 (wt. %)
FeO (wt. %)
0.0
4.0
8.0
12.0
c)
Group 3
Group 4
Group 2
Group 1
Lower Sunshine Tuff
Middle Sunshine Tuff
Upper Sunshine Tuff
MST pumice
UST pumice
High silica rhyolite intrusion
Syenite
Monzonite
Dacite lava
Syenite Inclusion
Monzonite Inclusion
Dacite Inclusion
Zr (ppm)
SiO2 (wt. %)
800
400
0
d)
Group 4
Group 1
Group 3
Group 2
TiO2 (wt. %)
Zr (ppm)
200
400
600
e)
Group 3
Group 4
Group 1
Group 2
Y (ppm)
SiO2 (wt. %)
60
40
20
f)
Group 4
Group 3
Group 1
Group 2
TiO2 (wt. %)
Y (ppm)
10
20
30
40
50

Sunshine Peak Tuff pumice, two Upper Sunshine Peak Tuff pumices, three enclaves from the syenite, and all of the monzonites and their respective enclaves.

Group 1 is the most evolved group, consisting of high silica rhyolites with 75 to 80 wt. % SiO_2 (Fig. 2a, c). The mafic oxides TiO_2, MgO, FeO, CaO are correspondingly low (Fig. 2a, b, d; Table 1). Incompatible trace elements such as Th are elevated (Th 41 to 55 ppm), while compatible trace elements such as Y and Zr are relatively low (Y 15 to 32 ppm, Zr 161 to 202 ppm) (Fig. 2c, d, e; Table 1). Group 2 consists of rhyolites ranging from 71 to 75 wt. % SiO_2, with most of the Middle Sunshine Peak Tuff clustered around 73 to 75 wt. %. The mafic oxides and compatible trace elements including Zr are correspondingly low but higher than for Group 1 (Fig. 2; Table 1).

Group 3 spans a larger range of compositions (i.e., SiO_2 64 to 70 wt. %, FeO 1 to 4 wt. %). and also contains the highest Zr (239 to 650 ppm) and some of the highest Y concentrations (20 to 50 ppm) (Fig. 2c, d; Table 1). Although the trachytes of the Upper Sunshine Peak Tuff are generally similar to the syenites, the trachytes tend to be more evolved. Mafic trachyte pumice samples from the Middle Sunshine Peak Tuff are included in Group 3 with the lowest SiO_2 and Y (SiO_2 65 to 67 wt. %, Y 28 to 30 ppm), and the highest Zr concentrations (580 to 660 ppm) of the Group 3 rocks (Fig 2; Table 1). The highest Y concentrations are found within the trachytic pumices, rather than the more mafic syenites or mafic trachyte pumices (Table 1).

Group 4 rocks are characterized by 55 to 68 wt. % SiO_2, high mafic oxide contents, but relatively low-Zr (121 to 433 ppm) and Y (20 to 41 ppm) for the corresponding SiO_2 content. In this Group, Zr behaves differently showing no significant trend (Fig. 2, Table

TABLE 1. Whole rock analysis using XRF and ICP-MS. Major, trace and rare earth elements are shown. Trace elements marked with an * and all major elements were analysed using XRF by McGill Geochemical Laboratories, Montréal. Trace elements and all rare earth elements were analysed using ICP-MS by Activation Laboratories, Ancaster.

Sample			SiO_2 wt (%)	TiO_2 wt (%)	Al_2O_3 wt (%)	Fe_2O_3 wt (%)	MnO wt (%)	MgO wt (%)	CaO wt (%)	Na_2O wt (%)	K_2O wt (%)	P_2O_5 wt (%)	LOI wt (%)	Total wt (%)
LC-34	bulk	LSPT	75.28	0.19	13.11	1.33	0.11	0.19	0.30	4.00	5.24	0.02	0.38	100.15
LC2004-15A	bulk	LSPT	75.66	0.18	12.56	1.21	0.06	0.14	0.60	3.58	5.42	0.02	0.72	100.15
LC2004-08D	pumice	LSPT	74.08	0.18	12.29	1.47	0.07	0.26	0.86	1.80	6.67	0.02	2.17	99.87
LC2004-44	pumice	LSPT	78.06	0.16	11.14	0.96	0.02	0.16	0.19	1.97	6.01	0.02	1.18	99.87
LC2004-49A	bulk	MSPT	67.79	0.49	14.48	2.54	0.08	0.69	1.57	2.18	6.81	0.13	3.12	99.88
LC2005-57C	bulk	MSPT	71.89	0.30	13.07	1.85	0.06	0.34	1.69	3.30	5.23	0.07	2.23	100.03
LC2004-48B	pumice	MSPT	76.78	0.16	11.75	1.16	0.03	0.17	0.24	2.63	5.85	0.02	1.10	99.89
LC2004-55B	pumice	MSPT	64.92	0.76	15.26	5.15	0.08	0.72	2.17	2.87	4.08	0.17	3.64	99.82
LC2004-57A	pumice	MSPT	62.96	0.78	16.85	3.04	0.09	0.86	2.00	5.47	4.49	0.20	3.29	100.03
LC2004-30	bulk	USPT	68.20	0.49	15.40	2.25	0.08	0.41	1.21	3.92	6.09	0.10	1.89	100.04
LC2004-50A	bulk	USPT	72.01	0.32	13.65	1.84	0.05	0.41	0.88	3.53	5.65	0.07	1.46	99.87
LC2004-50C	bulk	USPT	71.69	0.32	13.85	1.82	0.06	0.42	0.94	3.46	5.72	0.06	1.74	100.08
LC2004-50I	pumice	USPT	60.20	0.85	16.82	5.65	0.10	0.98	3.03	4.05	4.55	0.45	3.50	100.18
LC2004-04J	bulk	syenite	66.48	0.54	15.32	2.61	0.12	0.56	1.56	3.46	7.09	0.12	2.11	99.97
LC2004-18D	bulk	syenite	65.44	0.67	15.86	3.13	0.10	0.77	1.73	4.49	5.92	0.17	1.89	100.17
LC2004-40A	bulk	syenite	65.56	0.65	16.19	2.89	0.08	0.75	1.51	4.48	6.25	0.15	1.42	99.93
LC2004-58A	bulk	syenite	64.23	0.69	15.76	3.14	0.10	0.71	2.55	3.56	5.80	0.18	3.36	100.08
LC2004-15D	enclave	syenite	54.90	1.61	18.13	7.64	0.13	2.78	5.87	4.57	3.34	0.53	0.65	100.15
LC2004-40F	enclave	syenite	64.62	0.52	14.93	4.20	0.14	1.25	4.08	4.12	3.60	0.28	2.51	100.25
LC2004-85G	enclave	syenite	54.54	1.80	16.51	7.71	0.28	2.93	3.92	4.92	4.09	0.74	2.80	100.24
LC2004-23B	bulk	monzonite	65.52	0.85	15.42	4.17	0.10	1.28	2.57	4.09	5.09	0.30	0.55	99.94
LC2004-24	bulk	monzonite	65.14	0.91	15.60	4.54	0.10	1.39	2.80	4.30	4.78	0.33	0.44	100.33
LC2004-21	enclave	monzonite	70.13	0.66	13.44	3.38	0.11	0.94	1.59	3.61	5.18	0.22	0.67	99.93
LC2004-26A	enclave	monzonite	61.53	1.08	16.73	4.90	0.12	1.64	2.26	5.31	5.05	0.43	1.11	100.16
LC2004-52A	bulk	dacite	61.36	0.91	14.84	4.35	0.14	0.95	3.98	3.19	5.32	0.33	4.38	99.75
LC -67	enclave	dacite	63.66	0.91	15.49	4.24	0.12	1.71	1.91	3.64	5.30	0.32	2.90	100.20
LC2004-52CB	enclave	dacite	53.92	1.92	16.23	8.89	0.12	2.71	4.09	3.90	3.58	0.68	4.05	100.09
Detection Limits	(ppm):		60.00	35.00	120.00	30.00	30.00	95.00	15.00	75.00	25.00	35.00	100.00	

Sample			Sm	Eu	Gd	Tb	Dy	Ho	Er	Tm	Yb	Lu	Hf	Ta	W	Tl	Pb*	Pb	Bi	Th*	Th	U*	U
			ppm	ppm	ppm	ppm	ppm	ppm	ppm	ppm	ppm	ppm	ppm	ppm	ppm	ppm	ppm	ppm	ppm	ppm	ppm	ppm	ppm
LC-34	bulk	LSPT	0	0	0	0	0	0	0	0	0	0	0	0	1	0	23	5	0	55	0	10	0
LC2004-15A	bulk	LSPT	5	0	4	1	4	1	3	0	3	1	7	5	3	2	26	23	1	45	48	15	16
LC2004-08D	pumice	LSPT															32			53		15	
LC2004-44	pumice	LSPT															28			51		19	
LC2004-49A	bulk	MSPT	7	1	5	1	4	1	3	0	3	0	10	4	2	3	19	18	0	31	33	11	11
LC2005-57C	bulk	MSPT															21			40		14	
LC2004-48B	pumice	MSPT															23			52		18	
LC2004-55B	pumice	MSPT															25			14		6	
LC2004-57A	pumice	MSPT	9	3	6	1	5	1	3	0	3	0	13	3	1	2	17	23	0	16	17	7	5
LC2004-30	bulk	USPT	12	1	9	1	7	1	4	1	4	1	12	4	2	1	23	21	0	35	38	12	12
LC2004-50A	bulk	USPT															26			45		13	
LC2004-50C	bulk	USPT															27			45		16	
LC2004-50I	pumice	USPT	7	1	5	1	4	1	2	0	2	0	6	1	5	2	34	35	0	17	18	9	7
LC2004-04J	bulk	syenite															19			29		6	
LC2004-18D	bulk	syenite	12	2	9	1	6	1	4	1	4	1	12	4	2	1	18	24	0	25	28	7	7
LC2004-40A	bulk	syenite															19			25		7	
LC2004-58A	bulk	syenite															17			27		11	
LC2004-15D	enclave	syenite															5			10		6	
LC2004-40F	enclave	syenite															18			23		11	
LC2004-85G	enclave	syenite	12	3	10	1	7	1	4	1	3	0	7	3	5	0	41	28	2	15	16	8	7
LC2004-23B	bulk	monzonite															26			25		8	
LC2004-24	bulk	monzonite	9	2	7	1	5	1	3	0	3	0	8	3	1	1	17	19	0	23	27	7	6
LC2004-21	enclave	monzonite															33			37		11	
LC2004-26A	enclave	monzonite	11	2	7	1	5	1	3	0	3	0	9	2	2	1	16	17	0	10	11	5	3
LC2004-52A	bulk	dacite	10	2	7	1	5	1	3	0	3	0	8	3	2	1	22	24	0	22	22	7	6
LC -67	enclave	dacite															14			25		9	
LC2004-52CB	enclave	dacite	11	3	8	1	6	1	3	0	3	0	8	2	3	1	24	15	< 0.1	8	9	5	2
Detection Limits	(ppm):																1			1		1	

Sample			V* ppm	V ppm	Cr2O3* ppm	Cr ppm	Co ppm	Ni* ppm	Ni ppm	Cu ppm	Zn ppm	Ga ppm	Ga ppm	Ge ppm	As ppm	Rb* ppm	Rb ppm
LC-34	bulk	LSPT	3	5	130	20	1	15	20	10	30	20	1	1	5	297	1
LC2004-15A	bulk	LSPT	1	< 5	59	< 20	< 1	9	< 20	20	60	18	18	2	< 5	264	250
LC2004-08D	pumice	LSPT	8		48			11				13				291	
LC2004-44	pumice	LSPT	7		100			12				13				241	
LC2004-49A	bulk	MSPT	29	19	32	30	2	5	20	10	90	18	17	1	< 5	312	298
LC2005-57C	bulk	MSPT	18		31			6				18				237	
LC2004-48B	pumice	MSPT	7		47			9				16				255	
LC2004-55B	pumice	MSPT	97		39			6				19				173	
LC2004-57A	pumice	MSPT	34	22	26	< 20	3	3	< 20	< 10	110	19	17	2	8	179	160
LC2004-30	bulk	USPT	17	15	38	< 20	2	8	< 20	20	60	19	18	1	< 5	210	195
LC2004-50A	bulk	USPT	18		29			6				19				265	
LC2004-50C	bulk	USPT	17		30			8				20				271	
LC2004-50I	pumice	USPT	67	57	55	20	6	10	< 20	30	110	23	20	1	6	146	130
LC2004-04J	bulk	syenite	28		32			8				20				253	
LC2004-18D	bulk	syenite	35	25	43	< 20	3	7	< 20	10	70	19	18	2	< 5	163	152
LC2004-40A	bulk	syenite	25		37			5				19				167	
LC2004-58A	bulk	syenite	40		29			6				19				176	
LC2004-15D	enclave	syenite	126		23			10				22				86	
LC2004-40F	enclave	syenite	75		32			7				17				95	
LC2004-85G	enclave	syenite	131	117	16	20	13	-2	120	40	120	23	20	2	8	141	126
LC2004-23B	bulk	monzonite	56		29			4				20				154	
LC2004-24	bulk	monzonite	59	51	30	< 20	8	4	< 20	< 10	70	20	18	2	< 5	158	142
LC2004-21	enclave	monzonite	42		37			6				18				226	
LC2004-26A	enclave	monzonite	64	56	26	< 20	8	1	< 20	< 10	90	21	19	1	8	143	128
LC2004-52A	bulk	dacite	59	46	31	< 20	6	3	< 20	10	110	19	18	2	< 5	186	170
LC -67	enclave	dacite	50		25			5				20				172	
LC2004-52CB	enclave	dacite	120	107	15	< 20	19	-4	< 20	30	110	24	21	1	< 5	104	95
Detection Limits	(ppm):		10		15			3				1				1	

Sample			Y ppm	Zr* ppm	Zr ppm	Nb ppm	Nb ppm	Mo ppm	Ag ppm	In ppm	Sn ppm	Sb ppm	Cs ppm	Ba ppm	BaO* ppm	La ppm
LC-34	bulk	LSPT	1	202	1	81	0	2	1	0	1	0	0	3	80	0
LC2004-15A	bulk	LSPT	28	176	176	66	64	5	< 0.5	< 0.1	3	1	3	50	41	52
LC2004-08D	pumice	LSPT		171		65									416	
LC2004-44	pumice	LSPT		177		65									445	
LC2004-49A	bulk	MSPT	26	351	408	48	49	< 2	1	< 0.1	3	1	12	822	904	55
LC2005-57C	bulk	MSPT		249		59									395	
LC2004-48B	pumice	MSPT		172		72									440	
LC2004-55B	pumice	MSPT		252		18									1033	
LC2004-57A	pumice	MSPT	28	660	607	42	40	3	1	< 0.1	3	1	19	1280	1537	62
LC2004-30	bulk	USPT	38	436	482	61	59	< 2	1	< 0.1	3	1	4	476	524	86
LC2004-50A	bulk	USPT		261		66									282	
LC2004-50C	bulk	USPT		274		67									295	
LC2004-50I	pumice	USPT	22	195	199	20	18	< 2	< 0.5	< 0.1	4	1	3	941	1093	51
LC2004-04J	bulk	syenite		379		55									614	
LC2004-18D	bulk	syenite	36	461	517	49	51	2	2	< 0.1	3	1	4	866	979	77
LC2004-40A	bulk	syenite		505		49									1026	
LC2004-58A	bulk	syenite		413		49									926	
LC2004-15D	enclave	syenite		323		32									2040	
LC2004-40F	enclave	syenite		121		14									764	
LC2004-85G	enclave	syenite	37	327	291	42	42	3	1	< 0.1	3	1	4	988	1160	72
LC2004-23B	bulk	monzonite		277		34									1062	
LC2004-24	bulk	monzonite	29	281	302	34	40	< 2	< 0.5	< 0.1	3	0	3	851	995	64
LC2004-21	enclave	monzonite		259		40									395	
LC2004-26A	enclave	monzonite	28	433	389	37	39	< 2	< 0.5	< 0.1	2	1	3	1650	1936	69
LC2004-52A	bulk	dacite	31	300	304	35	38	< 2	< 0.5	< 0.1	3	0	6	931	1066	65
LC -67	enclave	dacite		339		41									1159	
LC2004-52CB	enclave	dacite	30	278	331	38	41	2	< 0.5	< 0.1	3	1	3	1140	1307	62
Detection Limits	(ppm):			1		1									17	

Sample			Sm	Eu	Gd	Tb	Dy	Ho	Er	Tm	Yb	Lu	Hf	Ta	W	Tl	Pb*	Pb	Bi	Th*	Th	U*	U
			ppm	ppm	ppm	ppm	ppm	ppm	ppm	ppm	ppm	ppm	ppm	ppm	ppm	ppm	ppm	ppm	ppm	ppm	ppm	ppm	ppm
LC-34	bulk	LSPT	0	0	0	0	0	0	0	0	0	0	0	0	1	0	23	5	0	55	0	10	0
LC2004-15A	bulk	LSPT	5	0	4	1	4	1	3	0	3	1	7	5	3	2	26	23	1	45	48	15	16
LC2004-08D	pumice	LSPT															32			53		15	
LC2004-44	pumice	LSPT															28			51		19	
LC2004-49A	bulk	MSPT	7	1	5	1	4	1	3	0	3	0	10	4	2	3	19	18	0	31	33	11	11
LC2005-57C	bulk	MSPT															21			40		14	
LC2004-48B	pumice	MSPT															23			52		18	
LC2004-55B	pumice	MSPT															25			14		6	
LC2004-57A	pumice	MSPT	9	3	6	1	5	1	3	0	3	0	13	3	1	2	17	23	0	16	17	7	5
LC2004-30	bulk	USPT	12	1	9	1	7	1	4	1	4	1	12	4	2	1	23	21	0	35	38	12	12
LC2004-50A	bulk	USPT															26			45		13	
LC2004-50C	bulk	USPT															27			45		16	
LC2004-50I	pumice	USPT	7	1	5	1	4	1	2	0	2	0	6	1	5	2	34	35	0	17	18	9	7
LC2004-04J	bulk	syenite															19			29		6	
LC2004-18D	bulk	syenite	12	2	9	1	6	1	4	1	4	1	12	4	2	1	18	24	0	25	28	7	7
LC2004-40A	bulk	syenite															19			25		7	
LC2004-58A	bulk	syenite															17			27		11	
LC2004-15D	enclave	syenite															5			10		6	
LC2004-40F	enclave	syenite															18			23		11	
LC2004-85G	enclave	syenite	12	3	10	1	7	1	4	1	3	0	7	3	5	0	41	28	2	15	16	8	7
LC2004-23B	bulk	monzonite															26			25		8	
LC2004-24	bulk	monzonite	9	2	7	1	5	1	3	0	3	0	8	3	1	1	17	19	0	23	27	7	6
LC2004-21	enclave	monzonite															33			37		11	
LC2004-26A	enclave	monzonite	11	2	7	1	5	1	3	0	3	0	9	2	2	1	16	17	0	10	11	5	3
LC2004-52A	bulk	dacite	10	2	7	1	5	1	3	0	3	0	8	3	2	1	22	24	0	22	22	7	6
LC -67	enclave	dacite															14			25		9	
LC2004-52CB	enclave	dacite	11	3	8	1	6	1	3	0	3	0	8	2	3	1	24	15	< 0.1	8	9	5	2
Detection Limits	(ppm):																1			1		1	

1). Monzonite samples tend to be more evolved than the dacites. The andesitic pumices and enclaves in the Upper Sunshine Peak Tuff, the syenite, monzonite and dacite are generally the least evolved and most enriched in elements such as TiO_2, MgO, FeO, and CaO. The enclaves in the monzonite have higher Zr than the other Group 4 samples with corresponding SiO_2 content. A late dacite dyke has exceptionally high TiO_2 and Y (Fig. 2, Table 1).

In summary, the major and trace element data reveal that Groups 1 to 3 share similar chemical affinities and follow a single fractionation trend, while Group 4 seems to be geochemically distinct.

RARE EARTH ELEMENTS

REE behave coherently in magmatic systems and are relatively resistant to secondary alteration. All REE except Eu are incompatible in mafic systems; in silicic systems, however, REE can become compatible and incorporated during the crystallization of accessory minerals such as chevkinite, titanite, and zircon (Hon, 1987). Figure 3a shows REE concentrations for bulk ignimbrites, Figure 3b for pumices, and Figure 3c for intrusions. The presence of distinct pumice populations in the Middle and Upper Sunshine Peak Tuff (Fig. 3b) indicates that the bulk composition (Fig. 3a) does not represent a magmatic composition but instead a mechanical mixture.

Figure 3a shows representative REE patterns for the ignimbrites of the first three magma groups, the Lower, Middle, and Upper Sunshine Peak Tuffs. The Lower Sunshine Peak Tuff of Group 1 has relatively low light and middle REE with a large negative Eu anomaly. The Middle Sunshine Peak Tuff of Group 2 shows REE similar to

FIGURE 3. REE normalized to chondritic composition of Taylor and McLennan (1985); normalized REE data from Hon (1987) are also shown. (a) Bulk REE concentrations for the Sunshine Peak Tuff. (b) REE concentrations for the various pumices of the Sunshine Peak Tuff. (c) REE concentrations for the post collapse intrusions and lava flows.

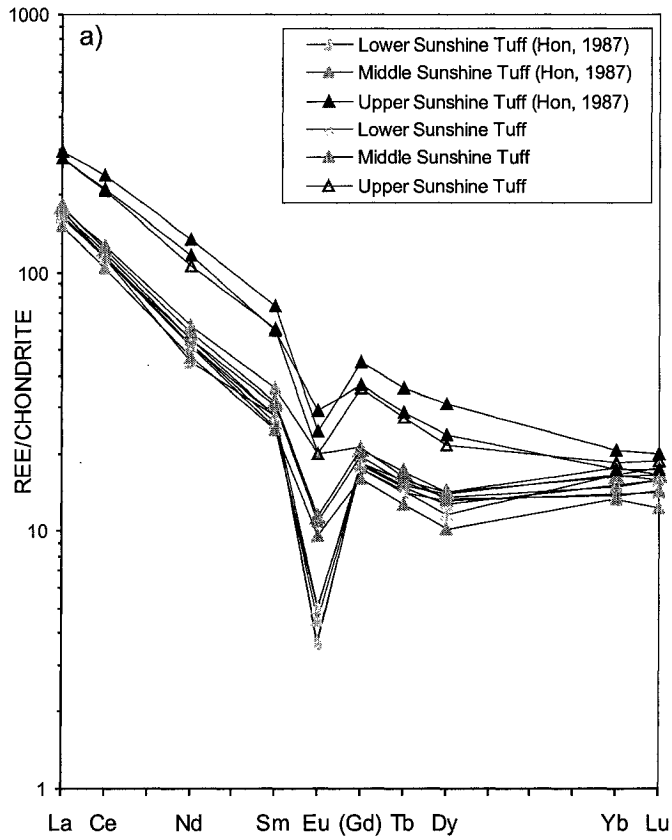
a)
Lower Sunshine Tuff (Hon, 1987)
Middle Sunshine Tuff (Hon, 1987)
Upper Sunshine Tuff (Hon, 1987)
Lower Sunshine Tuff
Middle Sunshine Tuff
Upper Sunshine Tuff
REE/CHONDRITE
1000
100
10
1
La Ce Nd Sm Eu (Gd) Tb Dy Yb Lu

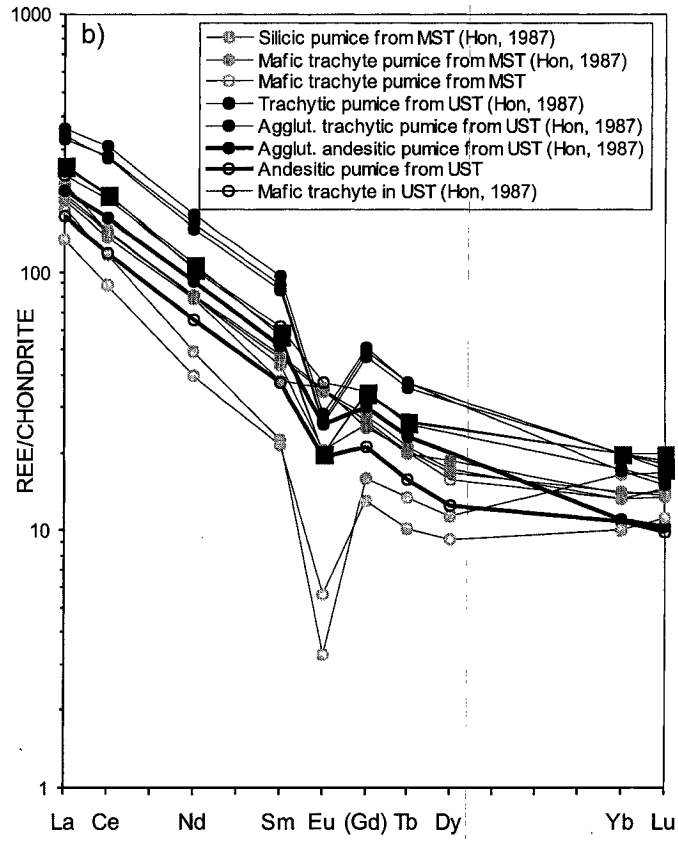
b)
Silicic pumice from MST (Hon, 1987)
Mafic trachyte pumice from MST (Hon, 1987)
Mafic trachyte pumice from MST
Trachytic pumice from UST (Hon, 1987)
Agglut. trachytic pumice from UST (Hon, 1987)
Agglut. andesitic pumice from UST (Hon, 1987)
Andesitic pumice from UST
Mafic trachyte in UST (Hon, 1987)
REE/CHONDRITE
1000
100
10
1
La Ce Nd Sm Eu (Gd) Tb Dy Yb Lu

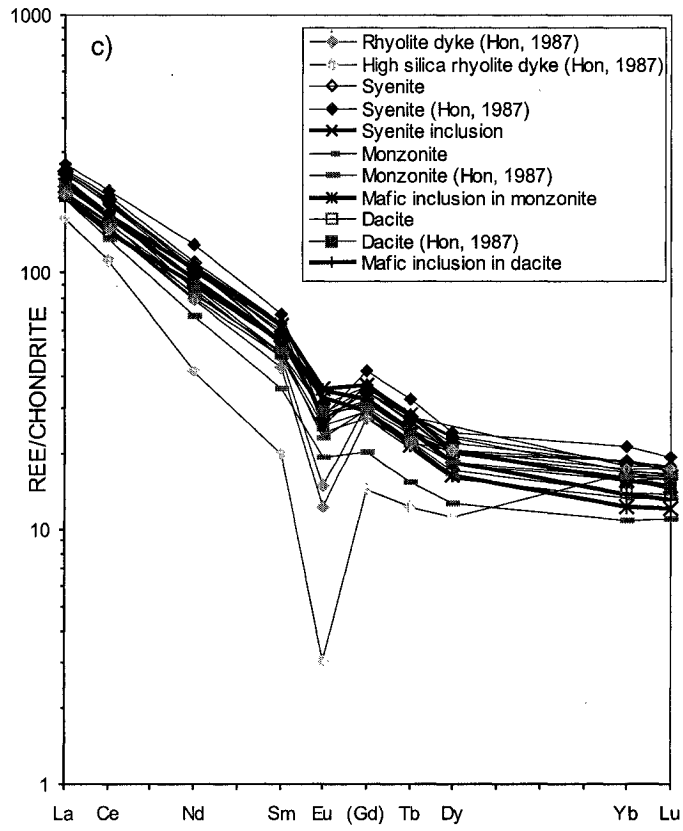
c)
Rhyolite dyke (Hon, 1987)
High silica rhyolite dyke (Hon, 1987)
Syenite
Syenite (Hon, 1987)
Syenite inclusion
Monzonite
Monzonite (Hon, 1987)
Mafic inclusion in monzonite
Dacite
Dacite (Hon, 1987)
Mafic inclusion in dacite
REE/CHONDRITE
1000
100
10
1
La Ce Nd Sm Eu (Gd) Tb Dy Yb Lu

the Lower Sunshine Peak Tuff, but with a significantly smaller Eu anomaly. One sample from the Middle Sunshine Peak Tuff shows higher middle and heavy REE pattern with a greatly reduced Eu anomaly. The Group 3 Upper Sunshine Peak Tuff has uniformly higher REE concentrations and a negative Eu anomaly.

Figure 3b illustrates the REE patterns of the different pumice types in the Middle and Upper Sunshine Peak Tuff. Magma from all four groups is represented by these pumices. The Middle Sunshine Peak Tuff has two distinct types of pumices: (1) silicic pumices with REE patterns similar to those from the Lower Sunshine Peak Tuff (Fig 3a); (2) mafic trachytic pumices with higher light and middle REE, no Eu anomaly, and heavy REE slightly higher than the Lower Sunshine Peak Tuff. This second pumice type is distinct from the bulk REE of Upper Sunshine Peak Tuff because no Eu anomaly is observed.

The Upper Sunshine Peak Tuff contains five pumice types. Figure 3b shows four of these: (1) mafic trachytic pumice similar to those in the Middle Sunshine Peak Tuff; (2) trachytic pumices with the highest REE and relatively large Eu anomalies; (3) agglutinated trachytic pumices with REE similar to the bulk Upper Sunshine Peak Tuff; (4) low-Zr andesitic agglutinate pumices with low heavy REE and small Eu anomalies (Fig. 3b). In addition to these four types, pumices with mineralogy similar to the Lower Sunshine Peak Tuff (Hon, 1987) also were found but not analyzed. Pumice types 1 to 4 show that the Group 3 magma, as defined by major elements, shows a range of distinct REE contents, which represent a range of magmatic compositions

Figure 3c shows REE for post-collapse intrusions and lava flows from Lake City caldera, and contains magma types from all groups. Overall, the intrusions and lavas have

REE patterns similar to the bulk Sunshine Peak Tuff samples and pumices. The high silica rhyolite intrusion has REE patterns characteristic of the Lower Sunshine Peak Tuff, while the other rhyolite intrusions have REE patterns similar to, although slightly higher than the Middle Sunshine Peak Tuff. The syenites have patterns similar and slightly higher than the Upper Sunshine Peak Tuff. The dacites, monzonites, and their enclaves from Group 4 have low heavy REE similar to the low-Zr andesitic pumice found in the Upper Sunshine Peak Tuff. The monzonites are generally slightly lower in most REE than the dacites. Interestingly, there are no intrusions or lavas with REE patterns as high as the trachytic Upper Sunshine Peak Tuff pumices.

ISOTOPIC DATA

Isotopic ratios are a useful tool to distinguish different magma groups and to provide additional information with which to consider mixing and fractionation models. The Sunshine Peak Tuff magmas of Groups 1 to 3 have $^{206}Pb/^{204}Pb$ ratios of 18.55 to 18.60, lower than those of the Group 4 magma (18.70 to 18.76) (Fig. 4). The Sunshine Peak Tuff and syenite show intermediate isotopic values, while the mafic trachyte pumice from Group 3 has the lowest $^{206}Pb/^{204}Pb$ ratio. The Pb^{208}/Pb^{204} and $^{207}Pb/^{204}Pb$ ratios for the dacites are also higher, while the monzonite has lower ratios closer to the syenite and the Upper Sunshine Peak Tuff. The Lower Sunshine Peak Tuff has high $^{208}Pb/^{204}Pb$ and $^{207}Pb/^{204}Pb$ ratios similar to the dacites (Hon, 1987).

The Sr concentration varies considerably in the Lake City rocks. Therefore, the Sr isotopic ratio of each rock responds differently to similar amounts of contamination. Low Sr samples, such as the Lower Sunshine Peak Tuff, are particularly sensitive to

FIGURE 4. Isotope data replotted from Hon (1987). (a) Pb^{206}/Pb^{204} plotted against Sr^{87}/Sr^{86} for Lake City rocks, a Tertiary volcanic country rock is also plotted for comparison. (b) Pb^{206}/Pb^{204} plotted against Pb^{208}/Pb^{204} for Lake City rocks and surrounding country rocks.

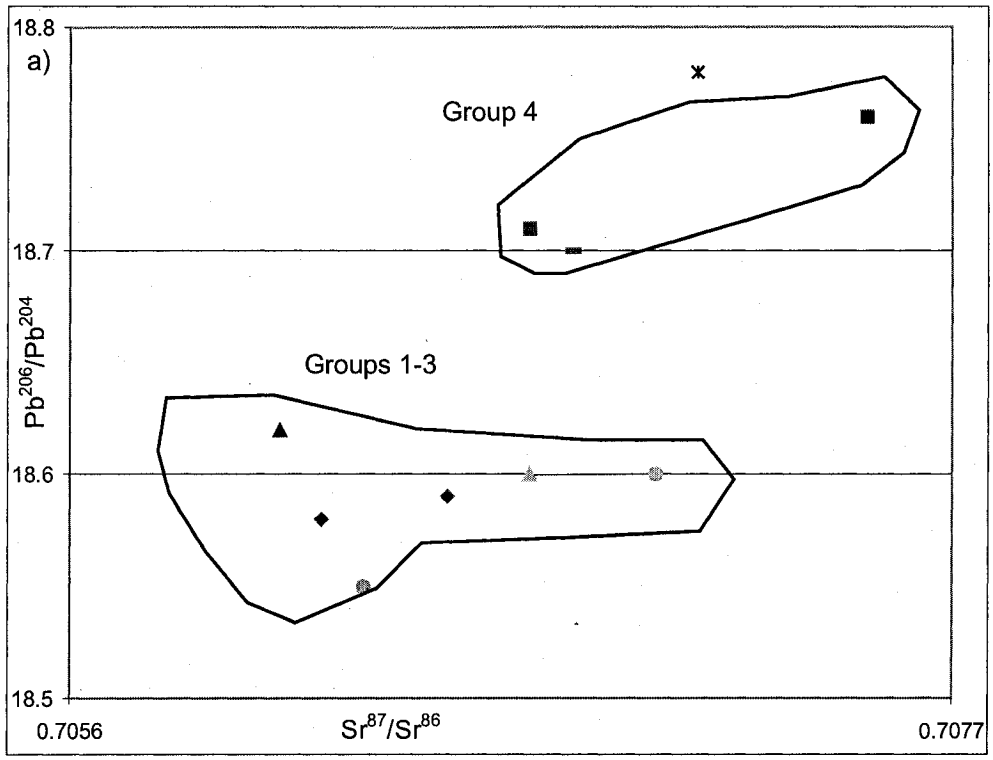
a)
Group 4
Groups 1-3
18.8
18.7
18.6
18.5
Pb^{206}/Pb^{204}
0.7056
Sr^{87}/Sr^{86}
0.7077

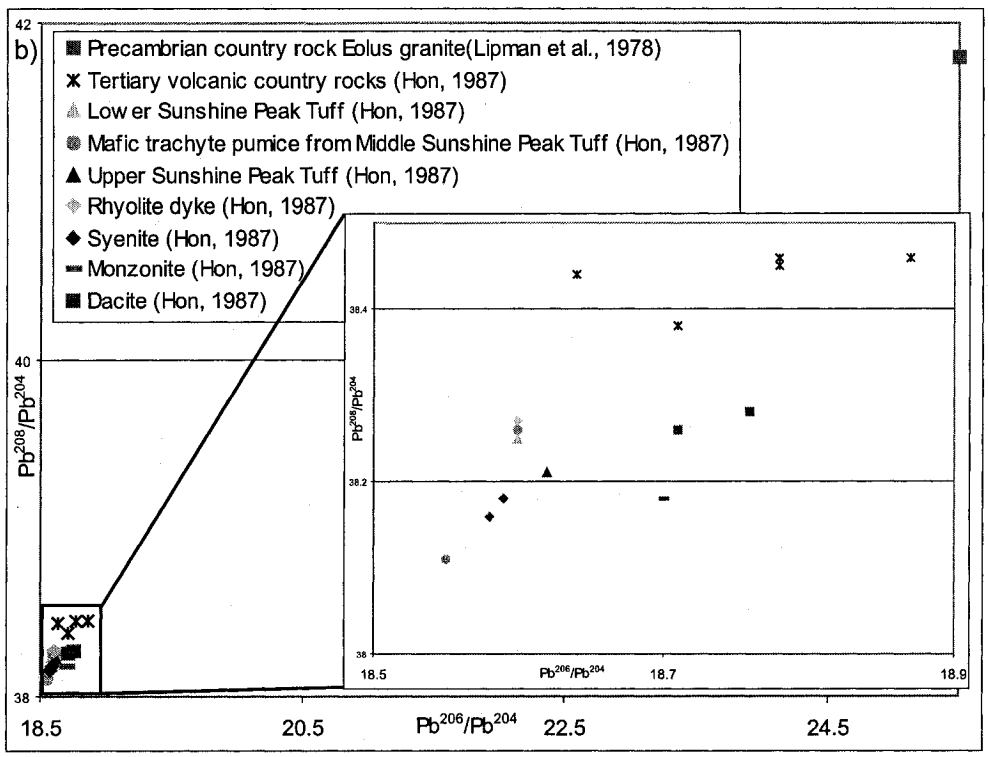
b)
Precambrian country rock Eolus granite(Lipman et al., 1978)
Tertiary volcanic country rocks (Hon, 1987)
Lower Sunshine Peak Tuff (Hon, 1987)
Mafic trachyte pumice from Middle Sunshine Peak Tuff (Hon, 1987)
Upper Sunshine Peak Tuff (Hon, 1987)
Rhyolite dyke (Hon, 1987)
Syenite (Hon, 1987)
Monzonite (Hon, 1987)
Dacite (Hon, 1987)
42
40
38
Pb^{208}/Pb^{204}
18.5
20.5
Pb^{206}/Pb^{204}
22.5
24.5
38.4
38.2
38
18.5
18.7
18.9

small amounts of contamination, in particular by material with high Sr and contrasting Sr isotopic ratios. Therefore, the high Sr^{87}/Sr^{86} ratios of the Lower Sunshine Peak Tuff are not necessarily an indicator of large amounts of assimilation. The highest Sr^{87}/Sr^{86} ratios are found in the dacites (Fig. 4a). The variable Sr contents of the Lake City rocks indicate that the Pb isotopic ratios are most reliable to assess the degree of contamination. Figure 4b shows the isotopic ratios of the Lake City rocks plotted with country rocks that crop out around the caldera which could serve as possible sources of contamination. Figure 4 reveals that the mafic trachyte found in the Middle Sunshine Peak Tuff suffered the least amount of crustal contamination, while the Lower and Upper Sunshine Peak Tuff and the syenite underwent moderate amounts of crustal contamination, from either very small volumes of Precambrian granite or greater volumes of Tertiary country rocks (Fig. 4b). The monzonites and dacites have distinct high isotopic ratios, possibly indicating higher isotopic ratios in the source regions where these magmas were generated (Hon, 1987).

FELDSPAR COMPOSITIONS

The composition of the different minerals can be used to distinguish the different magma types and identify crystal transfer between magmas. The compositional zoning of the feldspars indicates changing magmatic conditions as the crystal grew.

Figure 5 (Appendix I) shows the composition of feldspars analyzed in the different rock types at Lake City. Orthoclase compositions in the Lower Sunshine Peak Tuff and rhyolite intrusions are the most rich in sodium, while the Middle Sunshine Peak, Upper Sunshine Peak Tuff, syenite and monzonite orthoclases become progressively enriched in potassium. More sodic compositions are consistent with the temperature drop

FIGURE 5. Microprobe analyses of feldspar compositions (Appendix I). (a) Back scattered image of a plagioclase rimmed by an orthoclase in syenite. (b) Feldspar compositions from Lake City rocks plotted on a K, Na, Ca diagram, temperature fields are plotted from Nekvasil (1988). (c) CaO zoning in feldspars from various Lake City rocks.

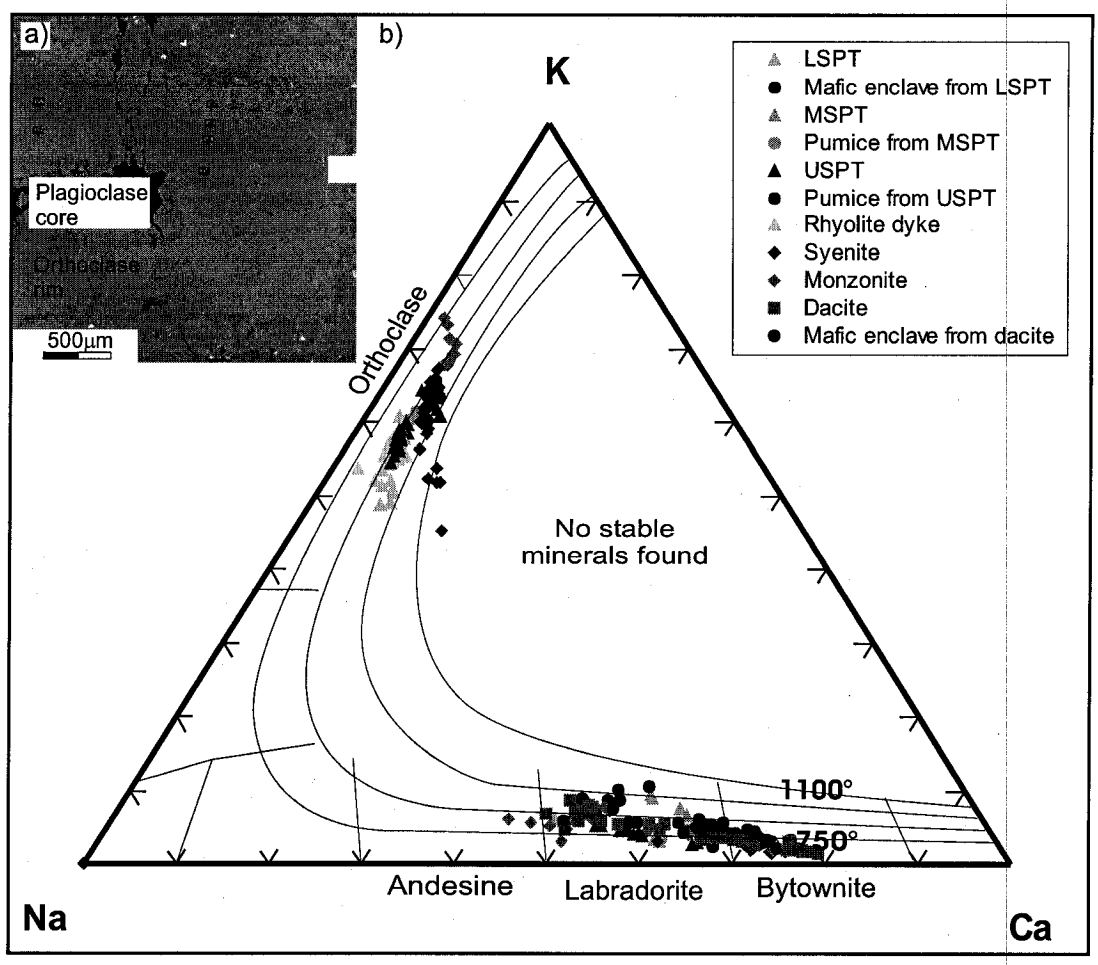
a)
Plagioclase core
Orthoclase rim
500µm
b)
K
Orthoclase
No stable minerals found
1100°
750°
Andesine
Labradorite
Bytownite
Na
Ca
LSPT
Mafic enclave from LSPT
MSPT
Pumice from MSPT
USPT
Pumice from USPT
Rhyolite dyke
Syenite
Monzonite
Dacite
Mafic enclave from dacite

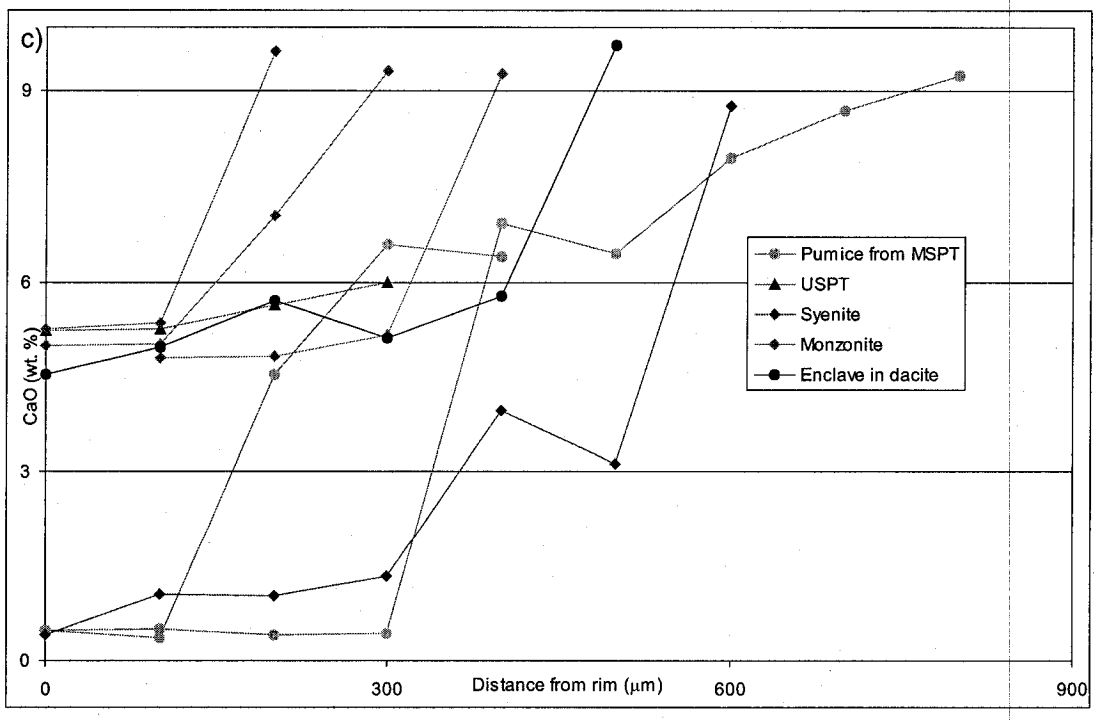
c)
CaO (wt. %)
0
3
6
9
0
300
600
900
Distance from rim (µm)
Pumice from MSPT
USPT
Syenite
Monzonite
Enclave in dacite

associated with crystallization and differentiation of the melt under constant H_2O pressure (Ginibre et al., 2004).

No plagioclase was found in the Lower Sunshine Peak Tuff. Plagioclases in the Middle Sunshine Peak Tuff, Middle Sunshine Peak Tuff pumice, and Upper Sunshine Peak Tuff trachytic pumices are relatively calcic, ranging from bytownite to labradorite (Fig. 5a). The plagioclase in the Upper Sunshine Peak Tuff is labradorite. Most plagioclases in the monzonites cluster at the sodium-rich end of labradorite and some are andesine. One crystal from a pumice in the Upper Sunshine Peak Tuff groups with the monzonite plagioclase (Fig. 5b). Plagioclase from the dacite range in composition from bytownite to andesine, while the plagioclase from the andesitic enclaves in the dacite plot as bytownite and labradorite.

Plagioclase crystals in the monzonite and the syenite are commonly rimmed by orthoclase (Fig. 5a). Most plagioclase in Groups 1 to 3 showed no zonation. However, some of the feldspars from the syenite, the monzonite, and mafic enclaves/pumices are normally zoned (Fig. 5c). The calcic plagioclase cores in the syenites and Group 4 magma indicate that the melt became more sodic during the crystallization of plagioclase. This could occur during fractional crystallization, magma mixing or by significant changes in H_2O pressure.

In summary, the feldspar data show that (1) the composition of orthoclase becomes increasingly sodic from Groups 3 to 1, (2) plagioclase feldspars in syenite and monzonite are often rimmed by orthoclase, and (3) Group 4 magmas contain normally zoned plagioclases.

DISCUSSION

We now discuss the geochemical and physical arguments that define magmatic evolution and interaction at Lake City. First, we use pumice compositions to geochemically identify distinct magma batches and the relationships among them. Second, we discuss the physical relationships within the mixed ignimbrites of the Middle and Upper Sunshine Peak Tuff, and the mixed magmatic intrusions. Third, we discuss how pumice and enclave proportions affect zonation patterns in the ignimbrites and intrusions.

MAGMA TYPES

The major and trace element data for the Lake City rocks allow us to distinguish distinct magma groups. Textural evidence indicates that the bulk ignimbrite compositions of Groups 2 and 3 are the result of mechanical mixing of pumice compositions. Therefore, only pumice and intrusion samples are used to distinguish magmas. REE and isotopic data show that two separate magma batches were present. The geochemically distinct magma batches are Batch A (Groups 1 to 3, high silica rhyolite, trachyte and mafic trachyte), and Batch B (Group 4, low-Zr dacite, and andesite).

The Group 1 high silica rhyolite magma is represented by the bulk composition of the Lower Sunshine Peak Tuff, a group of pumices in the Middle Sunshine Peak Tuff, and two resurgent high silica rhyolite dykes. This group represents most of the magma erupted at Lake City (200 to 250 km^3 DRE) (Hon, 1987) and is highly evolved with 75 to 80 wt. % SiO_2, less than 0.2 wt. % TiO_2, and a large negative Eu anomaly. The highest

SO_2 contents imply that there may have been some addition of silica by hydrothermal fluids.

The Group 2 rhyolite represents a mixed composition and is discussed in the following section. The Group 3 trachytic magma is represented by distinct trachyte and mafic trachyte pumices. The trachytes could be parental to the high silica rhyolite. The larger negative Eu anomaly of the high silica rhyolite is consistent with continued feldspar fractionation from the trachytic magma. The presence of accessory minerals of titanite, chevkinite, and zircon in the high silica rhyolite indicates that they may have also been crystallizing and fractionating (Hon 1987). This could explain the depleted REE of the high silica rhyolites compared to the trachytes (Table 1) (Hon, 1987).

Crystal fractionation modeling indicates that the high silica rhyolite evolved from the trachyte if 1.5 % titanite and 0.17 % each of chevkinite and 0.06 % zircon crystallized and were removed from the melt to deplete REE in the high silica rhyolites (Appendix II). The mafic trachyte has intermediate REE and no Eu anomaly, consistent with it being parental to the trachyte. Eu behaved compatibly during feldspar crystallization and was removed during crystal fractionation, while all other REE behaved incompatibly and were enriched in the melt to produce the high REE patterns of the trachyte.

Therefore, it is probable that crystal fractionation was responsible for the chemical difference between the high silica rhyolites of Group 1, and the trachytes and mafic trachytes of Group 3. The evolving composition of orthoclase in these rocks also supports this interpretation (Ginibre et al., 2004). However, there is a compositional gap of 6 wt. % SiO_2 between the trachyte and high silica rhyolite (Fig. 2), and only small differences in isotopic ratios exist between the trachytes and the high silica rhyolites (Fig.

4). These observations suggest that the magma of Group 1 could have been separated from that of Group 3 by viscosity and buoyancy contrasts, crystal mush zones, or even stored in separate subjacent chambers prior to eruption and caldera formation. The overall chemical similarities of these two groups indicate that they evolved from the same parental magma and should be geochemically considered as a single batch of magma (Batch A).

A second distinct magma (Batch B) is represented by the low-Zr dacites, monzonites, their andesitic enclaves, and the low-Zr andesitic pumices found in the Upper Sunshine Peak Tuff. This magma batch has (1) low-Zr and Y relative to its silica content (Fig. 2), and (2) high Sr and Pb isotopic ratios compared to the trachytes and high silica rhyolites (Fig. 4). Although the REE patterns are broadly similar to the trachytes, these magmas have generally lower heavy REE (Fig. 3). In addition, this magma batch contains the most sodic plagioclases and the most potassic orthoclases (Fig. 5). Considered together, this geochemical information indicates that these magmas were derived from a separate magmatic system. The major, trace element, and REE patterns of the low-Zr mafic enclaves indicate that these compositions may be parental to the dacites and monzonites. Feldspar removal could sufficiently deplete Eu to produce the Eu anomalies seen in the dacites. No accessory minerals rich in REE were found except for zircon. However, little zircon could have fractionated, as the heavy REE in the dacites are slightly enriched relative to the andesite enclaves (Fig. 3c). Feldspar fractionation and small amounts of zircon fractionation can explain the formation of the dacites and monzonites from the andesites. The mafic and intermediate rocks of this magma batch represent a fractional crystallization series that formed independently from Batch A.

In summary, the broad similarities between the high silica rhyolite, trachyte and mafic trachyte suggest that they had a similar parental magma and are genetically related as a single magma system. The distinct isotopic ratios and major, trace and rare earth element patterns of Batch B magmas clearly demonstrate that they had a magmatic history distinct from Batch A magmas.

MIXING AND MINGLING

Field evidence shows that two types of pumice are present in the Middle Sunshine Peak Tuff and four distinct types in the Upper Sunshine Peak Tuff (Hon, 1987). The bulk ignimbrite compositions of the Middle and Upper Sunshine Peak Tuffs represent mechanical mixtures of these pumice types. However, mingling textures in pumices, as well as hybrid pumice and intrusion compositions, indicate that magma mingling and mixing were also important in the generation of some of these magmas.

The mean bulk composition of the Middle Sunshine Peak Tuff is ~74 wt. % SiO_2 (Fig. 2). The presence of high silica rhyolite and mafic trachyte pumices in this unit indicates that the bulk composition is a mechanical mixture formed during simultaneous eruption of the two magmas. Mixing proportions have been calculated using the major, REE, and trace element data of individual pumices to produce the bulk ignimbrite compositions. These calculations indicate that a mechanical mixture of 88 % high silica rhyolite and 12 % mafic trachyte can produce a bulk composition similar to the Middle Sunshine Peak Tuff. The lack of hybrid intermediate-composition pumices in the Middle Sunshine Peak Tuff reveals that magma interaction was limited to mingling before eruption.

The resurgent rhyolite intrusions show mixed compositions, similar to the Middle Sunshine Peak Tuff, and represent true hybrids (Fig. 3c). These magmas show more affinity to the mafic trachytes than the rest of the Group 2 compositions and thus must contain larger proportions of trachyte. These intrusions represent hybrid magma which was mixed in the magma chamber prior to shallow emplacement.

The Upper Sunshine Peak Tuff represents a range of compositions from 65 to 70 wt. % SiO_2 and contains five different pumice types, indicating that the bulk composition is a mechanical mixture (Fig. 2). The presence of mingling textures (Fig. 6a) and a range of hybrid pumice compositions (Figs. 2, 3b) support a bulk composition formed from (a) mixing and mingling in the chamber, and (b) mechanical mixing during eruption and emplacement of ignimbrite. The agglutinate pumices appear to represent a mixed composition and therefore were not used in the mixing calculations. Four-component mixing calculations reveal that 60 % trachyte with high REE, 20 % mafic trachyte, 10% high silica rhyolite, and 10% low-Zr andesite could mix mechanically together to produce the bulk composition similar to the Upper Sunshine Peak Tuff (Appendix II). The presence of mingled and mixed pumices (Fig 6a) indicate that some liquid mingling and hybridization occurred either in the chamber or in the conduit, in addition to mechanical mixing during eruption.

The syenite intrusions have chemical signatures similar to the Upper Sunshine Peak Tuff and contain low-Zr andesite enclaves. Similar to the rhyolite intrusions, the syenite is a magmatic composition not a fragmental rock and cannot represent a mechanical mixture. The syenite shows crystal transfer and mixing between the host syenite and its magmatic enclaves (Fig. 6b). The syenite is generally more mafic than the

FIGURE 6. (a) Photomicrograph of a partially mixed mafic trachyte enclave found in the Upper Sunshine Peak Tuff. (b) Photograph of a mafic trachyte enclave in the syenite; mixed compositions have developed on the enclave margins and crystal transfer has occurred.

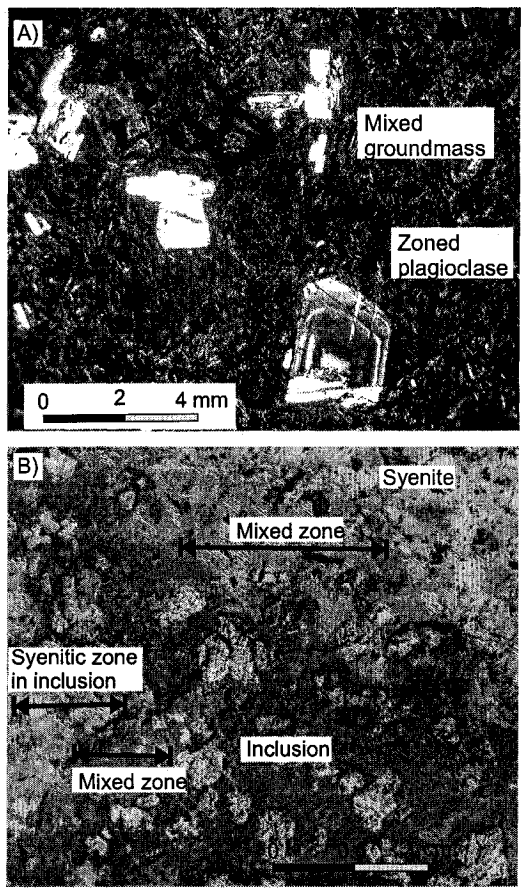
A)
Mixed groundmass
Zoned plagioclase
0 2 4 mm
B)
Syenite
Mixed zone
Syenitic zone in inclusion
Inclusion
Mixed zone

Upper Sunshine Peak Tuff with a slightly smaller Eu anomaly (Fig. 3c). Mixing calculations indicate that 40% trachyte, 40% mafic trachyte, 10% high silica rhyolite, and 10% low-Zr andesite could produce the syenite. It is thus a hybrid composition, produced by mixing in the magma

chamber.

In conclusion, both mechanical mixing during eruption and magma interaction in the chamber occurred during the formation of Lake City caldera. The style and timing of this mixing are illustrated in the zonation patterns.

COMPOSITIONAL ZONATION

The zonation in bulk composition and the different pumice types in the ignimbrites help constrain the configuration of the magma within the chambers, and the magmatic processes driving the magma mixing. Figure 7 shows the variation in Zr in the bulk composition of the Sunshine Peak Tuff with stratigraphic height.

The Lower Sunshine Peak Tuff shows no evidence for mixing and little evidence for zonation or compositional variation in Zr. Stratigraphic uncertainty prevents the outflow Lower Sunshine Peak Tuff from being plotted on Figure 8. However, these data were used when plotting the compositional variation, with the outflow sheet varying in Zr from 161 to 189 ppm, similar to the intracaldera Lower Sunshine Peak Tuff (Hon, 1987). Some trace elements show a weak zonation in the outflow sheet (Hon, 1987). The Lower Sunshine Peak Tuff must have erupted from an isolated large high silica rhyolite magma chamber.

FIGURE 7. Variation in Zr in the bulk composition of the Sunshine Peak Tuff with stratigraphic height.

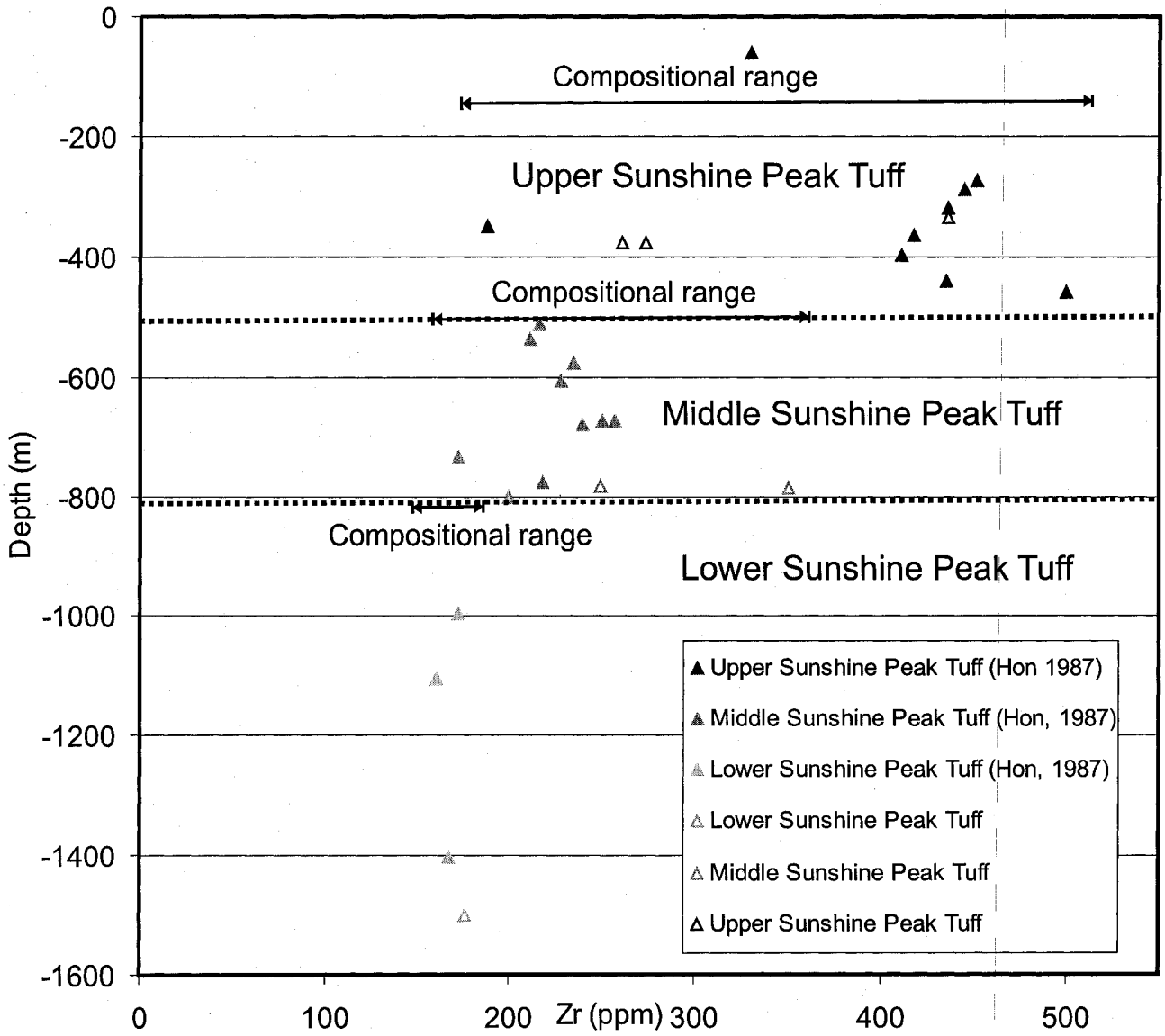
0
-200
-400
-600
-800
-1000
-1200
-1400
-1600
Depth (m)
0
100
200
300
400
500
Zr (ppm)
Compositional range
Upper Sunshine Peak Tuff
Compositional range
Middle Sunshine Peak Tuff
Compositional range
Lower Sunshine Peak Tuff
Upper Sunshine Peak Tuff (Hon 1987)
Middle Sunshine Peak Tuff (Hon, 1987)
Lower Sunshine Peak Tuff (Hon, 1987)
Lower Sunshine Peak Tuff
Middle Sunshine Peak Tuff
Upper Sunshine Peak Tuff

The Middle Sunshine Peak Tuff shows some systematic chemical zonation (Fig. 7) and contains two different pumice types. In some areas of the caldera, the base of the Middle Sunshine Peak Tuff is more mafic, and contains exceptionally large pumices of mafic trachyte (up to 50 cm long) (Hon, 1987). One mafic Middle Sunshine Peak Tuff sample from the base of the ignimbrite represents a mixture of ~55% high silica rhyolite, and ~45 % mafic trachyte (Fig. 7). At stratigraphically higher levels in the ignimbrite, the proportion of mafic trachyte pumices first fluctuates and then gradually decreases to ~12 % mafic trachyte (Fig. 7). The compositional range of the Middle Sunshine Peak Tuff is considerably greater than the Lower Sunshine Peak Tuff (Fig. 7), due to the mechanical mixing of the two pumice populations in varying proportions. The Middle Sunshine Peak Tuff is weakly inversely zoned, becoming gradually less mafic towards its top, in contrast to a normally zoned eruption from a density-stratified magma chamber (Blake and Ivey, 1986: Spera et al., 1986; Trail et al., 2002).

The Upper Sunshine Peak Tuff shows the largest range in composition. Similar to the Middle Sunshine Peak Tuff, most variation in composition occurs near the beginning of the eruption. After this initial variation, the eruption became systematically more Zr-rich, however, the last magma erupted had a Zr-poor compositions (Fig. 7). The proportions of mafic pumices initially varied, then increased steadily during the eruption, and dropped again at the end of the eruption. The last magma erupted was a high silica rhyolite of Group 1 (Figs. 2, 7).

Zoned syenite intrusions have marginal facies of mixed Group 2 rhyolite, and a core of mixed and mingled Group 3 syenite. The rhyolite represents a mixed composition of ~70 % high silica rhyolite and ~30 % mafic trachyte, while the syenite represents ~40

% trachyte, ~40 % mafic trachyte, ~10 % high silica rhyolite and ~10% low-Zr andesite. This compositional variation is consistent with intrusion from a chamber with residual magmatic stratification and parcels of different-composition magma remaining in the chamber after the eruption of the Upper Sunshine Peak Tuff.

In summary, the magmatic system at Lake City experienced three episodes of collapse and eruption: (1) the Lower Sunshine Peak Tuff (200 to 250 km^3), an unzoned high silica rhyolite ignimbrite; (2) the Middle Sunshine Peak Tuff (20 to 40 km^3), an inversely zoned ignimbrite with two pumice types and a mafic trachyte-rich base; (3) the Upper Sunshine Peak Tuff (40 to 60 km^3), a normally zoned ignimbrite with four distinct pumice types. In some areas of the caldera this ignimbrite also has a base rich in mafic trachyte pumices, and top rich in trachyte pumice. Resurgence occurred as dacite lavas erupted, and rhyolite, syenite, and monzonite intruded at shallow levels.

INTERPRETATION

The compositional variability in the Middle and Upper Sunshine Peak Tuffs and the mixed resurgent intrusions demonstrate a complex magmatic history. Below we address the origin of this complexity.

Prior to the eruption of the Lower Sunshine Peak tuff, a magma chamber containing high silica rhyolite existed at shallow levels in the crust (Fig. 8a). The Lower Sunshine Peak Tuff (200 to 250 km^3 of high silica rhyolite) then erupted, and a 12 km-diameter caldera formed (Fig. 8b). The Middle Sunshine Peak Tuff eruption was initiated with high proportions of mafic trachyte pumice. We interpret this event as the intrusion

FIGURE 8. A cartoon of the major magmatic processes and the arrangement of stratification in the magma chambers at Lake City.

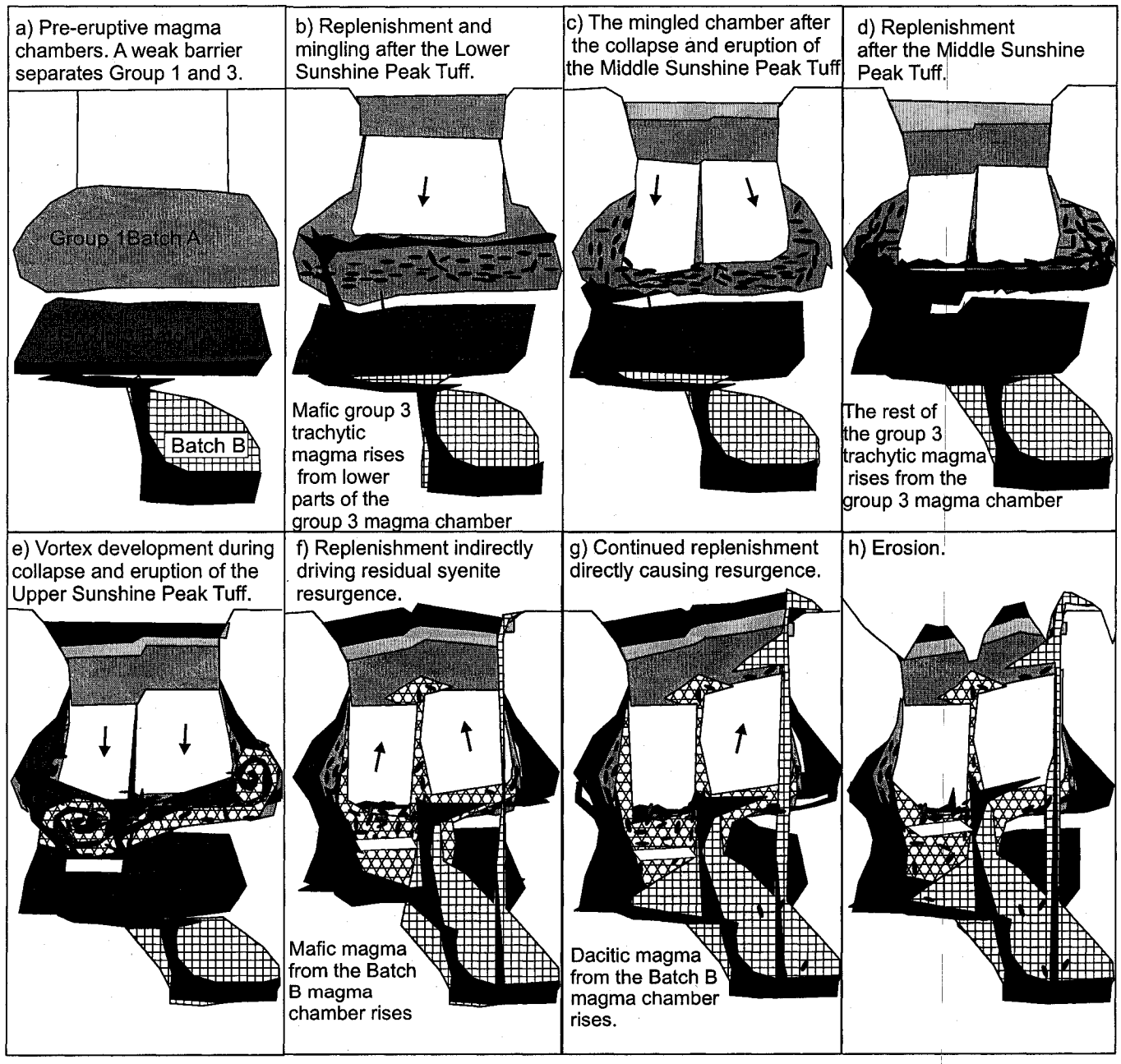
a) Pre-eruptive magma chambers. A weak barrier separates Group 1 and 3.
Group 1Batch A
Batch B
b) Replenishment and mingling after the Lower Sunshine Peak Tuff.
Mafic group 3 trachytic magma rises from lower parts of the group 3 magma chamber
c) The mingled chamber after the collapse and eruption of the Middle Sunshine Peak Tuff
d) Replenishment after the Middle Sunshine Peak Tuff.
The rest of the group 3 trachytic magma rises from the group 3 magma chamber
e) Vortex development during collapse and eruption of the Upper Sunshine Peak Tuff.
f) Replenishment indirectly driving residual syenite resurgence.
Mafic magma from the Batch B magma chamber rises
g) Continued replenishment directly causing resurgence.
Dacitic magma from the Batch B magma chamber rises.
h) Erosion.

of mafic trachyte at the top of the high silica rhyolite magma chamber between eruptions of the Lower and Middle Sunshine Peak Tuffs (Fig. 8b). This intrusion could have triggered the eruption of the Middle Sunshine Tuff (Sparks et al., 1977; Takeuchi, 2004; Chapter 4 this thesis). Alternatively, the mafic trachyte could have intruded the high silica rhyolite before the eruption of the Lower Sunshine Tuff. This model requires tapping of magma from the eruption of the Lower Sunshine Peak Tuff to have stopped just above the upper mafic trachyte layer in the pre-stratified chamber. The eruption could have then restarted by erupting the mafic trachyte layer.

The Middle Sunshine Peak Tuff contains an initial fluctuation in proportion of pumice types and is then inversely zoned (Fig. 7). We interpret the initial fluctuation as either a limited horizontal extent of the mafic trachyte intrusion, and/or variable eruption rates that tap different proportions of magmas within a stratified chamber (Trial et al., 1992; Chapter 3, this thesis). During the early stages of collapse, we envisage different areas of the caldera erupting ignimbrite at varying rates with different amounts of mafic trachyte, producing temporal fluctuations in bulk composition.

The inverse zonation is represented by a systematic decrease in proportion of mafic pumice at higher levels. As the volume of mafic trachyte is depleted, mafic trachyte is erupted in decreasing amounts while increasing proportions of the underlying high silica rhyolite are erupted. Alternatively, initially high eruption rates could tap deeper levels in a normally zoned density-stratified chamber, followed by a systematic decrease in eruption rate causing shallower levels to be tapped, thus erupting increasingly higher proportions of high silica rhyolite (e.g., Trial et al., 1992). The magma chamber after the eruption of the Middle Sunshine Peak Tuff contained mingled mafic trachyte

and high silica rhyolite (Fig. 8c). The Upper Sunshine Peak Tuff also has a mafic trachyte-rich base, but the rest of the deposit is normally zoned, and dominated by trachyte, except for a rhyolitic top in some areas. These observations suggest that this eruption also was triggered by a shallow intrusion of mafic trachytic magma, followed by progressively deeper tapping of a density-stratified magma chamber (Fig. 8d).

Trachytic magma and low-Zr andesite did not erupt with the Middle Sunshine Peak Tuff, yet are present in the Upper Sunshine Peak Tuff. After the eruption of the Middle Sunshine Peak Tuff the roof of the magma chamber may have stopped just above the deeper layer of zoned trachytes. During the eruption of the Upper Sunshine Peak Tuff, continued subsidence allowed these zoned trachytes to erupt together. The zoned trachyte magmas may have been protected at lower levels in the chamber due to crystal mush barriers, or in even in a separate chamber (Fig. 8d). Such configurations would require the collapse of a crystallization front (Parker, 1983), or stoping and chamber amalgamation (Hawkins and Wiebe, 2004) just prior to the eruption (Fig. 8d). Such events may be related to the intrusion of mafic trachyte to high levels and the introduction of low-Zr andesite from Batch B (Fig. 8d).

The majority of the Upper Sunshine Peak Tuff is normally zoned representing increasing proportions of mafic trachyte at higher stratigraphic levels. The progressive downward tapping of the zoned trachytic magma (Fig. 8e) probably produced this sequence. Trachyte and mafic trachyte pumices show distinct compositions, indicating that they were derived from distinct, rather than gradationally zoned layers within the chamber (Fig. 8e). These layers were progressively mingled during the eruption of the Upper Sunshine Peak Tuff (Fig. 8e). Parcels of high silica rhyolite and low-Zr andesite

were also erupted, although the changing proportions of these magmas are not well constrained. Mingling textures in some pumices indicate a dynamic chamber at this stage in the eruption (Fig. 8e). Further evidence for a dynamic chamber is seen by the presence of high silica rhyolitic magma at the top of the Upper Sunshine Peak Tuff. This magma may represent residual Group 1 magma from the upper parts of the chamber that could not be erupted until the chamber roof approached the base of the chamber. This magma was then squeezed out as the block or blocks reached the base of the largely liquid part of the chamber (Chapter 3, this thesis).

Resurgence began with relatively unmixed high silica rhyolite intrusions and was followed by mixed rhyolite and syenite intrusions (Fig 8f). We interpret these magmas as representing partially stirred magma, which remained in the chamber following the eruptions. Analogue experiments show that a dynamic period of chamber processes causes enhanced mixing and mingling as the collapsing block approached the base of the chamber, (Chapter 3, this thesis). During the eruption of the Upper Sunshine Peak Tuff, vortices may have developed that stirred different magmas and produced the mixed syenitic and rhyolitic intrusions (Folch et al., 2001; Chapter 3, this thesis). Resurgent magma from Batch B then rose, and dacite lavas erupted in the east (Figs. 8f,g). The Batch B magma also supplied the low-Zr andesite that is found in the Upper Sunshine Peak Tuff and the syenite intrusions. This low-Zr andesite may have rejuvenated the residual syenitic magma, reducing the viscosity and allowing it to intrude to shallow levels (Fig. 8f). The shallow syenitic intrusions caused doming of the ignimbrite in the caldera center (Fig. 8f). Resurgent Batch B magma also intruded within the ignimbrite to produce over 1 km of fault-controlled uplift in the northeastern part of the caldera (Fig.

8g). Similar resurgent intrusion styles are seen at other calderas (e.g. Fridrich and Mahood, 1984; McConnell et al., 1995). Hydrothermal systems remained active after resurgence, altering many of the intracaldera rocks and producing abundant mineralized quartz veins (Lipman et al., 1978). Following resurgence, erosion exposed deep levels of the caldera to reveal the full eruption sequence (Fig. 8h).

The eruptions and intrusions at Lake City show a complex history of magma interaction. After caldera-forming ignimbrite eruptions, new magma rose, replenished, and interacted in the shallow chamber beneath the caldera. This type of chamber replenishment is an integral part of caldera development at Lake City. Accelerated magmatic interaction as the caldera block or blocks approached the base of the chamber produced compositional variation in the ignimbrites and the hybrid resurgent intrusions. A distinctive style of shallow resurgence appears to be driven by replenishment of Batch B magma from deeper reservoirs.

CONCLUSIONS AND IMPLICATIONS

The formation, eruption, replenishment and possible amalgamation of magma chambers allowed repeated eruptions during the formation of Lake City caldera. Studies of large batholiths associated with caldera collapse have shown that replenishment and mixing are important processes in such magma chambers (Wiebe et al., 2004). Lake City caldera offers exposures of both the magma that was erupted and the magma that remained in chambers. This configuration allows an unusually complete view of the caldera-forming process.

Our study of Lake City caldera shows the following events within a single caldera cycle. (1) Three increasingly mafic ignimbrites erupted from a density-stratified, genetically-related magmatic system (Batch A). (2) These magmas did not erupt in regular stratigraphic order but instead intruded and restratified between collapse events, producing increasingly complex mixed and mingled magmas. (3) A small volume of mafic trachyte twice replenished the top of the main magma reservoir, initiating eruptions of the Middle and Upper Sunshine Peak Tuffs. (4) The Middle Sunshine Peak Tuff was weakly reversely zoned, reflecting a decreasing proportion of this mafic trachyte. (5) After its initially mafic start, the Upper Sunshine Peak Tuff was normally zoned, reflecting increasing proportions of mafic trachyte, low-Zr andesitic magma and high silica rhyolite, all of which also erupted as pumices in the Upper Sunshine Peak Tuff. (6) During the eruption of dacite lavas from Batch B, uplift was caused by shallow intrusions of residual mixed syenite, and monzonite from Batch B.

Our results at Lake City caldera demonstrate that magma interaction within a chamber during replenishment, collapse, and resurgence is an integral component of magmatism during a single caldera cycle. The mafic base of the Middle and Upper Sunshine Peak Tuffs illustrates that replenishment of a chamber may affect chamber pressure and initiate eruptions (Sparks et al., 1978; Chapter 4, this thesis). Continued replenishment after eruption is a manifestation of the lithostatic pressure decrease associated with caldera formation allowing magma to rise from deeper levels (Kennedy and Stix, 2003).

At Lake City, physical processes appear to control magma interaction. Magma interaction can occur during magma flow in a conduit during eruption (Blake and

Campbell, 1986; Koyaguchi, 1985), within a magma chamber during replenishment as magma is injected forcefully into the chamber (Campbell and Turner, 1989; Bergantz, 1999; Weinburg and Leitch, 1999), or in a magma chamber due to an external disturbance such as caldera collapse (Folch et al, 2001; Nunez and Branney; 2005; Chapter 3, this thesis). The timing and style of interaction indicate that replenishment, collapse, and eruption may have all contributed to produce the textures and chemical zonation observed at Lake City.

Magma interactions were restricted to certain parts of the Lake City magma chamber. During magma chamber replenishment, the location of the new magma entering the chamber limits the volume of the magma chamber involved in the mixing or mingling process. This process produces parcels of mixed or mingled magma in these areas. During caldera collapse, the roof of the magma chamber subsides, changing the geometry of the magma chamber (Fig. 8). The walls of the magma chamber and the edge of the subsiding block can limit the dimensions of mixing and mingling vortices (Folch et al., 2001). Either of these mechanisms could have restricted magmatic interaction at Lake City.

The shallow intrusion of magma at the base of the ignimbrite sequence was facilitated by subsidence-related structures and caused resurgence. This style of resurgence is well documented at Lake City (Hon, 1987) and other calderas (e.g. Fridrich and Mahood, 1984; McConnell et al., 1995) and may be a common style of caldera resurgence. This style of resurgence illustrates that the collapse process can affect the subsequent magmatic processes.

In summary, the increasing complexity of the mingled and mixed magmas at Lake City reflects the various roles of magma replenishment, eruptive velocity, collapse style, chamber geometry, and vent location during caldera development. These factors are important during collapse at most calderas but this information may be obscured either due to poor exposure of deep-levels of the caldera, or concealed if the replenishing magma is chemically similar to the erupting magma. At Lake City, the unusually diverse magma types illustrate the importance and diversity of magma interaction during caldera collapse.

ACKNOWLEDGEMENTS

Grant Heiken first suggested Lake City to us as an excellent example of caldera processes and Peter Lipman provided encouragement and advice during this study. We also thank Matthieu Richer, Marc-Antoine Longpré, John Davidson, and John Hanson for their assistance in the field. Andi Kron and Charlie Thorn provided much appreciated accommodations during our first field season. Financial support was provided to B.K. by funds from the Department of Earth and Planetary Sciences, McGill University, and from GEOTOP, Université du Québec à Montréal, and by a research grant to J.S. from the Natural Sciences and Engineering Research Council of Canada. We also acknowledge support from NSF Grant EAR-0125631 to James Vallance and John Stix.

REFERENCES

Bacon, C.R., 1983, Eruptive history of Mount Mazama and Crater Lake Caldera, Cascade Range, USA: Journal of Volcanology and Geothermal Research, v. 18, p. 57-115.

Bateman, R., 1995, The interplay between crystallization, replenishment and hybridization in large felsic magma chambers: Earth-Science Reviews, v. 39, p. 1-106.

Blake, S., and Campbell, I.H., 1986, The dynamics of magma-mixing during flow in volcanic conduits: Contributions to Mineral Petrology, v. 94, p. 72-81.

Blake, S., and Ivey G.N., 1986a, Magma mixing and the dynamics of withdrawal from stratified reservoirs: Journal of Volcanology and Geothermal Research, v. 27, p. 153-178.

Blake S., and Ivey, G.N., 1986b, Density and viscosity gradients in zoned magma chambers, and their influences on withdrawal dynamics: Journal of Volcanology and Geothermal Research, v. 30, p. 201-230.

Bove, D.J., Hon, K., Budding, K.E., Slack, J.F., Snee, L.W., and Yeoman, R.A., 2001, Geochronology and geology of late Oligocene through Miocene volcanism and mineralization in the western San Juan Mountains, Colorado: U. S. Geological Survey Professional Paper, Report: P 1642, 30p.

Campbell, I.H., and Turner, J.S., 1989, Fountains in magma chambers: Journal of Petrology, v. 30, p. 885-923.

Eichelberger, J.C., Chertkoff, D.G., Dreher, S.T., and Nye C.J., 2000, Magmas in collision; rethinking chemical zonation in silicic magmas: Geology, v. 28, p. 603-606.

Folch, A., Marti, J., and Codina, R., 2001, Numerical modeling of magma withdrawal during caldera-forming eruptions: Journal of Geophysical Research, v. 106, p. 16,163-16,175.

Fridrich, C.J., and Mahood, G.A., 1984, Reverse zoning in the resurgent intrusions of the Grizzly Peak cauldron, Sawatch Range, Colorado: Geological Society of America Bulletin, v. 95, p. 779-787.

Ginibre, C ., Wörner, G , and, Kronz, A . 2004, Structure and dynamics of the Laacher See magma chamber (Eifel, Germany) from major and trace element zoning in sanidine: a cathodoluminescence and electron microprobe study: Journal of Petrology, v. 45, 2197-2224.

Hildreth, E.W., 1979, The Bishop Tuff: evidence for the origin of compositional zonation in silicic magma chambers: In Chapin, C.E., and Elston, W.E. (eds.), Ash-Flow Tuffs: Geological Society of America Special Paper 180, p. 43-72.

Hildreth, E.W., 1981, Gradients in silicic magma chambers: Implications for lithospheric magmatism: Journal of Geophysical Research, v. 86, p. 10153-10192.

Hon, K.A., 1987, Geologic and petrologic evolution of the Lake City Caldera, San Juan Mountains, Colorado. Ph.D. Thesis, University of Colorado, Boulder, Colorado, 244p.

Hon, K., and Lipman, P.W., 1989, Western San Juan caldera complex: In Lipman, P.W. (ed.), Oligocene-Miocene San Juan volcanic field, Colorado: New Mexico Bureau of Mines and Mineral Resources Memoir 46, p. 350-380.

Huppert, H.E., Sparks, R.S.J., and Turner, J.S., 1984, Some effects of viscosity on the dynamics of replenished magma chambers: Journal of Geophysical Research, v. 89, p. 6857-6877.

Koyaguchi, T., 1985, Magma mixing in a conduit: Journal of Volcanology and Geothermal Research, v. 25, p. 365-369.

Lipman, P. W. 1976, Caldera-collapse breccias in the western San Juan Mountains, Colorado: Geological Society of America bulletin v. 87, p. 1397-1410.

Lipman, P.W., Doe, B.R., Hedge, C.E., and Steven, T.A., 1978, Petrologic evolution of the San Juan volcanic field, southwestern Colorado: Pb and Sr isotope evidence: Geological Society of America Bulletin, v. 89, p. 59-82.

Lipman, P.W., Dungan, M.A., and Bachmann, O., 1997, Comagmatic granophyric granite in the Fish Canyon Tuff, Colorado; implications for magma-chamber processes during a large ash-flow eruption: Geology, v. 25, p. 915-918.

Michael, P., 1988, Partition coefficients for rare earth elements in mafic minerals of high silica rhyolites: The importance of accessory mineral inclusions: Geochimica Cosmochimica Acta, v. 52, p. 215-202.

Nakamura, M., 1995, Continuous mixing of crystal mush and replenished magma in the ongoing Unzen eruption: Geology, v. 23, p. 807-810.

Nekvasil, H., 1988, Calculation of equilibrium crystallization paths of compositionally simple hydrous felsic melts: American Mineralogist, v. 73, p. 956-965.

Sparks, R.S.J., Sigurdsson, H., and Wilson, L., 1977, Magma mixing; a mechanism for triggering acid explosive eruptions: Nature, v. 267, p. 315–318.

Sparks, R.S.J., Huppert, H. E., and Turner, J. S., 1984, The Fluid dynamics of evolving magma chambers: Philosophical Transactions of the Royal Society of London, v. A310, p. 511-534.

Spera, F.J., Yuen, D.A., Greer, J.C., and Sewell, G., 1986, Dynamics of magma withdrawal from stratified magma chambers: Geology, v. 14, p. 723-726.

Steven, T.A., and Lipman, P.W., 1976, Calderas of the San Juan volcanic field, southwestern Colorado: U. S. Geological Survey Professional Paper, Report: P 0958, 35p.

Taylor, S.R., and McLennan, S.M., 1985, The Continental Crust: its Composition and Evolution: Blackwell Scientific Publications (Oxford), 312p.

Trial, A.F., Spera, F.J., Greer, J., and Yuen, D.A., 1992, Simulations of magma withdrawal from compositionally zoned bodies: Journal of Geophysical Research, v. 97, p. 6713-6733.

Troll, V.R., Sachs, P.M., Schmincke, H.U., and Sumita, M., 2003, The REE-Ti mineral chevkinite in comenditic magmas from Gran Canaria, Spain: a SYXRF-probe study: Contributions to Mineral Petrology, v. 145, p. 730–741.

Wiebe, R.A., Manon, M.R., Hawkins, D.P., and McDonough W.F., 2004, Late stage mafic injection and rejuvenation of the Vinalhaven granite, Coastal Maine: Journal of Peterology, v. 45, p. 2133-2153.

APPENDIX I

TABLE A-I. Feldspar compositions analyzed by McGill Microprobe Laboratory, Montréal. Uncertainties are less than 1% and measurement conditions are presented after the table.

Sample	Rock type	Approx. dist. from rim (mm)	SiO_2 (wt. %)	TiO_2 (wt. %)	Al_2O_3 (wt. %)	FeO (wt. %)	MgO (wt. %)	CaO (wt. %)	Na_2O (wt. %)	K_2O (wt. %)	BaO (wt. %)	SrO (wt. %)	Total (wt. %)
LC-2004-15A-C1-1	LSPT	0.00	67.19	0.00	18.94	0.18	0.00	0.35	6.14	8.07	0.04	0.00	100.92
LC-2004-15A-C1-2	LSPT	100.00	67.50	0.03	19.08	0.20	0.00	0.52	6.72	7.28	0.00	0.00	101.34
LC-2004-15A-C1-3	LSPT	200.00	67.22	0.01	18.93	0.23	0.01	0.45	5.96	8.26	0.00	0.00	101.07
LC-2004-15A-C1-4	LSPT	300.00	66.92	0.01	18.85	0.20	0.00	0.39	5.91	8.57	0.04	0.00	100.89
LC-2004-15A-C2-1	LSPT	0.00	67.14	0.02	18.91	0.23	0.00	0.43	6.69	7.27	0.00	0.00	100.67
LC-2004-15A-C2-2	LSPT	100.00	67.34	0.03	19.05	0.18	0.00	0.36	6.26	7.71	0.00	0.02	100.95
LC-2004-15A-C2-3	LSPT	200.00	67.11	0.00	19.02	0.16	0.00	0.43	6.48	7.49	0.09	0.01	100.79
LC-2004-15A-C2-4	LSPT	300.00	65.48	0.02	18.59	0.19	0.02	0.37	6.01	7.89	0.05	0.06	98.69
LC-2004-15A-C3-1	LSPT	0.00	66.96	0.01	18.86	0.22	0.00	0.36	6.00	8.25	0.00	0.01	100.67
LC-2004-15A-C3-2	LSPT	100.00	67.09	0.00	18.81	0.17	0.00	0.39	6.04	8.14	0.00	0.00	100.65
LC-2004-15A-C3-3	LSPT	200.00	66.53	0.00	18.73	0.18	0.00	0.39	6.11	7.98	0.00	0.00	99.92
LC-2004-15A-C3-4	LSPT	300.00	66.96	0.01	18.77	0.20	0.00	0.38	5.99	8.13	0.02	0.00	100.47
LC-34b-c1-1	LSPT	0.00	66.51	0.02	18.77	0.19	0.01	0.43	5.89	8.34	0.00	0.00	100.15
LC-34b-c1-2	LSPT	100.00	66.19	0.02	18.78	0.21	0.00	0.36	5.51	8.94	0.00	0.00	100.00
LC-34b-c1-3	LSPT	200.00	66.12	0.04	18.80	0.19	0.01	0.42	5.64	8.90	0.01	0.02	100.14
LC-34b-c1-4	LSPT	300.00	66.20	0.00	18.88	0.19	0.00	0.46	5.98	8.16	0.00	0.04	99.93
LC-34b-c1-5	LSPT	400.00	66.06	0.00	18.84	0.17	0.00	0.45	5.97	8.23	0.00	0.02	99.74
LC-34b-c1-6	LSPT	500.00	66.50	0.03	18.91	0.16	0.00	0.44	5.99	8.18	0.02	0.04	100.27
LC-34b-c2-1	LSPT	0.00	66.13	0.00	18.85	0.21	0.00	0.43	5.78	8.46	0.02	0.00	99.90
LC-34b-c2-2	LSPT	100.00	66.87	0.06	18.90	0.18	0.00	0.43	5.94	8.31	0.06	0.00	100.76
LC-34b-c2-3	LSPT	200.00	66.48	0.01	18.81	0.19	0.02	0.38	5.67	8.74	0.00	0.00	100.30
LC-34b-c2-4	LSPT	300.00	66.16	0.04	18.94	0.19	0.00	0.41	5.86	8.41	0.02	0.02	100.05
LC-34b-c4-1	Mafic pumice in LSPT	0.00	58.46	0.06	25.55	0.44	0.04	7.69	6.30	1.29	0.23	0.29	100.36
LC-34b-c4-2	Mafic pumice in LSPT	100.00	57.78	0.09	26.03	0.40	0.03	8.22	5.95	1.12	0.26	0.32	100.18
LC-34b-c4-3	Mafic pumice in LSPT	200.00	56.43	0.11	27.22	0.48	0.04	9.51	5.41	0.83	0.13	0.34	100.49
LC-34b-c4-4	Mafic pumice in LSPT	300.00	57.61	0.09	26.12	0.39	0.02	8.55	5.95	1.10	0.21	0.30	100.34
LC-34b-c5-1	LSPT	0.00	66.24	0.02	19.16	0.21	0.00	0.57	6.48	7.19	0.02	0.00	99.89
LC-34b-c5-2	LSPT	100.00	66.32	0.00	18.78	0.21	0.00	0.37	5.54	8.97	0.02	0.03	100.23
LC-34b-c5-3	LSPT	200.00	66.56	0.01	18.75	0.17	0.00	0.39	5.68	8.59	0.01	0.00	100.15
LC-34b-c5-4	LSPT	300.00	65.89	0.04	19.08	0.22	0.00	0.55	6.20	7.91	0.00	0.00	99.88
LC-34b-c5-5	LSPT	400.00	66.97	0.03	18.98	0.22	0.00	0.63	6.34	7.72	0.00	0.02	100.92

Sample	Rock type	Approx. dist. from rim (mm)	SiO_2 (wt. %)	TiO_2 (wt. %)	Al_2O_3 (wt. %)	FeO (wt. %)	MgO (wt. %)	CaO (wt. %)	Na_2O (wt. %)	K_2O (wt. %)	BaO (wt. %)	SrO (wt. %)	Total (wt. %)
LC-34b-c5-6	LSPT	500.00	66.86	0.03	19.07	0.23	0.00	0.66	6.34	7.34	0.01	0.04	100.57
LC-2004-57c-c2-1	MSPT	0.00	66.26	0.01	18.83	0.20	0.01	0.38	5.71	8.64	0.00	0.00	100.04
LC-2004-57c-c2-2	MSPT	100.00	66.07	0.03	18.70	0.19	0.00	0.42	5.79	8.40	0.01	0.00	99.60
LC-2004-57c-c2-3	MSPT	200.00	66.21	0.00	18.77	0.20	0.01	0.38	5.70	8.39	0.07	0.01	99.73
LC-2004-57c-c2-4	MSPT	300.00	66.11	0.00	18.63	0.19	0.00	0.42	5.83	8.32	0.00	0.03	99.54
LC-2004-57c-c2-5	MSPT	400.00	66.42	0.00	18.81	0.21	0.00	0.41	5.72	8.33	0.00	0.00	99.89
LC-2004-57c-c3-1	MSPT	0.00	60.63	0.03	24.35	0.41	0.02	6.09	7.02	1.65	0.19	0.25	100.65
LC-2004-57c-c3-2	MSPT	100.00	59.38	0.05	24.41	0.39	0.02	6.63	6.71	1.45	0.14	0.21	99.39
LC-2004-57c-c3-3	MSPT	200.00	60.32	0.08	23.78	0.37	0.03	5.96	6.89	1.75	0.21	0.26	99.64
LC-2004-57c-c3-4	MSPT	300.00	59.42	0.05	24.78	0.36	0.04	6.86	6.74	1.30	0.13	0.25	99.93
LC-2004-57c-c4-1	MSPT	0.00	66.62	0.00	18.96	0.19	0.00	0.47	6.03	8.06	0.02	0.00	100.35
LC-2004-57c-c4-2	MSPT	100.00	66.16	0.00	18.75	0.22	0.00	0.36	5.76	8.69	0.00	0.00	99.93
LC-2004-57c-c4-3	MSPT	200.00	61.97	0.05	22.67	0.25	0.01	4.55	8.44	1.01	0.10	0.10	99.14
LC-2004-57c-c4-4	MSPT	300.00	59.91	0.05	24.71	0.27	0.00	6.59	7.57	0.60	0.07	0.12	99.89
LC-2004-57c-c4-5	MSPT	400.00	60.31	0.07	24.43	0.28	0.00	6.39	7.55	0.60	0.03	0.09	99.73
LC-2004-57c-c5-1	MSPT	0.00	66.65	0.02	18.72	0.22	0.00	0.38	5.65	8.50	0.03	0.00	100.17
LC-2004-57c-c5-2	MSPT	100.00	66.74	0.00	18.64	0.20	0.00	0.44	5.76	8.32	0.01	0.01	100.12
LC-2004-57c-c5-3	MSPT	200.00	66.76	0.01	18.87	0.20	0.01	0.43	5.81	8.39	0.03	0.00	100.51
LC-2004-57c-c5-4	MSPT	300.00	66.89	0.04	18.90	0.18	0.00	0.46	5.89	8.25	0.01	0.02	100.64
LC-2004-57c-c5-5	MSPT	400.00	66.65	0.00	18.87	0.19	0.01	0.43	5.90	8.20	0.00	0.00	100.24
LC-2004-55b-c2-1	Pumice in MSPT	0.00	59.48	0.00	25.02	0.35	0.01	7.28	6.68	0.93	0.08	0.30	100.12
LC-2004-55b-c2-2	Pumice in MSPT	100.00	59.76	0.03	24.84	0.32	0.01	7.09	6.98	0.93	0.07	0.20	100.23
LC-2004-55b-c2-3	Pumice in MSPT	200.00	59.67	0.00	24.78	0.30	0.02	7.07	6.76	0.92	0.09	0.18	99.78
LC-2004-55b-c2-4	Pumice in MSPT	300.00	59.71	0.02	24.60	0.35	0.03	6.99	6.80	0.93	0.11	0.24	99.79
LC-2004-57c-c1-1	Pumice in MSPT	0.00	66.72	0.01	18.83	0.21	0.00	0.47	5.98	8.15	0.00	0.04	100.41
LC-2004-57c-c1-2	Pumice in MSPT	100.00	66.67	0.00	18.87	0.21	0.01	0.49	6.10	7.85	0.02	0.02	100.24
LC-2004-57c-c1-3	Pumice in MSPT	200.00	66.27	0.06	18.79	0.18	0.00	0.40	5.59	8.68	0.00	0.00	99.98
LC-2004-57c-c1-4	Pumice in MSPT	300.00	66.13	0.02	18.66	0.22	0.00	0.43	5.49	8.99	0.03	0.01	99.95
LC-2004-57c-c1-5	Pumice in MSPT	400.00	59.71	0.03	24.67	0.26	0.01	6.92	6.93	0.92	0.04	0.23	99.69
LC-2004-57c-c1-6	Pumice in MSPT	500.00	60.63	0.01	25.18	0.48	0.12	6.43	7.30	0.65	0.00	0.14	100.93
LC-2004-57c-c1-7	Pumice in MSPT	600.00	58.44	0.01	25.52	0.30	0.01	7.95	6.45	0.75	0.07	0.26	99.75

Sample	Rock type	Approx. dist. from rim (mm)	SiO_2 (wt. %)	TiO_2 (wt. %)	Al_2O_3 (wt. %)	FeO (wt. %)	MgO (wt. %)	CaO (wt. %)	Na_2O (wt. %)	K_2O (wt. %)	BaO (wt. %)	SrO (wt. %)	Total (wt. %)
LC-2004-57c-c1-8	Pumice in MSPT	700.00	56.37	0.00	26.08	0.26	0.01	8.70	5.96	0.62	0.01	0.15	98.16
LC-2004-57c-c1-9	Pumice in MSPT	800.00	56.96	0.06	26.57	0.30	0.02	9.23	5.91	0.59	0.02	0.17	99.84
LC-2004-50a-c1-1	USPT	0.00	60.32	0.10	24.16	0.33	0.01	6.11	7.61	0.77	0.20	0.14	99.74
LC-2004-50a-c1-2	USPT	100.00	60.81	0.08	23.83	0.39	0.01	5.86	7.57	0.82	0.21	0.16	99.74
LC-2004-50a-c1-3	USPT	200.00	59.90	0.06	23.72	0.38	0.03	5.70	7.62	0.90	0.24	0.23	98.76
LC-2004-50a-c1-4	USPT	300.00	58.86	0.08	25.12	0.35	0.01	7.20	6.90	0.60	0.12	0.17	99.41
LC-2004-50a-c1-5	USPT	400.00	58.03	0.04	25.12	0.37	0.00	7.15	7.04	0.59	0.18	0.19	98.70
LC-2004-50a-c1-6	USPT	500.00	60.84	0.04	23.69	0.33	0.01	5.79	7.66	0.89	0.14	0.20	99.60
LC-2004-50a-c2-1	USPT	0.00	61.51	0.07	23.54	0.35	0.02	5.22	8.02	0.99	0.11	0.09	99.91
LC-2004-50a-c2-2	USPT	100.00	60.96	0.07	23.48	0.31	0.00	5.24	7.88	0.98	0.13	0.11	99.16
LC-2004-50a-c2-3	USPT	200.00	60.76	0.05	23.94	0.33	0.01	5.63	7.72	0.91	0.20	0.12	99.67
LC-2004-50a-c2-4	USPT	300.00	59.67	0.03	24.11	0.30	0.02	5.99	7.58	0.85	0.21	0.12	98.88
LC-2004-50a-c3-1	USPT	0.00	65.87	0.00	18.79	0.17	0.00	0.40	5.80	8.55	0.04	0.01	99.64
LC-2004-50a-c3-2	USPT	100.00	66.18	0.00	18.90	0.16	0.01	0.45	6.01	8.22	0.05	0.00	99.98
LC-2004-50a-c3-3	USPT	200.00	66.48	0.02	18.76	0.21	0.00	0.35	5.57	8.79	0.02	0.01	100.21
LC-2004-50a-c3-4	USPT	300.00	66.36	0.02	18.74	0.17	0.00	0.38	5.61	8.85	0.03	0.00	100.15
LC-2004-50a-c3-5	USPT	400.00	65.97	0.03	18.64	0.21	0.01	0.44	5.76	8.58	0.00	0.00	99.63
LC-2004-50a-c4-1	USPT	0.00	66.27	0.00	18.74	0.16	0.00	0.36	5.56	8.87	0.03	0.02	100.01
LC-2004-50a-c4-2	USPT	100.00	65.69	0.01	18.78	0.16	0.00	0.35	5.51	8.86	0.02	0.00	99.38
LC-2004-50a-c4-3	USPT	200.00	65.76	0.02	18.77	0.16	0.01	0.40	5.57	8.73	0.04	0.00	99.45
LC-2004-50a-c4-4	USPT	300.00	65.31	0.03	18.69	0.21	0.00	0.35	5.38	9.16	0.06	0.00	99.20
LC-2004-50a-c5-1	USPT	0.00	65.71	0.01	18.88	0.23	0.01	0.37	5.69	8.64	0.02	0.01	99.57
LC-2004-50a-c5-2	USPT	100.00	65.79	0.01	19.06	0.23	0.00	0.46	5.74	8.46	0.01	0.00	99.76
LC-2004-50a-c5-3	USPT	200.00	65.57	0.03	18.92	0.19	0.01	0.42	5.70	8.83	0.00	0.04	99.71
LC-2004-50a-c5-4	USPT	300.00	60.71	0.00	17.52	0.20	0.00	0.36	5.46	8.86	0.01	0.02	93.15
LC-2004-50a-c5-5	USPT	400.00	65.78	0.02	18.90	0.20	0.00	0.45	5.83	8.30	0.01	0.02	99.51
LC-2004-50cb-c1-1	USPT	0.00	66.74	0.02	18.93	0.21	0.00	0.42	5.11	9.57	0.00	0.01	101.02
LC-2004-50cb-c1-2	USPT	100.00	66.21	0.05	19.19	0.20	0.00	0.70	5.36	9.27	0.06	0.01	101.07
LC-2004-50cb-c1-3	USPT	200.00	66.41	0.00	18.93	0.24	0.01	0.53	5.11	9.46	0.06	0.02	100.77
LC-2004-50cb-c1-4	USPT	300.00	66.29	0.02	19.21	0.21	0.00	0.62	5.24	9.29	0.03	0.00	100.90
LC-2004-50cb-c2-1	USPT	0.00	66.96	0.00	18.69	0.21	0.00	0.36	5.25	9.59	0.02	0.00	101.07

Sample	Rock type	Approx. dist. from rim (mm)	SiO_2 (wt. %)	TiO_2 (wt. %)	Al_2O_3 (wt. %)	FeO (wt. %)	MgO (wt. %)	CaO (wt. %)	Na_2O (wt. %)	K_2O (wt. %)	BaO (wt. %)	SrO (wt. %)	Total (wt. %)
LC-2004-50cb-c2-2	USPT	100.00	67.00	0.04	18.80	0.20	0.01	0.47	5.83	8.46	0.00	0.01	100.81
LC-2004-50cb-c2-3	USPT	200.00	66.88	0.04	18.85	0.22	0.00	0.42	5.74	8.59	0.00	0.00	100.73
LC-2004-50cb-c2-4	USPT	300.00	67.17	0.00	18.89	0.18	0.01	0.40	5.76	8.51	0.02	0.00	100.92
LC-2004-50cb-c2-5	USPT	400.00	66.85	0.00	19.00	0.22	0.01	0.54	6.13	7.98	0.01	0.01	100.74
LC-2004-50cb-c3-1	Pumice in USPT	0.00	62.64	0.02	23.14	0.25	0.01	5.25	7.15	1.77	0.12	0.12	100.45
LC-2004-50cb-c3-2	Pumice in USPT	100.00	61.61	0.02	23.53	0.22	0.01	5.94	6.86	1.96	0.00	0.06	100.20
LC-2004-50cb-c3-3	Pumice in USPT	200.00	61.88	0.00	23.25	0.15	0.00	5.45	7.39	1.54	0.13	0.20	99.99
LC-2004-50cb-c3-4	Pumice in USPT	300.00	61.91	0.02	22.89	0.19	0.00	5.14	7.41	1.48	0.09	0.27	99.40
LC-2004-50cb-c3-5	Pumice in USPT	400.00	60.32	0.01	24.42	0.23	0.01	6.73	6.95	1.07	0.10	0.14	99.98
LC-2004-50cb-c4-1	Pumice in USPT	0.00	59.06	0.03	25.20	0.42	0.03	7.65	6.54	0.90	0.08	0.22	100.14
LC-2004-50cb-c4-2	Pumice in USPT	100.00	58.92	0.00	24.93	0.42	0.01	7.42	6.47	1.11	0.04	0.19	99.51
LC-2004-50cb-c4-3	Pumice in USPT	200.00	59.29	0.02	24.98	0.39	0.02	7.45	6.49	1.06	0.00	0.17	99.86
LC-2004-50cb-c4-4	Pumice in USPT	300.00	59.50	0.05	24.84	0.42	0.03	7.21	6.65	1.20	0.08	0.17	100.13
LC-2004-50cb-c5-1	Pumice in USPT	0.00	48.78	0.01	36.65	0.38	0.04	6.86	5.09	0.44	0.04	0.20	98.48
LC-2004-50cb-c5-2	Pumice in USPT	100.00	59.26	0.00	25.06	0.35	0.02	7.60	6.59	1.05	0.11	0.21	100.25
LC-2004-50cb-c5-3	Pumice in USPT	200.00	59.28	0.02	24.79	0.37	0.00	7.35	6.57	1.07	0.03	0.19	99.65
LC-2004-50cb-c5-4	Pumice in USPT	300.00	59.30	0.06	25.15	0.35	0.03	7.74	6.44	1.04	0.00	0.14	100.24
LC-2004-50cb-c6-1	Pumice in USPT	0.00	59.03	0.03	25.27	0.31	0.01	7.89	5.43	0.80	0.03	0.18	98.99
LC-2004-50cb-c6-2	Pumice in USPT	100.00	59.82	0.02	24.52	0.33	0.02	7.03	7.03	0.86	0.08	0.21	99.92
LC-2004-50cb-c6-3	Pumice in USPT	200.00	59.60	0.04	24.57	0.33	0.01	7.07	6.06	0.76	0.00	0.18	98.60
LC-2004-50cb-c6-4	Pumice in USPT	300.00	57.72	0.00	25.80	0.29	0.02	8.67	6.20	0.63	0.02	0.14	99.48
LC-2004-50cb-c6-5	Pumice in USPT	400.00	59.59	0.00	24.83	0.31	0.02	7.22	6.66	0.99	0.06	0.17	99.84
LC-2004-50cb-c6-6	Pumice in USPT	500.00	57.26	0.06	26.37	0.33	0.02	8.85	5.99	0.70	0.03	0.16	99.78
LC-2004-52f-c1-1	Pumice in USPT	0.00	58.12	0.01	25.84	0.30	0.01	8.33	6.16	0.76	0.09	0.22	99.85
LC-2004-52f-c1-2	Pumice in USPT	100.00	58.13	0.03	25.97	0.37	0.02	8.50	6.21	0.72	0.06	0.19	100.20
LC-2004-52f-c1-3	Pumice in USPT	200.00	59.00	0.00	24.93	0.33	0.02	7.27	6.61	0.94	0.08	0.12	99.29
LC-2004-52f-c1-4	Pumice in USPT	300.00	58.69	0.00	25.11	0.36	0.02	7.75	6.44	0.86	0.08	0.23	99.53
LC-2004-52f-c1-5	Pumice in USPT	400.00	57.71	0.03	25.97	0.31	0.02	8.55	6.12	0.70	0.08	0.17	99.66
LC-2004-52f-c2-1	Pumice in USPT	0.00	58.92	0.03	25.53	0.32	0.01	7.95	6.39	0.90	0.05	0.18	100.29
LC-2004-52f-c2-2	Pumice in USPT	100.00	58.63	0.03	25.54	0.35	0.02	7.97	6.34	0.84	0.09	0.22	100.04
LC-2004-52f-c2-3	Pumice in USPT	200.00	57.87	0.01	26.09	0.33	0.02	8.44	6.21	0.78	0.09	0.14	99.97

Sample	Rock type	Approx. dist. from rim (mm)	SiO_2 (wt. %)	TiO_2 (wt. %)	Al_2O_3 (wt. %)	FeO (wt. %)	MgO (wt. %)	CaO (wt. %)	Na_2O (wt. %)	K_2O (wt. %)	BaO (wt. %)	SrO (wt. %)	Total (wt. %)
LC-2004-52f-c2-4	Pumice in USPT	300.00	57.62	0.02	26.04	0.33	0.01	8.43	6.02	0.83	0.08	0.21	99.60
LC-2004-52f-c2-5	Pumice in USPT	400.00	57.83	0.00	25.42	0.34	0.02	8.16	6.29	0.86	0.03	0.15	99.08
LC-2004-52f-c2-6	Pumice in USPT	500.00	57.78	0.05	25.88	0.29	0.01	8.39	6.19	0.74	0.00	0.18	99.49
LC-2004-52f-c3-1	Pumice in USPT	0.00	59.28	0.00	25.13	0.32	0.02	7.64	6.55	0.94	0.07	0.17	100.12
LC-2004-52f-c3-2	Pumice in USPT	100.00	59.23	0.00	25.05	0.34	0.02	7.60	6.53	0.91	0.05	0.19	99.91
LC-2004-52f-c3-3	Pumice in USPT	200.00	58.65	0.00	25.09	0.30	0.02	7.66	6.40	0.93	0.10	0.18	99.34
LC-2004-52f-c3-4	Pumice in USPT	300.00	58.77	0.00	25.57	0.34	0.01	7.92	6.41	0.85	0.13	0.20	100.19
LC-2004-52f-c4-1	Pumice in USPT	0.00	57.92	0.02	25.82	0.35	0.03	8.31	6.24	0.79	0.06	0.19	99.73
LC-2004-52f-c4-2	Pumice in USPT	100.00	57.29	0.03	26.35	0.32	0.03	8.93	5.97	0.72	0.00	0.19	99.83
LC-2004-52f-c4-3	Pumice in USPT	200.00	58.84	0.03	25.14	0.31	0.02	7.57	6.55	0.88	0.11	0.17	99.63
LC-2004-52f-c4-4	Pumice in USPT	300.00	59.00	0.02	25.39	0.29	0.02	7.65	6.78	0.49	0.14	0.21	99.98
LC-2004-52f-c5-1	Pumice in USPT	0.00	57.87	0.02	26.13	0.29	0.01	8.44	6.09	0.78	0.02	0.17	99.82
LC-2004-52f-c5-2	Pumice in USPT	100.00	57.15	0.03	26.50	0.32	0.03	9.13	5.88	0.67	0.05	0.18	99.94
LC-2004-52f-c5-3	Pumice in USPT	200.00	56.47	0.02	27.23	0.32	0.02	9.82	5.57	0.55	0.02	0.15	100.17
LC-2004-52f-c5-4	Pumice in USPT	300.00	57.76	0.02	25.92	0.32	0.02	8.60	6.09	0.74	0.06	0.18	99.70
LC-2004-52f-c5-5	Pumice in USPT	400.00	57.95	0.00	26.03	0.32	0.02	8.50	6.13	0.82	0.07	0.20	100.04
LC-2004-52f-c5-6	Pumice in USPT	500.00	57.45	0.02	26.34	0.30	0.02	8.92	5.92	0.71	0.05	0.21	99.93
LC-2004-52f-c5-7	Pumice in USPT	600.00	57.76	0.03	26.23	0.27	0.02	8.68	5.98	0.73	0.02	0.15	99.85
LC-2004-52f-c5-8	Pumice in USPT	700.00	57.70	0.02	26.12	0.32	0.01	8.83	6.07	0.75	0.08	0.15	100.06
LC-2004-52f-c6-1	Pumice in USPT	0.00	57.10	0.01	26.13	0.42	0.06	8.82	6.04	0.64	0.05	0.20	99.47
LC-2004-52f-c6-2	Pumice in USPT	100.00	57.75	0.02	25.95	0.27	0.03	8.59	6.02	0.83	0.05	0.18	99.67
LC-2004-52f-c6-3	Pumice in USPT	200.00	57.00	0.02	26.29	0.33	0.01	8.88	5.83	0.72	0.10	0.19	99.36
LC-2004-52f-c6-4	Pumice in USPT	300.00	57.18	0.00	26.15	0.31	0.02	8.87	6.11	0.71	0.04	0.17	99.56
LC-2004-52f-c6-5	Pumice in USPT	400.00	57.55	0.00	25.59	0.29	0.01	8.30	6.19	0.78	0.04	0.16	98.90
LC-2004-52f-c6-6	Pumice in USPT	500.00	58.03	0.02	25.88	0.32	0.02	8.41	6.23	0.80	0.00	0.16	99.85
LC-2004-52f-c6-7	Pumice in USPT	600.00	57.73	0.02	26.07	0.32	0.02	8.54	6.01	0.73	0.06	0.17	99.67
LC-2004-52f-c7-1	Pumice in USPT	0.00	57.52	0.03	25.87	0.32	0.01	8.48	6.19	0.69	0.05	0.18	99.34
LC-2004-52f-c7-2	Pumice in USPT	100.00	56.70	0.00	26.55	0.33	0.02	9.18	5.88	0.58	0.04	0.19	99.47
LC-2004-52f-c7-3	Pumice in USPT	200.00	56.04	0.01	27.19	0.31	0.02	9.89	5.48	0.50	0.09	0.20	99.73
LC-2004-52f-c7-4	Pumice in USPT	300.00	55.07	0.01	27.83	0.33	0.01	10.50	5.18	0.45	0.01	0.15	99.54
LC-2004-52f-c7-5	Pumice in USPT	400.00	57.27	0.02	25.80	0.28	0.02	8.35	6.01	0.83	0.05	0.12	98.75

Sample	Rock type	Approx. dist. from rim (mm)	SiO_2 (wt. %)	TiO_2 (wt. %)	Al_2O_3 (wt. %)	FeO (wt. %)	MgO (wt. %)	CaO (wt. %)	Na_2O (wt. %)	K_2O (wt. %)	BaO (wt. %)	SrO (wt. %)	Total (wt. %)
LC-2004-52f-c8-1	Pumice in USPT	0.00	57.31	0.01	26.20	0.32	0.00	8.72	6.01	0.72	0.04	0.20	99.53
LC-2004-52f-c8-2	Pumice in USPT	100.00	58.11	0.01	24.99	0.33	0.01	7.60	6.45	0.87	0.03	0.14	98.54
LC-2004-52f-c8-3	Pumice in USPT	200.00	56.53	0.02	26.28	0.33	0.02	8.95	5.89	0.70	0.00	0.14	98.85
LC-2004-52f-c8-4	Pumice in USPT	300.00	57.85	0.04	25.47	0.34	0.01	8.05	6.27	0.87	0.04	0.21	99.15
LC-2004-52f-c8-5	Pumice in USPT	400.00	59.33	0.02	24.63	0.34	0.03	7.11	6.76	0.95	0.10	0.20	99.47
LC-2004-52f-c8-6	Pumice in USPT	500.00	58.26	0.04	26.06	0.36	0.02	8.43	6.20	0.79	0.07	0.19	100.42
LC-2004-52f-c9-1	Pumice in USPT	0.00	57.35	0.03	25.77	0.35	0.02	8.61	5.98	0.72	0.09	0.21	99.12
LC-2004-52f-c9-2	Pumice in USPT	100.00	58.54	0.00	25.50	0.32	0.01	8.23	6.39	0.85	0.12	0.19	100.15
LC-2004-52f-c9-3	Pumice in USPT	200.00	58.09	0.04	25.52	0.33	0.02	8.20	6.34	0.82	0.08	0.24	99.67
LC-2004-52f-c9-4	Pumice in USPT	300.00	57.40	0.03	26.08	0.32	0.03	8.84	5.95	0.71	0.03	0.18	99.56
LC-2004-52f-c9-5	Pumice in USPT	400.00	58.83	0.05	25.01	0.35	0.01	7.66	6.50	0.98	0.12	0.19	99.70
LC-2004-52f-c9-6	Pumice in USPT	500.00	57.49	0.06	26.03	0.33	0.03	8.76	5.98	0.76	0.05	0.18	99.66
LC-81-c1-1	Rhyolite dyke	0.00	65.64	0.01	18.77	0.18	0.00	0.50	5.82	8.27	0.00	0.00	99.21
LC-81-c1-2	Rhyolite dyke	100.00	66.06	0.02	18.71	0.17	0.00	0.40	5.71	8.73	0.02	0.01	99.83
LC-81-c1-3	Rhyolite dyke	200.00	66.37	0.00	18.73	0.16	0.00	0.44	5.93	8.04	0.00	0.00	99.66
LC-81-c1-4	Rhyolite dyke	300.00	65.95	0.02	18.72	0.20	0.00	0.37	5.61	8.35	0.00	0.04	99.25
LC-81-c1-5	Rhyolite dyke	400.00	66.63	0.01	18.71	0.21	0.00	0.44	5.84	8.33	0.02	0.04	100.22
LC-81-c2-1	Rhyolite dyke	0.00	65.57	0.01	18.61	0.18	0.00	0.28	5.33	9.10	0.04	0.00	99.11
LC-81-c2-2	Rhyolite dyke	100.00	66.06	0.02	18.79	0.21	0.00	0.42	5.62	8.63	0.00	0.02	99.75
LC-81-c2-3	Rhyolite dyke	200.00	66.35	0.02	18.73	0.13	0.00	0.34	5.53	8.98	0.00	0.02	100.09
LC-81-c2-4	Rhyolite dyke	300.00	66.58	0.00	18.76	0.21	0.00	0.41	5.82	8.46	0.06	0.00	100.30
LC-81-c2-5	Rhyolite dyke	400.00	66.59	0.03	19.32	0.06	0.00	0.19	6.34	7.77	0.00	0.00	100.29
LC-81-c3-1	Rhyolite dyke	0.00	65.53	0.01	18.86	0.18	0.00	0.54	5.68	8.36	0.00	0.03	99.17
LC-81-c3-2	Rhyolite dyke	100.00	66.19	0.00	18.55	0.20	0.00	0.39	5.70	8.64	0.00	0.03	99.71
LC-81-c3-3	Rhyolite dyke	200.00	65.91	0.02	18.77	0.19	0.00	0.45	5.68	8.41	0.00	0.01	99.44
LC-81-c3-4	Rhyolite dyke	300.00	65.93	0.01	18.81	0.19	0.00	0.42	5.78	8.35	0.00	0.01	99.48
LC-81-c3-5	Rhyolite dyke	400.00	66.06	0.05	18.89	0.20	0.00	0.60	6.22	7.59	0.00	0.00	99.60
LC-100-c1-1	Syenite	0.00	65.24	0.03	18.73	0.19	0.00	0.55	5.12	9.36	0.03	0.01	99.25
LC-100-c1-2	Syenite	100.00	64.74	0.05	18.86	0.17	0.00	0.60	5.14	9.14	0.04	0.00	98.74
LC-100-c1-3	Syenite	200.00	65.66	0.05	18.62	0.23	0.01	0.38	4.84	9.77	0.05	0.00	99.61
LC-100-c1-4	Syenite	300.00	64.58	0.01	18.88	0.20	0.00	0.61	5.26	9.07	0.01	0.00	98.62

Sample	Rock type	Approx. dist. from rim (mm)	SiO_2 (wt. %)	TiO_2 (wt. %)	Al_2O_3 (wt. %)	FeO (wt. %)	MgO (wt. %)	CaO (wt. %)	Na_2O (wt. %)	K_2O (wt. %)	BaO (wt. %)	SrO (wt. %)	Total (wt. %)
LC-100-c1-5	Syenite	400.00	62.89	0.00	18.17	0.20	0.00	0.45	4.67	9.01	0.08	0.01	95.48
LC-100-c1-6	Syenite	500.00	64.58	0.03	18.71	0.20	0.00	0.46	5.06	9.41	0.00	0.03	98.47
LC-100-c2-1	Syenite	0.00	65.35	0.01	18.75	0.22	0.00	0.40	4.87	9.82	0.04	0.03	99.50
LC-100-c2-2	Syenite	100.00	64.19	0.02	18.79	0.21	0.00	0.47	5.10	9.64	0.01	0.04	98.47
LC-100-c2-3	Syenite	200.00	65.34	0.04	18.71	0.17	0.00	0.50	4.98	9.63	0.04	0.04	99.45
LC-100-c2-4	Syenite	300.00	65.06	0.05	18.82	0.17	0.00	0.45	5.03	9.55	0.04	0.02	99.18
LC-100-c3-1	Syenite	0.00	65.58	0.00	18.60	0.15	0.01	0.42	4.91	9.89	0.01	0.03	99.60
LC-100-c3-2	Syenite	100.00	65.43	0.00	18.87	0.20	0.01	0.50	5.20	9.24	0.00	0.00	99.45
LC-100-c3-3	Syenite	200.00	65.25	0.00	18.84	0.18	0.01	0.47	5.10	9.49	0.02	0.00	99.36
LC-100-c3-4	Syenite	300.00	65.60	0.04	18.90	0.22	0.00	0.64	5.51	8.65	0.00	0.04	99.60
LC-100-c3-5	Syenite	400.00	65.63	0.02	18.85	0.20	0.01	0.52	5.12	9.35	0.03	0.03	99.75
LC-2004-17C-c1-1	Syenite	0.00	66.35	0.02	18.82	0.17	0.01	0.42	5.11	9.45	0.18	0.04	100.56
LC-2004-17C-c1-2	Syenite	100.00	66.27	0.04	18.76	0.18	0.00	0.45	4.91	9.48	0.01	0.01	100.11
LC-2004-17C-c1-3	Syenite	200.00	66.26	0.01	18.74	0.17	0.00	0.50	4.84	9.56	0.02	0.00	100.10
LC-2004-17C-c1-4	Syenite	300.00	66.55	0.04	18.68	0.16	0.01	0.45	5.08	9.52	0.03	0.00	100.52
LC-2004-17C-c2-1	Syenite	0.00	66.08	0.03	18.83	0.22	0.01	0.41	5.01	9.46	0.10	0.02	100.17
LC-2004-17C-c2-2	Syenite	100.00	65.78	0.06	19.44	0.23	0.00	1.05	5.88	7.62	0.10	0.05	100.21
LC-2004-17C-c2-3	Syenite	200.00	65.26	0.05	19.35	0.21	0.00	1.03	5.90	7.55	0.17	0.08	99.59
LC-2004-17C-c2-4	Syenite	300.00	65.53	0.07	19.73	0.23	0.00	1.34	6.29	6.54	0.28	0.04	100.02
LC-2004-17C-c2-5	Syenite	400.00	63.49	0.11	22.35	0.31	0.00	3.96	8.45	1.33	0.08	0.10	100.17
LC-2004-17C-c2-6	Syenite	500.00	63.76	0.08	21.53	0.29	0.00	3.13	7.50	3.35	0.12	0.09	99.85
LC-2004-17C-c2-7	Syenite	600.00	57.02	0.12	26.68	0.36	0.01	8.76	6.11	0.72	0.11	0.29	100.18
LC-2004-17C-c3-1	Syenite	0.00	59.78	0.07	24.26	0.42	0.01	6.51	7.56	0.59	0.18	0.12	99.50
LC-2004-17C-c3-2	Syenite	100.00	56.11	0.07	27.36	0.37	0.01	9.56	5.74	0.36	0.09	0.35	100.01
LC-2004-17C-c3-3	Syenite	200.00	56.79	0.09	26.14	0.49	0.01	8.57	6.26	0.42	0.22	0.35	99.34
LC-2004-17C-c3-4	Syenite	300.00	56.04	0.07	26.50	0.37	0.00	9.06	5.98	0.40	0.09	0.27	98.77
LC-2004-17C-c3-5	Syenite	400.00	56.28	0.06	26.92	0.47	0.00	9.17	6.02	0.33	0.05	0.26	99.55
LC-2004-17C-c4-1	Syenite	0.00	66.05	0.00	19.17	0.17	0.00	0.92	6.03	7.69	0.02	0.04	100.09
LC-2004-17C-c4-2	Syenite	100.00	65.88	0.05	18.51	0.19	0.01	0.44	4.90	9.63	0.05	0.00	99.65
LC-2004-17C-c4-3	Syenite	200.00	66.22	0.02	18.50	0.18	0.01	0.42	4.85	9.73	0.05	0.00	99.98
LC-2004-17C-c5-1	Syenite	0.00	66.55	0.00	18.63	0.15	0.00	0.44	5.01	9.53	0.04	0.03	100.37

Sample	Rock type	Approx. dist. from rim (mm)	SiO_2 (wt. %)	TiO_2 (wt. %)	Al_2O_3 (wt. %)	FeO (wt. %)	MgO (wt. %)	CaO (wt. %)	Na_2O (wt. %)	K_2O (wt. %)	BaO (wt. %)	SrO (wt. %)	Total (wt. %)
LC-2004-17C-c5-2	Syenite	100.00	66.45	0.03	18.53	0.17	0.01	0.42	4.87	9.82	0.00	0.00	100.29
LC-2004-17C-c5-3	Syenite	200.00	66.15	0.00	18.55	0.16	0.01	0.45	4.44	10.00	0.00	0.00	99.74
LC-2004-17C-c5-4	Syenite	300.00	66.44	0.03	18.71	0.21	0.00	0.50	5.11	9.41	0.01	0.02	100.44
LC-2004-17C-c5-5	Syenite	400.00	66.58	0.04	18.80	0.21	0.00	0.48	4.97	9.37	0.02	0.00	100.46
LC-2004-17C-c6-1	Syenite	0.00	66.59	0.02	18.94	0.22	0.00	0.53	5.47	8.64	0.12	0.05	100.57
LC-2004-17C-c6-2	Syenite	100.00	66.56	0.03	18.74	0.16	0.00	0.37	4.93	9.60	0.09	0.04	100.52
LC-2004-17C-c6-3	Syenite	200.00	66.68	0.03	18.73	0.19	0.00	0.43	4.93	9.76	0.02	0.03	100.79
LC-2004-17C-c6-4	Syenite	300.00	66.28	0.00	18.70	0.23	0.00	0.53	4.96	9.40	0.01	0.00	100.12
LC-2004-17C-c6-5	Syenite	400.00	66.36	0.04	18.66	0.17	0.00	0.43	4.85	9.62	0.00	0.01	100.14
LC-31-c1-1	Monzonite	0.00	61.98	0.02	23.15	0.29	0.03	5.07	7.91	1.05	0.07	0.12	99.68
LC-31-c1-2	Monzonite	100.00	62.39	0.01	23.13	0.31	0.01	4.93	7.91	1.32	0.07	0.12	100.21
LC-31-c1-3	Monzonite	200.00	61.87	0.05	22.64	0.30	0.01	4.87	7.95	1.41	0.00	0.13	99.23
LC-31-c1-4	Monzonite	300.00	61.78	0.04	22.33	0.26	0.01	4.36	6.12	4.51	0.15	0.09	99.65
LC-31-c2-1	Monzonite	0.00	65.59	0.07	18.87	0.13	0.00	0.40	4.13	10.56	0.47	0.14	100.36
LC-31-c2-2	Monzonite	100.00	65.32	0.09	18.84	0.18	0.00	0.43	4.40	10.12	0.57	0.12	100.07
LC-31-c2-3	Monzonite	200.00	65.88	0.01	18.80	0.18	0.00	0.42	4.52	10.05	0.51	0.07	100.43
LC-31-c2-4	Monzonite	300.00	65.85	0.02	18.42	0.17	0.00	0.14	4.07	11.19	0.34	0.06	100.26
LC-31-c2-5	Monzonite	400.00	65.24	0.06	18.83	0.10	0.00	0.43	4.40	10.30	0.62	0.10	100.09
LC-31-c3-1	Monzonite	0.00	61.52	0.01	23.22	0.29	0.02	5.00	7.88	1.13	0.08	0.15	99.30
LC-31-c3-2	Monzonite	100.00	61.69	0.01	22.98	0.31	0.01	5.00	7.93	1.30	0.09	0.13	99.44
LC-31-c3-3	Monzonite	200.00	59.13	0.06	24.90	0.30	0.01	7.03	6.95	0.78	0.02	0.15	99.33
LC-31-c3-4	Monzonite	300.00	56.68	0.08	27.03	0.27	0.02	9.31	5.83	0.52	0.09	0.24	100.06
LC-31-c4-1	Monzonite	0.00	62.01	0.00	23.21	0.29	0.02	4.95	8.19	1.01	0.00	0.10	99.76
LC-31-c4-2	Monzonite	100.00	62.02	0.05	23.15	0.27	0.02	5.15	7.96	1.18	0.06	0.10	99.93
LC-31-c4-3	Monzonite	200.00	61.57	0.04	22.59	0.31	0.01	4.98	7.95	1.41	0.02	0.08	98.96
LC-31-c4-4	Monzonite	300.00	62.13	0.03	23.12	0.29	0.02	5.09	7.74	1.36	0.05	0.14	99.97
LC-31-c5-1	Monzonite	0.00	65.38	0.05	18.47	0.20	0.01	0.22	4.08	11.02	0.39	0.07	99.89
LC-31-c5-2	Monzonite	100.00	65.43	0.09	18.78	0.21	0.01	0.31	4.22	10.73	0.48	0.08	100.33
LC-31-c5-3	Monzonite	200.00	65.26	0.05	18.92	0.18	0.00	0.44	4.32	10.43	0.56	0.08	100.22
LC-31-c5-4	Monzonite	300.00	62.79	0.04	22.97	0.28	0.00	4.75	8.58	0.52	0.03	0.10	100.05
LC-31-c5-5	Monzonite	400.00	62.57	0.01	22.71	0.26	0.02	4.67	8.32	0.86	0.08	0.09	99.59

Sample	Rock type	Approx. dist. from rim (mm)	SiO_2 (wt. %)	TiO_2 (wt. %)	Al_2O_3 (wt. %)	FeO (wt. %)	MgO (wt. %)	CaO (wt. %)	Na_2O (wt. %)	K_2O (wt. %)	BaO (wt. %)	SrO (wt. %)	Total (wt. %)
LC-31-c5-6	Monzonite	500.00	61.95	0.03	22.60	0.28	0.01	4.74	8.38	0.95	0.00	0.14	99.07
LC-31-c5-7	Monzonite	600.00	62.49	0.03	22.87	0.31	0.01	4.84	8.48	0.80	0.02	0.08	99.94
LC-31-c5-8	Monzonite	700.00	65.22	0.06	18.59	0.19	0.01	0.44	4.22	10.23	0.51	0.14	99.60
LC-94-C2-1	Monzonite	0.00	98.94	0.01	0.04	0.03	0.00	0.00	0.01	0.02	0.03	0.00	99.08
LC-94-C2-2	Monzonite	100.00	62.48	0.02	22.91	0.28	0.00	4.79	8.12	1.06	0.07	0.10	99.83
LC-94-C2-3	Monzonite	200.00	62.19	0.03	23.09	0.32	0.01	4.82	7.78	1.37	0.07	0.14	99.82
LC-94-C2-4	Monzonite	300.00	62.06	0.00	23.22	0.30	0.01	5.16	7.81	1.12	0.07	0.14	99.88
LC-94-C2-5	Monzonite	400.00	56.52	0.05	26.73	0.22	0.02	9.25	5.94	0.45	0.05	0.12	99.35
LC-94-c3-1	Monzonite	0.00	63.66	0.00	22.31	0.26	0.01	4.15	8.59	0.89	0.01	0.09	99.97
LC-94-c3-2	Monzonite	100.00	62.31	0.04	22.93	0.24	0.00	5.00	8.01	1.22	0.00	0.13	99.88
LC-94-c3-3	Monzonite	200.00	62.42	0.00	23.02	0.29	0.01	4.91	7.89	1.15	0.07	0.09	99.85
LC-94-c3-4	Monzonite	300.00	62.03	0.04	23.10	0.29	0.01	5.03	7.86	1.19	0.00	0.09	99.64
LC-94-c4-1	Monzonite	0.00	64.08	0.01	22.29	0.27	0.02	3.84	8.77	0.97	0.04	0.11	100.39
LC-94-c4-2	Monzonite	100.00	62.36	0.04	22.97	0.29	0.01	4.92	7.76	1.37	0.02	0.09	99.83
LC-94-c4-3	Monzonite	200.00	62.68	0.00	22.81	0.30	0.02	4.85	7.72	1.48	0.04	0.11	100.01
LC-94-c4-4	Monzonite	300.00	62.63	0.04	22.94	0.30	0.01	4.84	7.73	1.45	0.06	0.13	100.12
LC-94-c5-1	Monzonite	0.00	63.21	0.04	22.39	0.30	0.00	4.45	8.43	0.83	0.00	0.12	99.78
LC-94-c5-2	Monzonite	100.00	62.28	0.04	23.16	0.28	0.01	5.23	7.96	0.95	0.03	0.12	100.06
LC-94-c5-3	Monzonite	200.00	62.49	0.05	22.91	0.28	0.01	4.85	7.99	1.18	0.03	0.11	99.89
LC-94-c5-4	Monzonite	300.00	60.79	0.03	24.23	0.30	0.01	6.20	7.47	0.83	0.03	0.13	100.03
LC-2004-52cb-c1-1	Dacite	0.00	58.46	0.06	25.67	0.27	0.02	8.07	6.40	0.76	0.07	0.19	99.96
LC-2004-52cb-c1-2	Dacite	100.00	55.59	0.16	27.07	0.54	0.44	9.57	5.50	0.76	0.05	0.26	99.92
LC-2004-52cb-c1-3	Dacite	200.00	55.34	0.04	27.66	0.29	0.01	10.23	5.15	0.44	0.05	0.29	99.49
LC-2004-52cb-c1-4	Dacite	300.00	55.48	0.04	27.72	0.28	0.01	10.00	5.42	0.47	0.08	0.21	99.72
LC-2004-52cb-c2-1	Dacite	0.00	62.46	0.02	22.74	0.30	0.01	4.72	7.93	1.25	0.11	0.17	99.71
LC-2004-52cb-c2-2	Dacite	100.00	60.51	0.04	24.19	0.28	0.01	6.37	7.05	1.12	0.12	0.14	99.82
LC-2004-52cb-c2-3	Dacite	200.00	58.74	0.04	25.54	0.29	0.00	7.71	6.43	0.80	0.09	0.17	99.82
LC-2004-52cb-c2-4	Dacite	300.00	58.22	0.05	25.63	0.29	0.02	8.10	6.25	0.75	0.11	0.20	99.62
LC-2004-52ca-c1-1	Dacite	0.00	56.93	0.09	26.51	0.27	0.00	8.70	6.19	0.62	0.12	0.21	99.62
LC-2004-52ca-c1-2	Dacite	100.00	55.56	0.09	27.23	0.30	0.03	9.60	5.72	0.49	0.05	0.27	99.35
LC-2004-52ca-c1-3	Dacite	200.00	54.52	0.12	28.23	0.30	0.02	10.59	5.21	0.42	0.03	0.26	99.70

Sample	Rock type	Approx. dist. from rim (mm)	SiO_2 (wt. %)	TiO_2 (wt. %)	Al_2O_3 (wt. %)	FeO (wt. %)	MgO (wt. %)	CaO (wt. %)	Na_2O (wt. %)	K_2O (wt. %)	BaO (wt. %)	SrO (wt. %)	Total (wt. %)
LC-2004-52ca-c1-4	Dacite	300.00	55.12	0.13	27.64	0.36	0.02	10.03	5.42	0.46	0.04	0.27	99.47
LC-2004-52ca-c1-5	Dacite	400.00	54.43	0.08	27.93	0.33	0.02	10.23	5.17	0.43	0.07	0.25	98.91
LC-2004-52ca-c1-6	Dacite	500.00	55.10	0.05	27.68	0.29	0.01	10.00	5.42	0.48	0.12	0.27	99.41
LC-2004-52ca-c2-1	Dacite	0.00	63.45	0.00	22.61	0.27	0.01	4.29	8.26	1.21	0.01	0.05	100.15
LC-2004-52ca-c2-2	Dacite	100.00	62.38	0.01	23.17	0.29	0.01	4.87	7.69	1.51	0.00	0.16	100.07
LC-2004-52ca-c2-3	Dacite	200.00	62.43	0.02	23.49	0.31	0.02	5.21	7.80	1.12	0.04	0.12	100.55
LC-2004-52ca-c2-4	Dacite	300.00	60.41	0.01	24.48	0.27	0.01	6.40	7.27	0.98	0.01	0.11	99.95
LC-2004-52ca-c2-5	Dacite	400.00	62.60	0.05	22.94	0.29	0.01	4.96	7.70	1.46	0.03	0.11	100.15
LC-2004-52ca-c3-1	Dacite	0.00	61.43	0.00	23.18	0.32	0.01	4.81	8.03	1.15	0.02	0.14	99.08
LC-2004-52ca-c3-2	Dacite	100.00	62.40	0.04	22.80	0.31	0.01	4.54	7.82	1.62	0.04	0.16	99.73
LC-2004-52ca-c3-3	Dacite	200.00	61.82	0.02	23.24	0.30	0.04	4.71	8.30	0.87	0.05	0.08	99.44
LC-2004-52ca-c3-4	Dacite	300.00	58.33	0.05	26.19	0.27	0.03	8.33	6.31	0.72	0.06	0.15	100.42
LC-2004-52ca-c3-5	Dacite	400.00	58.76	0.04	25.33	0.26	0.00	7.27	6.81	0.72	0.01	0.14	99.35
LC-2004-52ca-c3-6	Dacite	500.00	63.05	0.03	23.57	0.29	0.01	4.86	8.09	1.10	0.05	0.11	101.14
LC-2004-52ca-c4-1	Dacite	0.00	62.04	0.01	23.08	0.33	0.01	4.82	7.81	1.32	0.07	0.13	99.60
LC-2004-52ca-c4-2	Dacite	100.00	61.98	0.05	23.01	0.35	0.02	4.71	7.94	1.30	0.04	0.13	99.53
LC-2004-52ca-c4-3	Dacite	200.00	60.91	0.00	23.85	0.32	0.01	5.53	7.66	1.07	0.06	0.12	99.52
LC-2004-52ca-c4-4	Dacite	300.00	60.59	0.02	24.24	0.29	0.02	6.07	7.23	1.12	0.09	0.12	99.78
LC-2004-52ca-c4-5	Dacite	400.00	57.87	0.07	25.39	0.32	0.00	7.59	6.55	0.78	0.06	0.13	98.76
LC-2004-52ca-c4-6	Dacite	500.00	57.74	0.01	25.53	0.26	0.00	7.40	6.52	0.78	0.07	0.16	98.48
LC-2004-52ca-c5-1	Mafic enclave in dacite	0.00	62.19	0.03	23.09	0.33	0.03	4.70	7.64	1.64	0.03	0.20	99.89
LC-2004-52ca-c5-2	Mafic enclave in dacite	100.00	61.35	0.03	23.45	0.30	0.01	5.33	7.49	1.47	0.07	0.15	99.64
LC-2004-52ca-c5-3	Mafic enclave in dacite	200.00	58.73	0.01	25.61	0.27	0.01	7.65	6.63	0.83	0.12	0.24	100.11
LC-2004-52ca-c5-4	Mafic enclave in dacite	300.00	55.98	0.07	27.09	0.31	0.01	9.10	5.72	0.53	0.07	0.24	99.12
LC-2004-52ca-c5-5	Mafic enclave in dacite	400.00	56.42	0.03	27.00	0.27	0.01	9.27	5.81	0.55	0.05	0.32	99.74
LC-2004-52ca-c5-6	Mafic enclave in dacite	500.00	59.41	0.03	24.99	0.29	0.01	6.81	6.91	0.90	0.09	0.23	99.67
LC-2004-52ca-c5-7	Mafic enclave in dacite	600.00	56.85	0.06	26.60	0.26	0.02	8.69	6.09	0.63	0.08	0.23	99.50
LC-2004-52ca-c6-1	Mafic enclave in dacite	0.00	62.38	0.05	22.78	0.35	0.08	4.53	8.08	1.06	0.06	0.11	99.48
LC-2004-52ca-c6-2	Mafic enclave in dacite	100.00	61.91	0.02	23.31	0.29	0.01	4.96	7.72	1.35	0.08	0.16	99.82
LC-2004-52ca-c6-3	Mafic enclave in dacite	200.00	61.70	0.05	23.45	0.29	0.02	5.70	7.48	1.12	0.01	0.12	99.91
LC-2004-52ca-c6-4	Mafic enclave in dacite	300.00	60.71	0.00	23.24	0.31	0.02	5.10	7.80	1.30	0.07	0.16	98.70
LC-2004-52ca-c6-5	Mafic enclave in dacite	400.00	60.27	0.03	24.08	0.25	0.01	5.78	7.27	1.14	0.03	0.17	99.04
LC-2004-52ca-c6-6	Mafic enclave in dacite	500.00	55.47	0.00	27.49	0.27	0.01	9.71	5.50	0.47	0.04	0.18	99.13

Measurement Conditions for microprobe

WDS elements

Element	X-ray	Crystal	CH	Acc.v	Peak Pos. (Angstrom)	BG_L	BG_U (mm)
1 Na	Ka	TAP	(1)	15.0	129.466	11.91010	5.000 6.000
2 Mg	Ka	TAP	(2)	15.0	107.471	9.89000	5.000 4.000
3 K	Ka	PETJ	(3)	15.0	120.005	3.74140	5.000 6.000
4 Sr	La	PETJ	(4)	15.0	219.936	6.86280	2.200 3.000
5 Fe	Ka	LIFH	(5)	15.0	134.814	1.93604	5.000 5.000
6 Si	Ka	TAP	(1)	15.0	77.363	7.12542	7.000 7.000
7 Al	Ka	TAP	(2)	15.0	90.551	8.33934	5.000 5.000
8 Ca	Ka	PETJ	(3)	15.0	107.755	3.35839	5.000 4.000
9 Ba	La	LIFH	(5)	15.0	193.073	2.77595	2.400 3.000

Element	Peak	Back	Pksk	Gain	High.V	Base.L	Window.W	Mode
1 Na	20.0	10.0 (sec)	1	8	1702	0.2	9.3 (V)	Dif
2 Mg	20.0	10.0 (sec)	1	16	1702	0.2	- (V)	Int
3 K	20.0	10.0 (sec)	1	16	1684	0.2	- (V)	Int
4 Sr	30.0	15.0 (sec)	0	16	1676	0.2	- (V)	Int
5 Fe	20.0	10.0 (sec)	1	16	1698	0.2	- (V)	Int
6 Si	20.0	10.0 (sec)	1	8	1702	0.2	- (V)	Int
7 Al	20.0	10.0 (sec)	1	16	1702	0.2	- (V)	Int
8 Ca	20.0	10.0 (sec)	1	16	1684	0.2	3.0 (V)	Dif
9 Ba	20.0	10.0 (sec)	1	16	1698	0.2	- (V)	Int

Measurement Order of WDS

Order	Channel 1	2	3	4	5
1	Na	Mg	K	Sr	Fe
2	Si	Al	Ca	-	Ba

Calc. Elements : O (Anion)

Element	Standard name	Wt.(%)	ZAF Fac.	Z	A	F
1 Na2O	albite	11.4300	5.4858	10.7252	0.5094	1.0041
2 MgO	Diopside	17.9400	4.7341	7.8691	0.5985	1.0051
3 K2O	Orthoclase	16.9100	1.0758	1.2033	0.8940	1.0001
4 SrO	Sr-Feld	3.6300	2.8860	4.0306	0.7157	1.0004
5 FeO	Fe2O3m	89.9830	0.2140	0.2170	0.9864	1.0000
6 SiO2	Orthoclase	65.0300	3.2797	4.4186	0.7415	1.0011
7 Al2O3	Orthoclase	16.9800	4.3209	5.8692	0.7244	1.0163
8 CaO	Diopside	25.1800	0.8662	0.9351	0.9261	1.0002
9 BaO	Ba-Orth	4.0860	0.4646	0.4970	0.9348	1.0000

Standard Intensity of WDS

Element	Curr.(A)	Net(cps)	Bg-(cps)	Bg+(cps)	S.D.(%)	Date
1 Na	2.004E-08	1151.2	10.6	8.2	1.41	Feb 5 09:44 2004
2 Mg	2.001E-08	2600.3	14.2	10.9	0.66	Feb 5 09:31 2004
3 K	1.996E-08	1967.9	11.7	9.4	0.88	Feb 5 09:50 2004
4 Sr	2.009E-08	65.1	4.5	3.3	4.14	Feb 5 09:21 2004
5 Fe	2.008E-08	9852.6	53.6	51.1	0.34	Feb 5 09:12 2004
6 Si	1.996E-08	13057.3	51.2	46.7	0.34	Feb 5 09:50 2004
7 Al	1.996E-08	3448.7	28.1	18.4	0.81	Feb 5 09:50 2004
8 Ca	2.001E-08	2842.7	17.7	15.0	0.63	Feb 5 09:31 2004
9 Ba	2.007E-08	115.9	9.9	9.2	3.37	Feb 5 09:26 2004

UNK No. : 1

APPENDIX II

TABLE A-II. Fractional crystallization modeling.

Fractional crystallization from removal of accessory phases

Basic equation: Cl=Co*F^(D'-1)
where D' is the bulk distribution coefficient

Mineral-melt partition coefficients from Hanson, Mahood and Hildreth, and Troll

D=partition coefficient for a given mineral and element

wt frac=weight fraction of a mineral which is crystallizing
(i.e., wt frac of 0.01 is 1%, wt frac of 0.001 is 0.1 %, etc.)

bulk D=overall bulk distribution coefficient

Co=concentration of parent composition
Cl=concentration of daughter composition

F=amount of crystallization (F=1 means no crystallization, F=0 means 100% crystallization, i.e., all is solidified)

Table X Accessory phase crystallization to produce rhyolite from trachyte

Element	D chevkinite	D sphene	D zircon	wt. % frac chevkinite	wt frac sphene	wt frac zircon	bulk D	parent trachyte liquid	fraction magma crystallized	daughter rhyolite liquid	rhyolite (liquid)	Element
							D'	Co	F	Cl		
La	988	28	17	0.0017	0.015	0	2.1098	108	0.55	56	52	La
Ce	806	70	17	0.0017	0.015	0	2.4304	225	0.55	96	93	Ce
Sm	392	102	14	0.0017	0.015	0	2.2048	17.5	0.55	8.52	5.30	Sm
Eu	225	101	16	0.0017	0.015	0	1.9071	1.98	0.55	1.15	0.34	Eu
Gd	142	102		0.0017	0.015	0	1.7714		0.55	0	7.3	Gd
Dy	72	81	102	0.0017	0.015	0	1.3986		0.55	0	4.2	Dy
Y	74	99	224	0.0017	0.015	0	1.7452	44	0.55	28	25	Y
Yb	50	37.4	527	0.0017	0.015	0	0.9622	4.00	0.55	4.09	3.4	Yb
Lu	20	37.4	642	0.0017	0.015	0	0.9802	0.55	0.55	0.56	0.52	Lu
Th	100		76.8	0.0017	0.015	0	0.21608	30.5	0.55	49	46	Th
Rb				0.0017	0.015	0	0	170	0.55	309	300	Rb
Cs				0.0017	0.015	0	0	1.85	0.55	3.36	6.00	Cs
Hf			10000	0.0017	0.015	0	6	12	0.55	1	6.7	Hf
Nb	15	45	48	0.0017	0.015	0	0.7293	65	0.55	76	63	Nb
Ta	15	45	48	0.0017	0.015	0	0.7293	5	0.55	6	5.5	Ta

Partition coefficients from Hanson (1980), Mahood and Hildreth (1983), and Troll et al. (2003)

Mass balance check with zircon:

470 ppm Zr in trachyte
170 ppm Zr in rhyolite

497644 ppm Zr in zircon

Zr in trachyte - Zr in zircon = Zr in rhyolite

or

Zr in trachyte = Zr in rhyolite + Zr in zircon

Zr in rhyolite	Mass frac rhyolite	Zr in zircon	Mass frac zircon	**Zr in trachyte**
170	0.999	497644	0.0006	468.4844

CHAPTER 3

Disruption of magmatic stratification during caldera collapse: evidence from analogue models

Ben Kennedy, John Stix and Richard Breger

ABSTRACT

We present the first scaled analogue models representing caldera collapse into a stratified magma chamber. We build upon previous analogue models of withdrawal from chambers without collapse and numerical simulations of collapse and withdrawal. The experiments were designed to better understand ring dykes and zoned eruption sequences from natural calderas. During the experiments, one or two cylindrical or half cylindrical blocks subside into a chamber containing density- and viscosity- stratified fluids. The fluid is forced up ring conduits or between blocks and ponds above the block or blocks. Our experiments were scaled to investigate a silicic magma overlying a denser, more crystal-rich magma of similar composition. We investigated various subsidence velocities, tilting, and asymmetrically positioned vents. In addition, we investigated the effect of entirely subsiding one block, followed by the other. Our results show that the subsidence rate determines the point at which the stratified fluids begin to interact. This relationship is controlled by a power law relating the volumetric flow rate to density contrasts between the two stratified fluids. Our results also show that a period of rapid fluid flow in the chamber near the end of collapse defines the style of fluid interaction in the ring conduit and can produce reverse zoning. Asymmetric collapse styles and vent locations lead to earlier fluid interaction, lateral variability and more fluid interaction at the end of collapse. When subsidence was highly asymmetric or blocks subsided separately, mixing vortices developed in the chamber that completely disrupted fluid stratification in the chamber. These experiments with enhanced fluid interaction are associated with low Richardson numbers and flow separation due to diverging flow. Our

experimental results can be applied to pumice and bulk ignimbrite compositions of zoned ignimbrites, and zoned ring dykes. Our experiments show normally zoned ignimbrites with a brief period of reverse zoning can be expected to erupt from this chamber configuration at all but the slowest eruption rates. High subsidence rates will erupt relatively large volumes of ignimbrite containing two different pumice compositions compared to low eruption rates. Furthermore, asymmetrically subsiding calderas are more likely to produce mingled pumices, particularly if subsidence occurs independently on two different blocks. Ring dykes containing mingled magmas are likely in most instances. Ring dykes with lateral variation can be expected from asymmetrically subsiding calderas. Our experiments are the first to describe the effect of caldera collapse style on the composition of magma erupting from a stratified chamber.

INTRODUCTION

Scientists have never directly observed caldera collapse, and a large caldera forming eruption has not occurred since the development of modern scientific techniques. Therefore, our understanding of calderas is restricted to older structures (e.g. Moore and Kokelaar, 1999), observations and data from historic small caldera-forming eruptions (Geshi et al., 2002), and the results of numerical and analogue models (e.g., Folch et al., 2001; Kennedy et al., 2003).

Stratified magma chambers erupt ignimbrite sequences with stratigraphic zonation in either crystal content, major or trace elements, temperature, or volatiles (e.g., Bacon and Druitt, 1989). A normally zoned ignimbrite contains an inverted stratigraphy relative

to the chamber. Pumice compositions from zoned ignimbrite deposits are commonly used to infer the stratification or zonation of magma in a subsurface chamber (Hildreth, 1979). Experimental and numerical models of magma withdrawal from density- and viscosity-stratified reservoirs indicate that the magmatic stratification can be inverted, rearranged, or mingled in various proportions during withdrawal (Blake and Ivey, 1986a; Blake and Ivey, 1986b; Spera et al., 1986; Blake and Fink, 1987; Trial et al., 1992; Koyaguchi and Takada, 1994). Mingling can also occur in the conduit during eruption (Koyaguchi, 1985). Hence, compositional gradients in zoned ignimbrites may be complex, not necessarily reflecting the compositional gradients in the magma chamber (Spera, 1984). Thus, accurate models of magma withdrawal are essential for reconstructing magmatic stratigraphy from volcanic stratigraphy.

PREVIOUS STUDIES

Numerical models have shown that the maximum depth and the stratigraphic range over which magma can be tapped increase as the eruption progresses (Spera, 1984). The sequential tapping of fluid in a chamber can be illustrated using evacuation isochrons. An evacuation isochron joins points of equal time; they spatially illustrate the pattern by which a magma chamber empties (Fig. 1a). As a constant velocity eruption progresses, isochrons become closer packed and grow in size, indicating that magmas from various depths in the chamber are erupting together (Fig. 1a to c). Spera et al. (1984) used this model to explain changes in composition of Fe-Ti oxides in the Bishop Tuff, originally described by Hildreth (1979). Magma chambers are frequently density- and viscosity- stratified, and numerical models with density stratification predict flatter

FIGURE 1. Schematic illustration of the relationship between evacuation isochrons, draw-up height and deposit zonation from (a) central vent eruption with no caldera collapse and (b) ring fracture eruption with caldera collapse. Redrawn from Spera (1984), Spera et al. (1986), and Trial et al. (1992).

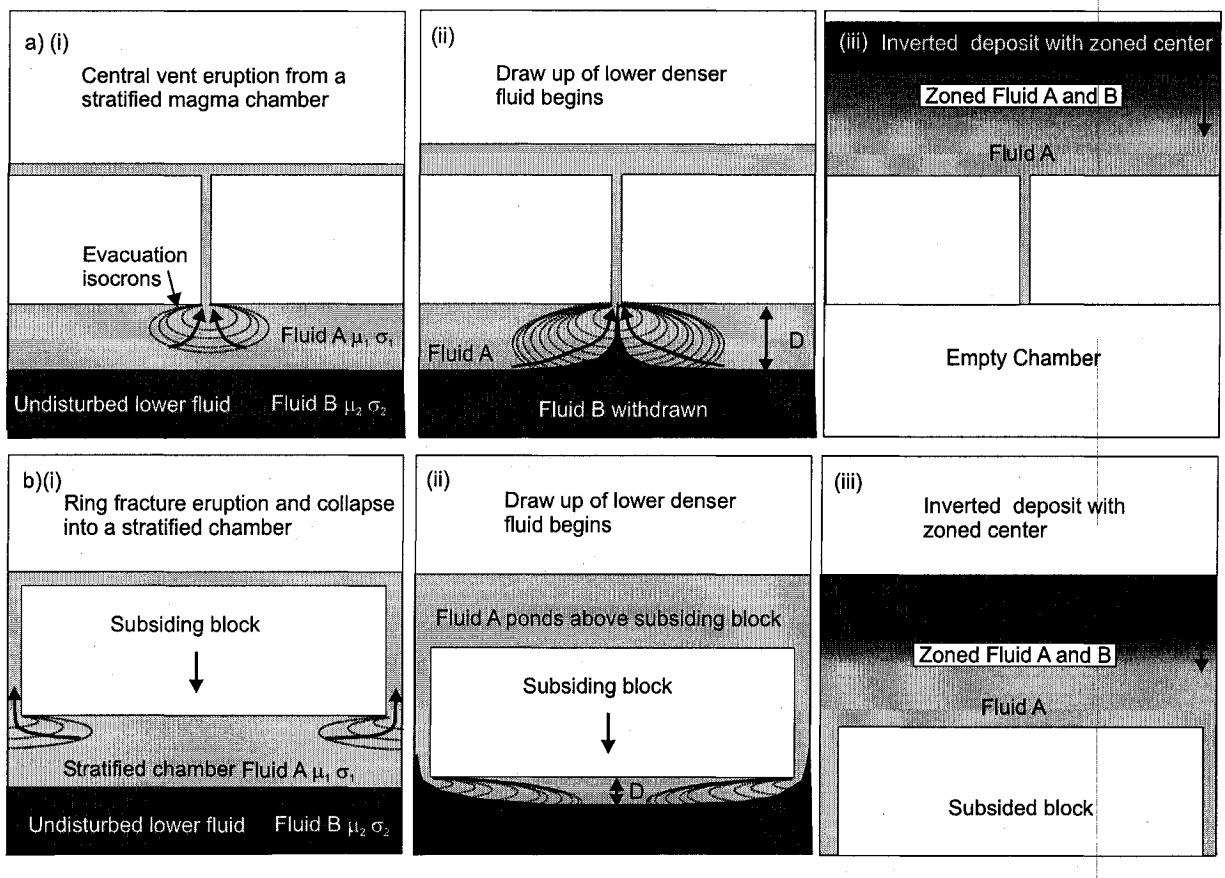
a) (i)
Central vent eruption from a stratified magma chamber
Evacuation isocrons
Fluid A μ_1 σ_1
Undisturbed lower fluid
Fluid B μ_2 σ_2
(ii)
Draw up of lower denser fluid begins
Fluid A
D
Fluid B withdrawn
(iii) Inverted deposit with zoned center
Zoned Fluid A and B
Fluid A
Empty Chamber
b)(i)
Ring fracture eruption and collapse into a stratified chamber
Subsiding block
Stratified chamber Fluid A μ_1 σ_1
Undisturbed lower fluid
Fluid B μ_2 σ_2
(ii)
Draw up of lower denser fluid begins
Fluid A ponds above subsiding block
Subsiding block
D
(iii)
Inverted deposit with zoned center
Zoned Fluid A and B
Fluid A
Subsided block

withdrawal isochrons (Spera et al., 1986; Trial et al., 1992) relative to the unstratified scenario (Spera, 1984). The other variables investigated include eruption rate, magma viscosity, density, size and shape of the chamber and vent (Spera, 1984; Spera et al., 1986; Trial et al., 1992).

Blake and Ivey (1986a) used analogue models to investigate withdrawal from density- and viscosity-stratified chambers. These experiments also indicated relatively flat isochrons. The flat isochrons allow a draw-up height to be defined. The draw-up height is the thickness of the magma in the chamber that is sampled in a single time instant (a visual estimate of the vertical extent of the isochron) (Fig. 1). The draw-up height is a controlling factor in the amount of magma interaction during an eruption (Fig 1). The draw-up height was measured in the experiments, and was shown to vary systematically with volumetric eruption rate, depending on the flow regime of the two layers. Inertial forces dominated at high Reynolds numbers (turbulent flow conditions), while viscous forces dominated at low Reynolds numbers (laminar flow conditions) (Blake and Ivey, 1986a; Blake and Ivey, 1986b).

Many zoned ignimbrite deposits are produced by eruptions where the roof of the magma chamber collapsed and a caldera formed at the surface (e.g., Hildreth, 1979). However, only piston-style collapse has been investigated numerically (Spera, 1984; Trial et al., 1992; Folch et al., 2001). Draw-up heights are reduced and isochrons flattened during caldera collapse because of increased lateral movement in the magma chamber caused by the subsiding piston (Fig. 1d-f) (Spera, 1984). Additionally, the dimensions of a ring fracture eruption will reduce draw-up heights compared to a central vent eruption (Blake and Ivey, 1986a; Trial et al., 1992). This implies that a substantially

smaller proportion of mixed magma is erupted in the case of a subsiding piston versus a stationary roof (Fig. 1c,d) (Trial et al., 1992). However, these conclusions can be applied only to the symmetric subsidence of a perfect piston-like caldera, a situation that is probably rare in nature (Kennedy and Stix, 2001).

These models also have shown that during caldera collapse, vorticity in the chamber increases due to the perturbations caused by the subsiding roof (Spera, 1984). Recent numerical models of caldera collapse support this conclusion and show that large vortices can develop in the chamber towards the end of caldera collapse (Folch et al., 2001). However, Folch et al. (2001) state that these vortices only develop in magma with viscosities of 10^4 Pa s or less. In summary, numerical models have shown that the formation of piston-style calderas (1) reduces the proportion of the eruption where two magmas are simultaneously erupted and (2) promotes the eruption of mingled magma, compared to eruptions where collapse does not occur. This apparent contradiction provides an interesting scientific problem that requires further investigation.

The effect of caldera collapse on the disruption of magmatic stratification has never been modeled directly using scaled analogue experiments. In particular, the effects of asymmetric collapse and multiple subsiding blocks require assessment and study. In this paper, we present results from scaled analogue models of different collapse styles and velocities. We model a relatively common situation where H_2O-rich, crystal-poor silicic magma overlies H_2O-poor, crystal-rich silicic magma (Wolff et al. 1990), by using a two-layer reservoir where the upper layer of fluid has a lower viscosity and density than the underlying fluid. First, we investigate how subsidence rate affects the initiation of draw-up of the lower layer. Second, we investigate the temporal variation in fluid

interaction, and how this is affected by different rates, degrees of asymmetry and vent geometries. Third, we investigate how lateral flow in the chamber can produce vortices and drive fluid interaction. Finally, we discuss implications of these experiments on the stratigraphy of zoned ignimbrite deposits, and on the compositional heterogeneity of ring dykes.

METHODS

We used a 36.5 cm diameter Plexiglas cylinder filled with two solutions of corn syrup and water (Fig. 2). The corn syrup was 43/43IX Clearsweet, manufactured by Cargill, with a nominal density of 1425 kg m^{-3} and viscosity of 81 Pa s at 26°C. It was thoroughly mixed with water in proportions of approximately 60 % syrup and 40 % water, to produce a viscosity suitable for the scaling parameters discussed below. Adjusting the proportions of corn syrup to water and adding food dye allowed us to produce two solutions with different densities and viscosities. One solution was dyed lighter in colour for visual purposes, had a density of 1200 kg m^{-3} and a viscosity of 0.018 Pa s, and the second solution was darker, had a density of 1250 kg m^{-3} and a viscosity of 0.028 Pa s. Before every experiment, viscosity was measured using a Brookfield LVDV-E rotational viscometer, which measures viscosities from 6 to 2,000,000 mPa s. In the range of viscosities we used the error bar was ±0.4 mPa. The fluid densities were measured by weighing known volumes. This allowed us to adjust the viscosity and density for temperature variation in the laboratory.

FIGURE 2. Experimental setup.

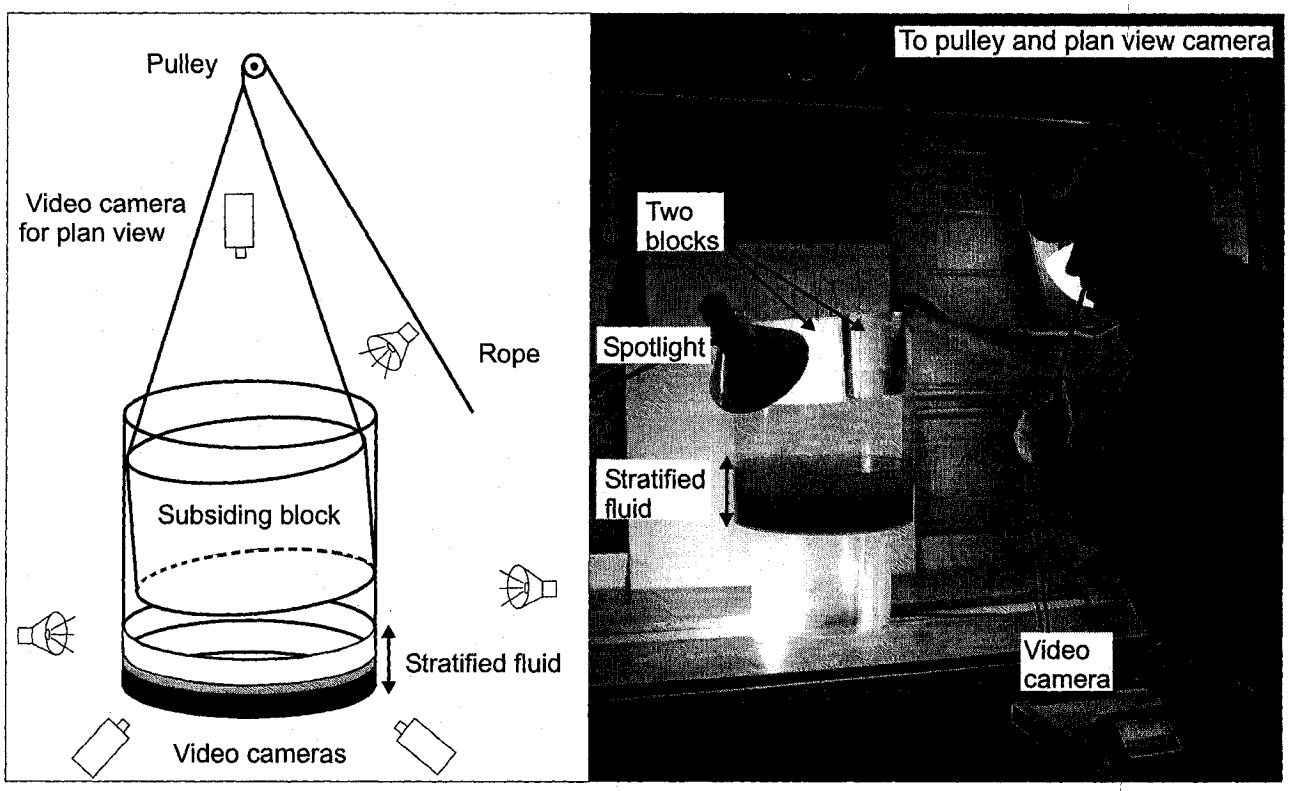
Pulley
Video camera
for plan view
Rope
Subsiding block
Stratified fluid
Video cameras
To pulley and plan view camera
Two
blocks
Spotlight
Stratified
fluid
Video
camera

We poured the low density, low viscosity fluid into the cylinder, producing a 7.5 cm-thick layer. We slowly and carefully poured the higher-density fluid down the side of the cylinder so that it ponded beneath the low-density fluid. The lower layer was dark colored and 2.5 to 4.0 cm thick. Above the lower layer, a mixed zone was produced that was 0 to 2 cm thick, and overlying this a 5.0 to 6.5 cm thick light layer (Fig. 2). The two fluids reached a total thickness of 10 cm.

We suspended a Plexiglas cylinder of 33 cm diameter or two half cylinders (equal to 33 cm diameter) filled with sand (density 1480 kg m^{-3}) above the cylinder containing the stratified liquids (Fig. 2). Before the experiment, the base of the sand-filled cylinder(s) was in contact with the upper surface of the upper liquid (Fig. 2). The cylinder(s) was then released to subside under gravity or lowered at different speeds into the cylinder containing the stratified fluids. The fluids rose around the edges of the subsiding cylinder(s) and ponded above the subsiding block. Video cameras recorded the experiment from the side, at two locations at 90° from each other, and a third camera recorded the experiment in plan view (Fig. 2). Spotlights were carefully positioned to illuminate the stratified fluids in the chamber. Every experiment was repeated at least once to check for reproducibility. The three different videos were viewed frame by frame, and measurements and descriptions were made concerning the amount and type of asymmetry, the displacement of magmatic stratification, and the style of mingling.

SCALING

An appropriate analogue model requires that geometric and dynamic similarity between the model and the natural system be maintained. To accomplish this, we first

identify the critical properties of the system being modeled. Second, we develop the model ensuring that the critical properties are correctly scaled (Sandford, 1959). We also verify that the dimensionless numbers that define the fluid dynamics of the system are equivalent between the model and nature.

Calderas range from 2 to 50 km in diameter (Lipman, 1984). For practical considerations, the experimental setup was limited to 36.5 cm in diameter. The length ratio was calculated using the diameter of the experiment and a typical value for nature:

$$\text{Length ratio } (L^*) = 0.365 \text{ m} / 20{,}000 \text{ m} = 1.83 \times 10^{-5} \quad (1)$$

The evacuation time ratio (T^*), the density ratio (ρ^*), the stress ratio (σ^*), and the viscosity ratio (μ^*) are critical properties that must be scaled correctly. The time required for a large caldera to form is not known. Wilson and Hildreth (1997) estimated that the eruption of the Bishop Tuff, which formed Long Valley caldera, lasted about four days. The climactic eruption of Krakatau, in 1883, continued for about 24 hours (Simkin and Fiske, 1983), while the caldera-forming phase of the 1991 Pinatubo eruption occurred over approximately nine hours (Wolfe and Hoblitt, 1996). For our scaling, we selected 1 to 100 hours eruption for a natural caldera and 1 to 90 seconds evacuation time for our experiments:

$$\text{Evacuation time ratio } (T^*) = 1 \text{ to } 90 \text{ s}/3600 \text{ to } 360000 \text{ s} = 2.50 \times 10^{-2} \text{ to } 2.78 \times 10^{-6} \quad (2)$$

The density of rhyolitic magma is well constrained; the dense rock equivalent (DRE) density of the Bishop tuff was 2200 kg m^{-3} (Hildreth, 1979). We use 2200 kg m^{-3} for the density of the upper layer in nature and 1200 kg m^{-3} for our experiments. Our lower layer has a density of 1250 kg m^{-3}, and therefore represents magma with a density of 2290 kg m^{-3}. This stratification is appropriate for that envisaged in the magma chamber beneath Long Valley caldera before the eruption of the Bishop Tuff (Wolff et al., 1990). The density ratio scales as:

Density ratio (ρ^*) =1200 kg m^{-3}/2200 kg m^{-3} = 0.545 (3)

According to the laws of dimensionless analysis, the appropriate stress ratio can be calculated using the density ratio, the gravity ratio (g *), and the length ratio, while the appropriate viscosity ratio can be calculated from the stress ratio and time ratio. Both the experiments and the calderas in nature are affected by 9.81 m s^{-2} of gravitational acceleration, and therefore the gravity ratio is one.

Stress ratio (σ^*) = $\rho^* g^* L^*$ = 9.97 x 10^{-6} (4)

Viscosity ratio (μ^*) = $\sigma^* T^*$ = 2.49 x 10^{-7} to 2.77 x 10^{-11} (5)

The uncertainty in the length of a large caldera forming eruption produces a range of viscosity ratios; our experiments are appropriate for magmas with a viscosity range 7.26 x 10^4 to 6.50 x 10^8 Pa s. This range is appropriate for dry rhyolite and trachyte

between 800 and 1100°C (Giordano and Dingwell, 2003), or rhyolite at ~800°C up to ~6 % water (Hess and Dingwell, 1996).

The Reynolds number and the densimetric Richardson number govern the fluid dynamics in these experiments. The Reynolds number defines the degree of turbulence in the system (Eq. 6). The densimetric Richardson number defines the ratio of damping forces resisting mixing (gravity) and inertial forces promoting mixing (velocity) (Eq. 7). We calculate the Reynolds and densimetric Richardson number using values for the conduit and the chamber as shown in Table 1. The draw-up height is used as the length scale in the magma chamber because only the fluid within the withdrawal layer is moving rather than from the whole chamber at any moment during eruption.

$$\text{Reynolds number} = \rho LV/\mu \quad (6)$$

$$\text{Densimetric Richardson number} = g(\Delta\rho/\rho)L/V^2 \quad (7)$$

where ρ is the density of the upper fluid, L is the draw up height, V is the velocity of fluid, g is the gravitational acceleration, and $\Delta\rho$ is the difference in density between fluids. The similitude of the Reynolds and densimentric Richardson numbers indicate that the experiments are suitable for caldera collapse into a zoned silicic magma chamber (Table 1).

LIMITATIONS

The scaling and application of analogue models are limited by our knowledge of the magmatic properties and processes that occur during caldera collapse. Recent years

TABLE 1. Parameters used in scaling calculations.

	Experiment	Nature
Diameter of chamber (m)	0.3650	2.0×10^4
Density (kgm^{-3})	1200	2200
Time for subsidence (sec)	90	$3.6 \times 10^3 - 10^5$
Viscosity (Pa.s)	0.0180	10^4-10^8
Width of ring conduit (m)	0.0175	30
Thickness of withdrawal layer (m)	0.0010	100
Cross sectional area of ring conduit (m^2)	0.0191	5.57×10^7
Cross sectional area of withdrawal layer (m^2)	0.0011	6.28×10^6
Volume of fluid (m^3)	0.0105	4.30×10^{11}
Volumetric flow rate (m^3s^{-1})	0.0001	1.120×10^6-10^8
Velocity of fluid in dyke (m/s)	0.0061	0.02 - 2.15
Velocity of fluid in chamber (ms^{-1})	0.1010	0.019 - 19.03
Reynolds number in dyke	7.10 - 639	0.0014 - 14.16
Reynolds number in chamber	6.76 - 608.	0.0419 - 419
Densimetric Richardson number in dyke	0.024 -193	2.66 - 26600
Densimetric Richardson number in chamber	0.040-0.132	0.11-1130

have shown substantial improvements in our knowledge of magmatic properties such as viscosity (e.g. Hess and Dingwell, 1996), but our knowledge of parameters associated with caldera collapse remain poorly constrained. Volumetric eruption rates and conduit areas are particularly difficult to assess during caldera forming eruptions. For example, a plinian eruption (500 m s^{-1}) from a 50 m diameter central vent gives a volumetric eruption rate of 9.82 $x10^5$ m^3 s^{-1}, a 50 m-diameter cylindrical ring fracture around a 20 km diameter caldera gives a volumetric eruption rate of 1.6 x 10^9 m^3 s^{-1}, while a plinian eruption of similar velocity from a ring fracture 500 m wide would produce a volumetric eruption rate of 1.53 x 10^{10} m^3 s^{-1}.

In our models, magma is treated as a single-phase fluid; however, magma in a chamber also contains crystals and bubbles. These were not introduced into our experiments because a 1cm diameter crystal or bubble would require an experimental crystal of 0.18 μm which is too small for practical purposes. In addition, the presence and abundance of bubbles and crystals are temperature- and pressure- sensitive, and therefore would require the scaling of additional dimensionless ratios and a complex experimental set up.

We did not investigate the effect of varying (1) the relative densities and viscosities, (2) the shape of the magma chamber, or (3) the configuration of the magmatic stratification. Parameters (1) and (2) have been investigated previously (Blake and Ivey, 1986a; Blake and Ivey, 1986b; Spera et al., 1986; Blake and Fink, 1987; Trial et al., 1992; Koyaguchi and Takada, 1994). The effect of parameter (3), e.g. a concentrically zoned chamber lies beyond the scope of our experiments but provides interesting lines of enquiry for future work. Hence the experiments are most relevant to cylindrical shaped

magma chambers (radius 10 km, 5.5 km thickness), containing vertically zoned silicic magma which increases by ~45 % in viscosity and by ~4% in density from top to bottom.

ERROR ANALYSIS

The draw-up height was measured when dark fluid was first seen in the ring conduits, and was calculated as the distance between the base of the subsiding block and the undisturbed dark interface. The estimates of the draw-up height of the dark fluid proved to have relatively large error bars of ~0.4 cm (Fig. 3), due to the blurred nature of the interface, and the slight variability of relative colors between experiments. In some experiments, it was difficult to distinguish exactly the dark fluid from the lower layer entering the ring conduit from the mingled fluid of the interface. The relative sharpness of this interface layer is shown in Table 2 as the apparent thickness of the mingled fluid. However, careful frame-by-frame video analysis from the three different camera angles allowed us to establish the draw-up height and associated error bars with relative confidence.

The estimate of flow velocity is critical to the analysis of our experimental results. We attempted to estimate the maximum velocity by tracking the flow in the ring conduit and chamber, but the errors involved proved substantial. Therefore, mean velocities for the chamber and conduit were calculated from the volumetric flow rate and the cross-sectional area of flowing liquid. These average velocities proved to be a more consistent estimate and allowed comparison between experiments.

FIGURE 3 Photograph sequences captured from video footage from the south camera (refer to 3a(v)) of experiments with varying subsidence velocities. 3a) Slow subsidence of a symmetrical single piston. Arrow in (iii) shows diffuse horizontal bands of light fluid which may be associated with a change in dip of the subsiding block. Arrows in (iv) show the faint, thin, horizontal bands of light fluid mingling with the dark fluid. 3b) Subsidence of a single piston dipping 3.5° to the east. Arrows in (iii) show the first appearance of horizontal bands. Arrow in (iv) shows a pulse of light fluid expelled as the block touched down. Arrow in (v) shows the disruption of bands by lateral movement of the fluids once subsidence ceased. 3c) Subsidence of a single piston dipping 2.5° to the west with varying subsidence rates. Arrow in (iii) shows a diffuse broad band of light fluid in the ring conduit. Arrows in (iv) show the development of horizontal bands as the subsided block touched down to the west. Arrows in (v) show the formation of mushroom-like structures once subsidence ceased. 3d) Rapid subsidence of an initially symmetrical single piston. Arrows in (iv) show the development of horizontal bands once the block touched down. Arrow in (v) shows the lateral movement of fluid once subsidence ceased, allowing fluids to mingle.

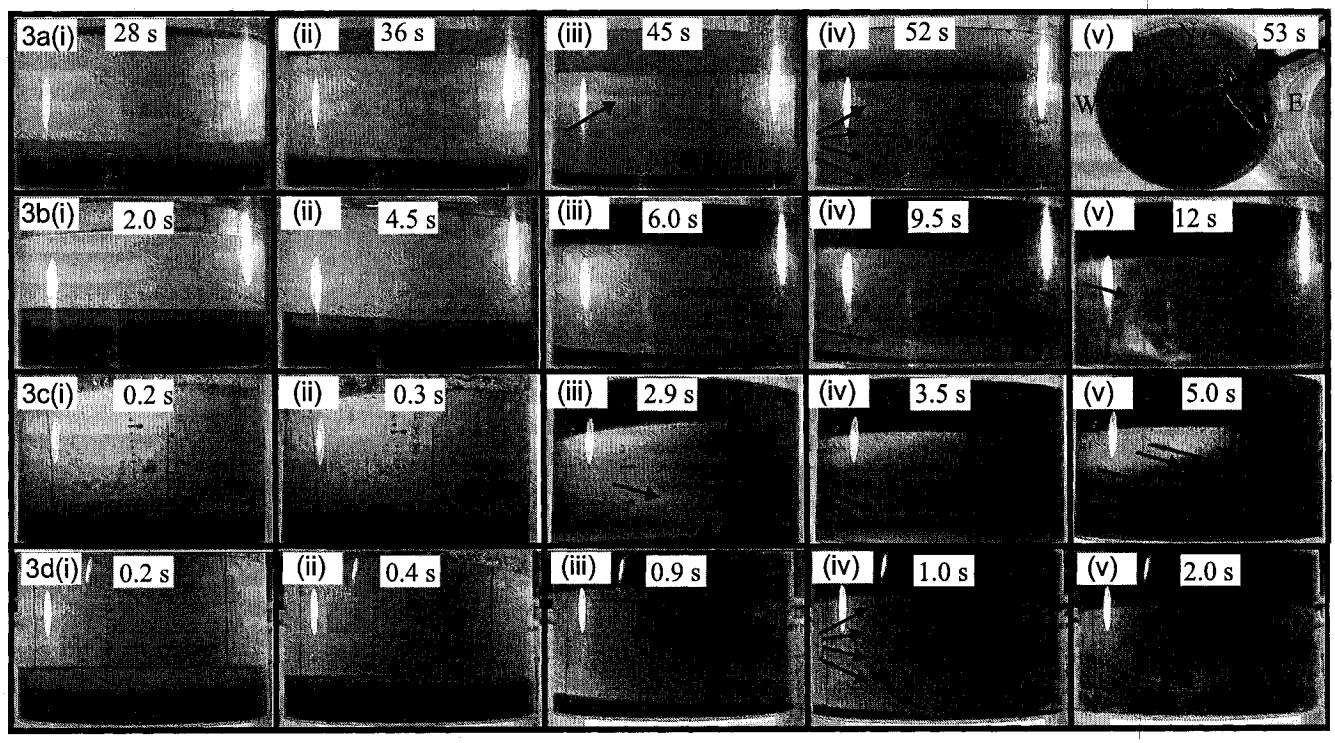
3a(i) 28 s
(ii) 36 s
(iii) 45 s
(iv) 52 s
(v) 53 s
W
E
3b(i) 2.0 s
(ii) 4.5 s
(iii) 6.0 s
(iv) 9.5 s
(v) 12 s
3c(i) 0.2 s
(ii) 0.3 s
(iii) 2.9 s
(iv) 3.5 s
(v) 5.0 s
3d(i) 0.2 s
(ii) 0.4 s
(iii) 0.9 s
(iv) 1.0 s
(v) 2.0 s

TABLE. 2. Experimental results. Subsidence rates were calculated using the volumetric flow rate up until touchdown of the first block.

Experiment number	Number of blocks	Experiment type	Draw-up height (m)	Height of lower fluid (m)	Thickness of interface (m)	Conduit width (m)	Calculated subsidence rate ($m\ s^{-1}$)	Subsidence time (s)	Draw-up time (s)	Max. dip (°)
1	1	Slow symmetric	0.0075	0.004	0.005	0.02	0.0011	88	60	2.5
2	1	Slow symmetric	0.004	0.004	0.005	0.02	0.0019	54	36	0.5
3	1	Slow symmetric	0.0075	0.004	0.005	0.02	0.0091	11	7	2.5
4	1	Moderate symmetric	0.01	0.04	0.01	0.02	0.0105	9.5	5	3.5
5	1	Variable symmetric	0.0175	0.04	0.005	0.02	0.0333	3	0.25	2.5
6	1	Fast symmetric	0.02	0.04	0.005	0.02	0.0546	1.83	0.23	4.5
7	1	Fast symmetric	0.02	0.05	0.005	0.02	0.0546	1.83	0.3	2
8	1	Fast symmetric	0.02	0.05	0.005	0.02	0.0500	2	0.43	1.5
9	1	Fast symmetric	0.02	0.04	0.01	0.02	0.0943	1.06	0.46	2
10	1	Fast symmetric	0.02	0.04	0.005	0.02	0.1000	1	0.3	2.5
11	1	Fast symmetric	0.0175	0.04	0.015	0.02	0.0685	1.46	0.36	12
12	1	Tilted	0.02	0.045	0	0.03	0.0699	1.43	0.3	12
13	1	Tilted	0.025	0.04	0	0.03	0.0752	1.33	0.26	14
14	1	Half closed conduit	0.025	0.03	0.005	0.02	0.0752	1.33	0.23	16
15	1	Half closed conduit	0.03	0.035	0.005	0.02	0.0602	1.66	0.33	4
16	2	Central fissure	0.025	0.04	0.005	0.025	0.1316	0.76	0.23	2
17	2	Central fissure	0.025	0.04	0.005	0.025	0.1587	0.63	0.23	2
18	2	Central fissure, diff rates	0.02	0.04	0.005	0.025	0.1163	0.86	0.46	1.5
19	2	Central fissure, diff rates	0.025	0.04	0.005	0.025	0.2500	0.4	0.23	5
20	2	First block closed	0	0.035	0.01	0.02	0.0292	3.43		0
21	2	First block closed	0	0.035	0.01	0.02	0.0769	1.3	0.5	0
22	2	First block open	0.01	0.035	0.01	0.02	0.3030	0.33	0.2	3
23	2	First block open	0.01	0.04	0.005	0.02	0.2000	0.5	0.3	0
24	2	Thin central fissure	0.0175	0.45	?	0.022	0.1316	0.76	0.33	6
25	2	Diff. Rates	0.015	0.45	?	0.022	0.1075	0.93	0.33	9
26	2	Diff. Rates	0.015	0.45	?	0.022	0.1075	0.93	0.36	10
27	2	Diff. Rates	0.01	0.45	?	0.02	0.0971	1.03	0.33	10
28	2	Diff. Rates	0.015	0.45	?	0.02	0.2174	0.46	0.23	3

RESULTS

In this section, we present descriptions, measurements, and analyses of video footage from our experiments using (a) a single piston and (b) two separate blocks. We carried out 45 experiments; here we present experimental data from 28 experiments relevant to caldera collapse. These data include the duration of the subsidence, the initiation of draw-up of the lower layer, the time of touchdown of the block or blocks, the maximum dip of the block, and the percentage of the ring conduit used to channel fluid. These data allow us to calculate the subsidence rate, the draw-up height, the average flow velocity, and the mean Reynolds and Richardson numbers (Tables 1, 2). In addition, we selected nine experiments to illustrate the range of styles of subsidence and fluid interaction. We describe (1) variable subsidence speeds with a single piston, (2) different vent and subsidence styles with a single piston, and (3) various vent and subsidence styles with two separately subsiding blocks. The experiments below show the effects of varying the principal parameters that influence fluid interaction during withdrawal from the chamber.

VARIABLE SUBSIDENCE VELOCITIES

Slow symmetric subsidence of a single piston

Figure 3a illustrates time sequence photographs from experiment 2 (Table 2). The block subsided fairly symmetrically (<0.5° from horizontal) at 1.85 x 10^{-4} m s^{-1} throughout the experiment (Fig. 3a(i)). Fluid flow was most rapid in the south (refer to Fig 3a(v)), where the ring conduit was widest. After 36 s and 5.6 cm of subsidence, dark

fluid began to enter the base of the ring conduit in the south, indicating a draw-up height of <0.4 cm. (Fig. 3 a(ii)). Fluid flowing in the ring conduit had a homogeneous color until 50 s when diffuse horizontal bands of lighter fluid were observed in the ring conduit (Fig. 3a(iii)). These bands represent rising lighter fluid in the darker fluid, which may have been associated with a change in the dip of the block. After 50 s the block had begun to dip slightly south but then corrected itself and leveled off. After 54 s, the block touched down; only dark fluid was observed as the block settled, indicating that all light fluid had been withdrawn earlier during subsidence. In the northern section of the conduit, dark fluid never entered the conduit, indicating some lateral variation in the width of the ring conduit (Fig. 3a(v)). Thin horizontal bands of light fluid remained in some areas of the ring conduit, buoyantly mingling with dark fluid in these areas (Fig. 3a(iv)). The ring conduit generally had darker fluid at the base than the top, indicating a vertical zonation. After subsidence stopped, the fluid above the subsided block still remained stratified, which indicates that the two fluids did not mingle in this experiment.

Moderate subsidence rate of a single piston

Figure 3b illustrates time sequence photographs from experiment 4 (Table 2). The block subsided at 1.1 x 10^{-3} m s^{-1} and, initially, was mildly asymmetric and the block dipped 3.5° to the east (Fig. 3 b(i)). Fluid flow was most rapid in the east where the conduit was widest. After 4.5 s and 4.5 cm of subsidence, the level of the interface in the south began to drop, indicating fluid was being withdrawn from the lower layer in the east, and that the draw-up height was 1 cm (Fig. 3b(ii)). Fluid flowing in the ring conduit had a homogeneous color until 6 s, when horizontal bands of light fluid were observed in

the ring conduit (Fig. 3b(iii)). At 10 s the block touched down; as it settled, a thick pulse of light fluid was expelled from beneath the block and then observed in the ring conduit (Fig. 3b(iv)). This fluid moved laterally in the ring conduit, and the band of light fluid then mingled with darker fluid (Fig. 3b(v)). After subsidence stopped, the darker fluid did not reach the top of the conduit, remaining partially stratified in the western section of the ring conduit.

Variable subsidence rate of a single piston

Figure 3c illustrates time sequence photographs from experiment 5 (Table 2). The block subsided at a mean rate of 2.04 x 10^{-3}m s^{-1}, initially dipping 2.5° to the west. Fluid flow was most rapid in the southwest, where the ring conduit was widest (Fig. 3 c(i)). After 0.25 s and 4.75 cm of subsidence, the diffuse interface between the two fluids could be seen descending, and darker fluid was seen entering the ring conduit, giving a draw-up height of 1.75 cm (Fig 3c(ii)). The ring conduit initially contained flowing light colored fluid; as dark fluid began to be drawn up, the flowing fluid became patchy, and eventually homogeneously dark colored. The block then slowed and moved horizontally westward, opening the ring conduit in the east. Lighter fluid higher in the chamber was then tapped and seen in the eastern ring conduit. This activity produced a diffuse band of light fluid in the ring conduit in the east. The block then re-accelerated, dark fluid was again tapped and entered the ring conduit (Fig 3c(iii)). At 3 s, the block touched down in the west, expelling light fluid into the ring dyke producing two horizontal bands in most of the ring conduit (Fig. 3c(iv)). After subsidence stopped, the light fluid bands then

buoyantly rose forming mushroom-like structures (Fig. 3c(v)). After subsidence stopped, some stratification was maintained in the ring conduit despite this mingling.

Rapid subsidence of a single piston

Figure 3d illustrates time sequence photographs from experiment 9 (Table 2). The block subsided at 9.4 $x10^{-3}$ m s^{-1}, initially symmetrically, and then began to dip slightly to the east by 2° (Fig. 3d(i)). Fluid flow was faster in the east, where the ring conduit was slightly wider. After 0.4 s and 4.5 cm of subsidence, the diffuse interface began to descend with at least 2 cm of light fluid above it (Fig. 3d(ii)). Dark fluid was then seen in the eastern section of the ring conduit, giving a draw-up height of 2 cm (Fig. 3d(ii)). In the west, light fluid was seen above the darker fluid until just before the block touched down (Fig. 3d(iii)). At 1.06 s, the block touched down in the east, expelling light fluid and creating several horizontal bands throughout the ring conduit (Fig. 3d(iv)). After subsidence stopped, the buoyancy of these bands and lateral flow in the ring conduit allowed fluids to mingle (Fig. 3d(iv, v)). Weak stratification of mingled dense fluid and light fluid remained in some areas of the conduit.

ASYMMETRIC SUBSIDENCE AND VENT POSITION

Subsidence of a tilted single block

Figure 4a illustrates time sequence photographs from experiment 12 (Table 2). The block was pre-tilted at 12° and subsided dipping strongly east at 7.0 x 10^{-2} m s^{-1} (Fig. 4a(i)). Tilting caused the ring conduit to close in the extreme east and west, and the fluid flow was thus most rapid and channeled to the northeast and southeast, where the ring

FIGURE 4. Photograph sequences captured from video footage from the south camera of experiments with asymmetric subsidence and varying vent position. 4a) Subsidence of a single block dipping 12° to the east. Arrows in (iii) show rising horizontal bands of light fluid as the block touched down. Arrows in (iv) show rotating vortices formed as the subsiding block leveled out after touchdown. Arrows in (v) point out the most rapid flow where the conduit was widest. 4b) Subsidence of a single piston with only half the ring conduit open. Arrows in (iv) show vertical bands in the ring conduit resulting from flow velocity variation as well as a weak horizontal band of light fluid forming as the block touched down. Arrow in (v) shows a vortex of mingled fluid in the ring conduit after complete subsidence. 4c) Subsidence with a 2 cm central fissure. Arrows in (iv) show bands of light and dark fluid that formed as the two blocks touched down. Arrow in (v) shows that light fluid flowed down after subsidence ceased.

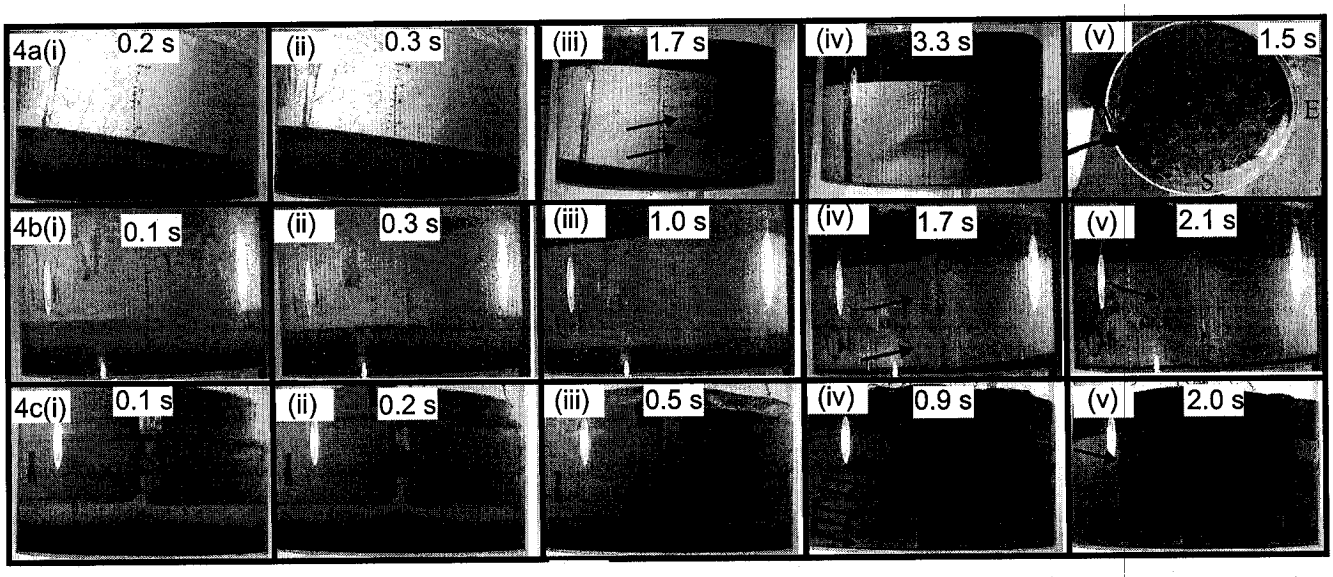
4a(i) 0.2 s
(ii) 0.3 s
(iii) 1.7 s
(iv) 3.3 s
(v) 1.5 s
E
S
4b(i) 0.1 s
(ii) 0.3 s
(iii) 1.0 s
(iv) 1.7 s
(v) 2.1 s
4c(i) 0.1 s
(ii) 0.2 s
(iii) 0.5 s
(iv) 0.9 s
(v) 2.0 s

conduit was widest (Fig. 4a(v)). After 0.3 s and 4 cm of subsidence, darker fluid was seen entering the eastern section of the ring conduit, indicating a 2 cm draw-up height (Fig. 4a(ii)). As fluid was removed in the east, the level of the dense interface descended in the west, and up to 5 cm of light fluid remained untapped in this area (Fig. 4a(ii)). Initially, the eastern ring conduit contained flowing light fluid. Dark fluid then began to be drawn up and briefly formed rising flame-like structures. The fluid in the ring conduit became homogeneously colored dark fluid (Fig. 4a(iii)). At 1.43 s, the block touched down in the east, expelling light fluid and creating horizontal bands. Light fluid continued to be expelled in pulses, producing rising horizontal bands of light fluid in the ring conduit during the remainder of subsidence (Fig. 4a(iii)). As the block touched down, it leveled out and opened the conduit in the extreme east. The settling of the block caused lateral flow of fluid and created vortices that rotated in opposite directions, disrupting the horizontal bands of light fluid (Fig. 4a(iv)). After subsidence stopped, no vertical stratification remained in the ring conduit, only strong lateral variation.

Subsidence of a single piston with half the ring conduit closed

Figure 4b illustrates time sequence photographs from experiment 15 (Table 2). The ring conduit was kept open in the west, and the block subsided at 4.34×10^{-3} m s^{-1} dipping 4° to the west (Fig. 4b(i)). After 0.3 s and 3.5 cm of subsidence, darker fluid was seen entering the ring conduit, indicating a 3 cm draw-up height (Fig. 4b(ii)). As fluid was removed in the west, the level of the dense interface descended in the east, with up to 4 cm of untapped light fluid in the chamber (Fig. 4b(iii)). Light and dark fluid flowed laterally from the east to the west, producing flow velocity variation and vertical bands of

compositional variation in the ring conduit (Fig. 4b(iv)). At 1.66 sec, the block touched down in the west, expelling light fluid and creating a weak horizontal band of light fluid in the west (Fig. 4b(iv)). Lateral flow from the east disrupted the band of light fluid before it rose in the ring conduit. This lateral flow in the ring conduit produced vortices and caused fluids to mingle. After subsidence stopped, only mingled fluid remained in the ring dyke with little stratification (Fig. 4b(v)).

Subsidence with a central fissure vent

Figure 4c illustrates time sequence photographs from experiment 16 with two blocks subsiding simultaneously separated by a gap of 2 cm (Table 2). The blocks descended rapidly at 1.0 x 10^{-2} m s^{-1} dipping 2° to the north, where the ring conduit was widest (Fig. 4c(i)). After 0.23 s and 3.5 cm of subsidence, darker fluid was seen entering the central conduit, indicating a draw-up height of 2.5 cm (Fig. 4c(ii)). After 0.5 s and 5.5 cm of subsidence, dark fluid was seen entering the ring conduit (Fig. 4c(iii)). The level of the dark fluid descended, and light fluid could be seen above dark fluid in the chamber until the block was within 2 cm of the chamber base. Initially, the ring conduit contained flowing light fluid, then dark fluid began to be drawn up and briefly formed rising flame-like structures. The fluid then became homogeneous and dark (Fig. 4c(iii)). The view from above showed flow was most rapid in the north and south where the central fissure conduit intersected the ring conduit. At 0.76 s, the eastern block touched down, expelling light fluid and creating two weak light fluid bands which quickly mingled and dissipated. At 0.9 sec, the western block touched down, expelling more light fluid and creating three more thin bands of light fluid (Fig. 4c(iv)). The two blocks created a total of five bands

around the western ring conduit. These bands mingled and dissipated as they rose. After subsidence stopped, stratification was re-achieved in the ring conduit as light fluid flowed down the ring conduit from above (Fig. 4c(v)).

DIFFERENTIAL SUBSIDENCE OF TWO INDEPENDENTLY SUBSIDED BLOCKS

First block with ring conduit closed, second block with conduit open

Figure 5a illustrates time sequence photographs from experiment 21 with two independently subsiding blocks (Table 2). The ring conduit around the eastern block was closed but open around the western block (Fig. 5a(i)). The eastern block subsided first at 7.69×10^{-2} m s^{-1}, while the western block was kept stationary until the eastern block had subsided entirely. After 0.17 s and 2.5 cm of subsidence of the eastern block, the interface level in the east began to descend; correspondingly, while both the block and the interface level in the west rose (Fig. 5a(ii)). Dark fluid could not enter the eastern ring conduit since it was closed. Instead, fluid was forced laterally from east to west, producing a rotating vortex in the light fluid in the western part of the chamber (Fig. 5a(ii)). At 0.5 s, small amounts of the partially mingled fluid were observed in the southwest section of the ring conduit; however, the block had now descended beneath the original interface level, indicating a draw-up height of zero. Until this point, only light fluid had been withdrawn from the chamber. Despite the eastern block slowing 2 cm before touchdown, the velocity and diameter of rotation of the vortex increased and disrupted the stratification in the western part of the chamber (Fig. 5a(iii)). At 1.3 s, the eastern block had subsided completely (Fig. 5a(iv)). A pause in subsidence occurred for

FIGURE 5. Photograph sequences captured from video footage from the south camera of experiments with two independently subsiding blocks. 5a) Subsidence with the eastern ring conduit closed and the western ring conduit open. Arrows in (ii) show the lateral movement of fluid developing into a large vortex in the western half of the chamber. Arrow in (iii) shows the increasing size of the vortex before complete subsidence of the western block. Arrows in (iv) point out the movement of the vortex during a 22 s pause in subsidence. 5b) Subsidence with the eastern ring conduit open and the western ring conduit closed. Arrows in (ii) show the contrasting interface levels in the east and west of the chamber. Arrows in (iii) and (iv) show evidence of a vortex in the eastern chamber as the western block subsided. 5c) Simultaneous subsidence of two blocks at different rates. Arrows in (iii) show horizontal bands forming as the eastern block touched down. Arrows in (iv) show the development of the horizontal bands in the western ring conduit and a vortex disrupting stratification in the eastern ring conduit.

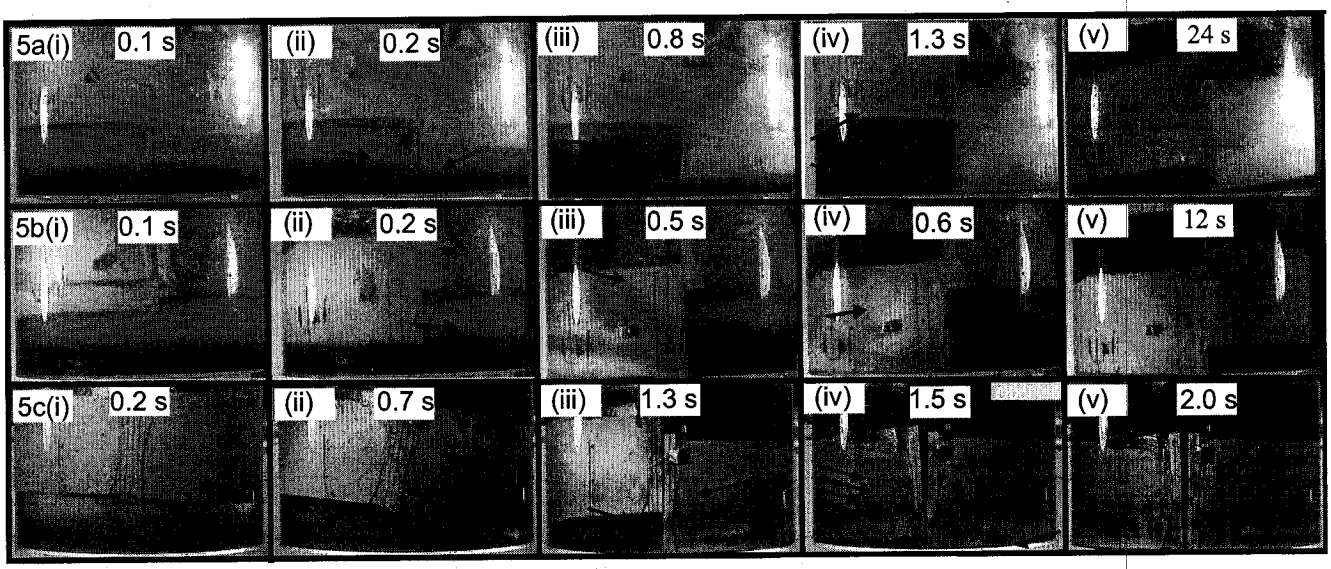
5a(i) 0.1 s
(ii) 0.2 s
(iii) 0.8 s
(iv) 1.3 s
(v) 24 s
5b(i) 0.1 s
(ii) 0.2 s
(iii) 0.5 s
(iv) 0.6 s
(v) 12 s
5c(i) 0.2 s
(ii) 0.7 s
(iii) 1.3 s
(iv) 1.5 s
(v) 2.0 s

22 seconds during which the vortex continued to rotate and mingled all the fluid under the western block (Fig. 5a(iv)). The western block then subsided for 0.9 s (Fig. 5a(v)). During the subsidence of the western block, only mingled fluid was seen in the ring conduit. This experiment indicates a dichotomy between unmingled light fluid withdrawn during the subsidence of the first block and well-mingled light and dark fluid withdrawn during the subsidence of the second block. After subsidence ceased, no stratification remained in any part of the chamber.

First block with ring conduit open, second block with ring conduit closed

Figure 5b illustrates time sequence photographs from experiment 23 with two independently subsiding blocks (Table 2). The ring conduit around the western block was open but closed around the eastern block (Fig. 5b(i)). The western block subsided first at 2.00 $x10^{-1}$m s^{-1}, while the eastern block was kept stationary until the western block had subsided entirely. After 0.2 s and 2 cm of subsidence of the western block, the interface level in the west began to descend (Fig. 5b(ii)) while the interface level and block in the east rose. Fluid flowed laterally from west to east. After 0.3 s and 4.5 cm of subsidence of the western block, dark fluid was seen in the western ring conduit, indicating a 1 cm draw-up height. This result contrasts with the subsidence of the first block of the previous experiment, when almost no dark fluid was withdrawn and the draw-up height was effectively zero. At 0.5 s the western block touched down, and a vortex began to develop in the eastern chamber; however, stratification was still visible in the chamber beneath the eastern block (Fig. 5b(iii, iv)). There was then a 10 s interval during which the vortex mingled with the fluid beneath the eastern block, disrupting the stratification. The eastern

block then subsided for 1.1 s. During the subsidence of the eastern block only mingled fluid was withdrawn (Fig. 5b(v)). After subsidence had stopped, no stratification remained in any parts of the chamber.

Simultaneous subsidence of two blocks at different rates

Figure 5c illustrates time sequence photographs from experiment 26 with two blocks of different density (1300 kg m^{-3} and 1500 kg m^{-3}) (Table 2). Both blocks initially dipped 10° to the northeast, the eastern block descended at 2.0 x 10^{-2} m s^{-1} and the western block at 1.1 x 10^{-2} m sec^{-1} (Fig. 5c(i)). The ring conduit was widest in the southeast but became more symmetric during subsidence. After 0.36 s and 4.5 cm of subsidence of the eastern block, darker fluid was seen in the ring conduit, indicating a draw-up height of 1.5 cm. Flow was most rapid in the east, and as dark fluid entered the ring conduit, flame-like structures could be seen. The flowing fluid then became homogeneously dark colored (Fig. 5c(ii)). At 0.93 s the eastern block touched down, expelling light fluid and creating two horizontal bands of light fluid in the ring dyke (Fig. 5c(iii, iv)). The western block dipped 10° to the north and flow in this section of the ring conduit also showed flame-like structures. Bands of light fluid could be seen in the southwest associated with the touch down of the eastern block. At 2 s the western block touched down, expelling light fluid and creating eastward lateral flow. This lateral flow formed a vortex in the chamber under the western block (Fig. 5c(iv)). This vortex disrupted stratification in the east and west of the ring conduit (Fig. 5c(v)). After subsidence stopped, fluid in the ring conduit was well-mingled and showed no stratification.

SUMMARY OF RESULTS

Our experiments investigated fluid behavior in the chamber and ring conduit as a function of caldera subsidence. We examined the effect of variable subsidence rates, block and vent asymmetry, and single vs. multiple subsiding blocks. As the subsidence speed of a block increased, (1) the draw-up height increased in the chamber, (2) more dark fluid was drawn up with light fluid during collapse, (3) light fluid remained in the chamber for a longer proportion of subsidence, and (4) the magma in the ring conduit was better mingled after subsidence stopped. Additionally, varying subsidence rates caused the draw-up height to fluctuate during an eruption, producing temporal compositional variation. As the tilt of the subsiding block increased we observed the following changes, (1) at any time instant, the composition of fluid in the ring conduit showed greater lateral variation, (2) light fluid remained in the chamber for a longer period, and (3) more lateral motion and mingling of fluid occurred in the ring conduit as the block reached the base of the chamber. This effect resulted in a locally better mingled, but laterally more heterogeneous ring conduit composition. Experiments with an asymmetrically positioned ring conduit had an effect similar to those with steeply dipping pistons, but the draw-up height was greater. Experiments with two blocks subsiding independently showed, (1) smaller draw-up heights, (2) a greater volume of light fluid withdrawn without interaction with dark fluid, (3) a higher proportion of chamber mingling, and (4) better mingled fluids in the ring conduit after subsidence stopped.

DISCUSSION

The results of the experiments show that the initiation of fluid interaction (draw-up height) during collapse of a single piston is controlled, in part, by the flow velocity and by relationships predicted by Blake and Ivey (1986a). Additionally, the experiments show that the style of fluid interaction in the chamber is strongly dependent on the subsidence rate, dip of the block, and conduit geometry. All experiments show a period of rapid flow as the block reaches the base of the chamber. The proportions of different fluids and the lateral flow rate in the chamber during this period will control the eventual textures and composition of the ring conduit. When two blocks subside independently, flow separation can occur during lateral flow. This drives enhanced fluid interaction in the chamber, similar to the vortices envisaged by Folch et al. (2001).

DRAW-UP HEIGHT

A power law relationship predicts the draw-up height, involving a balance between the inertial or viscous forces on one hand, and gravity forces on the other hand (Blake and Ivey, 1986a). When our results of subsidence rate are plotted against draw-up height for symmetrical subsidence of single pistons, the relationship is correctly predicted (Fig. 6). However, both tilted blocks and the independent subsidence of two blocks show significant deviation from this relationship (Fig. 6).

Previous experimental models show that the draw-up height controls the onset of fluid interaction during withdrawal. Our experiments show that the draw-up height increases with subsidence rate (Fig. 6). Draw-up occurs as viscous forces, or inertial

FIGURE 6. Draw-up height plotted against subsidence rate for the different experiments and the theoretical power-law relationships proposed by Blake and Ivey (1986a).

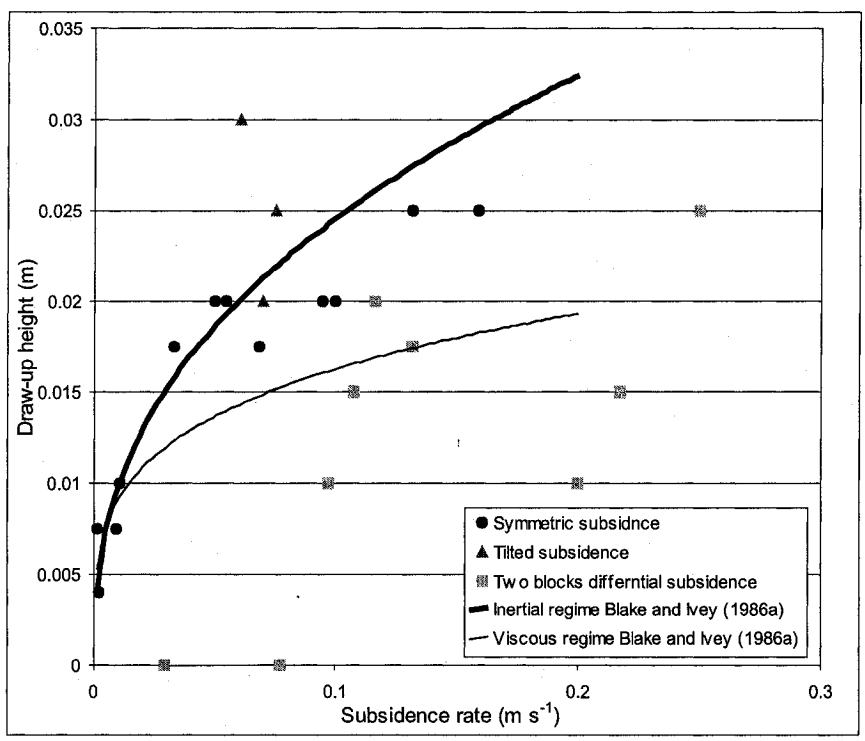
0.035
0.03
0.025
0.02
0.015
0.01
0.005
0
Draw-up height (m)
0
0.1
0.2
0.3
Subsidence rate (m s-1)
Symmetric subsidnce
Tilted subsidence
Two blocks differntial subsidence
Inertial regime Blake and Ivey (1986a)
Viscous regime Blake and Ivey (1986a)

forces of the flow begin to dominate over the gravitational forces of the dense fluid. Viscous and inertial forces can be calculated, since the subsidence rate is proportional to the volumetric flow rate (Fig. 6). Blake and Ivey (1986a), showed that the draw-up height can be calculated in both regimes. The form of these equations are based on the Reynolds and densimetric Richardson numbers and are as follows. For a viscous flow regime, the draw-up height is defined as:

$$d = c_1 (q \mu / g')^{1/4} \quad (10)$$

where c_1 was a constant used for experiments in the viscous regime to compare results to those of Blake and Ivey (1986), q is the volumetric flow rate, μ is the viscosity, g' is the reduced gravity $g(\rho_1-\rho_2)/\rho_1$), g is the acceleration due to gravity, with ρ_1 and ρ_2 the density of the light and dark fluids, respectively. For inertial flow the draw-up height is defined as:

$$d = c_2 (q^2 / g')^{1/5} \quad (11)$$

where c_2 was a second constant for the inertial experiments of Blake and Ivey, (1986a). In a similar way to Blake and Ivey (1986a), we calculate an experimental constant using mean values from our single piston experiments in both the viscous and inertial regimes. Our results for simple piston style subsidence show that as the volumetric flow rate increases, the draw-up height increases, agreeing with the power law relationships proposed by Blake and Ivey (1986a). This relationship is also shown in experiment 5,

where the fluctuating volumetric flow rate caused the draw-up height to fluctuate, thereby alternately tapping light and dark fluids (Fig. 3c(ii)). Numerical models also predict a similar effect caused by pauses in eruption (Trial et al., 2001).

The experiments with a tilted block and different ring conduit geometries have draw-up heights generally higher than the model predicts. The data in Figure 6 are plotted using the average volumetric flow rate, but the draw-up height that we measure is a maximum value. The maximum draw-up height likely is related to the maximum volumetric flow rate. When the block is tilted, the volumetric flow rate in the ring conduit varies appreciably, producing a large discrepancy between the mean and maximum volumetric flow rates. Therefore, the average flow rate that we plot underestimates the maximum flow rate that determines the maximum draw-up height. If maximum flow rates could have been accurately measured the results from the tilted block experiments may fit the relationship predicted by the models.

The experiments with two blocks also do not fit the predicted relationship, as much smaller draw-up heights are observed despite rapid subsidence. When two blocks subside independently, the level of the interface drops on the side of greatest subsidence before draw-up occurs. Correspondingly, the level of the interface rises on the side of least subsidence, producing a step in the interface level (e.g., Fig. 5a(ii)). This step indicates that fluid is pushed laterally in the chamber rather than out through the ring conduit (Fig. 7). In essence, when one block subsides independently to the other, fluid flows laterally within the chamber from under one block to under the other. This allows the subsidence rate of one block to increase while the subsidence rate of the other decreases. Indeed, when one block completely subsided before the other began, the

forces of the flow begin to dominate over the gravitational forces of the dense fluid. Viscous and inertial forces can be calculated, since the subsidence rate is proportional to the volumetric flow rate (Fig. 6). Blake and Ivey (1986a), showed that the draw-up height can be calculated in both regimes. The form of these equations are based on the Reynolds and densimetric Richardson numbers and are as follows. For a viscous flow regime, the draw-up height is defined as:

$$d = c_1 (q \mu / g')^{1/4} \quad (10)$$

where c_1 was a constant used for experiments in the viscous regime to compare results to those of Blake and Ivey (1986), q is the volumetric flow rate, μ is the viscosity, g' is the reduced gravity $g(\rho_1-\rho_2)/\rho_1$), g is the acceleration due to gravity, with ρ_1 and ρ_2 the density of the light and dark fluids, respectively. For inertial flow the draw-up height is defined as:

$$d = c_2 (q^2 / g')^{1/5} \quad (11)$$

where c_2 was a second constant for the inertial experiments of Blake and Ivey, (1986a). In a similar way to Blake and Ivey (1986a), we calculate an experimental constant using mean values from our single piston experiments in both the viscous and inertial regimes. Our results for simple piston style subsidence show that as the volumetric flow rate increases, the draw-up height increases, agreeing with the power law relationships proposed by Blake and Ivey (1986a). This relationship is also shown in experiment 5,

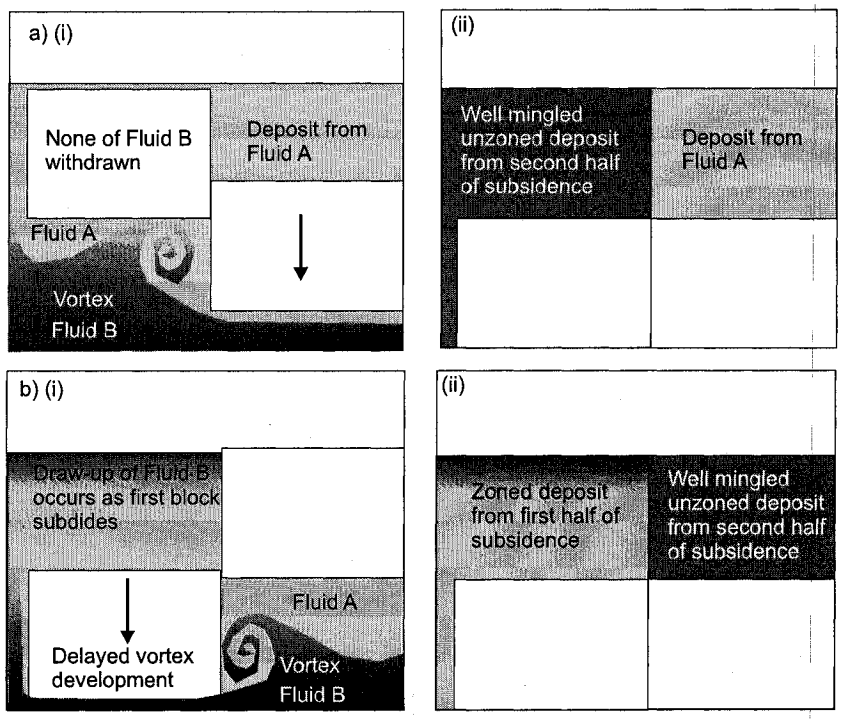
a) (i)
None of Fluid B withdrawn
Deposit from Fluid A
Fluid A
Vortex
Fluid B
(ii)
Well mingled unzoned deposit from second half of subsidence
Deposit from Fluid A
b) (i)
Draw-up of Fluid B occurs as first block subdides
Delayed vortex development
Fluid A
Vortex
Fluid B
(ii)
Zoned deposit from first half of subsidence
Well mingled unzoned deposit from second half of subsidence

lateral transfer of fluid was sufficient to cause uplift of the stationary block (Fig. 5 a, b). Since a portion of the fluid is channeled laterally into the other chamber instead of out the ring conduit, the fluid in the conduit moves relatively slowly for a given subsidence rate. As a result, the draw-up height is reduced. The lateral movement of fluid within the chamber not only affects the draw-up height, but also completely changes the style and timing of fluid interaction during the experiments.

EVOLUTION OF FLUID INTERACTIONS IN THE RING CONDUIT

Previous experimental models illustrated that the draw-up height controls the onset of magma interaction during withdrawal from a density-stratified chamber (Blake and Ivey, 1986a). Numerical models showed that the spatial distribution of the evacuation isochrons should also be considered in order to fully understand the duration of magma interaction (Fig. 1) (Spera, 1984; Spera et al., 1986; Trial et al., 1992). We could not create accurate evacuation isochrons from our experiments, but many experiments clearly showed the evolving proportions of the two different fluids within the chamber and ring conduit. We compared experiments using observations of the relative proportions of different fluids during and after subsidence.

Experiments with slow subsidence showed little fluid interaction in the conduit because of low Reynolds numbers and high densimetric Richardson numbers (Fig. 8). In addition, the slow experiments showed small draw-up heights, and no light fluid in the chamber at the end of subsidence. This produced relatively small volumes of mingled light and dark fluid, and a ring conduit that contained mostly unmingled dark fluid after subsidence ceased (Fig. 3a(iii)).

FIGURE 8. Richardson number plotted against fraction of fluid withdrawn from the chamber. As the block approaches the base of the chamber, the height of the chamber is reduced. The lateral velocity of fluid in the chamber increases because the subsidence rate and volumetric flow rate remain constant. Plot is based on experimental data for fastest and slowest subsidence rates and both single piston and two independently subsiding blocks. For complete data set, see Appendix I.

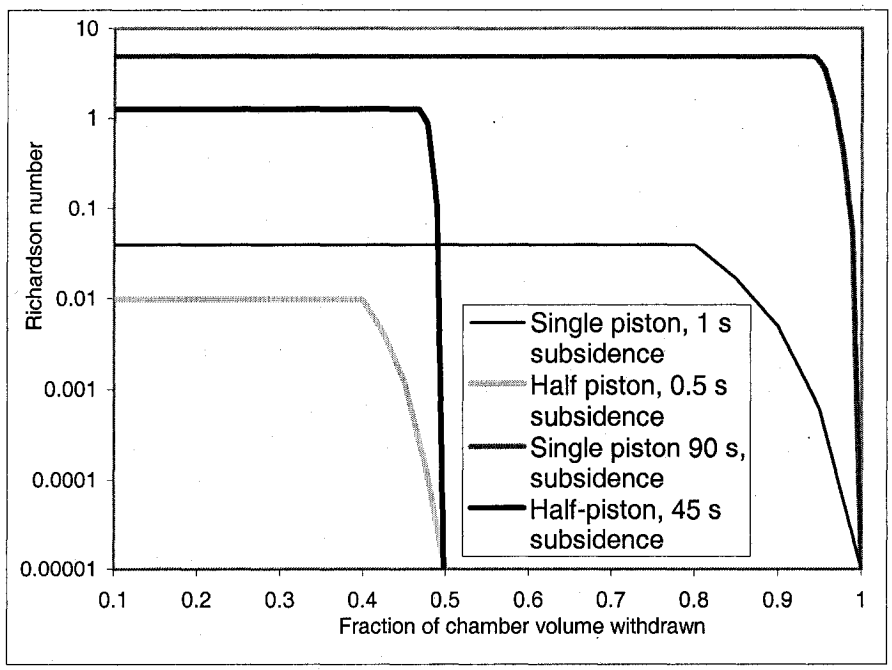
10
1
0.1
0.01
0.001
0.0001
0.00001
Richardson number
0.1
0.2
0.3
0.4
0.5
0.6
0.7
0.8
0.9
1
Fraction of chamber volume withdrawn
Single piston, 1 s subsidence
Half piston, 0.5 s subsidence
Single piston 90 s, subsidence
Half-piston, 45 s subsidence

The fast experiments showed enhanced fluid interaction in the conduit partly due to higher Reynolds and lower densimetric Richardson numbers (Fig. 8). More importantly, the fast experiments produced larger draw-up heights, and therefore dark fluid began to be withdrawn, while substantial volumes of light fluid remained in the chamber (Fig. 3d(iv)). Large draw-up heights produced a relatively large volume containing mingled light and dark fluid, and the dark fluid was never withdrawn alone. Towards the end of subsidence light fluid again was withdrawn producing a brief period of inverted zonation in the ring dyke. This observation is important because our experiments showed a period of rapid lateral flow as the subsiding block approached the base of the chamber (see below). At the end of subsidence the ring conduit contained a high proportion of light to dark fluid (Fig. 3a(iii)). The fluids continued to mingle after subsidence due to residual fluid motion and buoyancy contrasts (Fig. 3c (v), d(v)).

Experiments with tilted blocks altered the geometry of the chamber. The geometry of the tilted block allowed light fluid to remain beneath the uptilted block where subsidence was least, until a large proportion of the dark fluid had been withdrawn. As a result, light fluid fills large proportions of the ring conduit after subsidence had stopped (Fig. 4a). Trial et al. (1992) showed that tilted roofs allow the upper layers of the chamber to be erupted earlier compared to a flat roof. This apparent contradiction is easily explained by the location of the conduit relative to the slope of the chamber. In the numerical simulations, the roof sloped towards the conduit, while in our experiments the roof sloped away from the most active section of the conduit. Experiments with the ring conduit closed on one side also resulted in large proportions of light fluid in the ring conduit after subsidence ceased for similar reasons (Fig. 4b).

The presence of a central fissure between two blocks subsiding coherently increased the area of the ring conduit and consequently the subsidence rate and draw-up height. However, the increased vent area and decreased distance between vents allowed efficient extraction of light fluid from the chamber. This left a relatively small volume of light fluid as the block approached the base of the chamber. As a result, a small proportion of light fluid remained in the ring conduit compared to other rapid subsidence experiments (compare Fig. 3d(iv) with Fig. 4c(iv)).

The details of fluid interaction in the experiments could not be explained by draw-up heights alone. The volume of light fluid remaining in the chamber as the block reached the chamber base was also critical, particularly so in defining whether or not reverse zonation will be seen and the relative proportions of fluids that mingled in the ring conduit after subsidence stopped. Our experiments showed that the subsidence rate, the asymmetry of the block, and the location of the conduits influenced this volume of residual light fluid.

FLUID INTERACTIONS DURING LATERAL MOVEMENT IN THE CHAMBER

The velocity of lateral fluid movement increased as the block approached the base of the chamber. This acceleration can be explained because the height of the fluid remaining in the chamber became less than the draw-up height, while the subsidence rate and the volumetric flow rate remained constant. Therefore, the lateral velocity of the fluid in the chamber increased. The increased lateral velocity in the chamber and reduced chamber height caused the densimetric Richardson number to drop dramatically,

therefore, enhancing fluid interaction in the chamber (Fig. 8). This created a period of dynamic fluid interaction at the end of the experiment that defined the composition and textural variability in the ring conduit.

In slow experiments, the lateral flow velocity increased as the block approached the base of the chamber, rapidly decreasing the densimetric Richardson numbers. Despite lower densimetric Richardson numbers, however, there was no light fluid remaining to interact with the dark fluid, resulting in a ring conduit containing mostly unmingled dark fluid (Fig. 3a(iii)).

By contrast, fluid interaction in the fast experiments was enhanced as the block approached the base of the chamber because significant volumes of light fluid still remained in the chamber (Fig. 3c, d). As the block settled lateral flow accelerated, producing low densimetric Richardson numbers and mingling between the stratified layers. In addition, the accelerated evacuation of this light fluid produced a brief period of reverse zonation at the end of subsidence. After subsidence, the fluid in the ring conduit is relatively mingled (Fig. 3c(v), d(v)).

Lateral fluid movement in the chamber can further enhance fluid interaction, in particular, if fluid movement becomes circular and vortices develop in the chamber as fluid was withdrawn (Folch et al., 2001).

Experiments with two blocks caused a decrease in densimetric Richardson number and an increase lateral flow velocity at earlier stages compared to experiments with a single block (Fig. 8). This effect occurred because the first block approached the base of the chamber before the second block was released, and therefore, before the midpoint of the experiment. These experiments produced vortices in the chamber. We

hypothesize that the development of these vortices was additionally aided by flow separation. As the fluid was expelled from the narrow chamber under the subsiding block, it entered a wide chamber (Fig. 7). This situation is similar to the phenomenon of flow separation, which occurs as fluid flowing in a pipe suddenly experiences an increase in pipe diameter (Rouse, 1946). In several of these experiments, a large vortex was clearly visible in the chamber, which completely destroyed the chamber stratification, producing mingled fluid (Figs. 4a, b; 5a, b, c).

Vortices developed best in the case of the two independently subsiding blocks. In this situation, the location of the conduit influenced the flow velocity and vortex development. A vortex developed best when one block, with a closed ring conduit, subsided independently from the other block with an open ring conduit. In such a case, all of the fluid flowed laterally in the chamber before erupting through the conduit, thus increasing lateral flow rates (Fig 5a, 7b). In these experiments, the lateral flow velocity was highest, and the height of the chamber through which it flowed suddenly increased from narrow to wide. Both factors promote flow separation and vortex development. When the first subsiding block maintained an open conduit, the vortex developed later, rotating slower (Figs. 5b, 7a). This was because a large proportion of the fluid had flowed vertically out the open section of the ring conduit, and reduced the mean lateral flow velocity. The reduced lateral velocity delayed the development of the vortex until later during subsidence (Fig. 7a).

In both Figures 5a and 5b, the difference in thickness of the chamber under each block is at a maximum. This difference explains why the vortex is better developed in figure 5b(iv) compared to figure 5c(iii). In experiments where the block was intentionally

tilted, and with the eastern sections of the ring conduit closed, lateral flow rates in the chamber were also enhanced. The increased lateral flow velocity was sufficient to generate vortices of fluid in the chamber and ring conduit towards the end of subsidence (Figs. 4a(iv), 4b(v)).

The numerical models of Folch et al., (2001) showed similar vortex development at the chamber margins during subsidence of a single block. In these numerical simulations the chamber was wider than the subsiding block, also enabling flow separation. These models only allowed the development of vortices, when the magma had a viscosity of less than 10^4 Pa s, however, the effect of flow acceleration towards the end of subsidence was ignored in these models

In summary, the development of vortices involving two fluids increases the efficiency of the fluid interaction dramatically. It is an efficient mechanism to create large volumes of mingled or mixed fluids during caldera formation.

IMPLICATIONS FOR NATURAL SYSTEMS

We now discuss the relevance of these experiments for zoned eruption sequences and ring dykes. We consider different rates and styles of caldera formation above a chamber that contains two distinct density-stratified layers of silicic magma. However, the concepts are also applicable to other magmatic configurations.

ZONED ERUPTIONS

The fluid that rises up the ring conduit in the experiments and ponds above the subsiding block or blocks can be compared to zoned ignimbrite sequences from caldera forming eruptions. Ignimbrites can be zoned in terms of both pumice and bulk composition and are usually normally zoned, reflecting increasing proportions of denser more mafic magma from deeper within the chamber. Pumice compositions can be used to identify variations in composition within the magma chamber, while the bulk composition of the ignimbrite can be used to estimate the simultaneous withdrawal proportions associated with the draw-up height (Hildreth, 1979).

Our experiments indicate that a slow collapse rate implies a low volumetric eruption rate, and therefore a small draw-up height (Fig. 6). A slowly subsiding caldera would produce a zoned ignimbrite with an abrupt change in both pumice type and bulk composition over a short stratigraphic distance. Conversely, a rapid subsidence rate implies a high volumetric eruption rate and large draw-up height (Fig. 6). Therefore, a rapidly subsiding caldera would produce a zoned ignimbrite with a gradual increase in the relative proportions of pumice from the underlying denser magma, and a bulk composition that gradually changes over a relatively large stratigraphic distance. Our experiments show that changes in volumetric flow rate can cause fluctuations in the draw-up height, and thus, variations in the composition of fluid tapped (Fig. 3c(iii)). Therefore, large changes in the subsidence rate during caldera formation could produce a zoned ignimbrite that fluctuates in the proportion of pumice types and bulk composition. In these situations, our experiments broadly agree with previous models (Blake and Ivey, 1986a; Blake and Ivey, 1986b; Spera et al., 1986; Trial et al., 1992).

During the formation of Crater Lake caldera, Oregon, two zoned ignimbrites erupted: (1) the welded Wineglass Tuff associated with a central vent eruption, and (2) the Climactic Tuff associated with a ring fracture eruption. The proportion of ignimbrite containing pumices of two different compositions is higher in the Climactic Tuff than the Wineglass Tuff (Druitt and Bacon, 1989). Additionally, mixed pumices occur in the Climactic Tuff that are not seen in the Wineglass tuff. Our experiments explain this by higher volumetric eruption rates and larger draw-up heights associated with the ring fracture eruption of the Climactic Tuff. Larger volumetric eruption rates could be achieved during the ring fracture stage because of the greater cross-sectional vent area for a ring fracture compared to a central vent.

During the formation of Lake City caldera, Colorado the complexly zoned Sunshine Tuff erupted. The ignimbrite has an overall normal zonation broadly compatible with the downward tapping of a density-stratified chamber. However, towards the end of the eruption composition increasingly fluctuates and the end is marked by a brief period of reverse zonation. We propose that during the end of the eruption, the subsiding block approached the chamber base and lateral fluid flow accelerated, fluid interaction increased, and low-density magma preserved at the top of the chamber was erupted.

Our experiments imply that tilted subsidence and asymmetric vent dimensions cause different composition fluids to erupt simultaneously (Fig. 4a). Therefore, an asymmetrically subsiding or erupting caldera would produce a zoned ignimbrite with complex lateral, as well as vertical variation. Our experiments imply that lateral flow will occur within the chamber if subsidence and/or vent dimensions are highly asymmetric. If the lateral flow is sufficiently rapid or if the roof subsides in a piecemeal fashion, vortices

develop and cause a huge increase in fluid interaction. Therefore, an asymmetrically subsiding or erupting caldera could produce a zoned ignimbrite with substantial lateral and vertical compositional variation and a high percentage of mingled pumices.

The "TL" ignimbrite erupted from Gran Canaria caldera, Canary Islands, showed lateral variation in zonation patterns. Ignimbrite erupted from a vent in the west shows zonation distinct from ignimbrite erupted from a vent in the east (Sumner and Wolff, 2003). Sumner and Wolff (2003) explained this by asymmetric chamber replenishment. However, our experiments indicate that variation in flow velocity or subsidence asymmetry could also produce the different patterns of ignimbrite zonation.

The Lower Bandelier Tuff erupted during the formation of Toledo caldera, New Mexico shows a distinctive zonation. An initial plinian fall deposit homogeneous in Nb concentrations is followed by ignimbrite heterogeneous in Nb concentrations (Kuentz, 1986). The heterogeneous part of the ignimbrite shows no zonation, and so is difficult to explain by progressively tapping deeper layers in a density-stratified chamber (Kuentz, 1986). Kuentz (1986) has suggested that asymmetric collapse blocks could simultaneously tap various magma horizons. In addition, piecemeal or trapdoor style of subsidence has been suggested at Toledo caldera (Heiken et al, 1990). Our experimental models support this explanation and show that tilted collapse or piecemeal collapse could produce this style of zonation.

RING DYKES

Ring dykes commonly contain magma that was frozen in place as caldera collapse stopped. At the end of subsidence the ring conduits in our experiments illustrate various

compositional zonation patterns both vertically and horizontally. Some of these patterns also are seen in natural systems and can be used to infer particular subsidence styles. In some cases, however, post-collapse intrusion and eruption may have modified the ring dyke composition, so caution must be exercised.

Vertical variations in ring conduit composition were seen in several experiments. Slow experiments maintained the normal compositional zonation of the chamber, showing a darker compositional base in the ring conduit (Fig. 3a(iv)). However, in faster experiments, after subsidence stopped, light fluid formed bands at the base of the ring conduit. Initially, these bands produced reverse zonation in the ring conduits (e.g. Figs. 3c(iv), 3d(iv), 3e(iv)). These bands subsequently rose due to their buoyancy, causing mingling and erasing the vertical compositional zonation. The timescales of crystallization and flow due to buoyancy will determine whether reverse zonation in ring dykes is preserved in nature.

In our experiments, horizontal compositional variations were observed frequently. The horizontal variation was the result of several processes: (1) asymmetric subsidence caused the base of the ring conduit to be at different levels in the chamber, tapping different magma horizons (Fig. 4a(ii)); (2) variation in volumetric flow rate caused different draw-up heights at the base of the ring conduit, tapping different magma horizons (Fig. 4a(iii)); (3) diapirism of buoyant light fluid bands caused smaller scale horizontal and vertical variation (3d(v); (4) lateral flow and vortex development after collapse caused localized mingling in certain areas of the ring conduit (Fig. 4a(iv)). Our experiments demonstrate that these four mechanisms are important during asymmetric

collapse, indicating that asymmetric collapse and horizontal compositional variation in ring dykes are clearly linked.

The Peruvian Coastal batholith contains mingled ring dykes which are linked to caldera subsidence (Bussell, 1988). These dykes are stratified vertically and laterally. Each dyke is explained by a series of subsidence and magma emplacement events (Bussell, 1988). Our experiments demonstrate that these features do not necessarily indicate multiple intrusions. In fact, the ring dykes of the Peruvian Batholith and the Ossipee ring dyke, New Hampshire, show that compositional variation is usually gradational (Bussell, 1988; Chapter 1 this thesis). Gradational contacts are difficult to explain during multiple intrusions, but easily explained by mingling during simultaneous intrusion. Therefore, we propose that the processes associated with asymmetric collapse mentioned above could explain the horizontal compositional variation observed in many ring dykes. In addition to compositional horizontal variation, these processes may be responsible for the extensive mingling and magma mixing textures frequently present at ring dykes (Marshall and Sparks, 1984; Creasy and Eby, 1993; Johnson et al., 2002; Chapter 1, this thesis).

In summary, our experiments illustrate that most ring dykes associated with zoned magma chambers and caldera systems would be expected to show evidence of magma mingling and frequently exhibit compositional and textural variation.

CONCLUSIONS

Our analogue experiments are the first to directly model caldera collapse into a density-stratified chamber. The main conclusions of the study are as follows.

(1) Our results generally support the power-law relationship proposed by Blake and Ivey (1986a) that relates the beginning of fluid interaction (the draw-up height) to the volumetric flow rate and the relative densities of the fluids.

(2) Certain experiments also illustrate and support some of the numerical results of Trial et al. (1992), specifically: (a) a pause in eruption rate may cause compositional jumps; and (b) a tilted magma chamber roof affects how long fluid from the top of the chamber may remain in the chamber instead of being erupted.

(3) The experiments highlight the importance of the relative proportions of the fluids present as the block reaches the base of the chamber. In our experiments, this period of subsidence produces the most dynamic conditions and defines the compositions and textures of fluids erupted towards the end of subsidence and remaining in the ring conduit after subsidence terminates. We show that this period of flow can frequently produce reverse zonation in the ignimbrite or in the ring dyke.

(4) Asymmetric collapse and asymmetrically positioned vents lead to spatial variations in withdrawal rates and compositions, as well as the development of small volumes of mingled fluids at the end of the eruption. The experiments further indicate that asymmetric collapse events with rapid eruption rates generate large degrees of textural and compositional variation in ignimbrite and the ring dyke.

(5) Partial collapse of the chamber roof can produce large volumes of mingled fluid. Subsidence of part of a chamber roof causes lateral flow of magma into the un-collapsed volume of the chamber. Flow separation then occurs producing vortices. These vortices can be sufficiently large to disrupt and mingle stratification in the chamber. As the rest of the chamber roof collapses, a large unzoned mingled volume of magma forms in the chamber, forming compositionally heterogeneous ignimbrite and ring dykes.

Our experiments support old mechanisms and propose new mechanisms to interpret zoned ignimbrites and ring dykes. The realization of these mechanisms improves our ability to use ignimbrites and ring dykes to interpret magma chamber processes.

ACKNOWLEDGEMENTS

We thank Abby Peterson, Tyler Barton, and Geneviève Robert, for their assistance with the experiments. We also thank Steve Blake for useful input. Financial support was provided to B.K. by funds from the Department of Earth and Planetary Sciences, McGill University, and from GEOTOP, Université du Québec à Montréal, and by a research grant to J.S. from the Natural Sciences and Engineering Research Council of Canada. We also acknowledge support from NSF Grant EAR-0125631 to James Vallance and John Stix.

REFERENCES

Blake, S., and Ivey G.N., 1986a, Magma mixing and the dynamics of withdrawal from stratified reservoirs: Journal of Volcanology and Geothermal Research, v. 27, p. 153-178.

Blake S., and Ivey, G.N., 1986b, Density and viscosity gradients in zoned magma chambers, and their influences on withdrawal dynamics: Journal of Volcanology and Geothermal Research, v. 30, p. 201-230.

Blake, S., and Fink, J.H., 1987, The dynamics of magma withdrawal from a density stratified dyke: Earth and Planetary Science Letters, v. 85, p. 516-524.

Bussell, M.A., 1988, Structure and petrogenesis and a mixed-magma ring dyke in the Peruvian Coastal Batholith: eruptions from a zoned magma chamber: Transactions of the Royal Society of Edinburgh: Earth Sciences, v. 79, p. 87-104.

Creasy, J. W., and Eby, G. N., 1993, Ring dikes and plutons: a deeper view of calderas as illustrated by the White Mountain igneous province, New Hampshire: In Cheney, J. T., and Hepburn, J. C. (eds.), 1993, Field Trip Guidebook for the Northeastern United States.

Druitt, T.H., and Bacon, C.R., 1989, Petrology of the zoned calcalkaline magma chamber of Mount Mazama, Crater Lake, Oregon: Contributions to Mineralogy and Petrology, v. 101, p. 245-259.

Folch, A., Codina, R., and Marti, J., 2001, Numerical modeling of magma withdrawal during explosive caldera-forming eruptions: Journal of Geophysical Research, v. 106, p. 16,163-16,175.

Geshi, N., Shimano, T., Chiba, T., and Nakada, S., 2002, Caldera collapse during the 2000 eruption of Miyakejima Volcano, Japan: Bulletin of Volcanology, v. 64, p. 55-68.

Hess, K.U., and Dingwell, D.B., 1996, Viscosities of hydrous leucogranitic melts: A non-Arrhenian model: American Mineralogist, v.81, p. 1297-1300.

Giordano, D., and Dingwell, D.B., 2003, Non-Arrhenian multicomponent melt viscosity: a model: Earth and Planetary Science Letters, v. 208, p. 337-349.

Hildreth, W., 1979, The Bishop Tuff; evidence for the origin of compositional zonation in silicic magma chambers: Special Paper - Geological Society of America, no.180, p. 43-75.

Johnson, S.E., Schmidt, K.L., and Tait, M.C., 2002, Ring complexes in the Penninsular Ranges Batholith, Mexico and the USA: magma plumbing systems in the middle and upper crust: Lithos, v. 61, p. 187-208.

Kamata, H., Suzuki-Kamata, K., and Bacon, C.R., 1993, Deformation of the Wineglass Welded Tuff and the timing of caldera collapse at Crater Lake, Oregon: Journal of Volcanology and Geothermal Research, v. 56, p. 253-265.

Kennedy, B., and Stix, J., 2003, Igneous rock associations 1: Styles and mechanisms of caldera collapse; Geoscience Canada, v. 30, p. 59-72.

Kennedy B., Stix J., Lavallée Y., Richer M., and Longpré M.-A., 2003. A model for magmatism following caldera collapse: examples from Ossipee ring complex, New Hampshire, and Lake City caldera, Colorado (abstr.): IUGG General Assembly, Sapporo, Japan, June 30-July 11 2003, p. A526.

Koyaguchi, T., 1985, Magma mixing in a conduit: Journal of Volcanology and Geothermal Research, v. 25, p. 365-369.

Koyaguchi, T., and Takada, A., 1994, An experimental study on the formation of composite intrusions from zoned magma chambers: Journal of Volcanology and Geothermal Research, v. 59, p. 261-267.

Kuentz, D.C., 1986, The Otowi Member of the Bandelier Tuff; a study of the petrology, petrography, and geochemistry of an explosive silicic eruption, Jemez Mountains, New Mexico: Masters thesis, University of Texas, 168p.

Marshall, L.A., and Sparks, R.J., 1984, Origins of some mixed-magma and net-veined ring intrusions: Journal of the Geological Society of London, v. 141, p. 171-182.

Moore, I., and Kokelaar, P., 1998, Tectonically controlled piecemeal caldera collapse; a case study of Glencoe Volcano, Scotland: Geological Society of America Bulletin, v. 110, p. 1448-1466.

Rouse, H., 1946, Elementary Mechanics of Fluids: John Wiley & Sons, New York. 376p.

Simkin, T., and Fiske, R.S., 1983, Krakatau 1883—The volcanic eruption and its□effects: Smithsonian Institution Press, Washington, D.C., 464p.

Spera, F.J., 1984, Some numerical experiments on the withdrawal of magma from crustal reservoirs: Journal of Geophysical Research, v. 89, p. 8222-8236.

Spera, F.J., Yuen, D.A., Greer, J.C., and Sewell, G., 1986, Dynamics of magma withdrawal from stratified magma chambers: Geology, v. 14, p. 723-726.

Sumner, J.M., and Wolff, J., 2003, Petrogenesis of mixed-magma, high-grade, peralkaline ignimbrite "TL" (Gran Canaria); diverse styles of mixing in a replenished, zoned magma chamber: Journal of Volcanology and Geothermal Research, v. 126, p. 109-126.

Trial, A.F., Spera, F.J., Greer, J., and Yuen, D.A., 1992, Simulations of magma withdrawal from compositionally zoned bodies: Journal of Geophysical Research, v. 97, p. 6713-6733.

Wilson, C.J.N., and Hildreth, W.H., 1997, The Bishop Tuff; new insights from eruptive stratigraphy: Journal of Geology, v. 105, p. 407-439.

Wolfe E.W., and Hoblitt, R.P., 1996, Overview of the eruptions: In Newhall, C.G., and Punongbayan, R.S. (eds.), Fire and Mud, Eruptions and Lahars of Mount Pinatubo, Philippines: Philippine Institute of Volcanology and Seismology and the University of Washington Press, p. 3-20.

Wolff, J.A., Woerner, G., and Blake, S., 1990, Gradients in physical parameters in zoned felsic magma bodies; implications for evolution and eruptive withdrawal: Journal of Volcanology and Geothermal Research, v. 43, p. 37-55.

APPENDIX I

TABLE A-I. Complete data set used to create Figure 8.

Evolving fluid velocity during fast experiments

(s) time	(m^3) withdrawn volume	fraction withdrawn	(m) subsidence amount	($m\ s^{-1}$) volumetric flow rate	(m) thickness of withdrawal layer	(m^2) area of withdrawal layer	($m\ s^{-1}$) flow rate in ring conduit
0			0			0	0
0.05	0.000523	0.05	0.005	0.010463158	0.02	0.02293295	0.5478093
0.1	0.001046	0.1	0.01	0.010463158	0.02	0.02293295	0.5478093
0.15	0.001569	0.15	0.015	0.010463158	0.02	0.02293295	0.5478093
0.2	0.002093	0.2	0.02	0.010463158	0.02	0.02293295	0.5478093
0.25	0.002616	0.25	0.025	0.010463158	0.02	0.02293295	0.5478093
0.3	0.003139	0.3	0.03	0.010463158	0.02	0.02293295	0.5478093
0.35	0.003662	0.35	0.035	0.010463158	0.02	0.02293295	0.5478093
0.4	0.004185	0.4	0.04	0.010463158	0.02	0.02293295	0.5478093
0.45	0.004708	0.45	0.045	0.010463158	0.02	0.02293295	0.5478093
0.5	0.005232	0.5	0.05	0.010463158	0.02	0.02293295	0.5478093
0.55	0.005755	0.55	0.055	0.010463158	0.02	0.02293295	0.5478093
0.6	0.006278	0.6	0.06	0.010463158	0.02	0.02293295	0.5478093
0.65	0.006801	0.65	0.065	0.010463158	0.02	0.02293295	0.5478093
0.7	0.007324	0.7	0.07	0.010463158	0.02	0.02293295	0.5478093
0.75	0.007847	0.75	0.075	0.010463158	0.02	0.02293295	0.5478093
0.8	0.008371	0.8	0.08	0.010463158	0.02	0.02293295	0.5478093
0.85	0.008894	0.85	0.085	0.010463158	0.015	0.017199708	0.5478093
0.9	0.009417	0.9	0.09	0.010463158	0.01	0.011466471	0.5478093
0.95	0.00994	0.95	0.095	0.010463158	0.005	0.005733233	0.5478093
1	0.010463	1	0.1	0.010463158	-4.1813E-09	-4.79452E-09	0.5478093

Evolving fluid velocity during slow experiments

0	0	0	0	0	0	0	0
1	0.000116	0.011111	0.0011111	0.000116257	0.005	0.005733238	0.0060868
2	0.000233	0.022222	0.0022222	0.000116257	0.005	0.005733238	0.0060868
3	0.000349	0.033333	0.0033333	0.000116257	0.005	0.005733238	0.0060868
4	0.000465	0.044444	0.0044444	0.000116257	0.005	0.005733238	0.0060868
5	0.000581	0.055556	0.0055556	0.000116257	0.005	0.005733238	0.0060868
6	0.000698	0.066667	0.0066667	0.000116257	0.005	0.005733238	0.0060868
7	0.000814	0.077778	0.0077778	0.000116257	0.005	0.005733238	0.0060868
8	0.00093	0.088889	0.0088889	0.000116257	0.005	0.005733238	0.0060868
9	0.001046	0.1	0.01	0.000116257	0.005	0.005733238	0.0060868
10	0.001163	0.111111	0.0111111	0.000116257	0.005	0.005733238	0.0060868
11	0.001279	0.122222	0.0122222	0.000116257	0.005	0.005733238	0.0060868
12	0.001395	0.133333	0.0133333	0.000116257	0.005	0.005733238	0.0060868
13	0.001511	0.144444	0.0144444	0.000116257	0.005	0.005733238	0.0060868
14	0.001628	0.155556	0.0155556	0.000116257	0.005	0.005733238	0.0060868
15	0.001744	0.166667	0.0166667	0.000116257	0.005	0.005733238	0.0060868
16	0.00186	0.177778	0.0177778	0.000116257	0.005	0.005733238	0.0060868
17	0.001976	0.188889	0.0188889	0.000116257	0.005	0.005733238	0.0060868
18	0.002093	0.2	0.02	0.000116257	0.005	0.005733238	0.0060868
19	0.002209	0.211111	0.0211111	0.000116257	0.005	0.005733238	0.0060868
20	0.002325	0.222222	0.0222222	0.000116257	0.005	0.005733238	0.0060868
21	0.002441	0.233333	0.0233333	0.000116257	0.005	0.005733238	0.0060868
22	0.002558	0.244444	0.0244444	0.000116257	0.005	0.005733238	0.0060868
23	0.002674	0.255556	0.0255556	0.000116257	0.005	0.005733238	0.0060868

($m\ s^{-1}$) flow rate in chamber	Reynolds number in dyke	Reynolds number in chamber	Richardson number in dyke	Richardson number in chamber	(m) block he	($kg\ m^{-3}$) block density
#DIV/0!		#DIV/0!		#DIV/0!	0.15	1480
0.45625	639.1109	608.3333333	0.034596536	0.039271908	0.15	1480
0.45625	639.1109	608.3333333	0.034596536	0.039271908	0.15	1480
0.45625	639.1109	608.3333333	0.034596536	0.039271908	0.15	1480
0.45625	639.1109	608.3333333	0.034596536	0.039271908	0.15	1480
0.45625	639.1109	608.3333333	0.034596536	0.039271908	0.15	1480
0.45625	639.1109	608.3333333	0.034596536	0.039271908	0.15	1480
0.45625	639.1109	608.3333333	0.034596536	0.039271908	0.15	1480
0.45625	639.1109	608.3333333	0.034596536	0.039271908	0.15	1480
0.45625	639.1109	608.3333333	0.034596536	0.039271908	0.15	1480
0.45625	639.1109	608.3333333	0.034596536	0.039271908	0.15	1480
0.45625	639.1109	608.3333333	0.034596536	0.039271908	0.15	1480
0.45625	639.1109	608.3333333	0.034596536	0.039271908	0.15	1480
0.45625	639.1109	608.3333333	0.034596536	0.039271908	0.15	1480
0.45625	639.1109	608.3333333	0.034596536	0.039271908	0.15	1480
0.45625	639.1109	608.3333333	0.034596536	0.039271908	0.15	1480
0.45625	639.1109	608.3333333	0.034596536	0.039271908	0.15	1480
0.608333477	639.1109	608.3333333	0.034596536	0.016567825	0.15	1480
0.912500343	639.1109	608.3333333	0.034596536	0.004908983	0.15	1480
1.82500145	639.1109	608.3333333	0.034596536	0.000613622	0.15	1480
-2182315.812	639.1109	608.3333333	0.034596536	0.00001	0.15	1480
0	0	0	0	0	0	0
0.020277778	7.101232	6.759259259	280.2319394	4.97035091	0.15	1480
0.020277778	7.101232	6.759259259	280.2319394	4.97035091	0.15	1480
0.020277778	7.101232	6.759259259	280.2319394	4.97035091	0.15	1480
0.020277778	7.101232	6.759259259	280.2319394	4.97035091	0.15	1480
0.020277778	7.101232	6.759259259	280.2319394	4.97035091	0.15	1480
0.020277778	7.101232	6.759259259	280.2319394	4.97035091	0.15	1480
0.020277778	7.101232	6.759259259	280.2319394	4.97035091	0.15	1480
0.020277778	7.101232	6.759259259	280.2319394	4.97035091	0.15	1480
0.020277778	7.101232	6.759259259	280.2319394	4.97035091	0.15	1480
0.020277778	7.101232	6.759259259	280.2319394	4.97035091	0.15	1480
0.020277778	7.101232	6.759259259	280.2319394	4.97035091	0.15	1480
0.020277778	7.101232	6.759259259	280.2319394	4.97035091	0.15	1480
0.020277778	7.101232	6.759259259	280.2319394	4.97035091	0.15	1480
0.020277778	7.101232	6.759259259	280.2319394	4.97035091	0.15	1480
0.020277778	7.101232	6.759259259	280.2319394	4.97035091	0.15	1480
0.020277778	7.101232	6.759259259	280.2319394	4.97035091	0.15	1480
0.020277778	7.101232	6.759259259	280.2319394	4.97035091	0.15	1480
0.020277778	7.101232	6.759259259	280.2319394	4.97035091	0.15	1480
0.020277778	7.101232	6.759259259	280.2319394	4.97035091	0.15	1480
0.020277778	7.101232	6.759259259	280.2319394	4.97035091	0.15	1480
0.020277778	7.101232	6.759259259	280.2319394	4.97035091	0.15	1480
0.020277778	7.101232	6.759259259	280.2319394	4.97035091	0.15	1480
0.020277778	7.101232	6.759259259	280.2319394	4.97035091	0.15	1480
0.020277778	7.101232	6.759259259	280.2319394	4.97035091	0.15	1480
0.020277778	7.101232	6.759259259	280.2319394	4.97035091	0.15	1480
0.020277778	7.101232	6.759259259	280.2319394	4.97035091	0.15	1480

24	0.00279	0.266667	0.0266667	0.000116257	0.005	0.005733238	0.0060868
25	0.002906	0.277778	0.0277778	0.000116257	0.005	0.005733238	0.0060868
26	0.003023	0.288889	0.0288889	0.000116257	0.005	0.005733238	0.0060868
27	0.003139	0.3	0.03	0.000116257	0.005	0.005733238	0.0060868
28	0.003255	0.311111	0.0311111	0.000116257	0.005	0.005733238	0.0060868
29	0.003371	0.322222	0.0322222	0.000116257	0.005	0.005733238	0.0060868
30	0.003488	0.333333	0.0333333	0.000116257	0.005	0.005733238	0.0060868
31	0.003604	0.344444	0.0344444	0.000116257	0.005	0.005733238	0.0060868
32	0.00372	0.355556	0.0355556	0.000116257	0.005	0.005733238	0.0060868
33	0.003836	0.366667	0.0366667	0.000116257	0.005	0.005733238	0.0060868
34	0.003953	0.377778	0.0377778	0.000116257	0.005	0.005733238	0.0060868
35	0.004069	0.388889	0.0388889	0.000116257	0.005	0.005733238	0.0060868
36	0.004185	0.4	0.04	0.000116257	0.005	0.005733238	0.0060868
37	0.004302	0.411111	0.0411111	0.000116257	0.005	0.005733238	0.0060868
38	0.004418	0.422222	0.0422222	0.000116257	0.005	0.005733238	0.0060868
39	0.004534	0.433333	0.0433333	0.000116257	0.005	0.005733238	0.0060868
40	0.00465	0.444444	0.0444444	0.000116257	0.005	0.005733238	0.0060868
41	0.004767	0.455556	0.0455556	0.000116257	0.005	0.005733238	0.0060868
42	0.004883	0.466667	0.0466667	0.000116257	0.005	0.005733238	0.0060868
43	0.004999	0.477778	0.0477778	0.000116257	0.005	0.005733238	0.0060868
44	0.005115	0.488889	0.0488889	0.000116257	0.005	0.005733238	0.0060868
45	0.005232	0.5	0.05	0.000116257	0.005	0.005733238	0.0060868
46	0.005348	0.511111	0.0511111	0.000116257	0.005	0.005733238	0.0060868
47	0.005464	0.522222	0.0522222	0.000116257	0.005	0.005733238	0.0060868
48	0.00558	0.533333	0.0533333	0.000116257	0.005	0.005733238	0.0060868
49	0.005697	0.544444	0.0544444	0.000116257	0.005	0.005733238	0.0060868
50	0.005813	0.555556	0.0555556	0.000116257	0.005	0.005733238	0.0060868
51	0.005929	0.566667	0.0566667	0.000116257	0.005	0.005733238	0.0060868
52	0.006045	0.577778	0.0577778	0.000116257	0.005	0.005733238	0.0060868
53	0.006162	0.588889	0.0588889	0.000116257	0.005	0.005733238	0.0060868
54	0.006278	0.6	0.06	0.000116257	0.005	0.005733238	0.0060868
55	0.006394	0.611111	0.0611111	0.000116257	0.005	0.005733238	0.0060868
56	0.00651	0.622222	0.0622222	0.000116257	0.005	0.005733238	0.0060868
57	0.006627	0.633333	0.0633333	0.000116257	0.005	0.005733238	0.0060868
58	0.006743	0.644444	0.0644444	0.000116257	0.005	0.005733238	0.0060868
59	0.006859	0.655556	0.0655556	0.000116257	0.005	0.005733238	0.0060868
60	0.006975	0.666667	0.0666667	0.000116257	0.005	0.005733238	0.0060868
61	0.007092	0.677778	0.0677778	0.000116257	0.005	0.005733238	0.0060868
62	0.007208	0.688889	0.0688889	0.000116257	0.005	0.005733238	0.0060868
63	0.007324	0.7	0.07	0.000116257	0.005	0.005733238	0.0060868
64	0.00744	0.711111	0.0711111	0.000116257	0.005	0.005733238	0.0060868
65	0.007557	0.722222	0.0722222	0.000116257	0.005	0.005733238	0.0060868
66	0.007673	0.733333	0.0733333	0.000116257	0.005	0.005733238	0.0060868
67	0.007789	0.744444	0.0744444	0.000116257	0.005	0.005733238	0.0060868
68	0.007905	0.755556	0.0755556	0.000116257	0.005	0.005733238	0.0060868
69	0.008022	0.766667	0.0766667	0.000116257	0.005	0.005733238	0.0060868
70	0.008138	0.777778	0.0777778	0.000116257	0.005	0.005733238	0.0060868
71	0.008254	0.788889	0.0788889	0.000116257	0.005	0.005733238	0.0060868
72	0.008371	0.8	0.08	0.000116257	0.005	0.005733238	0.0060868
73	0.008487	0.811111	0.0811111	0.000116257	0.005	0.005733238	0.0060868
74	0.008603	0.822222	0.0822222	0.000116257	0.005	0.005733238	0.0060868
75	0.008719	0.833333	0.0833333	0.000116257	0.005	0.005733238	0.0060868

76	0.008836	0.844444	0.0844444	0.000116257	0.005	0.005733238	0.0060868
77	0.008952	0.855556	0.0855556	0.000116257	0.005	0.005733238	0.0060868
78	0.009068	0.866667	0.0866667	0.000116257	0.005	0.005733238	0.0060868
79	0.009184	0.877778	0.0877778	0.000116257	0.005	0.005733238	0.0060868
80	0.009301	0.888889	0.0888889	0.000116257	0.005	0.005733238	0.0060868
81	0.009417	0.9	0.09	0.000116257	0.005	0.005733238	0.0060868
82	0.009533	0.911111	0.0911111	0.000116257	0.005	0.005733238	0.0060868
83	0.009649	0.922222	0.0922222	0.000116257	0.005	0.005733238	0.0060868
84	0.009766	0.933333	0.0933333	0.000116257	0.005	0.005733238	0.0060868
85	0.009882	0.944444	0.0944444	0.000116257	0.005	0.005733238	0.0060868
86	0.009998	0.955556	0.0955556	0.000116257	0.00444444	0.005096207	0.0060868
87	0.010114	0.966667	0.0966667	0.000116257	0.00333333	0.003822154	0.0060868
88	0.010231	0.977778	0.0977778	0.000116257	0.00222222	0.002548101	0.0060868
89	0.010347	0.988889	0.0988889	0.000116257	0.00111111	0.001274048	0.0060868
90	0.010463	1	0.1	0.000116257	0	1E-17	0.0060868

Evolving fluid velocity during fast experiments with two independently subsiding blocks

(s) time	(m^3) eruption vo	% % erupted	(m) subsidence amount	($m\ s^{-1}$) volumetric flow rate	(m) thickness of withdrawal la	(m^2) area of withdrawal layer	($m\ s^{-1}$) flow rate in ring conduit
0	0	0	0		0.02	0.011466475	0
0.025	0.000262	0.025003	0.0050006	0.010463158	0.02	0.011466475	1.0956187
0.05	0.000523	0.050006	0.0100011	0.010463158	0.02	0.011466475	1.0956187
0.075	0.000785	0.075008	0.0150017	0.010463158	0.02	0.011466475	1.0956187
0.1	0.001046	0.100011	0.0200022	0.010463158	0.02	0.011466475	1.0956187
0.125	0.001308	0.125014	0.0250028	0.010463158	0.02	0.011466475	1.0956187
0.15	0.001569	0.150017	0.0300033	0.010463158	0.02	0.011466475	1.0956187
0.175	0.001831	0.175019	0.0350039	0.010463158	0.02	0.011466475	1.0956187
0.2	0.002093	0.200022	0.0400044	0.010463158	0.02	0.011466475	1.0956187
0.225	0.002354	0.225025	0.045005	0.010463158	0.02	0.011466475	1.0956187
0.25	0.002616	0.250028	0.0500055	0.010463158	0.02	0.011466475	1.0956187
0.275	0.002877	0.27503	0.0550061	0.010463158	0.02	0.011466475	1.0956187
0.3	0.003139	0.300033	0.0600066	0.010463158	0.02	0.011466475	1.0956187
0.325	0.003401	0.325036	0.0650072	0.010463158	0.02	0.011466475	1.0956187
0.35	0.003662	0.350039	0.0700078	0.010463158	0.02	0.011466475	1.0956187
0.375	0.003924	0.375042	0.0750083	0.010463158	0.02	0.011466475	1.0956187
0.4	0.004185	0.400044	0.0800089	0.010463158	0.02	0.011466475	1.0956187
0.425	0.004447	0.425047	0.0850094	0.010463158	0.01499059	0.00859446	1.0956187
0.45	0.004708	0.45005	0.09001	0.010463158	0.00999003	0.005727524	1.0956187
0.475	0.00497	0.475053	0.0950105	0.010463158	0.00498948	0.002860588	1.0956187
0.5	0.005232	0.5	0.1	0.010463158	-4.1813E-09	-4.79452E-09	1.0956187

Evolving fluid velocity during slow experiments with two independently subsiding blocks

(s) time	(m^3) eruption vo	% % erupted	(m) subsidence amount	($m\ s^{-1}$) volumetric flow rate	(m) thickness of withdrawal la	(m^2) area of withdrawal layer	($m\ s^{-1}$) flow rate in ring conduit
0		0	0		0.005	0.002866619	0
1	0.000116	0.011112	0.0022225	0.000116257	0.005	0.002866619	0.0121735
2	0.000233	0.022225	0.0044449	0.000116257	0.005	0.002866619	0.0121735
3	0.000349	0.033337	0.0066674	0.000116257	0.005	0.002866619	0.0121735
4	0.000465	0.044449	0.0088899	0.000116257	0.005	0.002866619	0.0121735
5	0.000581	0.055562	0.0111123	0.000116257	0.005	0.002866619	0.0121735

6	0.000698	0.066674	0.0133348	0.000116257	0.005	0.002866619	0.0121735
7	0.000814	0.077786	0.0155573	0.000116257	0.005	0.002866619	0.0121735
8	0.00093	0.088899	0.0177797	0.000116257	0.005	0.002866619	0.0121735
9	0.001046	0.100011	0.0200022	0.000116257	0.005	0.002866619	0.0121735
10	0.001163	0.111123	0.0222247	0.000116257	0.005	0.002866619	0.0121735
11	0.001279	0.122236	0.0244472	0.000116257	0.005	0.002866619	0.0121735
12	0.001395	0.133348	0.0266696	0.000116257	0.005	0.002866619	0.0121735
13	0.001511	0.14446	0.0288921	0.000116257	0.005	0.002866619	0.0121735
14	0.001628	0.155573	0.0311146	0.000116257	0.005	0.002866619	0.0121735
15	0.001744	0.166685	0.033337	0.000116257	0.005	0.002866619	0.0121735
16	0.00186	0.177797	0.0355595	0.000116257	0.005	0.002866619	0.0121735
17	0.001976	0.18891	0.037782	0.000116257	0.005	0.002866619	0.0121735
18	0.002093	0.200022	0.0400044	0.000116257	0.005	0.002866619	0.0121735
19	0.002209	0.211134	0.0422269	0.000116257	0.005	0.002866619	0.0121735
20	0.002325	0.222247	0.0444494	0.000116257	0.005	0.002866619	0.0121735
21	0.002441	0.233359	0.0466718	0.000116257	0.005	0.002866619	0.0121735
22	0.002558	0.244472	0.0488943	0.000116257	0.005	0.002866619	0.0121735
23	0.002674	0.255584	0.0511168	0.000116257	0.005	0.002866619	0.0121735
24	0.00279	0.266696	0.0533392	0.000116257	0.005	0.002866619	0.0121735
25	0.002906	0.277809	0.0555617	0.000116257	0.005	0.002866619	0.0121735
26	0.003023	0.288921	0.0577842	0.000116257	0.005	0.002866619	0.0121735
27	0.003139	0.300033	0.0600066	0.000116257	0.005	0.002866619	0.0121735
28	0.003255	0.311146	0.0622291	0.000116257	0.005	0.002866619	0.0121735
29	0.003371	0.322258	0.0644516	0.000116257	0.005	0.002866619	0.0121735
30	0.003488	0.33337	0.066674	0.000116257	0.005	0.002866619	0.0121735
31	0.003604	0.344483	0.0688965	0.000116257	0.005	0.002866619	0.0121735
32	0.00372	0.355595	0.071119	0.000116257	0.005	0.002866619	0.0121735
33	0.003836	0.366707	0.0733415	0.000116257	0.005	0.002866619	0.0121735
34	0.003953	0.37782	0.0755639	0.000116257	0.005	0.002866619	0.0121735
35	0.004069	0.388932	0.0777864	0.000116257	0.005	0.002866619	0.0121735
36	0.004185	0.400044	0.0800089	0.000116257	0.005	0.002866619	0.0121735
37	0.004302	0.411157	0.0822313	0.000116257	0.005	0.002866619	0.0121735
38	0.004418	0.422269	0.0844538	0.000116257	0.005	0.002866619	0.0121735
39	0.004534	0.433381	0.0866763	0.000116257	0.005	0.002866619	0.0121735
40	0.00465	0.444494	0.0888987	0.000116257	0.005	0.002866619	0.0121735
41	0.004767	0.455606	0.0911212	0.000116257	0.005	0.002866619	0.0121735
42	0.004883	0.466718	0.0933437	0.000116257	0.005	0.002866619	0.0121735
43	0.004999	0.477831	0.0955661	0.000116257	0.00443386	0.002542039	0.0121735
44	0.005115	0.488943	0.0977886	0.000116257	0.0022114	0.001267846	0.0121735
45	0.005232	0.500055	0.1000111	0.000116257	-1.1073E-05	-6.34831E-06	0.0121735

0.020277778	7.101232	6.759259259	280.2319394	4.97035091	0.15	1480
0.020277778	7.101232	6.759259259	280.2319394	4.97035091	0.15	1480
0.020277778	7.101232	6.759259259	280.2319394	4.97035091	0.15	1480
0.020277778	7.101232	6.759259259	280.2319394	4.97035091	0.15	1480
0.020277778	7.101232	6.759259259	280.2319394	4.97035091	0.15	1480
0.020277778	7.101232	6.759259259	280.2319394	4.97035091	0.15	1480
0.020277778	7.101232	6.759259259	280.2319394	4.97035091	0.15	1480
0.020277778	7.101232	6.759259259	280.2319394	4.97035091	0.15	1480
0.020277778	7.101232	6.759259259	280.2319394	4.97035091	0.15	1480
0.020277778	7.101232	6.759259259	280.2319394	4.97035091	0.15	1480
0.020277778	7.101232	6.759259259	280.2319394	4.97035091	0.15	1480
0.020277778	7.101232	6.759259259	280.2319394	4.97035091	0.15	1480
0.020277778	7.101232	6.759259259	280.2319394	4.97035091	0.15	1480
0.020277778	7.101232	6.759259259	280.2319394	4.97035091	0.15	1480
0.020277778	7.101232	6.759259259	280.2319394	4.97035091	0.15	1480
0.020277778	7.101232	6.759259259	280.2319394	4.97035091	0.15	1480
0.020277778	7.101232	6.759259259	280.2319394	4.97035091	0.15	1480
0.020277778	7.101232	6.759259259	280.2319394	4.97035091	0.15	1480
0.020277778	7.101232	6.759259259	280.2319394	4.97035091	0.15	1480
0.020277778	7.101232	6.759259259	280.2319394	4.97035091	0.15	1480
0.020277778	7.101232	6.759259259	280.2319394	4.97035091	0.15	1480
0.020277778	7.101232	6.759259259	280.2319394	4.97035091	0.15	1480
0.020277778	7.101232	6.759259259	280.2319394	4.97035091	0.15	1480
0.020277778	7.101232	6.759259259	280.2319394	4.97035091	0.15	1480
0.020277778	7.101232	6.759259259	280.2319394	4.97035091	0.15	1480
0.020277778	7.101232	6.759259259	280.2319394	4.97035091	0.15	1480
0.020277778	7.101232	6.759259259	280.2319394	4.97035091	0.15	1480
0.020277778	7.101232	6.759259259	280.2319394	4.97035091	0.15	1480
0.020277778	7.101232	6.759259259	280.2319394	4.97035091	0.15	1480
0.020277778	7.101232	6.759259259	280.2319394	4.97035091	0.15	1480
0.020277778	7.101232	6.759259259	280.2319394	4.97035091	0.15	1480
0.020277778	7.101232	6.759259259	280.2319394	4.97035091	0.15	1480
0.020277778	7.101232	6.759259259	280.2319394	4.97035091	0.15	1480
0.020277778	7.101232	6.759259259	280.2319394	4.97035091	0.15	1480
0.020277778	7.101232	6.759259259	280.2319394	4.97035091	0.15	1480
0.020277778	7.101232	6.759259259	280.2319394	4.97035091	0.15	1480
0.020277778	7.101232	6.759259259	280.2319394	4.97035091	0.15	1480
0.020277778	7.101232	6.759259259	280.2319394	4.97035091	0.15	1480
0.020277778	7.101232	6.759259259	280.2319394	4.97035091	0.15	1480
0.020277778	7.101232	6.759259259	280.2319394	4.97035091	0.15	1480
0.020277778	7.101232	6.759259259	280.2319394	4.97035091	0.15	1480
0.020277778	7.101232	6.759259259	280.2319394	4.97035091	0.15	1480
0.020277778	7.101232	6.759259259	280.2319394	4.97035091	0.15	1480
0.020277778	7.101232	6.759259259	280.2319394	4.97035091	0.15	1480
0.020277778	7.101232	6.759259259	280.2319394	4.97035091	0.15	1480
0.020277778	7.101232	6.759259259	280.2319394	4.97035091	0.15	1480
0.020277778	7.101232	6.759259259	280.2319394	4.97035091	0.15	1480
0.020277778	7.101232	6.759259259	280.2319394	4.97035091	0.15	1480
0.020277778	7.101232	6.759259259	280.2319394	4.97035091	0.15	1480
0.020277778	7.101232	6.759259259	280.2319394	4.97035091	0.15	1480
0.020277778	7.101232	6.759259259	280.2319394	4.97035091	0.15	1480
0.020277778	7.101232	6.759259259	280.2319394	4.97035091	0.15	1480

0.020277778	7.101232	6.759259259	280.2319394	4.97035091	0.15	1480
0.020277778	7.101232	6.759259259	280.2319394	4.97035091	0.15	1480
0.020277778	7.101232	6.759259259	280.2319394	4.97035091	0.15	1480
0.020277778	7.101232	6.759259259	280.2319394	4.97035091	0.15	1480
0.020277778	7.101232	6.759259259	280.2319394	4.97035091	0.15	1480
0.020277778	7.101232	6.759259259	280.2319394	4.97035091	0.15	1480
0.020277778	7.101232	6.759259259	280.2319394	4.97035091	0.15	1480
0.020277778	7.101232	6.759259259	280.2319394	4.97035091	0.15	1480
0.020277778	7.101232	6.759259259	280.2319394	4.97035091	0.15	1480
0.020277778	7.101232	6.759259259	280.2319394	4.97035091	0.15	1480
0.022812521	7.101232	6.759259259	280.2319394	3.49082689	0.15	1480
0.030416704	7.101232	6.759259259	280.2319394	1.472691209	0.15	1480
0.045625084	7.101232	6.759259259	280.2319394	0.43635213	0.15	1480
0.09125034	7.101232	6.759259259	280.2319394	0.054543708	0.15	1480
1.16257E+13	7.101232	0	280.2319394	0.00001	0.15	1480

($m\ s^{-1}$) flow rate in chamber	Reynolds i in dyke	Reynolds no. in chamber	Richardson number in dyke	Richardson number in chamber	(m) block he	($kg\ m^{-3}$) block density
0	0	0		#DIV/0!	0.15	1480
0.9125	1278.222	1216.666667	#REF!	0.009817977	0.15	1480
0.9125	1278.222	1216.666667	#REF!	0.009817977	0.15	1480
0.9125	1278.222	1216.666667	#REF!	0.009817977	0.15	1480
0.9125	1278.222	1216.666667	#REF!	0.009817977	0.15	1480
0.9125	1278.222	1216.666667	#REF!	0.009817977	0.15	1480
0.9125	1278.222	1216.666667	#REF!	0.009817977	0.15	1480
0.9125	1278.222	1216.666667	#REF!	0.009817977	0.15	1480
0.9125	1278.222	1216.666667	#REF!	0.009817977	0.15	1480
0.9125	1278.222	1216.666667	#REF!	0.009817977	0.15	1480
0.9125	1278.222	1216.666667	#REF!	0.009817977	0.15	1480
0.9125	1278.222	1216.666667	#REF!	0.009817977	0.15	1480
0.9125	1278.222	1216.666667	#REF!	0.009817977	0.15	1480
0.9125	1278.222	1216.666667	#REF!	0.009817977	0.15	1480
0.9125	1278.222	1216.666667	#REF!	0.009817977	0.15	1480
0.9125	1278.222	1216.666667	#REF!	0.009817977	0.15	1480
0.9125	1278.222	1216.666667	#REF!	0.009817977	0.15	1480
1.217430555	1278.222	1216.666667	#REF!	0.004134167	0.15	1480
1.826820523	1278.222	1216.666667	#REF!	0.001223582	0.15	1480
3.657695184	1278.222	1216.666667	#REF!	0.00015244	0.15	1480
-2182315.812	1278.222	608.3333333	#REF!	0.00001	0.15	1480

($m\ s^{-1}$) flow rate in chamber	Reynolds i in dyke	Reynolds no. in chamber	Richardson number in dyke	Richardson number in chamber	(m) block he	($kg\ m^{-3}$) block density
0	0	0		#DIV/0!	0.15	1480
0.040555556	14.20246	13.51851852	#REF!	1.242587728	0.15	1480
0.040555556	14.20246	13.51851852	#REF!	1.242587728	0.15	1480
0.040555556	14.20246	13.51851852	#REF!	1.242587728	0.15	1480
0.040555556	14.20246	13.51851852	#REF!	1.242587728	0.15	1480
0.040555556	14.20246	13.51851852	#REF!	1.242587728	0.15	1480

0.040555556	14.20246	13.51851852	#REF!	1.242587728	0.15	1480
0.040555556	14.20246	13.51851852	#REF!	1.242587728	0.15	1480
0.040555556	14.20246	13.51851852	#REF!	1.242587728	0.15	1480
0.040555556	14.20246	13.51851852	#REF!	1.242587728	0.15	1480
0.040555556	14.20246	13.51851852	#REF!	1.242587728	0.15	1480
0.040555556	14.20246	13.51851852	#REF!	1.242587728	0.15	1480
0.040555556	14.20246	13.51851852	#REF!	1.242587728	0.15	1480
0.040555556	14.20246	13.51851852	#REF!	1.242587728	0.15	1480
0.040555556	14.20246	13.51851852	#REF!	1.242587728	0.15	1480
0.040555556	14.20246	13.51851852	#REF!	1.242587728	0.15	1480
0.040555556	14.20246	13.51851852	#REF!	1.242587728	0.15	1480
0.040555556	14.20246	13.51851852	#REF!	1.242587728	0.15	1480
0.040555556	14.20246	13.51851852	#REF!	1.242587728	0.15	1480
0.040555556	14.20246	13.51851852	#REF!	1.242587728	0.15	1480
0.040555556	14.20246	13.51851852	#REF!	1.242587728	0.15	1480
0.040555556	14.20246	13.51851852	#REF!	1.242587728	0.15	1480
0.040555556	14.20246	13.51851852	#REF!	1.242587728	0.15	1480
0.040555556	14.20246	13.51851852	#REF!	1.242587728	0.15	1480
0.040555556	14.20246	13.51851852	#REF!	1.242587728	0.15	1480
0.040555556	14.20246	13.51851852	#REF!	1.242587728	0.15	1480
0.040555556	14.20246	13.51851852	#REF!	1.242587728	0.15	1480
0.040555556	14.20246	13.51851852	#REF!	1.242587728	0.15	1480
0.040555556	14.20246	13.51851852	#REF!	1.242587728	0.15	1480
0.040555556	14.20246	13.51851852	#REF!	1.242587728	0.15	1480
0.040555556	14.20246	13.51851852	#REF!	1.242587728	0.15	1480
0.040555556	14.20246	13.51851852	#REF!	1.242587728	0.15	1480
0.040555556	14.20246	13.51851852	#REF!	1.242587728	0.15	1480
0.040555556	14.20246	13.51851852	#REF!	1.242587728	0.15	1480
0.040555556	14.20246	13.51851852	#REF!	1.242587728	0.15	1480
0.040555556	14.20246	13.51851852	#REF!	1.242587728	0.15	1480
0.040555556	14.20246	13.51851852	#REF!	1.242587728	0.15	1480
0.040555556	14.20246	13.51851852	#REF!	1.242587728	0.15	1480
0.040555556	14.20246	13.51851852	#REF!	1.242587728	0.15	1480
0.040555556	14.20246	13.51851852	#REF!	1.242587728	0.15	1480
0.040555556	14.20246	13.51851852	#REF!	1.242587728	0.15	1480
0.040555556	14.20246	13.51851852	#REF!	1.242587728	0.15	1480
0.040555556	14.20246	13.51851852	#REF!	1.242587728	0.15	1480
0.045733877	14.20246	13.51851852	#REF!	0.866491047	0.15	1480
0.09169675	14.20246	13.51851852	#REF!	0.107501939	0.15	1480
-18.31312532	14.20246	13.51851852	#REF!	0.000001	0.15	1480

(kg m^{-3}) fluid density 1	(kg m^{-3}) fluid density 2	(m s^{-2}) gravity	(m) dyke width	(Pa s) viscosity 1	(Pa s) viscosity 2	(m^3) single block area of ring dyke	(m^3) double area of ring dyke
1200	1250	9.81	0.0254	0.018	0.028	0.0191	0.0275
1200	1250	9.81	0.0254	0.018	0.028	0.0191	0.0275
1200	1250	9.81	0.0254	0.018	0.028	0.0191	0.0275
1200	1250	9.81	0.0254	0.018	0.028	0.0191	0.0275
1200	1250	9.81	0.0254	0.018	0.028	0.0191	0.0275
1200	1250	9.81	0.0254	0.018	0.028	0.0191	0.0275
1200	1250	9.81	0.0254	0.018	0.028	0.0191	0.0275
1200	1250	9.81	0.0254	0.018	0.028	0.0191	0.0275
1200	1250	9.81	0.0254	0.018	0.028	0.0191	0.0275
1200	1250	9.81	0.0254	0.018	0.028	0.0191	0.0275
1200	1250	9.81	0.0254	0.018	0.028	0.0191	0.0275
1200	1250	9.81	0.0254	0.018	0.028	0.0191	0.0275
1200	1250	9.81	0.0254	0.018	0.028	0.0191	0.0275
1200	1250	9.81	0.0254	0.018	0.028	0.0191	0.0275
1200	1250	9.81	0.0254	0.018	0.028	0.0191	0.0275
1200	1250	9.81	0.0254	0.018	0.028	0.0191	0.0275
1200	1250	9.81	0.0254	0.018	0.028	0.0191	0.0275
1200	1250	9.81	0.0254	0.018	0.028	0.0191	0.0275
1200	1250	9.81	0.0254	0.018	0.028	0.0191	0.0275
1200	1250	9.81	0.0254	0.018	0.028	0.0191	0.0275
1200	1250	9.81	0.0254	0.018	0.028	0.0191	0.0275
0	0	0	0	0	0	0	0
1200	1250	9.81	0.0254	0.018	0.028	0.0191	0.0275
1200	1250	9.81	0.0254	0.018	0.028	0.0191	0.0275
1200	1250	9.81	0.0254	0.018	0.028	0.0191	0.0275
1200	1250	9.81	0.0254	0.018	0.028	0.0191	0.0275
1200	1250	9.81	0.0254	0.018	0.028	0.0191	0.0275
1200	1250	9.81	0.0254	0.018	0.028	0.0191	0.0275
1200	1250	9.81	0.0254	0.018	0.028	0.0191	0.0275
1200	1250	9.81	0.0254	0.018	0.028	0.0191	0.0275
1200	1250	9.81	0.0254	0.018	0.028	0.0191	0.0275
1200	1250	9.81	0.0254	0.018	0.028	0.0191	0.0275
1200	1250	9.81	0.0254	0.018	0.028	0.0191	0.0275
1200	1250	9.81	0.0254	0.018	0.028	0.0191	0.0275
1200	1250	9.81	0.0254	0.018	0.028	0.0191	0.0275
1200	1250	9.81	0.0254	0.018	0.028	0.0191	0.0275
1200	1250	9.81	0.0254	0.018	0.028	0.0191	0.0275
1200	1250	9.81	0.0254	0.018	0.028	0.0191	0.0275
1200	1250	9.81	0.0254	0.018	0.028	0.0191	0.0275
1200	1250	9.81	0.0254	0.018	0.028	0.0191	0.0275
1200	1250	9.81	0.0254	0.018	0.028	0.0191	0.0275
1200	1250	9.81	0.0254	0.018	0.028	0.0191	0.0275
1200	1250	9.81	0.0254	0.018	0.028	0.0191	0.0275
1200	1250	9.81	0.0254	0.018	0.028	0.0191	0.0275
1200	1250	9.81	0.0254	0.018	0.028	0.0191	0.0275

1200	1250	9.81	0.0254	0.018	0.028	0.0191	0.0275
1200	1250	9.81	0.0254	0.018	0.028	0.0191	0.0275
1200	1250	9.81	0.0254	0.018	0.028	0.0191	0.0275
1200	1250	9.81	0.0254	0.018	0.028	0.0191	0.0275
1200	1250	9.81	0.0254	0.018	0.028	0.0191	0.0275
1200	1250	9.81	0.0254	0.018	0.028	0.0191	0.0275
1200	1250	9.81	0.0254	0.018	0.028	0.0191	0.0275
1200	1250	9.81	0.0254	0.018	0.028	0.0191	0.0275
1200	1250	9.81	0.0254	0.018	0.028	0.0191	0.0275
1200	1250	9.81	0.0254	0.018	0.028	0.0191	0.0275
1200	1250	9.81	0.0254	0.018	0.028	0.0191	0.0275
1200	1250	9.81	0.0254	0.018	0.028	0.0191	0.0275
1200	1250	9.81	0.0254	0.018	0.028	0.0191	0.0275
1200	1250	9.81	0.0254	0.018	0.028	0.0191	0.0275
1200	1250	9.81	0.0254	0.018	0.028	0.0191	0.0275
1200	1250	9.81	0.0254	0.018	0.028	0.0191	0.0275
1200	1250	9.81	0.0254	0.018	0.028	0.0191	0.0275
1200	1250	9.81	0.0254	0.018	0.028	0.0191	0.0275
1200	1250	9.81	0.0254	0.018	0.028	0.0191	0.0275
1200	1250	9.81	0.0254	0.018	0.028	0.0191	0.0275
1200	1250	9.81	0.0254	0.018	0.028	0.0191	0.0275
1200	1250	9.81	0.0254	0.018	0.028	0.0191	0.0275
1200	1250	9.81	0.0254	0.018	0.028	0.0191	0.0275
1200	1250	9.81	0.0254	0.018	0.028	0.0191	0.0275
1200	1250	9.81	0.0254	0.018	0.028	0.0191	0.0275
1200	1250	9.81	0.0254	0.018	0.028	0.0191	0.0275
1200	1250	9.81	0.0254	0.018	0.028	0.0191	0.0275
1200	1250	9.81	0.0254	0.018	0.028	0.0191	0.0275
1200	1250	9.81	0.0254	0.018	0.028	0.0191	0.0275
1200	1250	9.81	0.0254	0.018	0.028	0.0191	0.0275
1200	1250	9.81	0.0254	0.018	0.028	0.0191	0.0275
1200	1250	9.81	0.0254	0.018	0.028	0.0191	0.0275
1200	1250	9.81	0.0254	0.018	0.028	0.0191	0.0275
1200	1250	9.81	0.0254	0.018	0.028	0.0191	0.0275
1200	1250	9.81	0.0254	0.018	0.028	0.0191	0.0275
1200	1250	9.81	0.0254	0.018	0.028	0.0191	0.0275
1200	1250	9.81	0.0254	0.018	0.028	0.0191	0.0275
1200	1250	9.81	0.0254	0.018	0.028	0.0191	0.0275
1200	1250	9.81	0.0254	0.018	0.028	0.0191	0.0275
1200	1250	9.81	0.0254	0.018	0.028	0.0191	0.0275
1200	1250	9.81	0.0254	0.018	0.028	0.0191	0.0275
1200	1250	9.81	0.0254	0.018	0.028	0.0191	0.0275
1200	1250	9.81	0.0254	0.018	0.028	0.0191	0.0275
1200	1250	9.81	0.0254	0.018	0.028	0.0191	0.0275
1200	1250	9.81	0.0254	0.018	0.028	0.0191	0.0275
1200	1250	9.81	0.0254	0.018	0.028	0.0191	0.0275
1200	1250	9.81	0.0254	0.018	0.028	0.0191	0.0275
1200	1250	9.81	0.0254	0.018	0.028	0.0191	0.0275
1200	1250	9.81	0.0254	0.018	0.028	0.0191	0.0275
1200	1250	9.81	0.0254	0.018	0.028	0.0191	0.0275
1200	1250	9.81	0.0254	0.018	0.028	0.0191	0.0275
1200	1250	9.81	0.0254	0.018	0.028	0.0191	0.0275

1200	1250	9.81	0.0254	0.018	0.028	0.0191	0.0275
1200	1250	9.81	0.0254	0.018	0.028	0.0191	0.0275
1200	1250	9.81	0.0254	0.018	0.028	0.0191	0.0275
1200	1250	9.81	0.0254	0.018	0.028	0.0191	0.0275
1200	1250	9.81	0.0254	0.018	0.028	0.0191	0.0275
1200	1250	9.81	0.0254	0.018	0.028	0.0191	0.0275
1200	1250	9.81	0.0254	0.018	0.028	0.0191	0.0275
1200	1250	9.81	0.0254	0.018	0.028	0.0191	0.0275
1200	1250	9.81	0.0254	0.018	0.028	0.0191	0.0275
1200	1250	9.81	0.0254	0.018	0.028	0.0191	0.0275
1200	1250	9.81	0.0254	0.018	0.028	0.0191	0.0275
1200	1250	9.81	0.0254	0.018	0.028	0.0191	0.0275
1200	1250	9.81	0.0254	0.018	0.028	0.0191	0.0275
1200	1250	9.81	0.0254	0.018	0.028	0.0191	0.0275

($kg\ m^{-3}$) fluid density 1	($kg\ m^{-3}$) fluid density 2	($m\ s^{-2}$) gravity	(m) dyke width	(Pa s) viscosity 1	(Pa s) viscosity 2	(m^3) single block area of ring dyke	(m^3) double area of ring dyke
1200	1250	9.81	0.0254	0.018	0.028	0.00955	0.0275
1200	1250	9.81	0.0254	0.018	0.028	0.00955	0.0275
1200	1250	9.81	0.0254	0.018	0.028	0.00955	0.0275
1200	1250	9.81	0.0254	0.018	0.028	0.00955	0.0275
1200	1250	9.81	0.0254	0.018	0.028	0.00955	0.0275
1200	1250	9.81	0.0254	0.018	0.028	0.00955	0.0275
1200	1250	9.81	0.0254	0.018	0.028	0.00955	0.0275
1200	1250	9.81	0.0254	0.018	0.028	0.00955	0.0275
1200	1250	9.81	0.0254	0.018	0.028	0.00955	0.0275
1200	1250	9.81	0.0254	0.018	0.028	0.00955	0.0275
1200	1250	9.81	0.0254	0.018	0.028	0.00955	0.0275
1200	1250	9.81	0.0254	0.018	0.028	0.00955	0.0275
1200	1250	9.81	0.0254	0.018	0.028	0.00955	0.0275
1200	1250	9.81	0.0254	0.018	0.028	0.00955	0.0275
1200	1250	9.81	0.0254	0.018	0.028	0.00955	0.0275
1200	1250	9.81	0.0254	0.018	0.028	0.00955	0.0275
1200	1250	9.81	0.0254	0.018	0.028	0.00955	0.0275
1200	1250	9.81	0.0254	0.018	0.028	0.00955	0.0275
1200	1250	9.81	0.0254	0.018	0.028	0.00955	0.0275
1200	1250	9.81	0.0254	0.018	0.028	0.00955	0.0275
1200	1250	9.81	0.0254	0.018	0.028	0.00955	0.0275
1200	1250	9.81	0.0254	0.018	0.028	0.00955	0.0275
1200	1250	9.81	0.0254	0.018	0.028	0.00955	0.0275

($kg\ m^{-3}$) fluid density 1	($kg\ m^{-3}$) fluid density 2	($m\ s^{-2}$) gravity	(m) dyke width	(Pa s) viscosity 1	(Pa s) viscosity 2	(m^3) single block area of ring dyke	(m^3) double area of ring dyke
1200	1250	9.81	0.0254	0.018	0.028	0.00955	0.0275
1200	1250	9.81	0.0254	0.018	0.028	0.00955	0.0275
1200	1250	9.81	0.0254	0.018	0.028	0.00955	0.0275
1200	1250	9.81	0.0254	0.018	0.028	0.00955	0.0275
1200	1250	9.81	0.0254	0.018	0.028	0.00955	0.0275
1200	1250	9.81	0.0254	0.018	0.028	0.00955	0.0275

1200	1250	9.81	0.0254	0.018	0.028	0.00955	0.0275
1200	1250	9.81	0.0254	0.018	0.028	0.00955	0.0275
1200	1250	9.81	0.0254	0.018	0.028	0.00955	0.0275
1200	1250	9.81	0.0254	0.018	0.028	0.00955	0.0275
1200	1250	9.81	0.0254	0.018	0.028	0.00955	0.0275
1200	1250	9.81	0.0254	0.018	0.028	0.00955	0.0275
1200	1250	9.81	0.0254	0.018	0.028	0.00955	0.0275
1200	1250	9.81	0.0254	0.018	0.028	0.00955	0.0275
1200	1250	9.81	0.0254	0.018	0.028	0.00955	0.0275
1200	1250	9.81	0.0254	0.018	0.028	0.00955	0.0275
1200	1250	9.81	0.0254	0.018	0.028	0.00955	0.0275
1200	1250	9.81	0.0254	0.018	0.028	0.00955	0.0275
1200	1250	9.81	0.0254	0.018	0.028	0.00955	0.0275
1200	1250	9.81	0.0254	0.018	0.028	0.00955	0.0275
1200	1250	9.81	0.0254	0.018	0.028	0.00955	1.0275
1200	1250	9.81	0.0254	0.018	0.028	0.00955	2.0275
1200	1250	9.81	0.0254	0.018	0.028	0.00955	3.0275
1200	1250	9.81	0.0254	0.018	0.028	0.00955	4.0275
1200	1250	9.81	0.0254	0.018	0.028	0.00955	5.0275
1200	1250	9.81	0.0254	0.018	0.028	0.00955	6.0275
1200	1250	9.81	0.0254	0.018	0.028	0.00955	7.0275
1200	1250	9.81	0.0254	0.018	0.028	0.00955	8.0275
1200	1250	9.81	0.0254	0.018	0.028	0.00955	9.0275
1200	1250	9.81	0.0254	0.018	0.028	0.00955	10.0275
1200	1250	9.81	0.0254	0.018	0.028	0.00955	11.0275
1200	1250	9.81	0.0254	0.018	0.028	0.00955	12.0275
1200	1250	9.81	0.0254	0.018	0.028	0.00955	13.0275
1200	1250	9.81	0.0254	0.018	0.028	0.00955	14.0275
1200	1250	9.81	0.0254	0.018	0.028	0.00955	15.0275
1200	1250	9.81	0.0254	0.018	0.028	0.00955	16.0275
1200	1250	9.81	0.0254	0.018	0.028	0.00955	17.0275
1200	1250	9.81	0.0254	0.018	0.028	0.00955	18.0275
1200	1250	9.81	0.0254	0.018	0.028	0.00955	19.0275
1200	1250	9.81	0.0254	0.018	0.028	0.00955	20.0275
1200	1250	9.81	0.0254	0.018	0.028	0.00955	21.0275
1200	1250	9.81	0.0254	0.018	0.028	0.00955	22.0275
1200	1250	9.81	0.0254	0.018	0.028	0.00955	23.0275
1200	1250	9.81	0.0254	0.018	0.028	0.00955	24.0275
1200	1250	9.81	0.0254	0.018	0.028	0.00955	25.0275

CHAPTER 4

Magmatic processes associated with the development of large silicic calderas

Ben Kennedy, John Stix and Ken Hon

ABSTRACT

Magma chamber processes beneath large calderas are poorly understood. Here we present evidence of three processes central to caldera development: (1) magma chamber rejuvenation before caldera formation, (2) magma interaction within the chamber during caldera subsidence, and (3) shallow intrusion after collapse. We discuss these processes using field and geochemical data from Ossipee ring complex, New Hampshire, Lake City caldera, Colorado, and scaled analogue models. At Ossipee, intrusion of hot magma at the base of a magma mush lowered the bulk viscosity and reduced the crystallinity of the resident magma. Crystallinity reduction associated with chamber rejuvenation created an underpressure sufficient to cause failure of the roof of the magma chamber. As the roof collapses to form a caldera, magmatic processes accelerate as magma flows within the chamber at rates up of 10^5 to 10^7 m^3 s^{-1}. Scaled analogue experiments of asymmetric or piecemeal caldera collapse into density-stratified chambers show that this type of collapse drives lateral magma flow in the chamber which can develop vortices. These experiments demonstrate the mechanisms responsible for mingled and mixed liquids erupted and intruded at Ossipee ring complex and Lake City caldera during caldera subsidence. The development of the caldera influences magma behavior subsequent to collapse. Renewed magmatism at Lake City caldera resulted in the emplacement of magma at shallow levels, and similar styles of resurgence are seen at other calderas. During caldera collapse, new lithostatic pressure gradients and magma pathways develop, which facilitate the propagation of dykes and the rise of new magma above the main magma reservoir. In summary, when a caldera forms, a series of closely spaced magmatic

and structural events cause profound changes in the plumbing system of high-level silicic magma systems. Hot mafic magma rejuvenates stagnant crystallizing silicic magma causing underpressure and consequent caldera collapse. The asymmetric or piecemeal collapse of the caldera generates vigorous lateral magma movements within the magma chamber, resulting in efficient magma interaction. After collapse, magmas rise along structures created during subsidence and pond at shallow levels in the caldera, thereby causing resurgence.

INTRODUCTION

The scientific view of large shallow silicic magma chambers is undergoing a profound re-examination. The image of a single, spherical, fluid-filled magma chamber that dominated early petrological models (e.g. Smith, 1979) is oversimplified and in some instances misleading. Geophysicists have not identified large bodies of liquid magma at shallow levels in the crust under currently active calderas. This fact has led to the view of a large silicic magma chamber as a slowly crystallizing crystal mush with largely crystalline margins and the highest liquid contents at the chamber center (Marsh, 2000). But silicic crystal mushes are problematic to erupt (Takeuchi, 2004), requiring magma rejuvenation (Halliday et al., 1989; Bachman and Bergantz, 2003). Magma replenishment causes chamber rejuvenation and affects the magma within the chamber by locally altering the crystallinity and producing magmatic stratification (Eichelberger et al., 2000).

The scientific view of how calderas collapse is also undergoing re-examination. Calderas that subside symmetrically as single pistons are rare (Branney, 1991; Kennedy and Stix, 2003). Most young calderas are not exposed sufficiently to accurately assess the style of caldera collapse. As a result, piston styles of collapse commonly have been inferred, e.g., Valles caldera, New Mexico (Smith and Bailey, 1968), and Glencoe caldera, Scotland (Williams, 1941). Most numerical caldera models also have assumed symmetric piston-style subsidence, the results showing limited magma interactions (e.g., Spera, 1984; Spera et al., 1986; Trail et al., 1992). However, detailed studies of the intracaldera deposits at Glencoe (Moore and Kokelaar, 1998), and drillhole and geophysical data at Valles (Heiken et al., 1990), reveal substantial variations in intracaldera thickness at both calderas. These important observations show that calderas frequently collapse as a series of blocks or involve significant amounts of tilting (Branney, 1991). The style of caldera collapse affects the geometry of the magma chamber and the spatial evolution of pressure and magma flow in the chamber (Chapter 3, this thesis). In turn, chamber geometry, pressure differentials and magmatic flow rates play a fundamental role in determining magmatic processes during collapse.

A period of resurgence commonly follows caldera collapse. The mechanism of resurgence has been attributed to chamber inflation, regional detumesence, amongst other mechanisms (Smith and Bailey, 1968; Marsh, 1984). Detailed field studies of well-exposed calderas (e.g. Hon, 1987), drillhole data (e.g. McConnell et al., 1995), and analogue models (Acocella and Funicello, 1999) have revealed that shallow intrusions are an important cause of caldera resurgence.

In this paper we integrate the current understanding of magma chambers, caldera collapse, and resurgence into a synthetic view of magmatic processes associated with caldera formation. For this synthesis we draw on the following: (1) a discussion of magmatic properties that affect these processes, (2) a numerical model that links chamber rejuvenation with underpressure development, (3) textural and chemical characteristics of rocks from Lake City caldera and Ossipee ring complex, and (4) scaled analogue models of magma movement during caldera collapse.

MAGMA CHAMBER REJUVENATION

A large silicic magma chamber may require rejuvenation to allow dykes from the top of the chamber to reach the surface and erupt (Takeuchi and Nakamura, 2001; Takeuchi, 2004). The transport and accumulation of silicic magma at shallow levels in the crust require about 10^5 years (Petford et al., 2000; Jellinek and DePaolo, 2003). Magmatic evolution from crystal fractionation may require a further 10^4 to 10^6 years to separate evolved liquid from crystals (e.g. Wolff et al., 1990). These lines of evidence indicate that shallow silicic magma chambers accumulate and evolve over a long period of time (e.g., 4 x10^6 years, Coleman et al., 2004). As a result, these chambers are in variable states of crystallization and can be visualized as crystal mush (Marsh, 2000). Large silicic chambers have warm wall rocks which deform visco-elastically, making it difficult to build up gas pressure through crystallization (Jellinek and DePaolo, 2003). In addition, a silicic crystal mush has high viscosity that impedes its transport through dykes to the surface, making this type of magma difficult to erupt (Rubin, 1995; Takeuchi and

Nakamura, 2001; Takeuchi, 2004). If gas pressure does build up sufficiently to fracture the partially molten roof rocks, the magma may be too viscous to propagate within the fracture. Instead only gas may leak out of the fracture, reducing overpressure. Therefore, an external eruption trigger may be necessary to initiate silicic eruptions in many cases.

The initiation of some large caldera-forming eruptions may be caused by rejuvenation from hotter mafic magma (Bachman and Bergantz, 2003). In the case of smaller andesitic eruptions, the hotter lower-viscosity magma may interact briefly with the resident magma and form a dyke to the surface, allowing eruption from the chamber (Takeuchi, 2004). In large silicic systems, however, there is less evidence for precursory mafic dykes, and replenishing magma frequently ponds at the base of the chamber (Troll and Schminke, 2002; Sumner and Wolf, 2003; Troll et al., 2004; Wiebe et al., 2004). The mafic magma will heat the overlying silicic magma, and also may provide volatiles necessary to drive the eruption (Bachman and Bergantz, 2003).

A stratified chamber can form from fractional crystallization (Hildreth, 1981), or as replenishing magmas pond at the chamber base (Eichelberger et al., 2000). Stratification will be maintained if the replenished magma does not vesiculate sufficiently to become buoyant (Eichelberger, 1980). Magma chamber replenishment is often associated with the generation of overpressure, either due to magma mixing and vesiculation (Sparks et al., 1977), or from rapid replenishment (Woods and Koyaguchi, 1994). However, we suggest that chamber replenishment, accompanied by chamber floor subsidence (Cruden, 1998), can occur without the creation of significant overpressure, creating a stratified magmatic system. Heat transfer occurs between the two magmas, and a sufficiently thick layer of hot mafic magma induces melting in the silicic crystal mush

(Wiebe et al., 2004). Only a small temperature change is required to produce melting because the resident silicic magma is at or near a eutectic composition (Halliday et al., 1989). Therefore, replenishment is an efficient mechanism to reduce the crystallinity of the resident crystal mush.

We propose that this reduction in crystallinity produces a reduction in chamber pressure. Tait et al. (1989) have shown that crystallization of anhydrous crystals reduces the volume of liquid magma in which volatiles can be dissolved, thereby increasing the mass of free gas, and hence overpressure. Inverting this argument, melting anhydrous crystals will increase the volume of liquid magma in which volatiles can be dissolved, thereby, reducing the mass of free gas in bubbles, and decreasing gas pressure. In both scenarios, the elastic deformation of the chamber is insufficient to accommodate the volumetric changes involved in the magma. The basic pressure equation of Tait et al. (1989) can be used to model this process:

$$P = P_i(1-M_m/M)^{1/n} \quad (1)$$

where P is the new lower pressure in the chamber, P_i is the initial pressure, M_m is the mass of melt generated during rejuvenation, M is the total mass of magma (crystals, vesicles and liquid), n is the exponent for the solubility law of water in rhyolite. Hence M_m/M is the mass fraction of melt generated during rejuvenation, $P-P_i$ is the underpressure (negative value) in the chamber (Fig. 1). Terms that include melting expansion, elastic deformation, and initial mass of gas are calculated in the same manner as Tait et al. (1989) and used in full to plot Figure 1.

FIGURE 1. Mass fraction of remaining crystals plotted against the underpressure produced in the chamber. Appropriate parameters for a large silicic magma chamber and based on equations presented in Tait et al. (1989).

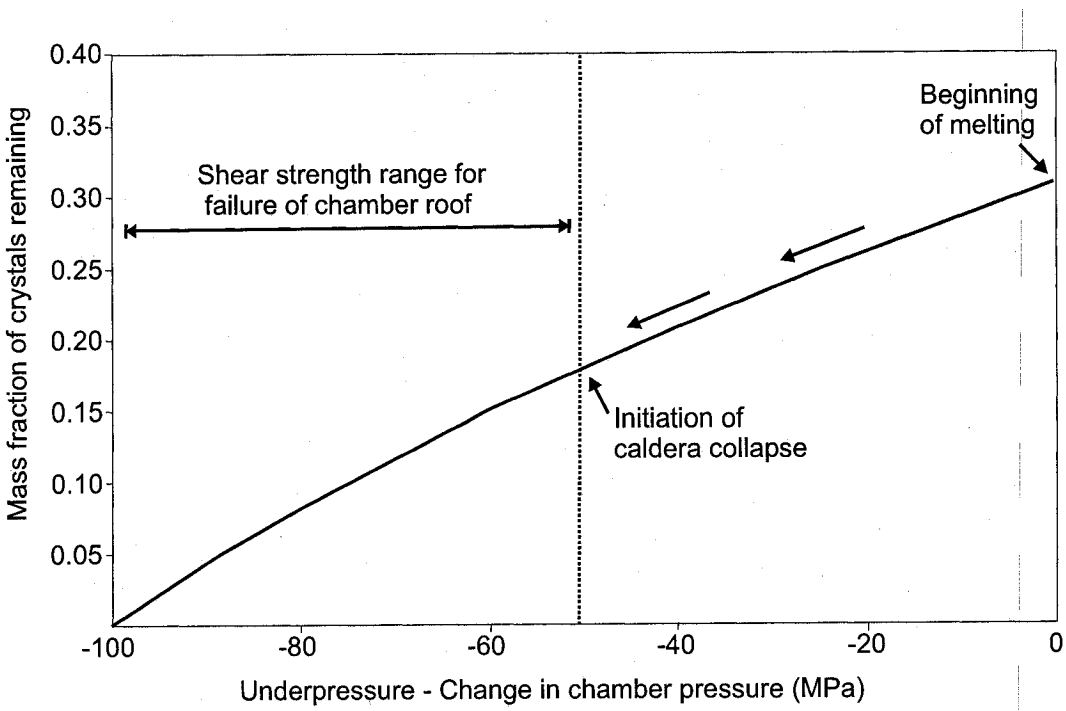
0.40
0.35
0.30
0.25
0.20
0.15
0.10
0.05
Mass fraction of crystals remaining
Shear strength range for
failure of chamber roof
Beginning
of melting
Initiation of
caldera collapse
-100
-80
-60
-40
-20
0
Underpressure - Change in chamber pressure (MPa)

Figure 1 shows the pressure decrease as the melt fraction increases. The elastic contraction of the chamber, and volume increase caused by expansion during melting are insufficient to compensate for the decrease in pressure in the bubbles. As a result, the chamber pressure drops, producing increasingly negative underpressures. If the magnitude of the pressure drop is greater than the compressive strength of the chamber roof 50 to 100 MPa (Rosenberg and Handy, 2005), the roof will fail, opening conduits to the surface and forming a caldera. This sequence of events is seen at Ossipee ring complex, New Hampshire.

The Ossipee ring complex shows extensive evidence for magmatic rejuvenation immediately prior to caldera formation. Fine-grained enclaves with partially dissolved cumulate crystals are observed in ring dyke rocks (Fig. 2a), suggesting that they were derived from the base of the magma chamber. In contrast to all other Ossipee rocks, these enclaves exhibit positive Eu anomalies on REE plots (Fig. 2b). We interpret these enclaves as a remelted cumulate from the base of the silicic magma chamber. The fine-grained groundmass of the rocks indicates that this remelting event immediately preceded eruption. Basalt also crops out in the ring dyke, showing evidence of being liquid at the same time as the cumulate enclaves. However, there is little evidence of magma mixing between the basalt and the remelted cumulate. This observation indicates that mafic magma ponded beneath silicic magma before collapse producing a stable magmatic stratification, rather than large-scale mixing and overpressure development (Chapter 1, this thesis).

FIGURE 2. (a) Photograph of an enclave in quartz syenite of remelted syenitic cumulate. (b) REE concentrations for whole-rock compositions of silicic samples at Ossipee; mean values from Eby (unpublished data) are plotted for comparison. REE concentrations are normalized to the chondritic meteorite of Taylor and McLennan (1985).

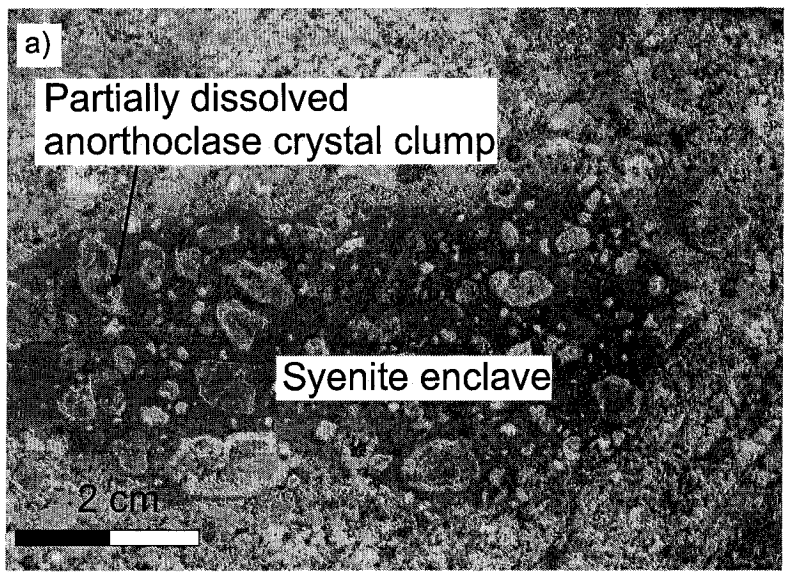
a)
Partially dissolved anorthoclase crystal clump
Syenite enclave
2 cm

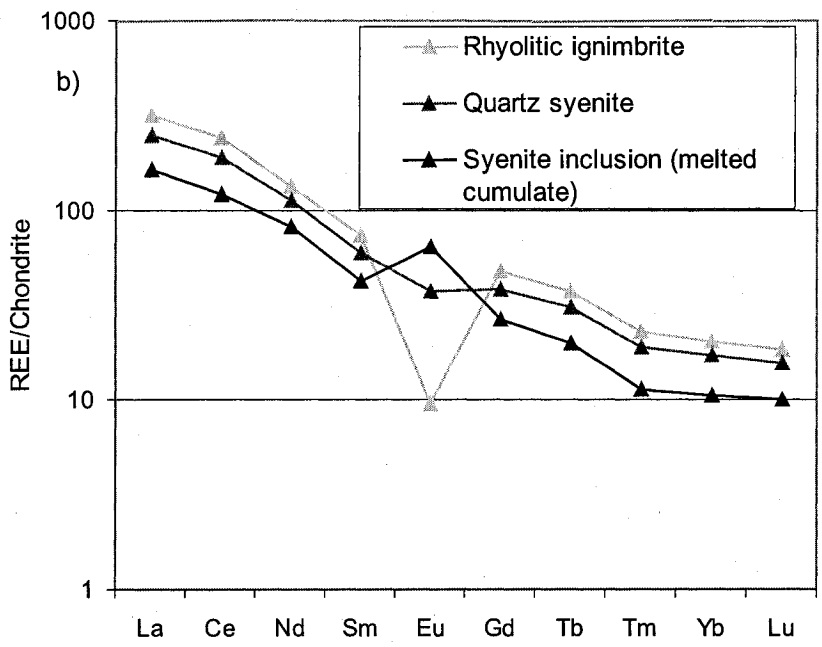
b)
Rhyolitic ignimbrite
Quartz syenite
Syenite inclusion (melted cumulate)
REE/Chondrite
1000
100
10
1
La
Ce
Nd
Sm
Eu
Gd
Tb
Tm
Yb
Lu

In summary, magma replenishment rejuvenates silicic systems by increasing the proportion of liquid in the magma and producing an underpressure sufficiently large for caldera formation.

MAGMA FLOW DURING CALDERA COLLAPSE

Once a magma chamber has been rejuvenated by the mechanism outlined above, it contains density-stratified magmas. Magma chambers are frequently vertically stratified according to density. Stratification from replenishment is common in large silicic chambers (Eichelberger et al., 2000). Also, stratification can develop from fractional crystallization or double diffusive convection (Anderson et al., 2000; Sparks et al., 1984). Sidewall crystallization also leads to concentric variations in magma properties (e.g. Marsh, 2000). A large silicic magma chamber may contain both concentric and vertical variation. During caldera collapse large volumetric flow rates (10^5 to 10^8 m^3 s^{-1}) occur in the chamber which cause magmatic interaction between these stratified layers.

During caldera collapse, magma is progressively expelled through a vent or vents, and magmatic flow may disrupt chamber stratification. As a caldera subsides symmetrically, the temporal pattern of this magma withdrawal, as well as the proportion of simultaneous withdrawal of different layers, is linked to the eruption rate, density contrasts between magmatic layers, vent locations, and chamber dimensions (Blake and Ivey, 1986a; Blake and Ivey, 1986b; Spera, 1984; Spera et al., 1986; Trail et al., 1992). When a caldera collapses, the geometry of the magma chamber may change, affecting the flow of magma within a chamber. Magma may not be expelled directly through a vent,

but instead form vortices in the magma chamber. In this manner, magmas may interact in the chamber before they erupt (Folch et al., 2001; Chapter 3, this thesis). Scaled analogue experiments of caldera collapse into density- and viscosity-stratified chambers indicate that magma interaction is enhanced by (1) partial collapse of a large chamber (Fig. 3b), (2) a steeply dipping collapse block (Fig. 3c), and (3) asymmetrically positioned vents (Fig. 3d). Piecemeal collapse of the chamber roof is particularly efficient at producing large volumes of mixed fluid (Fig. 3b). Additionally, the experiments indicate that an accelerated phase of fluid interaction occurs as the collapsing block approaches the base of the chamber. This acceleration can produce mixed and mingled fluid in the ring conduit, even during slow symmetric subsidence (Fig. 3a).

At both Ossipee ring complex and Lake City caldera, there is evidence for substantial magma mingling towards the end of caldera collapse. At Ossipee, enclaves of remelted syenite cumulate occur in small amounts in the rhyolitic ignimbrite but are abundant and efficiently redistributed in the quartz syenite ring dyke emplaced at the end of caldera collapse (Fig. 2a). In addition, the ring dyke shows lateral compositional variation from granite and rhyolitic tuff in some areas to quartz syenite and syenite in other zones (Chapter 1, this thesis). This variation is similar to the lateral compositional variation and mingling observed in the ring conduits in many asymmetric experiments (Fig. 3c).

At Lake City caldera, the first ignimbrite to erupt was the Lower Sunshine Tuff; this unit contains only high silica rhyolite pumice and shows little chemical variation (Fig. 4). The second ignimbrite to erupt was the Middle Sunshine Tuff; this unit contains both high silica rhyolite and mafic trachyte pumices. The base of the unit is rich in mafic

FIGURE 3. (a) Two images of an experiment with slow symmetric subsidence. Fluid interaction was limited in this experiment. (b) Two images of an experiment where only part of the chamber roof initially subsided. During the subsidence of the first block, a vortex was produced in the chamber beneath the part of the roof that did not collapse, disrupting the stratification. Only light fluid was expelled during the subsidence of the first block; no interaction occurred with the denser fluid below. The fluid expelled during the subsidence of the second block was all mingled fluid. (c) Two images of an experiment where the subsiding block was strongly tilted. During the first half of the experiment the composition of fluid in the ring conduit varied. In the second half of the experiment, as the block touched down a vortex was created that mingled fluid in the east of the ring conduit. (d) Two images of an experiment where only the western half of the ring conduit was open. In the first half of the experiment fluid was expelled up the western conduit. In the second half of the experiment, fluid formed a vortex in the conduit and mingled.

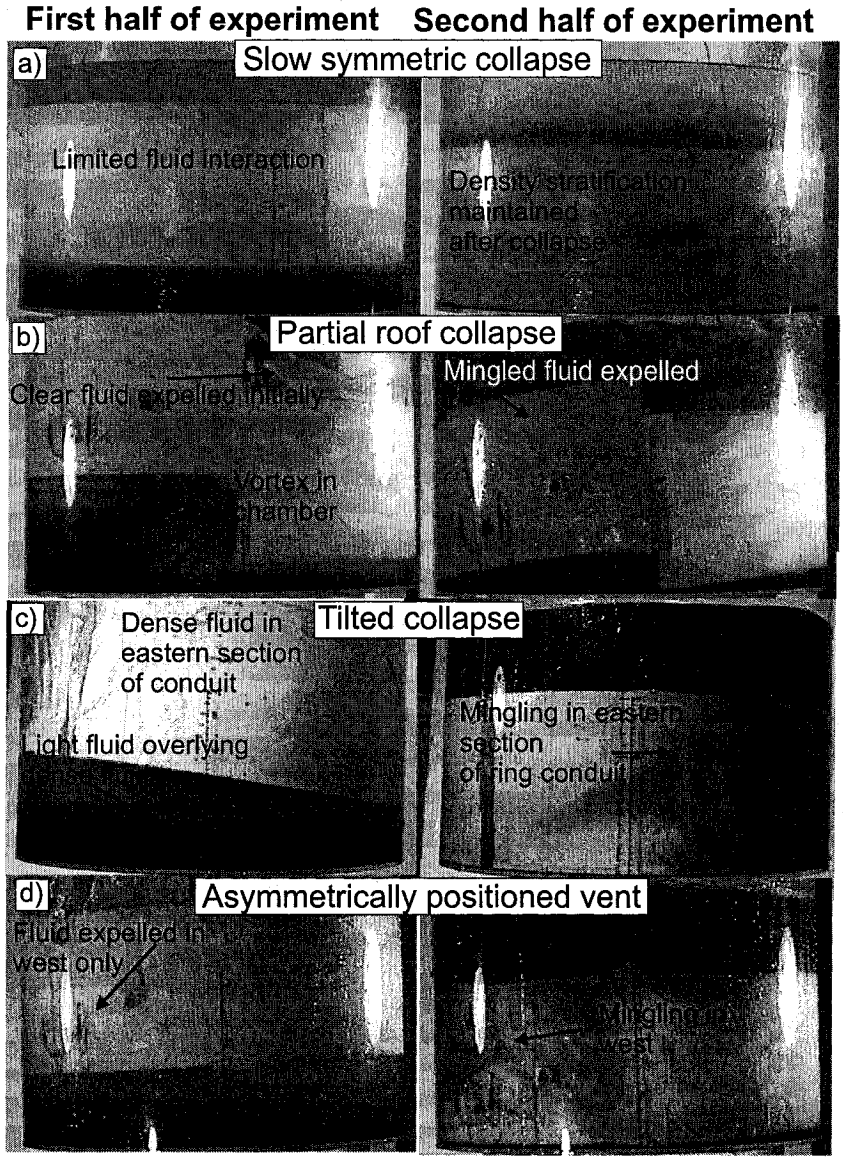
First half of experiment
Second half of experiment
a)
Slow symmetric collapse
Limited fluid interaction
Density stratification maintained after collapse
b)
Partial roof collapse
Clear fluid expelled initially
Vortex in chamber
Mingled fluid expelled
c)
Tilted collapse
Dense fluid in eastern section of conduit
Light fluid overlying
Mingling in eastern section of ring conduit
d)
Asymmetrically positioned vent
Fluid expelled in west only
Mingling in west

FIGURE 4. Variation in the bulk ignimbrite composition erupted during the formation of Lake City caldera. Data presented are from Hon (1987) and Chapter 2 (this thesis). The graph shows the stratigraphic position of each sample; samples where the stratigraphic position is unsure have been omitted, however it should be noted that these samples plot within the compositional variation bands shown on the diagram. The compositional variation increases from the Lower to the Upper Sunshine Tuff. However, there is not a gradual change from one composition to the next as expected for symmetric collapse of the whole roof.

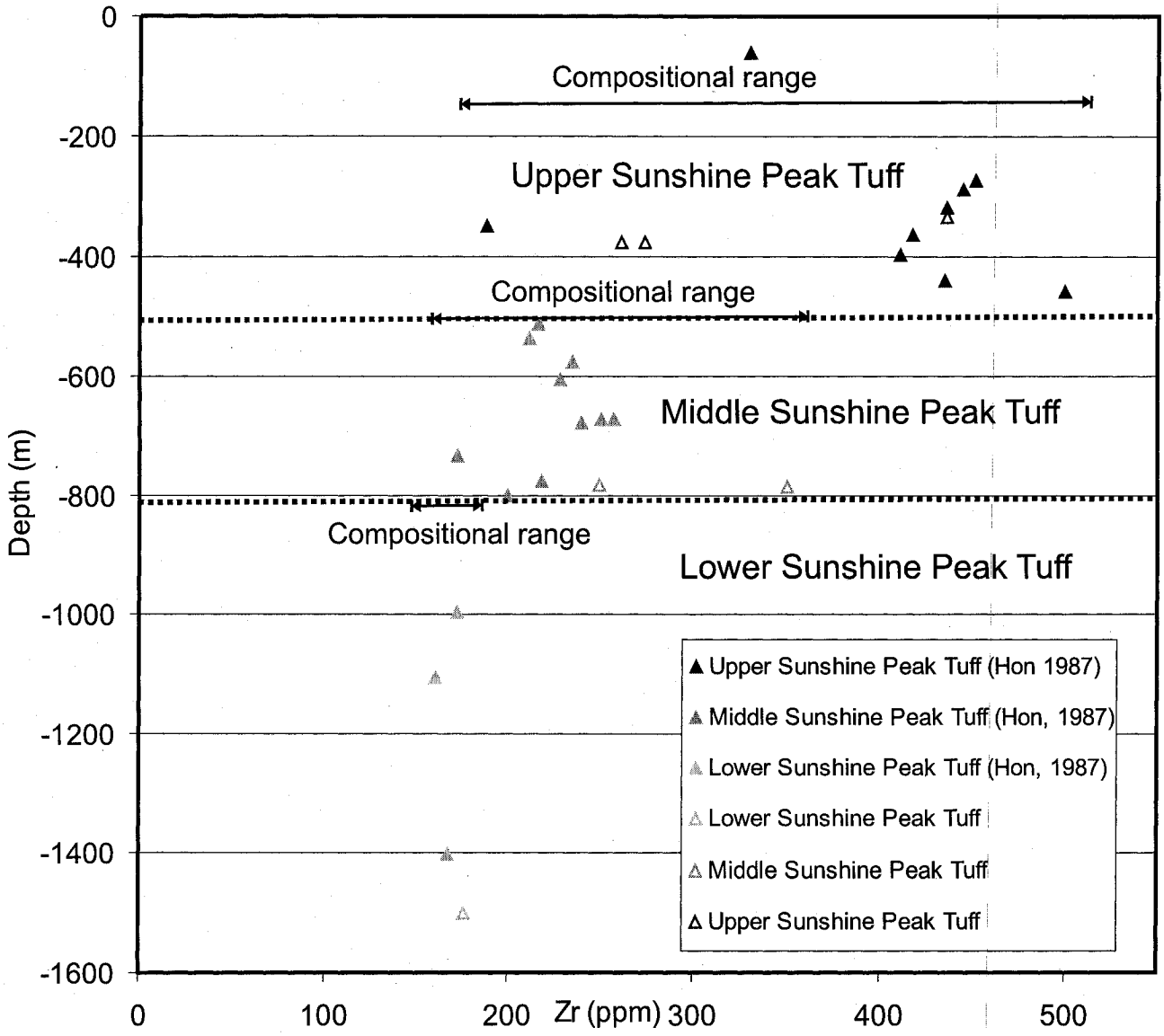
0
-200
-400
-600
-800
-1000
-1200
-1400
-1600
Depth (m)
0
100
200
300
400
500
Zr (ppm)
Compositional range
Upper Sunshine Peak Tuff
Compositional range
Middle Sunshine Peak Tuff
Compositional range
Lower Sunshine Peak Tuff
Upper Sunshine Peak Tuff (Hon 1987)
Middle Sunshine Peak Tuff (Hon, 1987)
Lower Sunshine Peak Tuff (Hon, 1987)
Lower Sunshine Peak Tuff
Middle Sunshine Peak Tuff
Upper Sunshine Peak Tuff

trachyte pumices; at higher stratigraphic levels, bulk composition fluctuates and becomes reversely zoned (Fig. 4). The third ignimbrite to erupt was the Upper Sunshine Tuff; this unit contains four different types of pumice, shows the largest compositional range with complex zonation, and terminates by erupting dominantly silicic magma (Fig. 4). To summarize, the Lower Sunshine Tuff was erupted without magma interaction, while the magmas of the Middle Sunshine Tuff and Upper Sunshine Tuff were intruded by mafic trachyte before they erupted, and show zonation and evidence of dynamic magma movement at the end of collapse (Hon 1987; Chapter 2, this thesis).

In summary, our experiments indicate that piecemeal collapse into a density stratified silicic magma chamber forms vortices within the chamber that disturb or destroy magmatic stratification (Fig. 3). This magmatic interaction will cause the bulk composition of the erupted magma to vary temporally in a manner different from the zonation originally present in the chamber (Fig. 3). Lateral and vertical compositional variation and mingling textures can be expected in magma remaining in the ring dyke and post-collapse chamber.

MAGMA RISE DURING RESURGENCE

The collapse process reconfigures the architecture of the roof of the magma chamber. The chamber roof is physically displaced and extensively fractured and faulted, creating new structural pathways between the roof and the surface. After collapse, lithostatic equilibrium is no longer maintained at the base of the magma chamber

(Kennedy and Stix, 2003); for this reason, magma commonly rises from depth. The new magma that rises may either (1) cause chamber rejuvenation, driving further eruptions or intrusions of the magma remaining in the chamber, or (2) bypass the main magma body, erupting or intruding at shallow levels. Either mechanism will produce deformation primarily through shallow intrusion (Hon and Fridrich, 1989).

The magma remaining in the chamber is likely to be a crystal mush similar to the material found in ring dykes, requiring thermal or volatile rejuvenation to drive further magma rise. The rising magma can be either silicic or mafic. The buoyancy of the new magma and the directional strength of the rocks will determine where the magma ponds. After collapse, the crystal-rich magma chamber and the crust above the magma chamber both contain new structural pathways that reduce the tensile strength of the partially solid rock in the chamber and the solid country rock above the chamber. These weaknesses reduce the overpressure necessary to propagate a crack and form a dyke. This reduction in strength after caldera formation will decrease the likelihood of ponding at the base of the chamber, and instead promote magma rise along pre-existing fractures. The rising magma may erupt or intrude at shallow levels at the base of the erupted ignimbrite. The silicic nature of the ignimbrite provides a buoyancy barrier to rising magma. Additionally the silicic ignimbrite may contain strongly welded horizontal horizons with high tensile strengths. These strong silicic layers may act as cap rock that traps the rising magma. Field studies and drillhole data have shown this style of magma rise is common at many calderas (Hon and Fridrich, 1989; Hon, 1987; Fridrich and Mahood, 1984; McConnell et al., 1995).

Post-collapse magmatic activity at Lake City caldera illustrates this style of resurgence. After the Upper Sunshine Tuff erupted and caldera collapse ceased, the magma remaining in the chamber was crystal-rich, volatile-poor syenite. At this point, monzonitic magma rose from depth and initially ponded beneath the syenitic crystal mush. This caused partial rejuvenation of the syenite, and it intruded into the base of the ignimbrite at the center of the caldera (Chapter 2, this thesis). Simultaneously, the monzonitic magma bypassed much of the syenite in the chamber and followed collapse-related pathways to form separate shallow monzonitic intrusions. The shallow intrusions of syenite and monzonite formed near the base of the ignimbrite within the caldera, causing broad doming of the intracaldera ignimbrite and reactivating subsidence-related faults, which produced up to 1 km uplift in some areas of the caldera (Fig. 5) (Hon, 1987). During this uplift, some of the replenishing magma followed pre-existing fractures to the surface. This magma erupted as dacite lava flows above the ring fracture in the eastern part of the caldera (Fig. 5) (Hon, 1987: Chapter 2 this thesis).

CONCLUSIONS

We have synthesized field, geochemical, and experimental data to illustrate the importance of magma chamber rejuvenation before caldera formation, magma flow within the magma chamber during caldera collapse, and magma movement during resurgence. We illustrate the respective roles and links among these processes during caldera formation.

FIGURE 5. Map and cross-sections of Lake City caldera, Colorado. In the caldera center, post-collapse syenite intruded at the base of the ignimbrite, doming the overlying rocks. In the east, the ring fault was used to channel dacitic magmas to the surface, the fault reactivated without doming the overlying rocks.

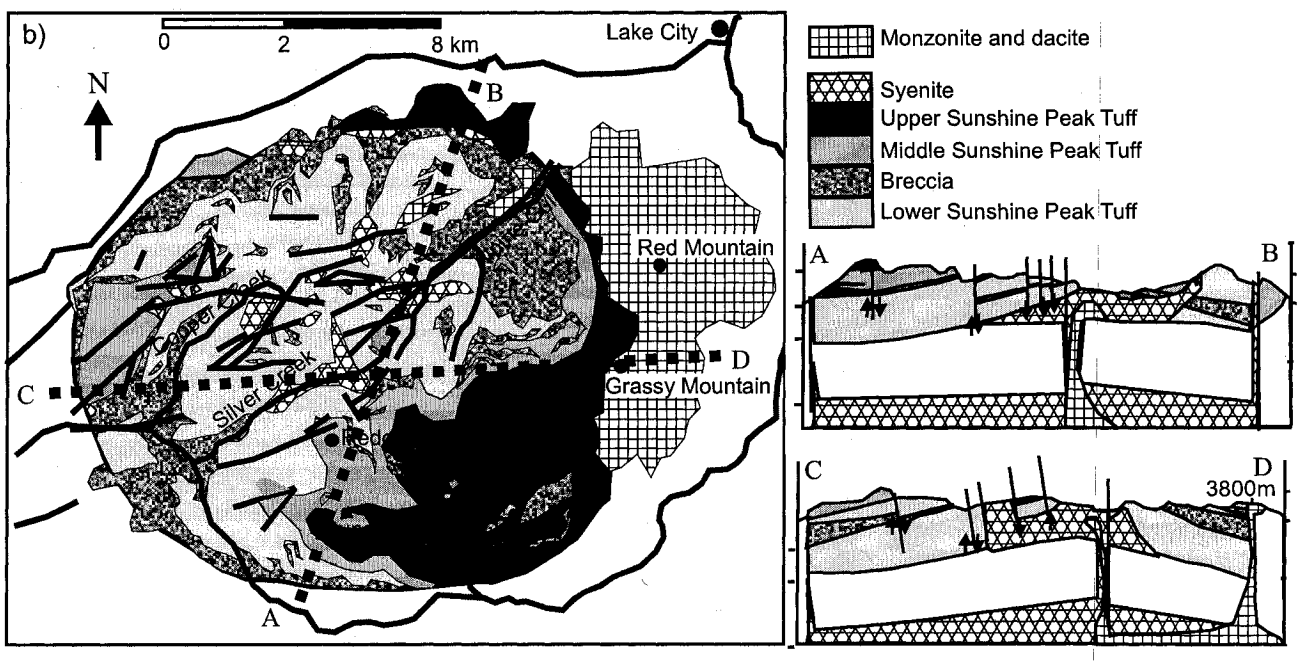
b)
0
2
8 km
N
Lake City
B
Red Mountain
D
Grassy Mountain
C
Silver Creek
A
Monzonite and dacite
Syenite
Upper Sunshine Peak Tuff
Middle Sunshine Peak Tuff
Breccia
Lower Sunshine Peak Tuff
A
B
C
D
3800m

Mechanical considerations indicate the difficulty of maintaining overpressures sufficiently high to propagate dykes to the surface from large silicic magma chambers (Takeuchi and Nakamura, 2001; Jellinek and DePaolo, 2003; Takeuchi, 2004). This situation indicates that magma chamber rejuvenation is frequently necessary to initiate eruptions from large silicic magma chambers. We have shown that chamber rejuvenation can generate underpressure sufficient to cause failure of the chamber's roof, opening conduits to allow dyke propagation and eruption. At Ossipee ring complex, basalt replenishment at the base of the chamber produced sufficient heat to rejuvenate the magma chamber and initiate caldera formation. Chamber rejuvenation has also been described at other large silicic calderas (e.g., Bachman and Bergantz, 2003; Wiebe et al., 2004; Troll et al., 2004).

Magma chamber rejuvenation produces stratified magma prior to caldera formation. Experiments show how the style and rate of collapse will affect magma movement in the chamber, and hence the composition of liquid withdrawn from a collapsing chamber. These experiments show that piecemeal roof collapse strongly influences the degree of liquid interaction during caldera formation. The timing and styles of liquid interaction observed in the experiments are mimicked in the ignimbrite at Lake City and the ring dyke at Ossipee. The style of collapse not only affects magma interaction during collapse but also influences the style of magmatism after collapse.

The collapse style defines the structures created during collapse, and these structures can be used for magma transport. After collapse, structurally weak magma pathways in the chamber and crust allow magmas to rise to shallow levels. Thick intracaldera silicic ignimbrite with sub-horizontal welding horizons provides cap rocks to

contain resurgent intrusions. This framework can explain the type of post-collapse magmatism at Lake City and other caldera systems.

These three magmatic processes define early, middle, and late stages of caldera development in and around large silicic magma chambers. The complementary nature of our field studies and analogue models illustrate some of the intricacies of magmatic processes associated with these stages. Theses intricacies will affect (1) the style of precursory volcanic activity and deformation before a catastrophic caldera-forming eruption (Wolff and Gardner, 1995), (2) the volume, composition, and hence severity of the catastrophic eruption (Civetta et al., 1997) and (3) the style of deformation and magmatism following a catastrophic eruption (Gottsmann et al., 2003). Furthermore, the intricacies of the post-collapse magmatic processes will influence the economic resource potential of the hydrothermal system of the caldera (Elston, 1994; Stix et al, 2003).

REFERENCES

Acocella V., and Funiciello R., 1999, The interaction between regional and local tectonics during resurgent doming: the case of Ischia Island (Southern Italy): Journal of Volcanology and Geothermal Research, v. 88, p. 109-123.

Anderson, A.T., Davis, A.M., and Lu, F.Q., 2000, Evolution of Bishop Tuff rhyolitic magma based on melt and magnetite enclaves and zoned phenocrysts: Journal of Petrology, v. 41, p. 449-473.

Bachman, O., and Bergantz, G.W., 2003, Rejuvenation of the Fish Canyon magma body: A window into the evolution of large-volume silicic magma systems: Geology, v. 31, p. 789-792.

Blake, S., and Ivey G.N., 1986a, Magma mixing and the dynamics of withdrawal from stratified reservoirs: Journal of Volcanology and Geothermal Research, v. 27, p. 153-178.

Blake S., and Ivey, G.N., 1986b, Density and viscosity gradients in zoned magma chambers, and their influences on withdrawal dynamics: Journal of Volcanology and Geothermal Research, v. 30, p. 201-230.

Branney, M.J., 1991, Eruption and depositional facies of the Whorneyside Tuff: an exceptionally large magnitude phreatoplinian eruption: Geological Society of America Bulletin, v. 202, p. 886-897.

Civetta, L., Orsi, G., Pappalardo, L., Fisher, R.V., Heiken, G., and Ort, M., 1997, Geochemical zoning, mingling, eruptive dynamics and depositional processes; the Campanian Ignimbrite, Campi Flegrei caldera, Italy: Journal of Volcanology and Geothermal Research, v. 75, p. 183-219.

Coleman, D.S., Gray, W., and Glazner, A.F., 2004, Rethinking the emplacement and

evolution of zoned plutons; geochronologic evidence for incremental assembly of the Tuolumne Intrusive Suite, California: Geology, v. 32, p. 433-436.

Cruden, A.R., 1998, On the emplacement of tabular granites: Journal of the Geological Society of London, v. 155, p. 853-862.

Eichelberger, J.C., Chertkoff, D.G., Dreher, S.T., and Nye C.J., 2000, Magmas in collision; rethinking chemical zonation in silicic magmas: Geology, v. 28, p. 603-606.

Elston, W.E., 1994, Siliceous volcanic centers as guides to mineral exploration; review and summary: Economic Geology and the Bulletin of the Society of Economic Geologists, v. 89, p. 1662-1686.

Folch, A., Codina, R., and Marti, J., 2001, Numerical modeling of magma withdrawal during explosive caldera-forming eruptions: Journal of Geophysical Research, v. 106, p. 16,163-16,175.

Fridrich, C.J., and Mahood, G.A., 1984, Reverse zoning in the resurgent intrusions of the Grizzly Peak cauldron, Sawatch Range, Colorado: Geological Society of America Bulletin, v. 95, p. 779-787.

Fulignati, P., Marianelli, P., Santacroce, R., and Sbrana, A, 2004, Probing the Vesuvius magma chamber-host rock interface through xenoliths: Geological Magazine, v. 141, p. 417-428.

Gottsmann, J., Berrino, G., Rymer, H., and Williams-Jones, G., 2003, Hazard assessment during caldera unrest at the Campi Flegrei, Italy; a contribution from gravity-height gradients: Earth and Planetary Science Letters, v. 211, p. 295-309.

Gualda, G.A.R., Cook, D.L., Chopra, R., Qin, L., Anderson, A.T. Jr., and Rivers, M., 2004, Fragmentation, nucleation and migration of crystals and bubbles in the Bishop Tuff

rhyolitic magma: Transactions of the Royal Society of Edinburgh: Earth Sciences, v. 95, p. 375-390.

Halliday, A.N., Mahood, G.A., Holden, P., Metz, J.M.,; Dempster, T.J., and Davidson, J.P., 1989, Evidence for long residence times of rhyolitic magma in the Long Valley magmatic system; the isotopic record in precaldera lavas of Glass Mountain: Earth and Planetary Science Letters, v. 94, p. 274-290.

Heiken, G., Goff, F., Gardner, J.N., Baldridge, W.S., Hulen, J.B., Nielson, D.L., and Vaniman, D.T., 1990, The Valles/Toledo caldera complex, Jemez volcanic field, New Mexico: Annual Review of Earth and Planetary Sciences, p. 27-53.

Hildreth, E.W., 1981, Gradients in silicic magma chambers: Implications for lithospheric magmatism: Journal of Geophysical Research, v. 86, p. 10153-10192.

Hon, K.A., 1987, Geologic and petrologic evolution of the Lake City Caldera, San Juan Mountains, Colorado. Ph.D. Thesis, University of Colorado, Boulder, Colorado, 244p.

Hon, K., and Fridrich, C.J., 1989, How calderas resurge: Bulletin - New Mexico Bureau of Mines & Mineral Resources, Report: 131, p. 135.

Jellinek, A.M., and DePaolo, D.J., 2003, A model for the origin of large silicic magma chambers; precursors of caldera-forming eruptions: Bulletin of Volcanology, v. 65, p. 363-381.

Kennedy, B., and Stix, J., 2003, Stages in the temporal evolution of calderas: Geoscience Canada, v. 30, p. 129-140.

Marsh, B.D., 1984, On the mechanics of caldera resurgence: Journal of Geophysical Research, v. 89, p. 8245-8251.

Marsh, B.D., 2000, Magma Chambers: In Sigurdsson, H., Houghton, B., McNutt, S., Rymer, H., and Stix, J. (eds.), Encyclopedia of Volcanoes: Academic Press, San Diego, USA, p. 191-206.

McConnell, V.S., Shearer, C.K., Eichelberger, J.C., Keskinen, M.J., Layer, P.W., and Papike, J.J, 1995, Rhyolite intrusions in the intracaldera Bishop Tuff, Long Valley Caldera, California: Journal of Volcanology and Geothermal Research, v. 67, p. 41-60.

Moore, I., and Kokelaar, P., 1998, Tectonically controlled piecemeal caldera collapse; a case study of Glencoe Volcano, Scotland: Geological Society of America Bulletin, v. 110, p. 1448-1466.

Petford, N., Cruden, A.R., McCaffrey, K.J.W., and Vigneresse, J.L., 2000, Granite magma formation, transport and emplacement in the Earth's crust: Nature, v. 408, p. 669-673.

Rubin, A.M., 1995, Getting granite dikes out of the source region: Journal of Geophysical Research, v. 100, p. 5911-5929.

Rosenberg, C.L., and Handy, M.R., 2005, Experimental deformation of partially melted granite revisited; implications for the continental crust: Journal of Metamorphic Geology, v. 23, p. 19-28.

Sisson, T.W., and Bacon, C.R., 1999, Gas driven filter pressing in magmas: Geology, v 27, p. 613-616.

Smith, R.L., and Bailey, R.A., 1968, Resurgent cauldrons: Memoir - Geological Society of America, p. 613-662.

Smith, R.L., 1979, Ash-flow magmatism: Special Paper - Geological Society of America, no.180, p. 5-27

Sparks, R.J., Huppert, H.E., and Turner, J.S., 1984, The Fluid dynamics of evolving magma chambers: Philosophical Transactions of the Royal Society of London, v. A310, p. 511-534.

Spera, F.J., 1984, Some numerical experiments on the withdrawal of magma from crustal reservoirs: Journal of Geophysical Research, v. 89, p. 8222-8236.

Spera, F.J., Yuen, D.A., Greer, J.C., and Sewell, G., 1986, Dynamics of magma withdrawal from stratified magma chambers: Geology, v. 14, p. 723-726.

Sparks, R.J., Sigurdsson, H., and Wilson, L., 1977, Magma mixing: a mechanism for triggering acid explosive eruptions: Nature, v. 267, p. 315-318.

Stix, J., Kennedy, B., Hannington, M., Gibson, H., Fiske, R., Mueller, W., and Franklin, J., 2003,Caldera-forming processes and the origin of submarine volcanogenic massive sulfide deposits: Geology, v. 31, p. 375-378.

Sumner, J.M., and Wolff, J., 2003, Petrogenesis of mixed-magma, high-grade, peralkaline ignimbrite "TL" (Gran Canaria); diverse styles of mixing in a replenished, zoned magma chamber: Journal of Volcanology and Geothermal Research, v. 126, p. 109-126.

Tait, S., Jaupart, C., and Vergniolle, S., 1989, Pressure, gas content and eruption periodicity of a shallow, crystallising magma chamber: Earth and Planetary Science Letters, v. 92, p. 107-123.

Takeuchi, S., and Nakamura, M., 2001, Role of precursory less-viscous mixed magma in the eruption of phenocryst-rich magma; evidence from the Hokkaido-Komagatake 1929 eruption: Bulletin of Volcanology, v. 63, p. 365-376.

Takeuchi, S., 2004, Precursory dike propagation control of viscous magma eruptions: Geology, v. 32, p. 1001-1003.

Taylor, S.R., and McLennan, S.M., 1985, The Continental Crust: its Composition and Evolution. Blackwell Scientific Publications (Oxford), 312p.

Trial, A.F., Spera, F.J., Greer, J., and Yuen, D.A., 1992, Simulations of magma withdrawal from compositionally zoned bodies: Journal of Geophysical Research, v. 97, p. 6713-6733.

Troll, V. R. and Schmincke, H.-U., 2002, Magma mixing and crustal recycling recorded in ternary feldspar from compositionally zoned peralkaline ignimbrite 'A', Gran Canaria, Canary Islands: Journal of Petrology v. 43, p. 243–270.

Troll, V.R., Donaldson, C.H., and Emeleus, C.H., 2004, Pre-eruptive magma mixing in ash-flow deposits of the Tertiary Rum Igneous Centre, Scotland: Contributions to Mineralogy and Petrology, v. 147, p. 722–739.

Wiebe, R.A., Manon, M.R., Hawkins, D.P., and McDonough W.F., 2004, Late stage mafic injection and rejuvenation of the Vinalhaven granite, Coastal Maine: Journal of Peterology, v. 45, p. 2133-2153.

Williams, H., 1941, Calderas and their origin: University of California Publications in Geological Sciences, v. 25, p.239-346.

Wolff, J.A., Woerner, G., and Blake, S., 1990, Gradients in physical parameters in zoned felsic magma bodies; implications for evolution and eruptive withdrawal: Journal of Volcanology and Geothermal Research, v. 43, p. 37-55.

Wolff, J.A., and Gardner, J.N., 1995, Is the Valles Caldera entering a new cycle of activity?: Geology, v. 23, p. 411-414.

Woods, A.W., and Koyaguchi, T., 1994, Transitions between explosive and effusive eruptions of silicic magmas: Nature, v. 370, p. 641-644.

CONCLUSION

PRINCIPAL CONCLUSIONS

1. A large silicic magma chamber formed by fractional crystallization and was rejuvenated by basaltic magma before caldera formation at Ossipee ring complex.
2. The mingled ring dyke at Ossipee demonstrates that magma interactions were enhanced in the chamber towards the end of caldera collapse.
3. The complex zonation patterns seen in ignimbrites and intrusions at Lake City caldera are the result of magma replenishment events at the top of the magma chamber and magma interactions during caldera collapse.
4. At Lake City, resurgence was characterized by the rise of a chemically distinct batch of magma. This event rejuvenated the magma mush remaining in the chamber, and allowed this residual mush to intrude along subsidence structures to shallow levels above the main magma body.
5. Analogue experiments indicate that magmatic interactions increase towards the end of caldera collapse, with asymmetric and piecemeal subsidence promoting lateral and vertical variation in zoning patterns of ignimbrites and intrusions.
6. Numerical modeling shows that magma rejuvenation can lead to a decrease in chamber pressure, failure of the chamber roof, and the formation of a caldera.

CONTRIBUTIONS TO KNOWLEDGE

The thesis proposes a new and novel mechanism to explain caldera formation, with support from field and geochemical data and a numerical model. In addition, this thesis presents new and innovative interpretations of two classic calderas, Ossipee ring complex and Lake City caldera. These interpretations highlight the fact that magmatic interactions accelerate as calderas collapse. Scaled analogue experiments provide a new mechanism to explain this observation. The experiments are the first investigation addressing how asymmetric caldera formation influences magmatic interaction. The results are striking, showing that magmatic interactions are drastically enhanced in cases of asymmetric collapse. In summary, the thesis presents a multifaceted study of fieldwork, geochemical data, experimental studies and numerical modeling to demonstrate ways in which magmatic processes influence caldera collapse, and in turn, how caldera collapse affects these magmatic processes.

TOPICS FOR FUTURE RESEARCH

This thesis has emphasized the importance of magma chamber rejuvenation and syn-eruption magmatic processes. For my post-doctoral study at the University of British Columbia, I plan to investigate these topics further using numerical and experimental investigations. I will study the development of magma chamber rejuvenation in mechanically realistic crust which deforms visco-elastically, rather than elastically as in the current models. I will also study the movement of liquid in a magma chamber containing both crystals and liquid during eruptions. I propose such movements could cause crystal-melt segregation and crystal fractionation to occur on eruptive timescales. In other words, can crystal fractionation occur instantaneously on a geologic timescale?